Surface Science Studies of Model Oxide Catalysts: Molybdenum Oxide on Single Crystal Iron Oxide

Chanut Bamroongwongdee

March 2010

Thesis submitted for PhD degree

Cardiff School of Chemistry

Cardiff University, 2010

ProQuest LLC
789 East Eisenhower Parkway
P.O. Box 1346
Ann Arbor, MI 48106-1346

To my parents

แด่บิดามารดา

ACKNOWLEDGEMENTS

This thesis is accomplished whereby I have been advised and supported by many people. I have pleasure to express my gratitude for a number of persons who became involved with this thesis.

The first person I would like to thank is my supervisor Professor Michael Bowker. His support, enthusiasm, encouragement and suggestions on research led me throughout this thesis. He has always been willing to answer my question.

The second person I would like to thank is my mentor Dr. Philip Davies who kept an eye on the progress of my work and always was available when I needed his advises. I would also like to thank the other members of my PhD committee who monitored my work and gave valuable comments: Dr. Damien Murphy and Dr. Peter Griffiths. I thank you all.

Moreover, I wish to extend my warm and sincere thanks to all of my colleagues for all their help and support. My colleagues of the Bowker's group all gave me the feeling of being at home at work.

In addition, this research has been supported and funded by Thai Government Science and Technology Scholarship, Ministry of Science and Technology, Thailand and I am grateful for their support.

Finally, I feel a deep sense of gratitude for my parents who provided me all the love and the greatest support in all times and over all distances. I am grateful for my sisters and my brothers for their loving support. I am glad to be one of them.

Chanut Bamroongwongdee,

March 11, 2010

ABSTRACT

This thesis is concerned with the study of molybdenum oxide layer deposited on a single crystal iron oxide substrate.

The surface structure of an iron oxide single crystal was investigated by X-ray photoelectron (XPS), low-energy He^+-ion scattering (LEIS), low-energy electron diffraction (LEED), and scanning tunneling microscopy (STM). XPS measurement reveals the presence of both Fe^{2+} and Fe^{3+} oxidation states. LEED and STM results obtained from this surface were consistent with a formation of an $Fe_3O_4(111)$ surface termination. LEED pattern and STM images reveal an hexagonal array with a periodicity of ~6 Å and steps in multiples of ~5 Å. LEIS result shows the presence of both Fe and O in the topmost layer.

Well ordered epitaxial molybdenum oxide films were grown on iron oxide single crystal substrates. Their surface structure, morphology and composition were characterized by XPS, LEIS, LEED, and STM. They were prepared by depositing molybdenum oxide onto the substrate and then oxidizing it in 10^{-7} mbar of oxygen. In the sub-monolayer regime, molybdenum oxide formed islands of ordered structure. XPS measurement yields a Mo $3d_{5/2}$ binding energy consistent with the presence of Mo^{6+}. High resolution STM images reveal a large hexagonal lattice of protrusions with a 12 Å periodicity. This pattern is consistent with a p(4×4) structure. At the monolayer coverage, a $(2\sqrt{3}\times 2\sqrt{3})R30°$ surface structure is produced by annealing in oxygen (10^{-7} mbar) at 973 K. STM topographies show clear hexagonal distribution with the period of 1.1 nm corresponding to the pattern observed in LEED. These results suggest that molybdenum oxide may interact with $Fe_3O_4(111)$ to form iron molybdate which is stable on the surface.

CONTENTS

1 Introduction

Chapter I

Introduction

In this chapter, the motivation for the research presented in this thesis is discussed. The interest in metal oxide surfaces has continued to grow. Metal oxide surfaces play a very important role in many areas of technology including sensing, energy storage, and especially heterogeneous catalysis. Several surface science techniques including X-ray photoelectron spectroscopy (XPS), low-energy electron diffraction (LEED), ion scattering spectroscopy (ISS), and scanning tunnelling microscopy (STM) are used to study these metal oxide films in a model system.

1.1. Introduction

Over several decades, mixed metal oxides have been used in a vast variety of fields that is involved in electronic and magnetic devices, chemical sensors, environmental science, biology and other fields. One of the most important applications is heterogeneous catalysis. Mixed metal oxides are widely used as catalysts in a variety of catalytic reactions, but the atomic-scale mechanism of catalytic reactions on mixed metal oxides is not well understood. Basic knowledge of the chemistry of mixed metal oxide surface greatly lags behind those of metals and semiconductors because of the difficulty in surface preparation of metal oxides for ultrahigh vacuum (UHV) surface science studies [1]. This knowledge is essential for understanding the physical and chemical properties of these mixed metal oxides, which play a technologically important role in developing effective targeted catalysts.

Modern techniques of surface science can provide significant new insight into the structure of a metal oxide surface, its composition, and the oxidation states present. Within the last decade, surface science studies on single-crystal metal-oxide samples have received considerable attention. For example, the selective oxidation of hydrogen sulphide to sulphur over three vanadium-based mixed-oxide catalysts including the binary oxides of V-Mo, V-Bi, and V-Mg was studied by Li et al [2]. They found the new compounds $Mo_6V_9O_{40}$, $BiVO_4/Bi_4V_6O_{21}$, and MgV_2O formed in the binary oxides. The binary oxides show much higher performance than those of the corresponding single-oxide catalysts for the selective oxidation of hydrogen sulphide. Fe-Cr mixed oxides are more widely employed commercial catalysts for hydrogen production through the water-gas shift (WGS) reaction [3]. Due to their complex and time-consuming activation protocol before use and their instability in contact with air, new WGS catalysts have been developed. Ceria and titania are important compounds in catalysts used for the WGS reaction and for the oxidation of carbon monoxide [4-6]. Rodriguez et al. found that in the $CeO_x/TiO_2(110)$ system, cerium cations were in an oxidation state of 3+ that are quite different from those seen in bulk ceria or for ceria nanoparticles deposited on metal [7].

In addition, Fe–Mo mixed oxides are widely used as catalysts for several catalytic reactions. For example, it is known that iron molybdate are active for the oxidation of hydrocarbons and alcohols, particularly for the commercial oxidation of methanol to formaldehyde [8-11]. This thesis concerns model system study of the formaldehyde synthesis reaction, a selective oxidation of methanol to formaldehyde over iron molybdate catalysts. Thin Fe–Mo mixed oxide model catalyst films were grown onto the iron oxide substrates. Their surface structures were investigated with STM and LEED, their electronic structures and surface compositions by photoelectron spectroscopy (XPS and ISS).

1.2. Heterogeneous catalysis

Catalysis plays an important role in our society. Most important chemicals and fuels produced in industry involve catalysts. Catalysis has also become indispensable in environmental pollution control e.g. the catalytic converter in automobiles to reduce the pollution (such as NO) from automotive vehicles. Catalytic reactions are preferred in environmentally friendly green chemistry to replace stoichiometric processes in which all reactants are consumed and large amounts of waste are generated. Nowadays, catalysis is important for our economies and it will be more important in the future.

In heterogeneous catalysis, the catalyst and the reactant are in different phases. Most heterogeneous catalysis is usually referred to a system where the catalyst is a solid and the reactants and products are liquids or gases. The advantage of heterogeneous catalysis is that the catalysts are in general easy to handle, separate, and recycle.

A simple example of gas/solid heterogeneous catalysis is the catalytic oxidation of carbon monoxide. In this reaction, an oxygen atom is added to the carbon monoxide in the presence of a noble metal catalyst. The catalytic cycle (Figure 1.1) involves several steps. First, a carbon monoxide molecule is adsorbed onto "active sties" on the surface of catalyst. Meanwhile, oxygen molecules are also adsorbed on the catalyst. The O–O bond of oxygen molecule is then broken, and the O atoms move across the metal surface. Eventually, an O atom diffuses close to the CO molecule. The C–metal bond is then replaced by a C–O bond. When this happens, the connection with the surface breaks and the new carbon dioxide molecule diffuses back into the gas phase, thereby regenerating the active sites on the surface for the following catalytic cycle. Catalysts work by providing an energetically favourable pathway to the desired product, in which the activation energies of all intermediate steps are lower than that of the gas phase reaction.

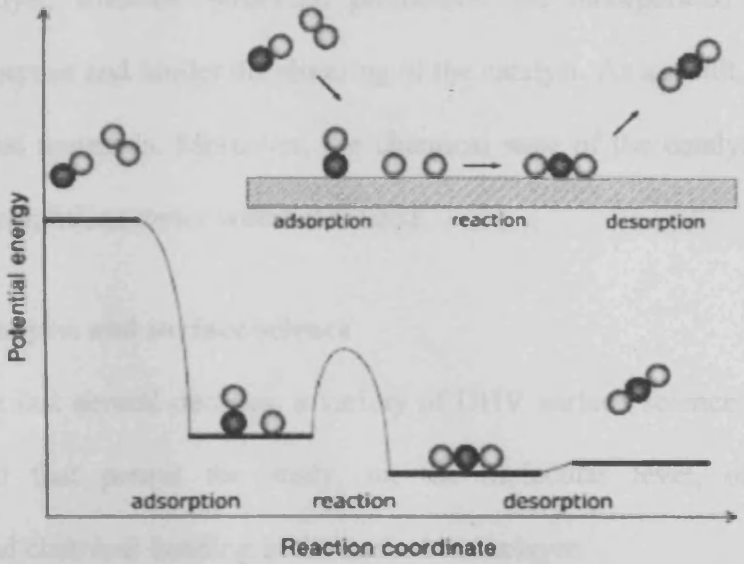

Figure 1.1. Schematic representation of the oxidation of carbon monoxide on noble metal catalysts: $CO + \frac{1}{2} O_2 \rightarrow CO_2$ [12].

Many heterogeneous catalysts, which should preferably contain nanometer-sized particles, can function by being highly dispersed on solid surfaces that enhances the effectiveness or minimises their cost. In general, industrial supports are mainly based on porous, high-surface-area materials such as silica, alumina, silica/alumina, titania, active carbon, or zeolite. Unsupported catalysts have also found application in industry, e.g. iron-based catalyst for CO hydrogenation (the Fischer-Tropsch process). Iron molybdate catalysts are one of the unsupported catalysts which are widely used in industrial and commercial processes to produce formaldehyde.

Metals, metal oxides, sulphides, nitrides, carbides, organometallic complexes, and enzymes can be use as catalysts. The fundamental properties of a catalyst, that are the main key to determining the suitability of a catalyst for a process, are its activity, selectivity and stability. "Chemical promoters" are chemical species/elements that, added in small amounts, contribute to enhancing and/or stabilising the product selectivity and

activity of catalyst, whereas "structural promoters" are incorporated to improve the mechanical properties and hinder the sintering of the catalyst. As a result, catalysts can be quite complicated materials. Moreover, the chemical state of the catalytic surface often depends on the conditions under which it is used.

1.3. Model catalysts and surface science

Over the last several decades, a variety of UHV surface science techniques have been developed that permit the study, on the molecular level, of the structure, composition, and chemical bonding in the surface monolayer.

The most obvious model systems for heterogeneous catalysis are single crystals because they are highly uniform, crystalline, and high-purity materials. Single crystals of metal, as shown in Figure 1.2(a), were used as model systems for studying the structure, composition, and chemical bonding at surfaces. They can be cleaved to expose different crystal facets, allowing the density variation of surface atoms in various surroundings such as those on terraces, steps, kinks, and corners and they are particularly useful for determining relationships between surface structure and catalytic activity. These relationships have provided the basis for inferring the identities of catalytic sites for many reactions. In addition, single crystals offer the advantage that they can be used for studying the effects of promoters and multicomponent catalysts. For example, Kim and Somorjai determined the role of each component in the Pt-Re-S catalyst system on hydrocarbon conversion reactions [13].

Investigations of single crystals have been extended to metal oxide surfaces in order to understand the surface chemistry on metal oxides. Ordered metal oxide surfaces can be obtained by using either single crystal metal oxide samples, as shown in Figure 1.2(b), or thin epitaxial metal oxide films grown on single crystals. As most surface science experiments, including electron spectroscopy or STM, require conducting

samples, the studies of metal oxide single crystals are restricted. Some oxides such as TiO_2, Al_2O_3, SiO_2, and Fe_2O_3 have a small band gap, which facilitate conduction and can perform these measurements. Well ordered thin oxide films therefore offer a wide range of opportunities for investigating the more complex systems of catalysis.

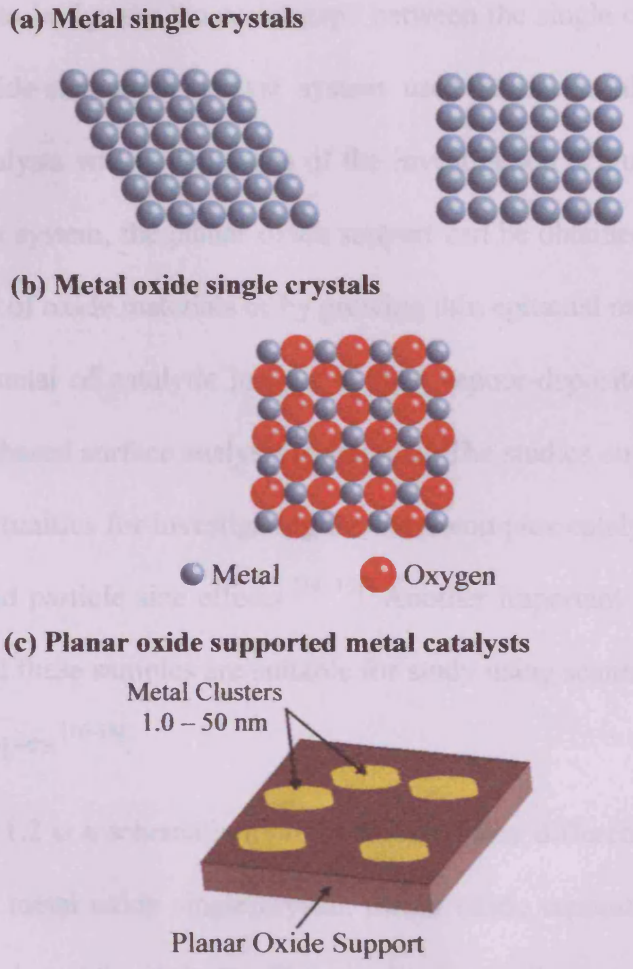

Figure 1.2. Schematic representation of four types of catalysts.

However, there is the discrepancy between the model catalysts and the real catalysts. Model catalysts are well-ordered single crystals, which are often studied under low pressures or even UHV, feed streams of pure component, and small reactors, while most real catalysts consist of porous, high surface area materials (typically 50-400 m^2g^{-1}), which are commonly used as the support materials. For example, silica, alumina, or titania are commonly used the oxide supports. This difference is so-called the material gap. In order to bridge the "material gap" between the single crystal model systems and the "real" oxide-supported catalyst system used in industrial processes, planar oxide supported catalysts will be the focus of the investigation (Figure 1.2(c)). In this type of model catalyst system, the planar oxide support can be obtained by using the conductive single crystals of oxide materials or by growing thin epitaxial metal oxide films. Onto this support, the metal of catalytic interest is then vapour-deposited and investigated using modern UHV based surface analysis techniques. The studies on these models offer a wide range of opportunities for investigating the more complex catalysts such as metal-support interactions and particle size effects [14, 15]. Another important feature of utilising model catalysts is that these samples are suitable for study using scanning tunnelling and atomic force microscopies [16-18].

Figure 1.2 is a schematic representation of four different types of catalysts: metal single crystal, metal oxide single crystal, planar oxide supported, and high surface area oxide-supported metal catalysts. The employment of planar model oxide supported catalysts provides many of the advantages associated with single crystals relative to high surface are catalysts [19, 20]. For example, Goodman's group [19] reported that nanoclusters (Au, Pd, and Ag) supported on $TiO_2(110)$ grew three-dimensional clusters, but at low coverages, Au and Pd formed quasi-two dimensional clusters. Additionally, they found

that the electronic structure of these clusters depends on the cluster size by the appearance of a band gap as the cluster size decreased.

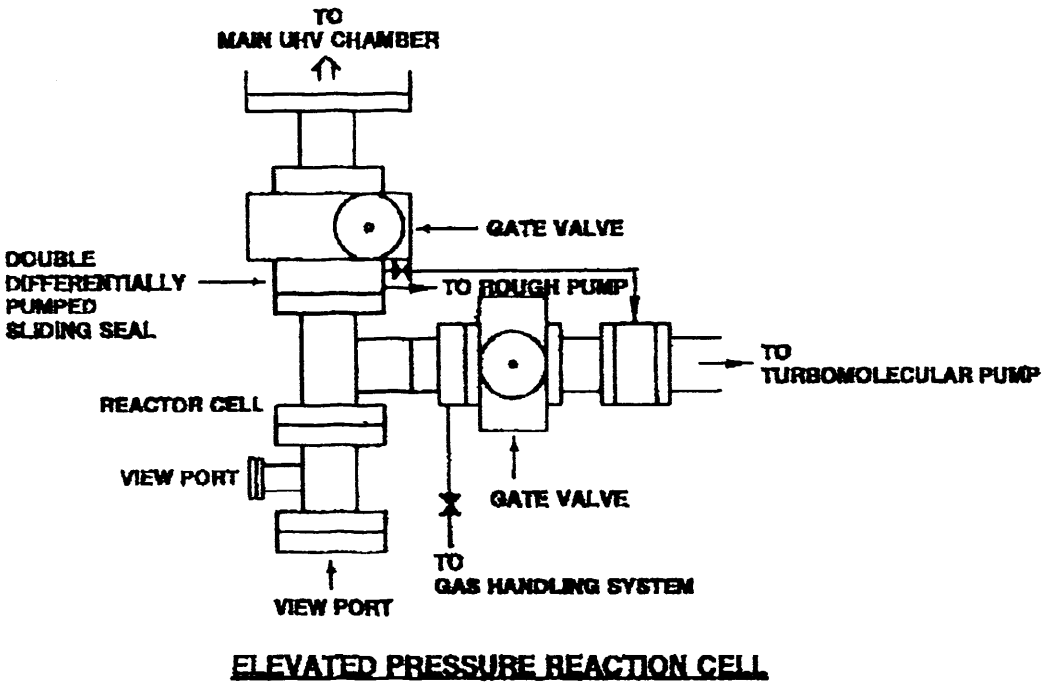

Figure 1.3. Side view of the elevated pressure cell/reactor showing the connections to the UHV chamber, the turbomolecular pump and gas handling system [21].

Furthermore, there is still the other problem of the pressure gap between conventional UHV and industrial conditions which originates from the difference between the pressures at which most typical surface analytical techniques can work ($P < 10^{-7}$ torr) and those employed in typical industrial processes (realistic (near-) atmospheric pressure or higher). To bridge the so-called pressure gap between UHV and high pressure studies, experimental systems have been developed that integrate a high-pressure cell or micro-reactor with an UHV surface analysis chamber. Figure 1.3 displays an example of an elevated pressure reaction cell that shows the connection to the UHV chamber, the turbomolecular pump and gas handling system [21]. This feature allows a sample to be transferred between the UHV surface analysis chamber and the high-pressure reaction

cell via a series of differentially pumped sliding seals. This combined elevated pressure reactor cell–UHV surface analysis chamber system is advantageous over traditional vacuum systems because repair of the sample and/or holder does not significantly perturb the UHV analysis chamber vacuum.

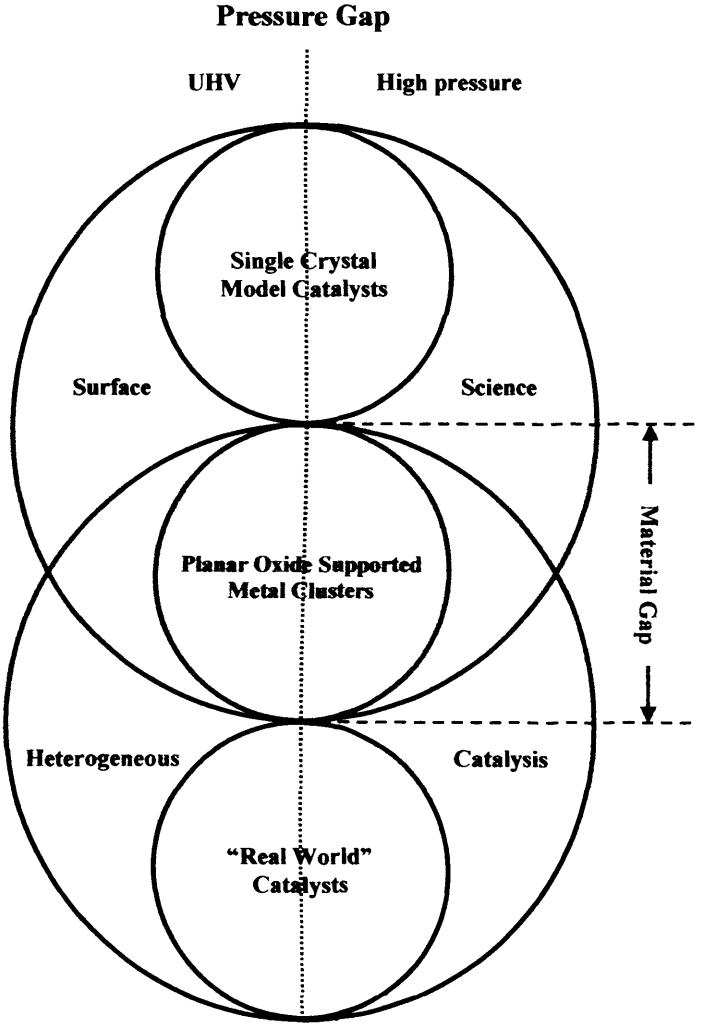

Figure 1.4. Schematic drawing of the relationship between surface science and heterogeneous catalysis [22].

A schematic drawing of the relationship between surface science and heterogeneous catalysis is shown in Figure 1.4, which displays a fundamental approach to

the study of a heterogeneous catalytic process. As shown in this sketch, the first step is started from the top and then move to the bottom (the material gap). That means the well-defined metal single crystals are first examined and then move through the studies of planar oxide supported metal clusters. Finally, "real world" catalysts are studied using modern surface science techniques. Additionally, the problem of the pressure gap (from left to right) has been addressed through the employment of a combined UHV-high pressure apparatus. As shown in Figure 1.4, the critical model system for both the surface science and heterogeneous catalysis studies is the study of planar oxide supported metal clusters.

1.4. The concept of the active site

Since heterogeneous catalysis takes place on the catalyst surface, the nature of the surface is crucial to performance. It is therefore essential to consider the structure of the surface which exerts a strong effect on the heterogeneous catalysis. The surfaces of a real catalyst, used in a large process, are not entirely uniform. At the microscopic level, crystal surfaces are found to consist of terraces and steps. In addition, terraces, which are also shown in Figure 1.5, have a variety of surface sites and may also exhibit kinks, vacancies, adatoms, and point defects. These irregular points often serve as the sites to catalyse a reaction. This is because the surface atoms at those individual surface sites are not fully co-ordinated so that there are many different ways for interacting with molecules of substrate. This concept of "active sites" originally proposed in the 1920s by the English chemist Sir Hugh Taylor, who also suggested that chemically active sites on the surface of a catalyst might be sparse [23, 24], is well established now. Figure 1.5 shows a ball model of a surface, indicating the different kinds of defects which may be present. The coordination numbers for each of the different atoms positions are different. For example, the terrace atoms are most coordinated which contains nine nearest neighbours in the

surface; the steps have only seven, while the isolated adatoms on terrace have three nearest neighbours.

Following Sabatier's principle, the active sites of catalysts should facilitate the adsorption of the reactants and should also be able to remove the products from the surface in order to regenerate the active surface sites.

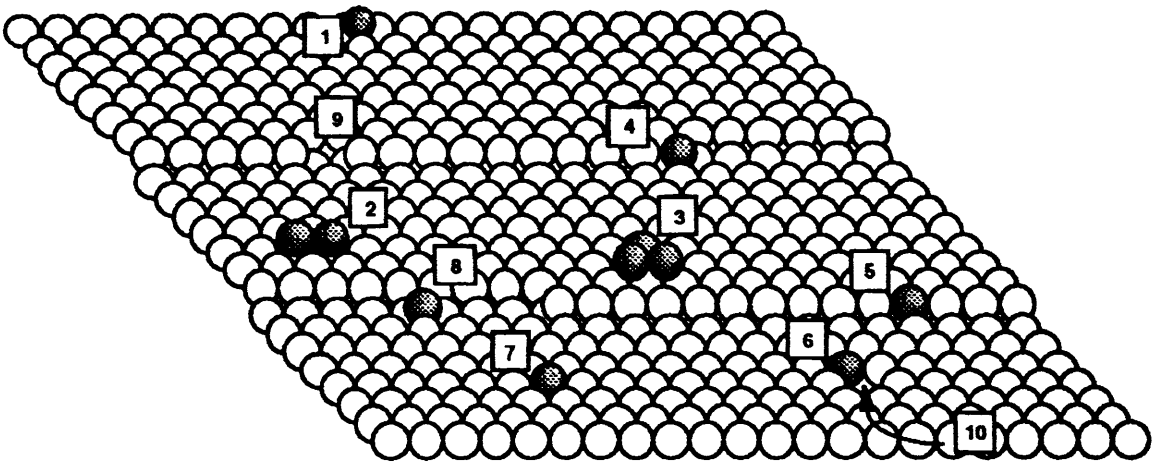

	Atom type	Top plane co-ordination	Total co-ordination
1	Adatom	0	3
2	Dimer	1	4
3	Trimer	2	5
4	Kink edge	3	6
5	Step	4	7
6	Terrace vacancy neighbour	5	8
7	Terrace	6	9
8	Step adatom	2	5
9	Step vacancy	-	-
10	Terrace vacancy	-	-

Figure 1.5. Schematic representation of a solid catalyst crystal surface showing different defects on the surface [25].

1.5. Catalytic oxidation of methanol

Since the first commercial production of formaldehyde in Germany in the 1880s, formaldehyde has become one of the most important industrial chemicals in the world. Formaldehyde is a primary derivative of methanol, and accounts for about 40 percent of its single end uses. At present, a new formaldehyde plant has a capacity corresponding to about 40,000 tons per year expressed as formalin consisting of a 37% solution in water of formaldehyde. The most prominent industrial use of formaldehyde is in the production of

urea-formaldehyde resins and phenolic resins which are used in manufacturing "pressed wood" products such as plywood, particleboard, and fiberboard. Other well-established applications are in the production of textiles, plastics, paper products, fertilizers, dyes, cosmetics, and paints. At present, the commercial production of formaldehyde starts from methanol as the feedstock, other processes such as oxidation of hydrocarbons have only limited success, and are no longer economically feasible.

The production of formaldehyde from methanol is based on two reactions, namely the dehydrogenation and oxidation of methanol.

Dehydrogenaiton

$$CH_3OH \rightarrow CH_2O + H_2 \qquad \Delta H = +85 \text{ kJ mol}^{-1} \qquad (1.1)$$

Oxidation

$$CH_3OH + \tfrac{1}{2}O_2 \rightarrow CH_2O + H_2O \qquad \Delta H = -157 \text{ kJ mol}^{-1} \qquad (1.2)$$

Methanol dehydrogenation to formaldehyde is not controlled by thermodynamics, and so requires a catalyst having good selectivity. Today, manufacturing formaldehyde from methanol can be divided into two primary routes – silver catalysed and metal oxide (Formox) catalysed processes, and to date neither technology has established a leading role. The mechanism of the silver-catalysed process is a combination of two reactions involving the dehydrogenation and oxidation of methanol, whereas the metal oxide catalysed process employs the oxidation reaction only.

1.5.1. The metal oxide catalysed process

The direct oxidation of methanol to formaldehyde using metal oxide catalysts was originally developed in the 1930s and has been increasingly used in commercial production since the 1950s. Recently, the use of metal oxide catalysts for methanol oxidation has been receiving increasing attention. The drawing in Figure 1.6 is a schematic flow diagram illustrating the typical metal oxide catalysed process. The process

comprises feeding an appropriate mixture of methanol and air to a vaporiser where the methanol is vaporised and passed into the tubular reactor usually containing several thousand tubes, each packed with a metal oxide catalyst. Since the oxidation of methanol to formaldehyde is exothermic, the temperature is controlled by a suitable heat-transfer medium circulated in a shell containing the tubes. The reacted gases containing formaldehyde are passed to an absorber system, which normally includes refrigeration for exhaust-gas scrubbing. With the increasing attention to environmental problems, the removal of trace levels of formaldehyde from process exhaust gas becomes more important. The conversion of methanol to formaldehyde for this process is higher than that for the silver catalysed process, and may be as high as 97-98%. The greatest advantage of this process is that the products which contain typically 50% formaldehyde with less than 1% methanol can be obtained directly without distillation.

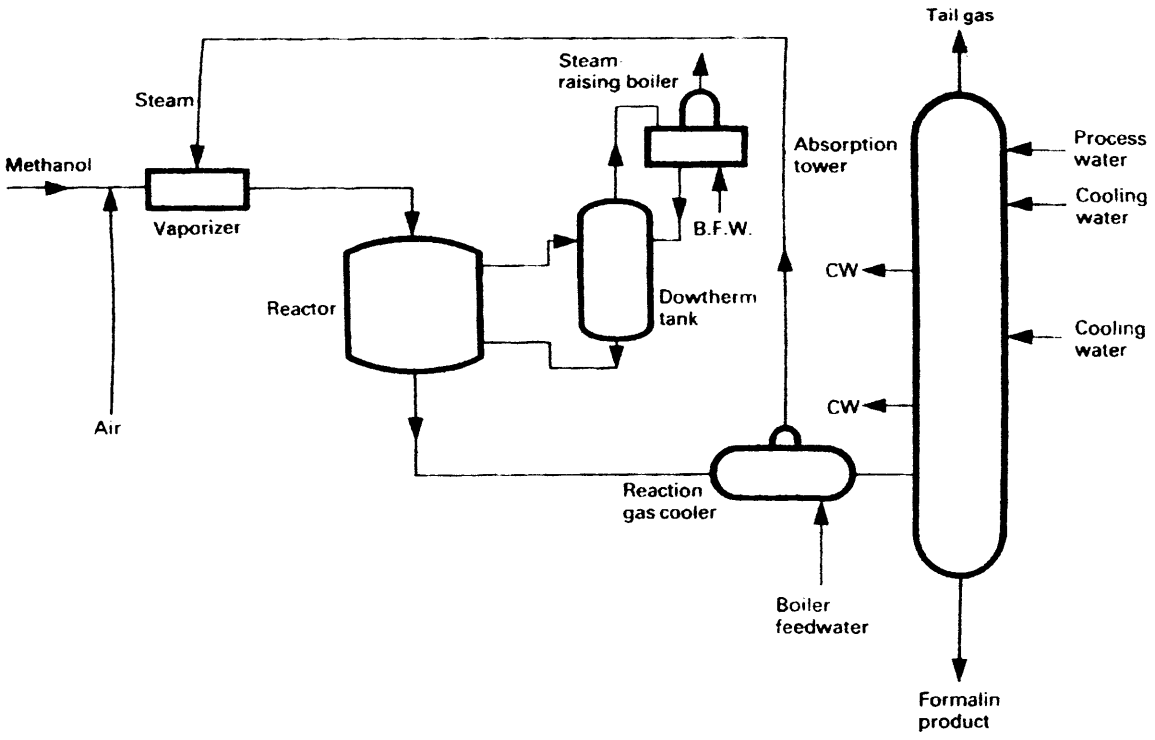

Figure 1.6. Flowchart of a typical metal oxide catalysed formaldehyde process [26].

1.5.2. Metal oxide catalysed reactions

Oxidising methanol to formaldehyde using a metal oxide catalyst is a highly exothermic process. To achieve high selectivity in the conversion of methanol to formaldehyde, the removal of the reaction heat is an important consideration. The heat is removed to limit secondary reactions and to prevent overheating the catalyst. The catalyst contained in tubes is cooled by a circulating heat exchange medium and the operating temperature is usually in the range of about 300-400°C. Under these operation conditions, side reactions are less important than at the higher temperatures of the silver catalyst process, and decomposition of formaldehyde as in reaction (1.3) is considered to be the only significant secondary reaction [27].

$$CH_2O + \tfrac{1}{2}O_2 \rightarrow CO + H_2O \qquad \Delta H = -236.5 \text{ kJ mol}^{-1} \qquad (1.3)$$

The industrially widely used mixed metal oxide catalysts for the catalytic oxidation of methanol are composite oxides between iron and molybdenum manufactured from the coprecipitation of aqueous solutions of iron and molybdenum salts which are subsequently calcined and pelleted. The pellets may be cylindrical pellets or Raschig rings which are widely used due to providing low pressure drop characteristics. Ferric molybdate, $Fe_2(MoO_4)_3$, is reported to be the catalytically active component in the iron molybdenum oxide.

The life of a catalyst is limited by a number of factors; two limitations are the build-up of pressure drop across the reactor and decrease of catalyst activity. In order to limit these adverse effects, temperature control is very important in this reaction, which is based on the heat removal from the tubes by the circulating heat exchange medium. Examination of the catalyst shows that molybdenum oxide, MoO_3, leaves the catalyst surface and crystallise as a fibre-like material in the voids of the catalytic bed. The loss of

MoO_3 leads to increasing pressure drop and degradation of the catalyst mechanical resistance. In addition, MoO_3 loss causes the formation of molybdenum-deficient phases which result in the formation of hot spots in the catalyst bed. Molybdenum deficiency is associated with loss in overall conversion of methanol to formaldehyde. The deactivation of iron-molybdate catalysts is the main cause in the limitation of catalyst life, or cycle length, which typically range from one to two years. Burriesci et al. showed that ferric molybdate catalyst at "hot spot" regions can exhibit an improvement in the selectivity toward formaldehyde with lower production of carbon monoxide which is probably due to the loss of MoO_3 [28].

1.6. Heterogeneous catalysis by molybdenum oxides

1.6.1. Overview of molybdenum

The element molybdenum has been used since ancient times. The element was identified by Carl Wilhelm Scheele, the Swedish scientist, in 1778 when it was discovered in natural minerals. In 1782, Peter Jacob Hjelm showed that Scheele's *substance*, previously believed to be the metal, was in fact the oxide form. Shortly thereafter, in 1782, Peter Jacob Hjelm showed that it was possible to produce the metal by reduction of molybdenum oxide by carbon. The construction of the periodic table by Mendeléev in 1872 focused attention on molybdenum as it was then one of most heavy known elements. This stimulated much research on the element but it was not until 1891 that the French Schneider Company first used molybdenum alloys in the production of armour plate.

The average concentration of molybdenum in the earth's crust is around 1.5 ppm by weight in the lithosphere [29]. Molybdenum is obtained mainly from the mineral molybdenite (MoS_2). Molybdenite mineral resources are mined by a combination of open-cast pit and underground block caving techniques.

Heterogeneous catalysis by compounds of molybdenum, and in particular the oxides of molybdenum, is well established and has a long history. The versatility of molybdenum oxide based catalysts is related to the rich and diverse properties of the wide variety of phases and mixed phases that can be synthesised.

1.6.2. Molybdenum oxide in selective oxidation catalysts

Molybdenum oxides have been investigated as catalysts and catalyst components for selective oxidation. They are more commonly used as catalyst components, but there are also reports of molybdenum oxide alone as a selective oxidation catalyst. The oxidation of methanol over molybdenum trioxide has been studied by Sleight et al. [30] using the technique of temperature programmed desorption (TPD). The production of formaldehyde from methanol indicates the ability of molybdenum trioxide to oxidise alcohols in a relatively facile manner owing to the lability of lattice oxygen.

Smith and Ozkan [31, 32] have used several characterisation techniques including X-ray diffraction (XRD), laser Raman spectroscopy, *in situ* laser Raman spectroscopy combined with isotopic labelling, scanning electron microscopy, three-dimensional imaging technique, XPS, BET surface area measurement, and temperature-programmed reduction to investigate the oxygen insertion pathway in the partial oxidation of methane to formaldehyde over molybdenum trioxide catalysts. Their studies have suggested that the oxygen insertion to form formaldehyde takes place preferentially at Mo=O sites located on the side plane, while the bridging Mo–O–Mo sites located on the basal planes are involved in complete oxidation.

More commonly, molybdenum has been used as a catalyst component for mixed-metal oxide catalysts for selective oxidation. Probably the most well known of these mixed oxide catalysts are those based on molybdenum and iron. The molybdenum–iron catalysts are exceptionally active and selective and they have been applied industrially.

The catalytic activity of mixed iron–molybdenum oxides for methanol oxidation to formaldehyde was reported in 1931 by Adkins and Peterson [33] who discovered this catalyst. Nowadays, the iron molybdate catalyst has been extensively used for the oxidation reaction of methanol to formaldehyde as shown in Figure 1.7. Industrial iron molybdate catalysts are non-stoichiometric iron-molybdenum mixed oxides with molybdenum excess. The effect of molybdenum excess for iron molybdate catalysts has been studied by several authors [9, 10, 34]. In these studies, molybdenum excess does not significantly change the activity for the oxidation of methanol per unit surface area but it improves the stability of catalysts and provides higher surface area, higher conversion, and higher selectivity for formaldehyde.

Figure 1.7. Selective oxidations over ferric molybdate catalysts.

The mechanism of methanol oxidation over ferric molybdates is believed to take place via the Mars and van Krevelen (MvK) mechanism [9]. The rate determining step, which it is desired to catalyse for formaldehyde formation is activation of the C–H bond. With this two-component catalyst, the first step was found to be the C–H bond cleavage from an adsorbed methoxy group, which is catalysed by the basic site acting as the nucleophile. The next step is activation of a second hydrogen and insertion of an oxygen atom into the organic molecule resulting in formation of reduced iron molybdate catalyst [28, 35].

Some further mixed-metal oxides containing molybdenum, such as bismuth molybdates, are known to be effective catalysts in certain selective oxidation reactions, for instance the oxidation of propene to acrolein and the ammoxidation of propene to acrylonitrile [36].

1.7. Iron molybdate literature review

Iron-molybdenum mixed oxides are widely employed catalysts for several catalytic reactions. For example, it is known that iron-molybdenum oxides exhibit good catalytic activity for the selective oxidation of hydrocarbons and alcohols, particularly for the commercial formaldehyde production by selective oxidation of methanol [37-39]. There are two stoichiometric iron molybdates, ferric molybdate, $Fe_2(MoO_4)_3$, and ferrous molybdate, $FeMoO_4$ [34]. The former is generally considered to be the active phase of the iron-molybdenum mixed oxide catalyst for the selective oxidation of methanol to formaldehyde while the latter is formed during the redox catalytic process.

Several researchers attribute that the deactivation of the iron molybdate catalysts results from the loss of molybdenum trioxide by volatilisation [11]. Burriesci et al. studied the catalysts discharged from industrial plants and found that the catalyst samples from the hot spot changed significantly compared to those from other zones [28]. At the hot spot, there was both a decrease of the MoO_3 content and of the specific surface area of the catalyst whereas above this zone, they were similar to those of the fresh catalyst. Below this zone, the decrease of surface area and the increase in the MoO_3 content were found which can be due to the condensation of the MoO_3 arising at the hot spot. They also found that α-$FeMoO_4$ and β-$FeMoO_4$ were present in the outer layer of the hot spot catalyst pellets in addition to ferric molybdate, while inside these pellets only ferric molybdate was found. These results led them to propose that during industrial operation, the reduction of Fe^{3+} to Fe^{2+} only occurs in the outer layer of the hot spot catalyst. They concluded that catalysts discharged from industrial plants are accompanied by the increasing pressure drop in the catalytic bed and the decrease of activity. However, an increase in formaldehyde selectivity often occurs.

As mentioned above, when iron molybdate catalysts are reduced by methanol, ferrous molybdates are formed and the iron oxide, which is found on the surface of catalyst pellets, results from the reoxidation of ferrous molybdate according to the reaction (1.4) [28]:

$$3FeMoO_4 + \tfrac{3}{4}O_2 \rightarrow Fe_2(MoO_4)_3 + \tfrac{1}{2}Fe_2O_3 \qquad (1.4)$$

Pernicone reported that there are two different causes of deactivation of Fe-Mo oxide catalyst in industrial plants: formation of iron oxide and the MoO_3 loss by volatilisation [40]. He also found that the catalyst samples from the hot spots have a Mo/Fe atomic ratio equal to 1 which evidenced the presence of a molar mixture of $Fe_2(MoO_4)_3$–$\frac{1}{2}Fe_2O_3$. Additionally, he concluded that the oxidation of methanol proceeds with a reduction of the catalyst bulk according to the reaction (1.5):

$$Fe_2(MoO_4)_3 + CH_3OH \rightarrow 2FeMoO_4 + MoO_3 + HCHO + H_2O \qquad (1.5)$$

Molybdenum trioxide and ferrous molybdate formed in the reaction (1.5) are less active than ferric molybdate and the iron oxide is formed by reoxidation of ferrous molybdate according to the reaction (1.4) as proposed by Burriesci et al. [28].

Carbucicchio et al. [41] and Forzatti [42] investigated the deactivation of silica supported Fe_2O_3-MoO_3 catalyst in the oxidation of methanol to formaldehyde. They reported that the loss of activity during reaction was due to a partial destruction of ferric molybdates. In addition, Fe^{3+} ions within silica increase and molybdenum sublimates during the deactivation process.

As mentioned above, iron-molybdenum oxide mixed oxides and their catalytic properties have been extensively investigated, whereas there are few works focusing on the XPS characterisation of iron molybdate catalysts.

Okamoto et al. found that the binding energies of the Fe $2p_{3/2}$ and Fe 3p levels for the Fe_2O_3-MoO_3 mixed oxides catalysts seemed to be dependent on the composition, with values of 711.4 and 56.2 eV, respectively, at low Mo content (Mo/Fe ≤ 1.5) but consistently higher values of 711.7 and 56.5 eV, respectively at Mo/Fe ≥ 1.63 [43]. The binding energies of Fe with Mo/Fe ≥ 1.63 were attributed to the presence of ferric molybdate. Comparing the catalyst composition of the surface and the bulk, they concluded that at Mo/Fe ≤ 1.5, the catalyst surface is enriched in Fe, forming a structure in which iron oxide covers the ferric molybdate, whereas at Mo/Fe ≥ 1.63, a considerable segregation of Mo occurs over the ferric molybdate. They also concluded that the presence of MoO_3 excess in Fe_2O_3-MoO_3 catalysts is essential to produce stoichiometric ferric molybdate at the catalyst surface.

Al-Shihry et al. studied unsupported MoO_3-Fe_2O_3 mixed catalysts [44]. The binding energies of Mo 3d and Fe 2p levels for MoO_3-Fe_2O_3 obtained by these authors are summarized in the Table 1.1. The binding energies for MoO_3 and for MoO_3-0.5% Fe_2O_3 are characteristic of Mo^{6+}. For the other MoO_3-Fe_2O_3 samples, the binding energies of Mo 3d level indicated the presence of Mo^{5+} and Mo^{6+}. In case of Fe_2O_3, the binding energy of Fe $2p_{3/2}$ level is characteristic of Fe^{3+}. For all MoO_3-Fe_2O_3 samples, the Fe 2p binding energies are lower than that of Fe_2O_3 and are consistent with the results obtained by other authors [45, 46] for iron molybdate catalysts.

Soares et al. studied stoichiometric and industrial like catalysts. For all characterized catalysts, only Mo(VI) molybdate species with the binding energies between 232.1 and 232.4 eV have been found, while Fe(II) and Fe(III) with the binding energies of 709.9 and 711.9 eV, respectively were found for fresh and post-reaction catalysts [11]. As expected, the Fe^{2+}/Fe^{3+} surface atomic ratio in post-reaction catalysts is greater than that in fresh catalysts, however only the industrial like catalyst presented

reduced iron species (ferrous molybdate detected by Mössbauer spectroscopy) in the bulk. They also concluded that Mo excess is beneficial since it maintains activity and selectivity and keeps the surface in higher oxidation state.

Table 1.1. Binding energies of Mo 3d and Fe 2p levels for MoO_3-Fe_2O_3 catalysts [44].

Sample	Mo (eV)		Fe (eV)	
	$3d_{5/2}$	$3d_{3/2}$	$2p_{3/2}$	$2p_{1/2}$
MoO_3	233.4	236.5	–	–
MoO_3-Fe_2O_3				
0.5% Fe_2O_3	233.4	236.5	712.4	726.0
5% Fe_2O_3	230.7	233.5	711.8	725.4
10% Fe_2O_3	229.7	233.0	710.6	724.6
30% Fe_2O_3	230.7	233.0	710.1	724.4
50% Fe_2O_3	230.3	233.2	712.6	727.6
70% Fe_2O_3	230.2	233.1	712.5	727.2
90% Fe_2O_3	230.2	233.2	713.4	725.6
Fe_2O_3	–	–	713.6	727.2

Bowker et al. studied the selective oxidation of methanol on Fe_2O_3, MoO_3 and an industrial iron molybdate catalyst in order to establish the role of each catalyst component [47]. Using pulsed-flow reactor and TPD experiments, they found that formaldehyde was never detected when haematite was used as catalyst. The molybdate materials displayed high selectivity towards formaldehyde and was found more active than molybdenite alone. They attributed the different behaviour between iron and molybdenum samples to the stronger binding energy of oxygen in the former and the higher concentration of

cation sites. From TPD results, they postulated that, over Fe_2O_3, only bidentate formate species are formed whereas the major intermediate present on the molybdate materials is the methoxy species.

Recently, House et al. studied the reduction process of an iron molybdate catalyst (Mo:Fe = 2.2:1) using pulsed-flow reactors, TPD, XRD, and XPS [8]. These authors found that, with reduction at temperature above 250°C, oxygen migration occurs through the catalyst sample and leads to the formation of new phases of MoO_2, Mo_4O_{11}, and α-$FeMoO_4$. The selectivity of the catalysts during reduction is changed toward CO and shifted toward CO_2 with reduction above 300°C. Using XRD, Raman, TPD, and pulse-flow reactor, House et al. found differences in the behaviour between pure Fe_2O_3 and Fe–Mo catalysts with even low levels of Mo present [48]. This effect strongly depends on the molybdenum loading. They also found by scanning transmission electron microscopy (STEM) and XPS that Mo enrichment occurs at the surface of iron molybdate catalysts [49].

However, the application of UHV surface science methods to study the iron molybdate surface has not been reported. Thus, in this work, the molybdenum oxide films grown on the iron oxide single crystal are characterised using a variety of the surface science techniques including XPS, LEED, low-energy He^+-ion scattering (LEIS or ISS), and STM.

1.8. Aims of this work

This research deals primarily with the preparation of model catalyst systems related to selective oxidation catalysis. The aim is to investigate the chemistry of model iron molybdate surface towards probe molecules relevant to heterogeneous catalysis. These model catalyst systems were prepared by the growth of molybdenum oxide onto

the iron oxide single crystal using the hot-filament metal oxide deposition technique (HFMOD). The surface structures of molybdenum oxide films deposited on iron oxide single crystal were characterised via a traditional surface science approach using UHV conditions including LEED, XPS, ISS, and STM.

1.9. Thesis synopsis

An overview of this thesis is presented as follows. This thesis starts with a general introduction of heterogeneous catalysis and explains the connection between catalysis and surface science. Then it introduces the concept of the active site, the catalytic oxidation of methanol, the heterogeneous catalysis by iron molybdate catalyst, and literature review of iron molybdate.

Chapter 2 describes the experimental equipment employed in this work, to the whole experimental set up and the working of the apparatus, and as well the preparation and characterisation of the iron oxide-supported molybdenum oxide catalysts deposited on iron oxide single crystal substrates. Also discussed is detailed information about the XPS, LEED, ISS, and STM which are the tools used in this research.

In Chapter 3, an analysis of the data and the experimental results for the study of the surface morphology of the iron oxide single crystal are presented. Also presented are the different crystallographic structures of the iron oxides i.e. FeO (wüstite), Fe_3O_4 (magnetite), α-Fe_2O_3 (hematite), and γ-Fe_2O_3 (maghemite). Furthermore, the interaction of the crystal surface with gaseous methanol is discussed in this chapter.

Chapter 4 describes the synthesis and characterisation of the epitaxial molybdenum oxide films with different loadings using XPS, LEED, ISS, and STM measurements. Molybdenum oxide could easily be created by hot-filament metal oxide deposition technique. The interaction of molybdenum oxide with clean iron oxide surface

which depends on the annealing temperature is also presented in this chapter. In the end, the most important results of this work are summarised in Chapter 5, overall conclusion are drawn and some indications of future research directions in this subject are given.

1.10. References

[1] V. E. Henrich and P. A. Cox, *The surface science of metal oxides*, Cambridge University Press, Cambridge, **1994**.

[2] K.-T. Li, M.-Y. Huang and W.-D. Cheng, *Industrial & Engineering Chemistry Research* **1996**, *35*, 621-626.

[3] K. Atwood and M. R. Arnold, *Industrial & Engineering Chemistry* **1953**, *45*, 424-426.

[4] Q. Fu, H. Saltsburg and M. Flytzani-Stephanopoulos, *Science* **2003**, *301*, 935-938.

[5] I. D. González, R. M. Navarro, M. C. Álvarez-Galván, F. Rosa and J. L. G. Fierro, *Catalysis Communications* **2008**, *9*, 1759-1765.

[6] J. A. Rodriguez, S. Ma, P. Liu, J. Hrbek, J. Evans and M. Perez, *Science* **2007**, *318*, 1757-1760.

[7] J. B. Park, J. Graciani, J. Evans, D. Stacchiola, S. Ma, P. Liu, A. Nambu, J. F. Sanz, J. Hrbek and J. A. Rodriguez, *Proceedings of the National Academy of Sciences of the United States of America* **2009**, *106*, 4975-4980.

[8] M. P. House, A. F. Carley and M. Bowker, *Journal of Catalysis* **2007**, *252*, 88-96.

[9] A. P. V. Soares, M. Farinha Portela and A. Kiennemann, *Catalysis Communications* **2001**, *2*, 159-164.

[10] A. P. V. Soares, M. Farinha Portela, A. Kiennemann, L. Hilaire and J. M. M. Millet, *Applied Catalysis A: General* **2001**, *206*, 221-229.

[11] A. P. V. Soares, M. F. Portela, A. Kiennemann and L. Hilaire, *Chemical Engineering Science* **2003**, *58*, 1315-1322.

[12] J. W. Niemantsverdriet, *Spectroscopy in catalysis an introduction*, Wiley-VCH, Weinheim, **2007**.

[13] C. Kim and G. A. Somorjai, *Journal of Catalysis* **1992**, *134*, 179-185.

[14] D. W. Goodman, *Surface Science* **1994**, *299-300*, 837-848.

[15] D. W. Goodman, *Chemical Reviews* **1995**, *95*, 523-536.

[16] W. W. Crew and R. J. Madix, *Surface Science* **1994**, *319*, L34-L40.

[17] D. R. Rainer, C. Xu and D. W. Goodman, *Journal of Molecular Catalysis A: Chemical* **1997**, *119*, 307-325.

[18] U. Schröder, B. J. McIntyre, M. Salmeron and G. A. Somorjai, *Surface Science* **1995**, *331-333*, 337-342.

[19] X. Lai, T. P. S. Clair, M. Valden and D. W. Goodman, *Progress in Surface Science* **1998**, *59*, 25-52.

[20] C. Xu, X. Lai, G. W. Zajac and D. W. Goodman, *Physical Review B* **1997**, *56*, 13464-13482.

[21] J. Szanyi and D. W. Goodman, *Review of Scientific Instruments* **1993**, *64*, 2350-2352.

[22] M. W. Roberts and A. F. Carley, *Surface chemistry and catalysis*, Kluwer Academic/Plenum Publishers, New York, **2002**.

[23] H. S. Taylor, *Proceedings of the Royal Society of London. Series A* **1925**, *108*, 105-111.

[24] H. S. Taylor, *Proceedings of the Royal Society of London. Series A* **1926**, *113*, 77-86.

[25] M. Bowker, *The basis and applications of heterogeneous catalysis*, Oxford University Press, Oxford, **1998**.

[26] M. V. Twigg, *The catalyst handbook*, Manson, 2009, **2008**.

[27] M. Dente and I. Pasquon, *Chem. Ind. (Milan)* **1965**, *47*.

[28] N. Burriesci, F. Garbassi, M. Petrera, G. Petrini and N. Pernicone in *Catalyst Deactivation, Vol. 6* Eds.: B. Delmon and G. F. Froment), Elsevier, Amsterdam, **1980**, pp. 115-126.

[29] J. Emsley, *Nature's building blocks an A-Z guide to the elements*, Oxford University Press, Oxford, **2001**.

[30] W. E. Farneth, F. Ohuchi, R. H. Staley, U. Chowdhry and A. W. Sleight, *The Journal of Physical Chemistry* **1985**, *89*, 2493-2497.

[31] M. R. Smith and U. S. Ozkan, *Journal of Catalysis* **1993**, *141*, 124-139.

[32] M. R. Smith and U. S. Ozkan, *Journal of Catalysis* **1993**, *142*, 226-236.

[33] H. Adkins and W. R. Peterson, *Journal of the American Chemical Society* **1931**, *53*, 1512-1520.

[34] A. P. V. Soares, M. F. Portela and A. Kiennemann, *Catalysis Reviews: Science and Engineering* **2005**, *47*, 125 - 174.

[35] M. Niwa, M. Mizutani, M. Takahashi and Y. Murakami, *Journal of Catalysis* **1981**, *70*, 14-23.

[36] Z. Jirak, R. Salmon, L. Fournes, F. Menil and P. Hagenmuller, *Inorg. Chem.* **1982**, *21*, 4218-4223.

[37] Y. Huang, L. Cong, J. Yu, P. Eloy and P. Ruiz, *Journal of Molecular Catalysis A: Chemical* **2009**, *302*, 48-53.

[38] W. Kuang, Y. Fan and Y. Chen, *Journal of Colloid and Interface Science* **1999**, *215*, 364-369.

[39] J. A. Rodriguez, J. C. Hanson, S. Chaturvedi, A. Maiti and J. L. Brito, *The Journal of Physical Chemistry B* **2000**, *104*, 8145-8152.

[40] N. Pernicone, *Catalysis Today* **1991**, *11*, 85-91.

[41] M. Carbucicchio, P. Forzatti, F. Trifiro, E. Tronconi and P. L. Villa, *Studies in Surface Science and Catalysis* **1980**, *6*, 103-113.

[42] P. Forzatti, *Reaction Kinetics and Catalysis Letters* **1982**, *20*, 213-218.

[43] Y. Okamoto, K. Oh-Hiraki, T. Imanaka and S. Teranishi, *Journal of Catalysis* **1981**, *71*, 99-110.

[44] S. S. Al-Shihry and S. A. Halawy, *Journal of Molecular Catalysis A: Chemical* **1996**, *113*, 479-487.

[45] M. Del Arco, C. Martin, V. Rives, A. M. Estevez, M. C. Marquez and A. F. Tena, *Materials Chemistry and Physics* **1989**, *23*, 517-528.

[46] M. Del Arco, C. Martin, V. Rives, A. M. Estevez, M. C. Marquez and A. F. Tena, *Journal of Materials Science* **1989**, *24*, 3750-3755.

[47] M. Bowker, R. Holroyd, A. Elliott, P. Morrall, A. Alouche, C. Entwistle and A. Toerncrona, *Catalysis Letters* **2002**, *83*, 165-176.

[48] M. P. House, A. F. Carley, R. Echeverria-Valda and M. Bowker, *The Journal of Physical Chemistry C* **2008**, *112*, 4333-4341.

[49] M. House, M. Shannon and M. Bowker, *Catalysis Letters* **2008**, *122*, 210-213.

2 Experimental

Chapter II

Experimental

2.1. Introduction

The experiments which are described in this thesis were performed mainly in an ultra-high vacuum (UHV) system. This UHV system, a customised Omicron Multiprobe® (Omicron nanotechnology GmbH., UK), is a multi-technique surface science UHV system. Initially, a general description of the UHV system is given in this chapter, after which several specific items are treated in more detail.

2.2. Multi-technique UHV system: Multiprobe®

2.2.1. General description

There are some great advantages of using UHV to investigate model supported catalysts. First of all, it allows for the preparation of very well-defined sample surfaces for study and it provides a means to maintain the surface clean for a prolonged period of time. UHV is also required for many of the standard surface science techniques. The customised Omicron Multiprobe® is shown in Figures 2.1 and 2.2.

The Multiprobe® consists of three parts, which are separated by valves: a sample preparation chamber equipped with a scanning tunnelling microscope (STM/AFM) for use at the room temperature and a fast entry lock chamber (FEL chamber), a central chamber and an analysis chamber equipped with a retarding field analyzer for low energy electron diffraction (LEED), ISE 100 fine focus ion source for ion scattering spectroscopy (ISS), DAR 400 X-ray source and EA 125 hemispherical analyser for X-ray

photoelectron spectroscopy (XPS), and a quadrupole mass spectrometer (QMS) for analysing residual gases during the experiments. New substrates can be added or changed without breaking the vacuum of the system. Also new tips in the microscope can be introduced or changed while the vacuum in the system is maintained. The system is pumped by three 240 l/s turbo molecular pumps, a rotary pump, four titanium sublimation pumps and four getter ion pumps.

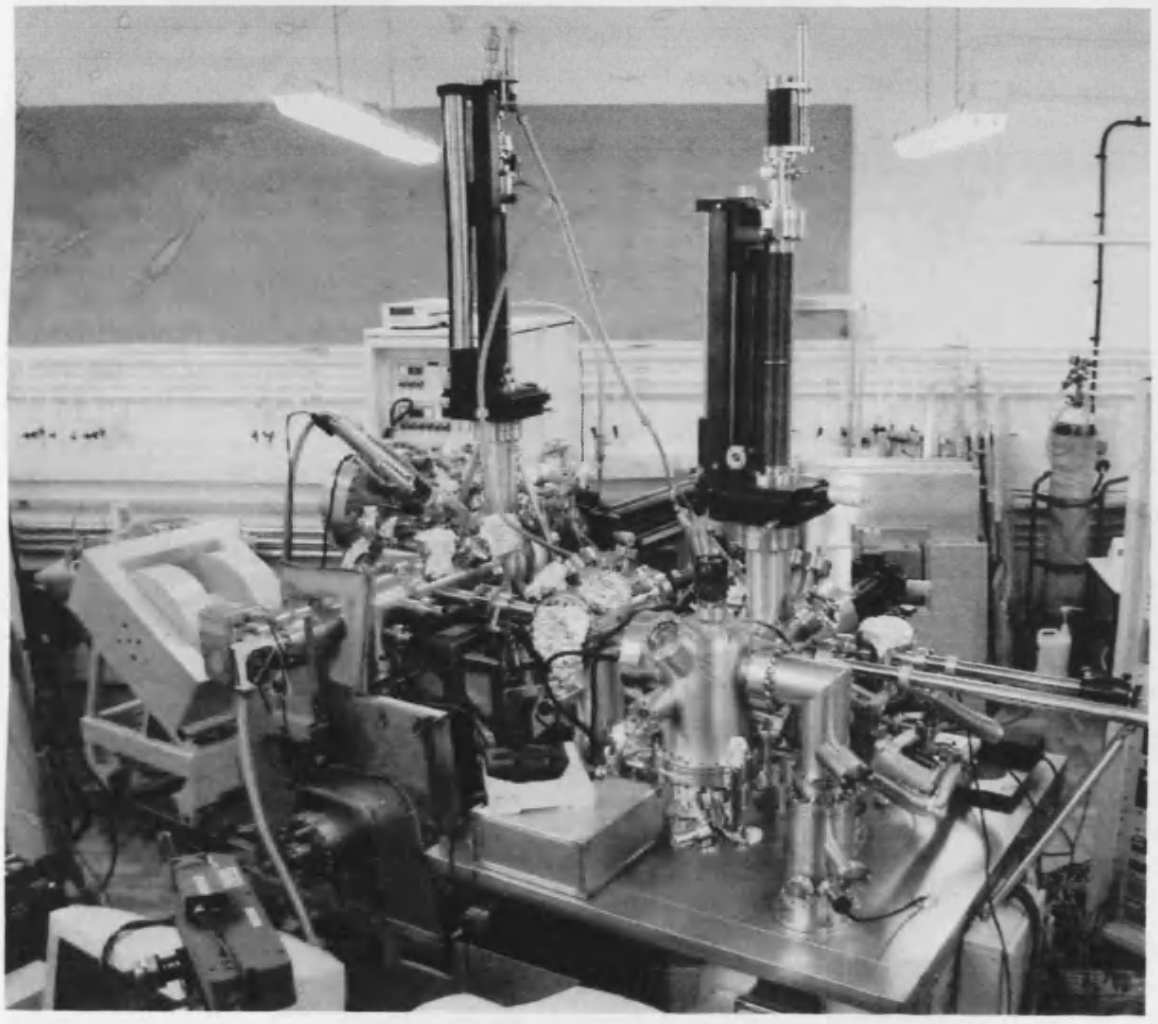

Figure 2.1. Multi-technique UHV system - the customised Omicron Multiprobe®.

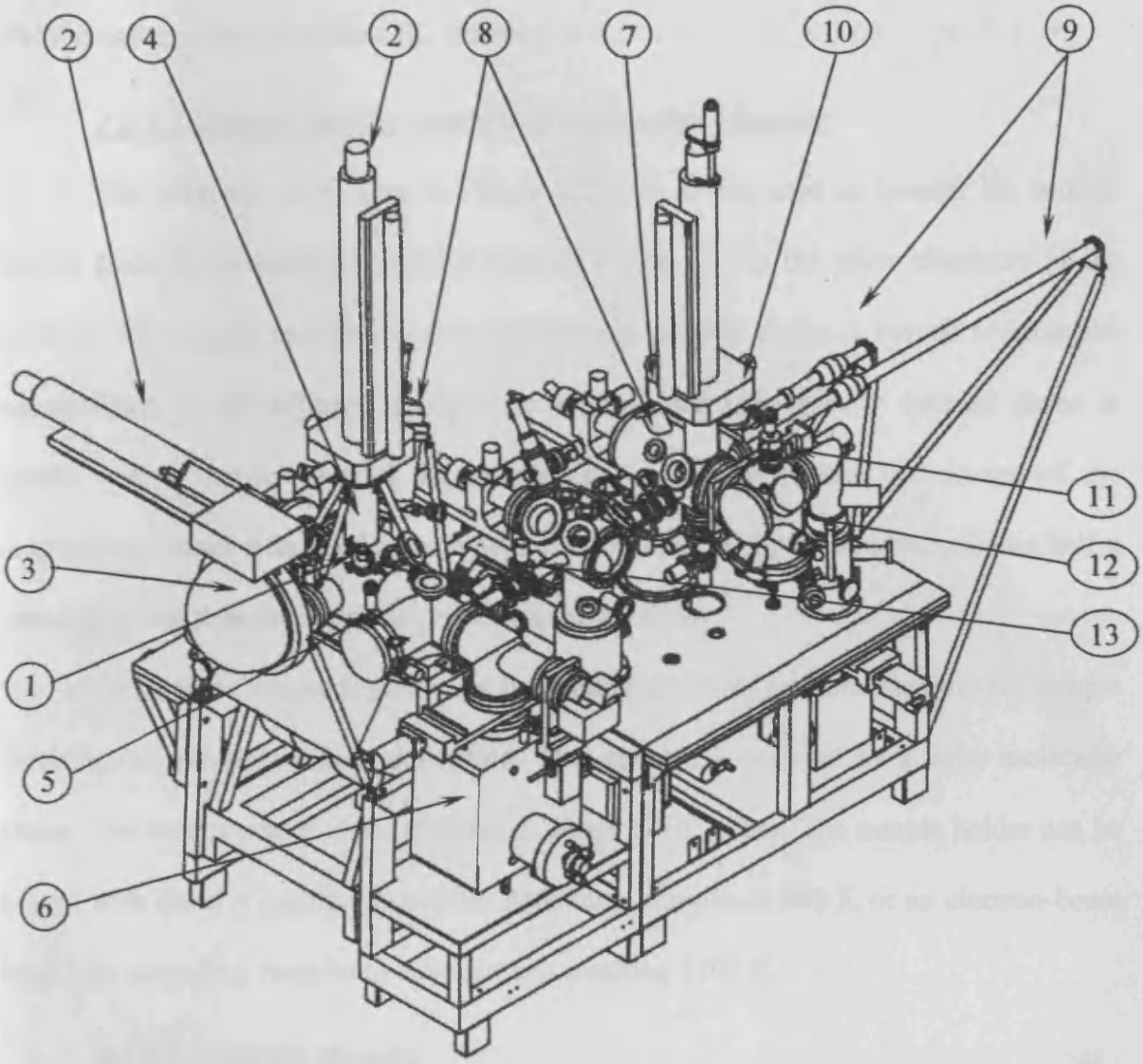

Figure 2.2. Schematic view of the system. (1) Analysis chamber, (2) sample manipulator, (3) hemispherical analyzer with a detector assembly consisting of seven channeltrons, (4) X-ray source, (5) LEED optics, (6) ion pump with a titanium sublimation pump (TSP), (7) Preparation chamber, (8) sputter gun, (9) magprobe (10) Special fast entry lock, (11) VT-STM chamber, (12) wobble stick, (13) evaporator.

2.2.1.1. Fast entry lock chamber (FEL chamber)

The fast entry lock (see in Figure 2.2) is pumped by a turbo molecular pump. The FEL chamber is separated from the preparation chamber by a gate valve. Valves between

the FEL chamber and the turbo molecular pump are used if the continuous pumping is undesirable. Samples and tips can be introduced into the system without breaking the UHV conditions by use of the FEL chamber.

2.2.1.2. Sample transfer system and preparation chamber

The magnetic probe (see in Figure 2.2) is a device used to transfer the sample holder from the preparation chamber (see in Figure 2.2) to the other chambers of the system. The sample mounted to the magnetically coupled probe is moved towards the manipulator. In the adjusted manipulator position, the magnetically coupled probe is gently pushed further in until the sample plate slides underneath the clamps of the manipulator head. Afterwards the sample plate is released by rotating the magnet half a revolution and then the magnetic probe is retracted back.

Besides the magnetic probe, the preparation chamber contains facilities for sample cleaning and physical vapour deposition. The chamber is pumped by a turbo molecular pump. The base pressure of the chamber is about 1×10^{-9} mbar. The sample holder can be heated with either a resistive heater for annealing samples to 900 K or an electron-beam heater for annealing samples to temperatures reaching 1500 K.

2.2.1.3. Analysis chamber

The spherical shaped analysis chamber (see in Figure 2.2) consists of several ports for instruments, windows, and other accessories such as manipulator. The analysis chamber is integrated into the centre chamber via a gate valve. The chamber is pumped by a turbo molecular pump and an ion pump with an integrated filament assembly for TSP. For pressure monitoring, an ion gauge is attached as in the other main chambers. The base pressure of the analysis chamber is about 1×10^{-9} mbar.

The XPS system includes a dual anode (Mg Kα and Al Kα) X-ray source and a hemispherical electron energy analyser with a seven channeltron detector for fast data

acquisition. The analyser can be operated in constant analyser energy (CAE) or constant retard ratio (CRR) mode, and it is computer controlled by the Omicron EIS data acquisition software (version 2.2.5). The manipulator in the analysis chamber allows sample translation with x, y, z, and θ degrees of freedom, enabling sample positioning for XPS, ISS, depth profiling, and angle resolved measurements. This chamber is also equipped with an Omicron rear view LEED optics mounted horizontally onto a 200 mm flange.

2.2.1.4. STM chamber

The STM chamber is attached onto the preparation chamber via a gate valve. An ion pump with TSP is connected at the bottom of the chamber. Sample holders and tip transfer holders are delivered to the tip/sample carousel by a wobble stick. The base pressure of the chamber is below 1×10^{-9} mbar.

2.2.1.5. Gas handling

The gases used in these experiments were scientific grade oxygen, helium and argon of 99.999% purity. Methanol (Lab. reagent grade, 99.5% purity) used in this study was from a commercial source (Fisher Scientific) and was firstly purified by repeated freeze-pump thaw cycles. All gas lines are bakeable and continuously pumped by a rotary pump. Gas lines are constructed from 6 mm steel tube with Swagelok® connections and their lengths are kept as short as possible. All metal leak valves are used for gas dosing into the various chambers.

2.2.1.6. Bakeout procedure

The complete system can be baked using heaters and bakeout panels which enclose the vacuum system. A typical bakeout takes a minimum of 18 hours at a temperature of 125°C. This results in a base pressure of 1×10^{-9} mbar in all the chambers. The gas lines can be baked out separately with heater tapes. The residual gas composition

is monitored constantly, especially after the bakeout, by the QMS located at both the analysis chamber and preparation chamber.

2.2.2. Sample preparation and characterisation

The experiments were performed in the Multi-technique UHV system (or Mulitprobe®) described above. The based pressure of the system is approximately 1×10^{-9} mbar. The sample was attached to a stainless steel sample plate with tantalum foil, and mounted on a transferring arm before its introduction into the preparation chamber via the FEL chamber.

After its introduction into the UHV vessel, the clean surface is prepared. In this work, two different samples were used, iron oxide and silver. The surface cleaning procedure for each sample is presented below.

2.2.2.1. Iron oxide single crystal preparation

The sample used in this study is monocrystalline Fe_2O_3 (the nature of this crystal is described in Chapter 3). The 1 cm × 1 cm × 2 mm thick Fe_2O_3 crystal (Pi-Kem Ltd., (0001) orientation) was sliced from a naturally occurring single crystal, mechanically polished to a mirror finish, and then mounted on a manipulator in the UHV system with a base pressure of 1×10^{-9} mbar.

The sample was prepared by repeated cycles of sputtering with 600 eV Ar^+ ions at room temperature for 30 minutes and subsequent annealing to 873 K in 1×10^{-7} mbar oxygen for 30 minutes. The sample is heated through a resistive heater using a tungsten filament positioned behind it. A thermocouple located at the heater gives an indication of the sample plate temperature. During annealing, the chamber was backfilled with oxygen, the oxygen pressure being maintained during the cooling of the sample. Following

cleaning, XPS showed no contamination, and LEED showed a sharp, hexagonal LEED pattern and a regular step-terrace structure in STM images.

2.2.2.2. Ag (111) preparation

The clean Ag(111) was prepared by cycles of argon ion sputtering (600 eV) at room temperature, followed by annealing at a temperature of 723K for 30 minutes. This procedure was repeated until no contaminants such as carbon, oxygen, sulphur, or chlorine were detectable using XPS.

2.2.2.3. Sample characterisation

After preparation, the samples were characterized by means of XPS, ISS, LEED, and STM. The results of these measurements will be presented in the following chapters. All STM measurements were performed in constant current mode at room temperature. Tips were made from electrochemically etched tungsten wire (Goodfellow, 99.95%).

The LEED measurements were performed at room temperature. XPS analysis was done at room temperature usually using the Kα X-ray line of aluminium. The ISS experiments were carried out at room temperature by using $^4He^+$ ions having an incident kinetic energy of 1 keV. The energy distribution of $^4He^+$ ions backscattered at the surface is measured.

2.2.3. Metal oxide deposition

Metal oxide films may be prepared by a number of means. The experiments here concern the deposition of molybdenum oxide. Thin films of this material can be obtained by various different techniques such as thermal evaporation [1, 2], sputtering [3-11], vacuum evaporation [12-14], plasma-enhanced chemical vapour deposition [15, 16], atmospheric pressure chemical vapour deposition [17, 18], and sol-gel [19-22].

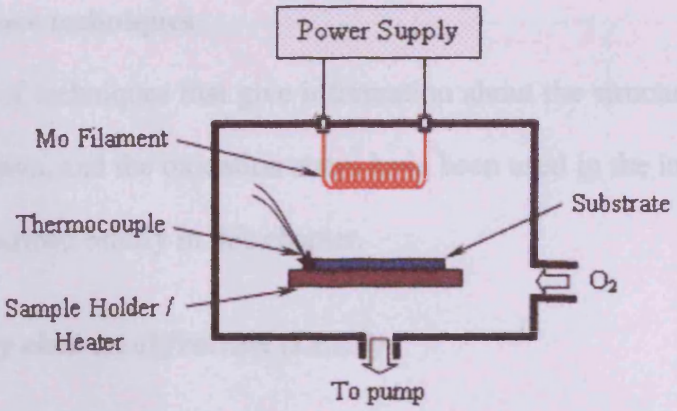

Figure 2.3. Schematic representation of the experimental arrangement inside the chamber. The filament was made of 0.25-mm-diameter molybdenum wire, shaped into a nineteen-turn coil of 3.5-mm diameter and 20 mm length; filament-to-substrate separation: 80 mm.

Recently, a new deposition method called hot-filament metal oxide deposition (HFMOD)[23] has been used to obtain films of metal oxide such as tungsten oxide [24, 25], molybdenum oxide [23-25], and vanadium oxide [24]. The details of this technique used in these experiments are described below.

Thin film deposition took place in the preparation chamber equipped with a four point electrical feedthrough and pumped by a turbo molecular pump. Two points of the feedthrough were extended with molybdenum wires (Goodfellow Metals, 99.95%). The other two points of the feedthrough were used to support a shield around the filament. The deposition system is shown schematically in Figure 2.3. A molybdenum filament was resistively heated by a dc current of 2-10 A from a laboratory dc power supply, with the current displayed by an ammeter. Oxygen is introduced into the chamber via a metal leak valve. The pressure is measured using a thermo-ionic ion gauge located in the chamber. The distance between the sample and molybdenum source is kept as close as possible (5-10 cm). The films are obtained from the vaporisation of oxides formed on the filament surface.

2.3. Surface science techniques

A number of techniques that give information about the structure of a surface, its chemical composition, and the oxidation states have been used in the investigation. These techniques are described briefly in this chapter.

2.3.1. Low energy electron diffraction (LEED)

2.3.1.1. Introduction

Low energy electron diffraction (LEED) is one of the most widely used surface techniques, based on the physical principle of wave-particle duality for the determination of surface structures.

In 1921 Davisson and Germer [26] reported the observation of the angular distributions of electrons backscattered from a polycrystalline nickel sample and explained their experimental data in terms of the electron diffraction from the Ni crystal. Despite these early beginnings, however, LEED was not developed further until about 1960 when the development of UHV technology prompted widespread interest in use of LEED as the surface structural probe.

2.3.1.2. Surface diffraction

The de Broglie wavelength of a particle is given by

$$\lambda = \frac{h}{\sqrt{2mE}} \tag{2.1}$$

where h is Planck's constant, m is the mass of the particle, and E is the energy of the particle. Considering electrons, the wavelength (in Angstroms) is related to their energy E (given in electron volts) by:

$$\lambda_{e^-} = \sqrt{\frac{150.4}{E(eV)}} \tag{2.2}$$

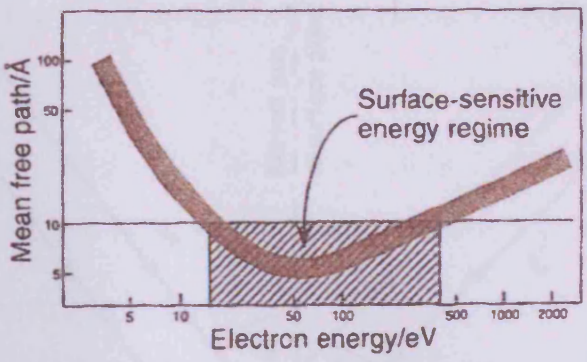

Figure 2.4. The universal curve of electron mean free path as a function of energy [27].

Low-energy electrons (around 200 eV) are surface sensitive since the penetration depth into the solid is of the order of a few tens of Angstrom as illustrated by the data in Figure 2.4. The mean free path of electrons in the solid is only dependent on the energy of the electrons. Electrons with energies between about 20 and 500 eV interact strongly with matter and their mean free path is in the range of 5-10 Å. Hence LEED is considered to be a surface structural probe.

The diffraction effects can be explained by considering Figure 2.5. In case of an incident beam scattered off a one-dimensional array, constructive interference occurs if scattered electrons from adjacent atoms differ only by an integer number of the wavelength λ. If an incident beam strikes the surface with an incident angle θ_0, scattered beams interfere constructively at an angle θ_n as shown in Figure 2.5. The Bragg equation is modified to

$$n\lambda = a(\sin\theta_n - \sin\theta_0) \qquad (2.3)$$

where a is the interatomic distance and n is an integer denoting the diffraction order. The wavelength λ of electrons is given by equation (2.2). This is normally called the *Laue condition*. Periodic lattice points arise from parallel rows of scatters and can be defined by the two-dimensional Miller indices $[h'k']$ of rows. Therefore, Equation (2.3) can be rewritten as:

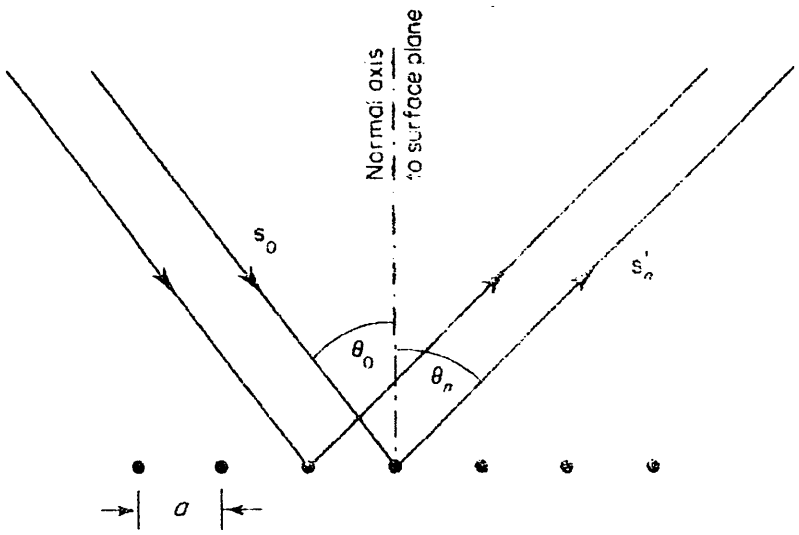

Figure 2.5. Diffraction from a one-dimensional array [28].

$$n\lambda = a_{h'k'}(\sin\theta_n - \sin\theta_0) \tag{2.4}$$

Usually normal incidence of the primary electrons is used in LEED experiments ($\theta_0 = 0$), then Equation (2.4) is more conveniently expressed:

$$\sin\theta_n = \frac{n\lambda}{a_{h'k'}} \tag{2.5}$$

2.3.1.3. Instrumentation

The experimental apparatus for viewing the diffracted spots is shown schematically in Figure 2.6. The electron gun produces focussed electrons with kinetic energy of 20-500 eV. These electrons are collimates by a lens system and finally leave the drift tube with the desired energy. After passing the drift tube of the electron gun, the electrons strike the sample surface where they are coherently scattered by the regular arrangement of surface atoms. The backscattered electrons are of two types; elastically scattered electrons which are used in the diffraction experiment, and inelastically scattered electrons which are not required. The scattered electrons pass a series of hemispherical concentric grid. The first grid is at the potential of the crystal, and the second grid is a repelling grid that allows only elastically scattered electrons to pass.

Afterwards these electrons are accelerated by a positive potential toward a fluorescent screen on which the diffraction pattern is exhibited. The LEED pattern can then be recorded with a video camera and displayed on a monitor. Figure 2.7 shows the LEED optics assembly produced by Omicron which is used in this work.

2.3.1.4. LEED interpretation

In two-dimensional space, the two-dimensional reciprocal space can be described in terms of two basis vectors of the reciprocal unit mesh. The basis vectors $\vec{a}_1$ and $\vec{a}_2$ represent the surface two-dimensional unit cell, and the basis vectors space lattice $\vec{a}_1^*$ and $\vec{a}_2^*$ describe the reciprocal space. The relationship between the basis vectors in reciprocal and real space are defined by

$$\vec{a}_i \cdot \vec{a}_j^* = \delta_{ij} \tag{2.6}$$

where $i, j = 1$ or 2, and δ_{ij} is the Kronecker delta function, where $\delta_{ij} = 0$ if $i \neq j$, and $\delta_{ij} = 1$ if $i = j$. In other words, $\vec{a}_1 \perp \vec{a}_2^*$, $\vec{a}_2 \perp \vec{a}_1^*$. Introducing γ and γ^*, the enclosed angles between ($\vec{a}_1$ and $\vec{a}_2$) and ($\vec{a}_1^*$ and $\vec{a}_2^*$), respectively, we have

$$\left|\vec{a}_1^*\right| = \frac{1}{\left|\vec{a}_1\right| \sin\gamma} \tag{2.7}$$

$$\left|\vec{a}_2^*\right| = \frac{1}{\left|\vec{a}_2\right| \sin\gamma} \tag{2.8}$$

$$\sin\gamma = \sin\gamma^* \tag{2.9}$$

This is explained in Figure 2.8.

The area A of the elementary cell of the real lattice is given by

$$A = \vec{a}_1 \vec{a}_2 \sin\gamma = \left|\vec{a}_1 \times \vec{a}_2\right| \tag{2.10}$$

The corresponding relation for the reciprocal lattice is defined:

$$A^* = \vec{a}_1^* \vec{a}_2^* \sin\gamma^* = \left|\vec{a}_1^* \times \vec{a}_2^*\right| = 1/A \tag{2.11}$$

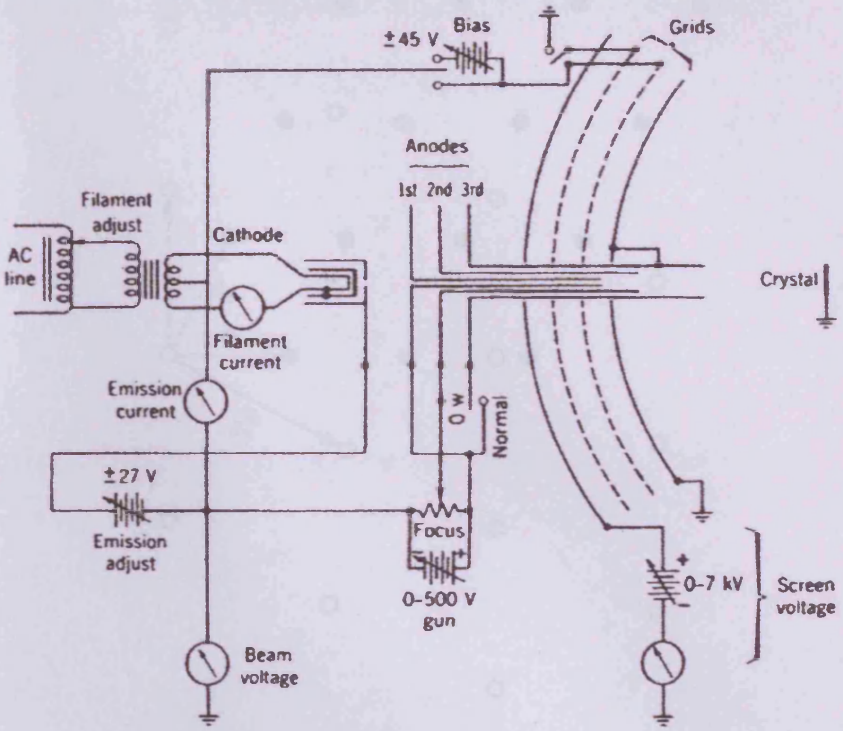

Figure 2.6. Schematic view of the LEED system [29].

Figure 2.7. Omicron SpectralLEED system. The grids are clearly visible at the top and the view-port is at the bottom. The magnetic shield has been removed.

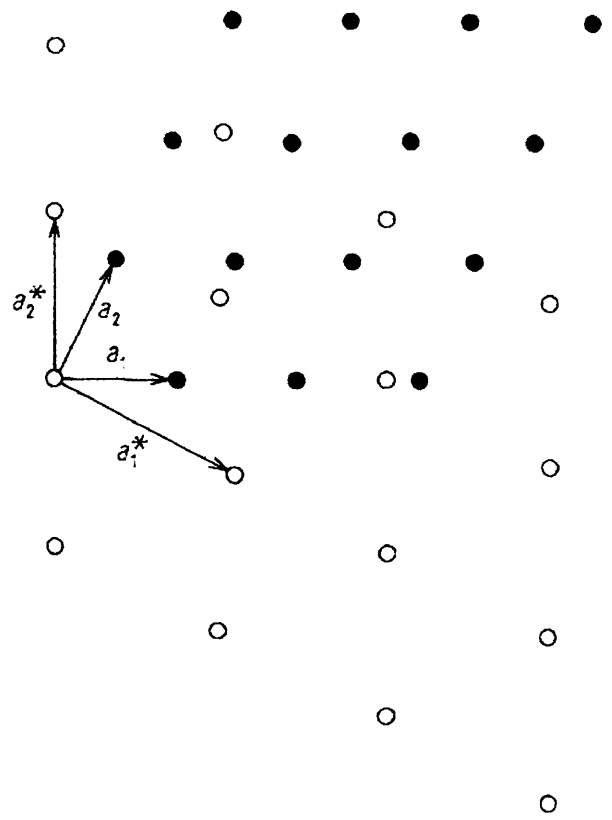

Figure 2.8. The relationship between a two-dimensional real lattice and its reciprocal lattice [30].

For ideal clean surfaces, the surface structure generates a rather simple diffraction pattern, whereas a complex pattern may be obtained from an overlayer structure with a rather large unit mesh and a number of domains. If a surface structure has lattice vectors $\vec{b}_1$ and $\vec{b}_2$ overlaid on a substrate with lattice vectors $\vec{a}_1$ and $\vec{a}_2$, then they can described in terms of the substrate lattice vectors as follows:

$$\vec{b}_1 = m_{11}\vec{a}_1 + m_{12}\vec{a}_2 \tag{2.12}$$

$$\vec{b}_2 = m_{21}\vec{a}_1 + m_{22}\vec{a}_2 \tag{2.13}$$

where the m_{ij} are four coefficients which form a matrix M determined from the observed diffraction pattern.

$$M = \begin{bmatrix} m_{11} & m_{12} \\ m_{21} & m_{22} \end{bmatrix} \tag{2.14}$$

A similar relationship between reciprocal lattice vectors may be defined:

$$\vec{b}_1^* = m_{11}^* \vec{a}_1^* + m_{12}^* \vec{a}_2^* \tag{2.15}$$

$$\vec{b}_2^* = m_{21}^* \vec{a}_1^* + m_{22}^* \vec{a}_2^* \tag{2.16}$$

where

$$M^* = \begin{bmatrix} m_{11}^* & m_{12}^* \\ m_{21}^* & m_{22}^* \end{bmatrix} \tag{2.17}$$

It can be shown that M^* is the inverse transposed matrix of M, which yields

$$m_{11} = \frac{1}{\det M^*} m_{22}^* \tag{2.18}$$

$$m_{12} = -\frac{1}{\det M^*} m_{21}^* \tag{2.19}$$

$$m_{21} = -\frac{1}{\det M^*} m_{12}^* \tag{2.20}$$

$$m_{22} = \frac{1}{\det M^*} m_{11}^* \tag{2.21}$$

The determinant of the matrix M^* is obtained by cross multiplication.

$$\det M^* = m_{11}^* m_{22}^* - m_{21}^* m_{12}^* \tag{2.22}$$

This relationship allows the real lattice structure to be derived from the corresponding reciprocal lattice. The determination of the unit cell of a surface structure is demonstrated in the following example.

The diffraction pattern is shown in Figure 2.9(a). The open circles indicate the arrangement of diffracted beam corresponding to a clean unreconstructed surface and the "extra spots" caused by the adsorbed surface structure are marked differently. The reciprocal lattice vectors $\vec{b}_1^*$ and $\vec{b}_2^*$ are related to the substrate vectors $\vec{a}_1^*$ and $\vec{a}_2^*$ as follows:

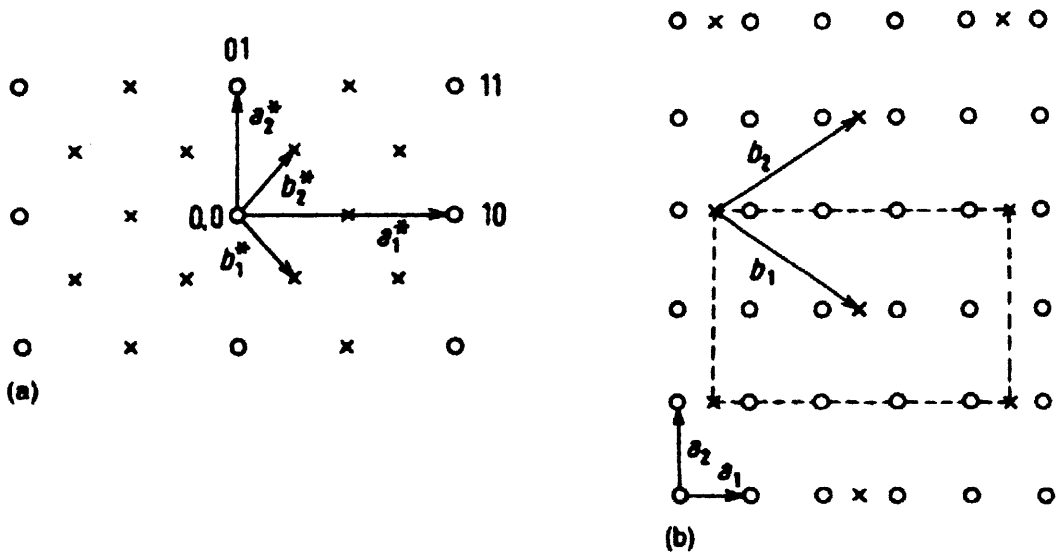

Figure 2.9. Analysis of a simple diffraction pattern. (a) reciprocal lattice (LEED pattern) composed of substrate (normal) spots (o) and overlayer (extra) spots (×); (b) real lattice of the substrate (o) and overlayer (×). The dashed line denotes the c(4x2) unit cell [27].

$$\vec{b}_1^* = 0.25\vec{a}_1^* - 0.5\vec{a}_2^* \tag{2.23}$$

$$\vec{b}_2^* = 0.25\vec{a}_1^* + 0.5\vec{a}_2^* \tag{2.24}$$

from which

$$\det M^* = (0.25)(0.5) - (0.25)(-0.5) = 0.25 \tag{2.25}$$

and

$$M = \frac{1}{0.25}\begin{bmatrix} 0.5 & -0.25 \\ -(-0.5) & 0.25 \end{bmatrix} = \begin{bmatrix} 2 & -1 \\ 2 & 1 \end{bmatrix} \tag{2.26}$$

So, in real space, the overlayer structure is described by the lattice vectors

$$\vec{b}_1 = 2\vec{a}_1 - \vec{a}_2 \tag{2.27}$$

$$\vec{b}_2 = 2\vec{a}_1 + \vec{a}_2 \tag{2.28}$$

as illustrated in Figure 2.9(b).

In order to identify the overlayer pattern, the common nomenclature proposed by Wood [31] is often used. The overlayer structure is expressed in terms of $m = \left|\vec{b}_1 / \vec{a}_1\right|$ and $n = \left|\vec{b}_2 / \vec{a}_2\right|$, and the angle between $\vec{b}_1$ and $\vec{b}_2$ is the same as that between $\vec{a}_1$ and $\vec{a}_2$, then the overlayer is said to be primitive and to have a $p(m \times n)$. If overlayer mesh vectors are rotated through an angle α with respect to $\vec{a}_1$, the lattice may be described as $(m \times n)R\alpha°$. In addition, a letter 'c' must be added if the overlayer has a structure similar to the p(2×2) with the addition of an extra lattice point at the centre of the square.

2.3.2. X-ray photoelectron spectroscopy (XPS)

X-ray photoelectron spectroscopy (XPS), also known as Electron Spectroscopy for Chemical Analysis (ESCA), is one of the most widely used techniques for investigating the chemical composition of various material surfaces. It is generally regarded that the analysis depth of the sample is in the 1 - 10 nm range.

The main strength of XPS lies in its ability not simply to supply qualitative information but also to provide quantitative information on the chemical composition of the sample surface and on the charge state of atoms. This technique is widely used as a tool for characterisation of heterogeneous catalyst.

2.3.2.1. Principles of XPS

In XPS, the solid surface in a vacuum is irradiated with a monochromatic beam of X-rays to produce photoelectrons by direct transfer of energy from the X-ray photons to core-level electrons in the atom of the sample, as shown schematically in Figure 2.10. This diagram illustrates the X-ray photon interacting with a core or valence electron with binding energy E_B, causing the emission of photoelectron with kinetic energy:

$$E_K = h\nu - E_B - \Phi \qquad (2.29)$$

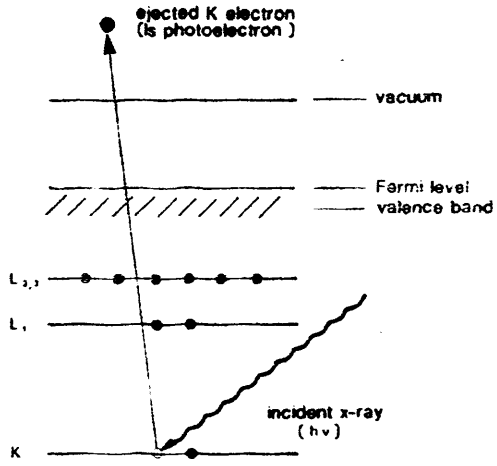

Figure 2.10. Photoemission process [32].

where E_K is the kinetic energy of the emitted electron that is measured in the XPS spectrometer, $h\nu$ is the energy of the X-ray source (a known value), E_B is the binding energy of the electron in the atom (a function of the type of atom and its environment), and Φ is the spectrometer work function.

The binding energy of an emitted photoelectron is equal to the energy difference between the n-electron initial state atom and (n-1)-electron final (ionic) states. This is written as:

$$E_B(k) = E_f(n-1) - E_i(n) \tag{2.30}$$

where $E_f(n-1)$ is the final state energy and $E_i(n)$ is the initial state energy. If no rearrangement of other electrons in the atom occurred during the photoemission process, then the observed binding energy is simply equal to the negative orbital energy, $-\varepsilon_k$, of the ejected electron. This approximation is called Koopmans' theorem and is written as:

$$E_B(k) \approx -\varepsilon_k \tag{2.31}$$

The Hartree-Fock method is used to calculate the values of ε_k which are within 10-30 eV of the actual binding energy values. This approximation is certainly not correct because other remaining electrons in the sample are not 'frozen'. They may relax to

minimise their total energy in the final state. Relaxation occurs for both electrons in the atom (atomic relaxation) and those on neighbouring atoms (extra-atomic relaxation). In addition to relaxation, the Hartree-Fock and Koopmans scheme also neglect electron correlation and relativistic effects which usually both increase the core electron binding energy. Hence, a more accurate expression of the binding energy is written as:

$$E_B(k) = -\varepsilon_k - \delta\varepsilon_{relax} + \delta\varepsilon_{corr} + \delta\varepsilon_{rel} \qquad (2.32)$$

where $\delta\varepsilon_{relax}$, $\delta\varepsilon_{corr}$ and $\delta\varepsilon_{rel}$ are corrections for the relaxation, differential correlation and relativistic energies, respectively. Both the correlation and relativistic terms are usually neglected because they are small.

Moreover, the energy of an electronic state is determined by angular momentum coupling. This is known as '*spin-orbit splitting*' which arises from a coupling between magnetic field of the total spin (s) and the orbital angular momentum (l). In the 'LS' coupling scheme, the total angular momentum is given by $j = |l + s|$. For any state with an orbital angular momentum $l > 0$, one unpaired electron is split into two different states (i.e. $j_+ = l + ½$ and $j_- = l - ½$) with different energy. The splitting is often observable in photoelectron spectra. The number of spin-orbit splitting levels, denoted degeneracy, at each total angular momentum value is equal to $(2j + 1)$. The intensity ratio of these two atomic ½ states can to a first approximation be $(2j_+ + 1)/(2j_- + 1)$ i.e. 2.0 for p-subshells, 1.5 for d-subshells, 1.33 for f-subshells, and so on.

2.3.2.2. Initial state effects

As shown in Equation (2.30), both initial state and final state effects influence the observed binding energy. The binding energy of electrons in the atom will change if the energy of initial state is changed, for instance, by chemical bonding. The change in the binding energy, ΔE_B, is known as a chemical shift.

The accurate binding energy of an electron will depend critically on the chemical environment surrounding the atom. Changes in this give rise to small shifts in the peak positions in the spectrum - the so called *chemical shifts*. In general, as the formal oxidation state of an element increases, the binding energy of emitted photoelectrons increases. Atoms of a higher positive oxidation state exhibit a higher binding energy because of the coulombic interaction between core electrons and the nucleus. Figure 2.11 shows the example of chemical shift which is the C1s photoelectron spectrum of ethyl-trifluoroacetate. In this molecule, four carbon atoms are located in four different chemical environments resulting in four well resolved lines in the spectrum, corresponding to each of the different carbon atoms.

2.3.2.3. Final state effects

From the above discussion, the electron rearrangements occurring during photoemission affects the energy distribution of the emitted electrons in different ways. There are several type of the "final state" effects which will be briefly provided below.

The relaxation energy for a given core level can be divided into two parts [33-35] i.e. (intra-) atomic and extra-atomic contribution. An intra-atomic relaxation results from rearrangement of outer-shell electrons in the free atom and an extra-atomic relaxation arises from polarisation of free valence electron in a conducting material such as a metal, leading to a screening charge which tends to neutralise the core hole and their magnitude is of the order of 5 to 10 eV.

Multiplet splitting of a photoelectron may occur when unpaired electrons in the valence band of the atom couple with any other unpaired electrons in the atom or molecule, resulting in different spin distributions in the electrons of the band structure. This causes different energies of states which produces the asymmetry in the photoelectron spectrum.

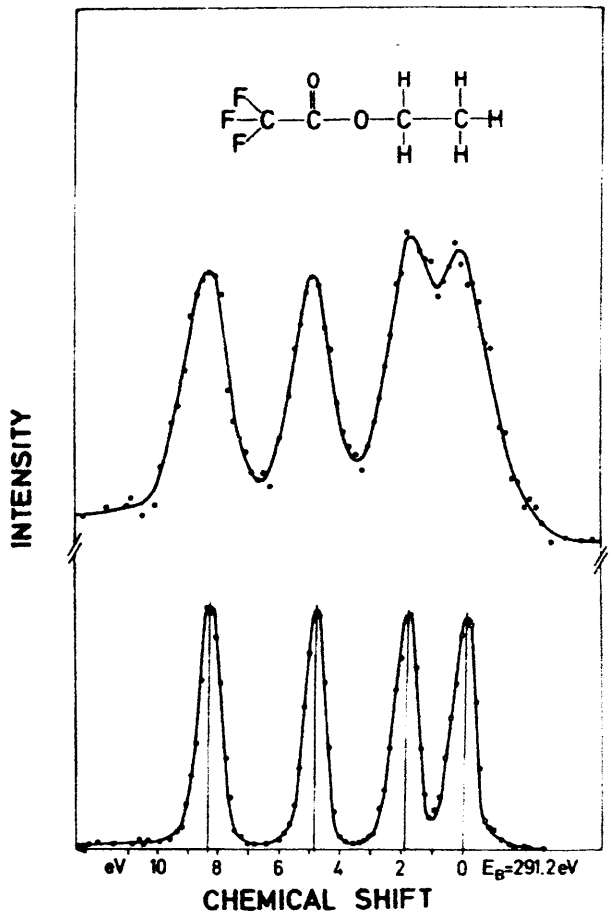

Figure 2.11. C1s photoelectron spectrum of ethyl-trifluoroacetate showing four different lines due to the chemical shift [36].

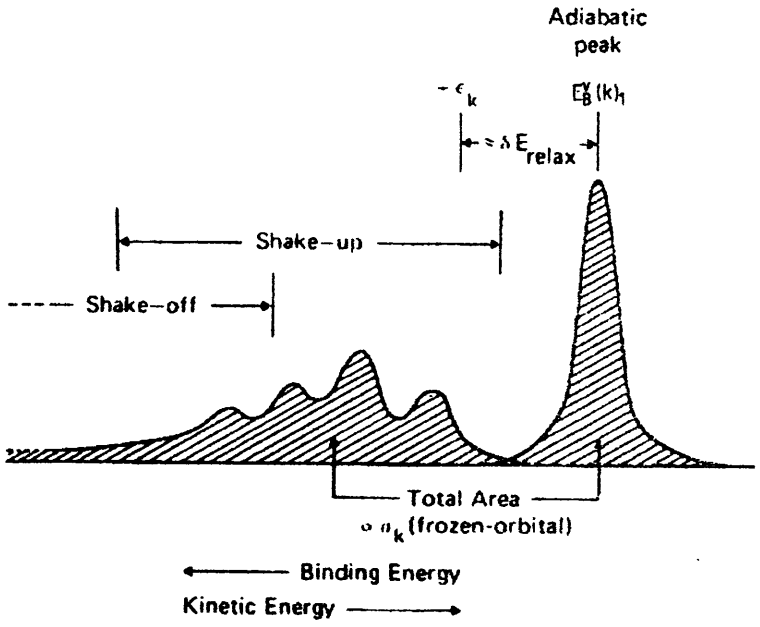

Figure 2.12. XPS spectrum with shake-up and shake-off satellites [30].

Shake-up satellites occur when the outgoing electron excites a valence electron to a higher-lying bound state. Shake-up features are observed as a characteristic satellite structure on the high binding energy side of the main photoemission peak due to the energy reduction of the outgoing photoelectron. Shake-up satellites arise from the excitation of valence electron to higher energy level such as being the 2p spectra of the d-band metals and bonding to anti-bonding transitions of the π or σ molecular orbital transitions in aromatic organics. Occasionally, the valence electron is ejected completely from the atom, such double ionisation occurrence is denoted a "shake-off" process. Shake-off events usually show up as either very broad structures within the large background of inelastic secondary electrons or as low-energy tails on the photoelectron peaks. Figure 2.12 represents such final state effects. The peak with lowest binding energy corresponds to the ground state of ion and peaks of shake-up and shake-off satellites appear at higher binding energy.

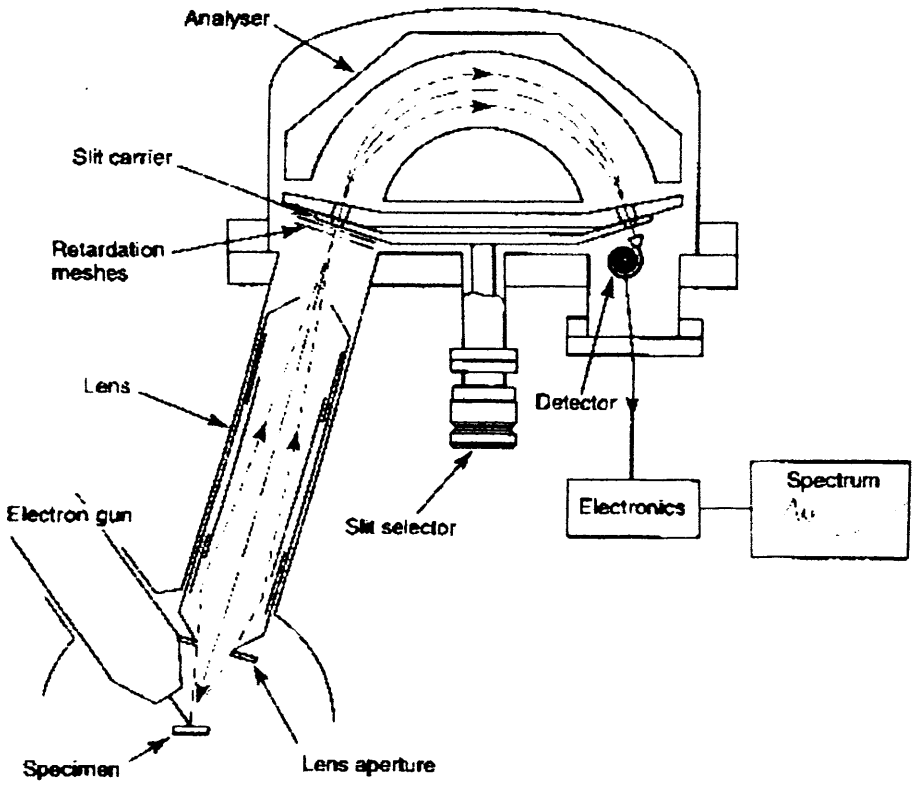

Figure 2.13. Schematic of a photoelectron spectrometer [37].

2.3.2.4. Instrumentation for XPS

A schematic drawing of a typical commercial photoelectron spectrometer is illustrated in Figure 2.13. The primary components that make up the XPS instrument are X-ray source, electron energy analyser, and detector system, all contained within an UHV system.

(a) X-ray source

XPS data in these experiments were obtained by using an X-ray tube in which a switchable dual anode, with Al Kα ($h\nu$ = 1486.6 eV) and Mg Kα ($h\nu$ = 1253.6 eV) is held at a high voltage (12-20 keV). A thin aluminium foil (~20 μm thick) window separates the X-ray source from the sample and will minimise the flux of electrons, high energetic electrons, Bremsstrahlung, and also eliminates contamination of the sample by the X-ray source. Figure 2.14 is a schematic representation of a dual anode X-ray source, DAR 400, produced by Omicron.

(b) Electron energy analyser

The EA 125 spectrometer (see in Figure 2.15) used in these experiments consists of multi-element electrostatic lens to collect emitted electrons from the sample and focus them on the entrance of the hemispherical energy analyser, a set of slits at the entrance to the energy analyser, a hemispherical energy analyser with 125 mm mean radius, a set of slits at the exit of the energy analyser, and a detector which is described below.

The EA 125 energy analyser comprises two concentric hemispherical sectors. The ejected electrons are retarded immediately before entering the hemispheres. From here, the emitted electrons pass through the spherically symmetric field that is created between two hemispherical electrodes. The electron energy analyser disperses the photoelectrons according to their kinetic energy and then measures their flux of a particular energy.

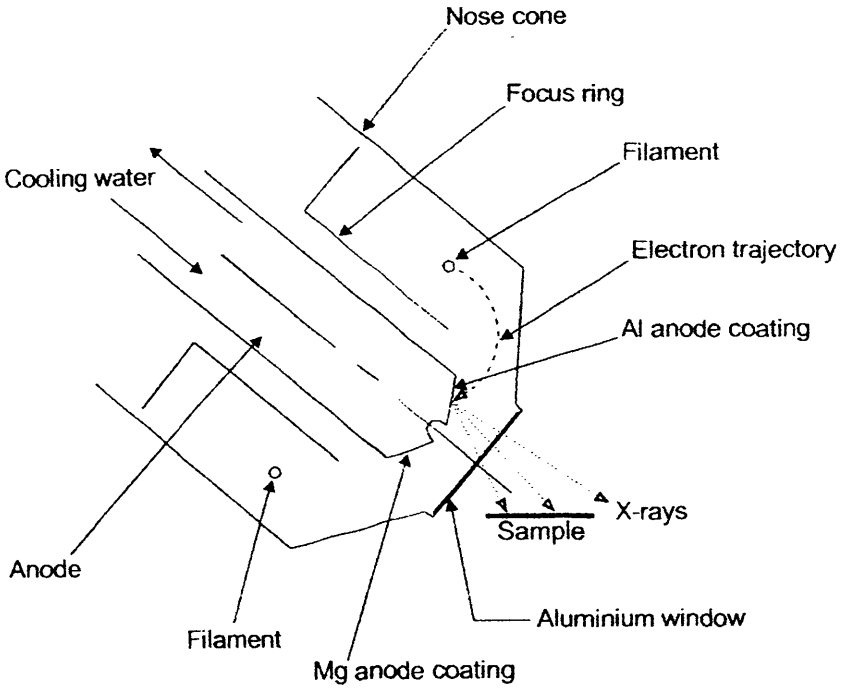

Figure 2.14. A schematic diagram of DAR 400 X-ray source [38].

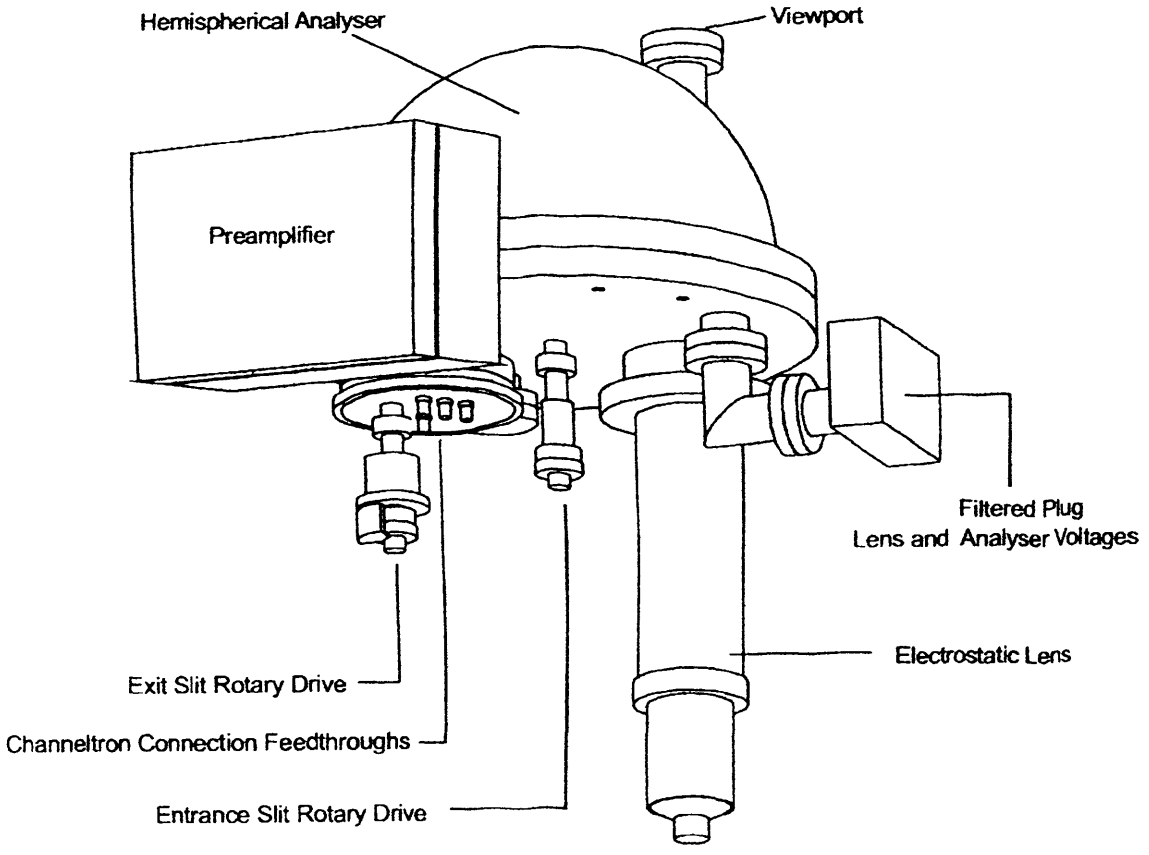

Figure 2.15. EA 125 hemispherical analyser major component [39].

(c) Detector system

The channel electron multiplier (Channeltron®) in an array of seven is employed for detection of the energy-selected electrons and is placed across the exit plane of the analyser. Electrons entering the Channeltron® detector generate secondary electrons. They strike the Channeltron® wall, producing further secondary electrons until, at the output end a pulse of 10^7 to 10^8 electrons emerges. Small current pulse (10^{-16} to 10^{-13} A) of electrons passes into the preamplifier. From here, the electron pulse is converted to the signal which is passed onto a pulse counter to produce a spectrum of emission intensity versus electron binding energy.

For each and every atom or molecule, there will be a characteristic binding energy associated with each core atomic orbital i.e. each atom will give rise to a characteristic set of peaks in the XPS spectrum at kinetic energies determined by the photon energy and the respective binding energies.

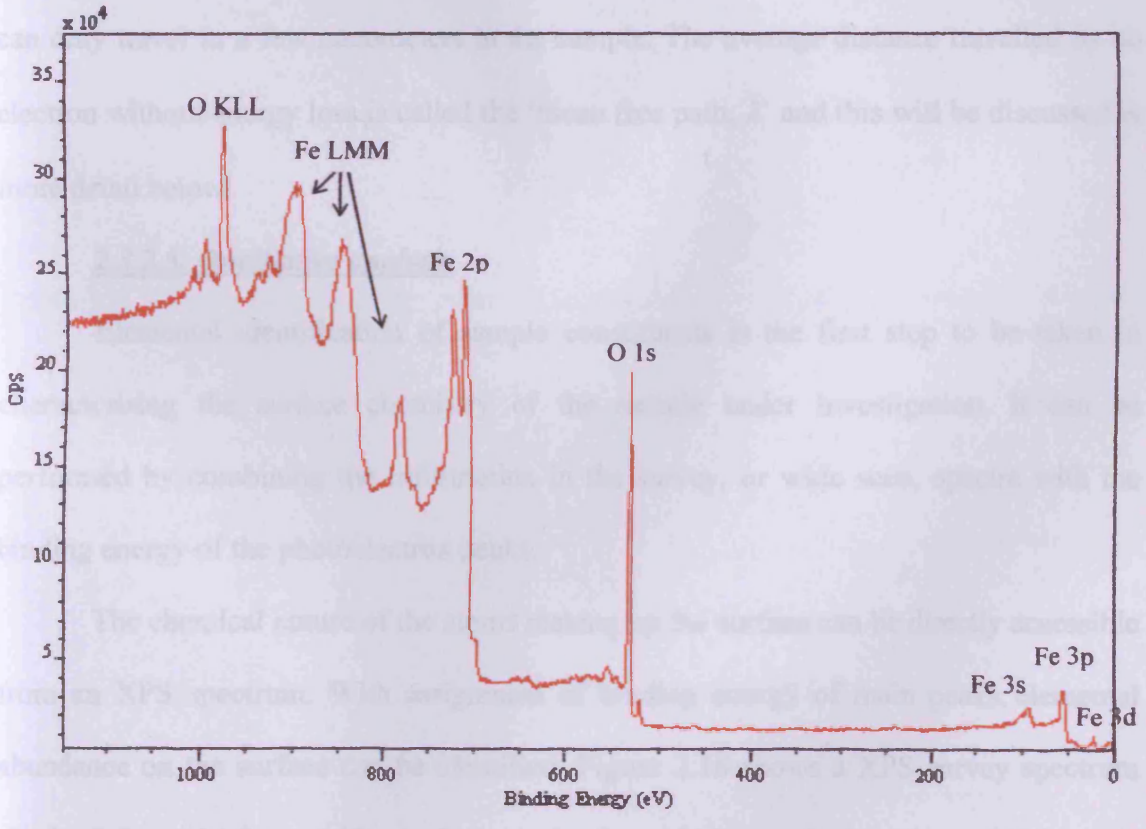

Figure 2.16. XPS survey spectrum of $Fe_3O_4(111)$ surface (see Chapter 3).

The XPS survey spectrum of the iron oxide surface obtained using Al Kα X-ray (1486.6 eV) is illustrated on Figure 2.16. In XPS spectra, each peak having certain quantised energy is designated according to the level from which it is ejected. The commonly used nomenclature is designated as nL_j (n = principle quantum number, L = s, p, d, f, ... corresponding to l = 0, 1, 2, 3, ..., and j = total angular momentum).

The Auger peaks are designated as three letters indicative of (i) the shell level of the initial core hole created, (ii) the shell level from which the electron drops to fill the hole, and (iii) the shell level from which the electron is ejected. The shell derives its name from n according to K, L, M, N, ... for n = 1, 2, 3, 4, ... A subscript further indicates the subshell. The number starts at 1 for the lowest (l, j) state and continues in unit steps up to the highest (l, j) state. Thus the shell corresponding to l = 2 has levels L_1, L_2, and L_3 corresponding to 2s, $2p_{1/2}$, and $2p_{3/2}$.

Certainly, XPS is a surface analysis technique because the photoelectrons emitted can only travel in a few nanometers in the sample. The average distance travelled by an electron without energy loss is called the 'mean free path, λ' and this will be discussed in more detail below.

2.3.2.5. Qualitative analysis

Elemental identification of sample constituents is the first step to be taken in characterising the surface chemistry of the sample under investigation. It can be performed by combining the information in the survey, or wide scan, spectra with the binding energy of the photoelectron peaks.

The chemical nature of the atoms making up the surface can be directly accessible from an XPS spectrum. With assignment of binding energy of main peaks, elemental abundance on the surface can be identified. Figure 2.16 shows a XPS survey spectrum obtained from the iron oxide single crystal using Al K_α x-radiation ($h\nu$ = 1486.6 eV).

This spectrum comprises the various peaks with different binding energies which can be identified and designated as shown in Table 2.1 and Table 2.2. As expected, the binding energy of Fe2p tends to increase with the degree of oxidation.

Table 2.1. XPS and Auger Peaks observed in the iron oxide substrate together with their photoionisation cross-sections towards Al Kα X-ray (1486.6 eV) [40].

Element	Level	B.E. (eV)	Cross Section [41] (Relative)	Auger Peak	K.E. (eV)
C	1s	285	1.00	KVV	1223
O	1s	531	2.93	KLL	978
Fe	3p	53	1.67	LMM	784
	3s	92	0.75	LMM	839
	$2p_{3/2}$	707	10.82	LMM	888
	$2p_{1/2}$	720	5.60		
	2s	845	4.57		

Table 2.2. The influence of the chemical environment on the binding energy of the Fe 2p electrons [40].

Fe chemical environment	Binding energy (eV)
Metal Fe	706.5 to 707.5
FeO	709.0 to 710.0
Fe_2O_3	710.5 to 711.0
FeOOH	711.0 to 712.0

2.3.2.6. Quantitative analysis

(a) Surface concentration

The area below a photoelectron peak is related to the amount of material present which is proportional to the number of atoms in the detected volume. So, by integrating the peak area and correcting them for the suitable instrumental factors, the surface concentration of each element detected can be determined. The equation used for determining the intensity I_i of an element i is given by [42]

$$I_i = kT(E_{K,i})\sigma_i L_i(\gamma)\int n_i(z)\exp[-z/\lambda(E_{K,i})\cos\theta dz] \quad (2.33)$$

where k is the instrumental constant such as analyser transmission and detector efficiency, $T(E_{K,i})$ is the spectrometer transmission, σ_i is the photo-ionisation cross section, $L_i(\gamma)$ is the angular asymmetry factor of the photoelectron with respect to the angle γ between the direction of incidence and of detection, $n_i(z)$ is the density of atoms i at a distance z below the surface, $\lambda(E_{K,i})$ is the mean free path of an excited electron with kinetic energy $E_{K,i}$, and θ is the angle between the surface normal and the collection axis of electrons.

The density of atoms i, n_i, in Equation (2.33) is the unknown quantity. Once it is known for each atom present in the XPS spectrum, the atomic percentages can be calculated as

$$\%n_i = 100(n_i/\sum n_i) \quad (2.34)$$

where $\%n_i$ is the atomic percent of atom i. Atomic ratios (n_i/n_k) can also be calculated. If the sample is homogeneous, then Equation (2.33) simplifies to

$$I_i = kT(E_{K,i})\sigma_i L_i(\gamma)n_i\lambda(E_{K,i})\cos\theta \quad (2.35)$$

The spectrometer transmission function includes the efficiency of the collection lens, the analyser, and the detector. Most spectrometers are operated in the constant-pass

energy mode. Thus the transmission function is only dependent on the kinetic energy of photoelectrons. The transmission function of instruments is normally provided by the manufacturer. For the Multiprobe®, the transmission factor, $T(E_{K,i})$, of the EA 125 energy analyser is proportional to $1/E_{K,i}$ for CAE scan mode. The intensity of an XPS peak can thus be written as

$$I_i = \frac{k\sigma_i L_i(\gamma) n_i \lambda(E_{K,i}) \cos\theta}{E_{K,i}} \tag{2.36}$$

From Equation (2.36), the relative concentration of absorbate A and substrate S becomes

$$\frac{n_A}{n_S} = \frac{E_{K,A}}{E_{K,S}} \cdot \frac{I_A}{I_S} \cdot \frac{\sigma_S L_S(\gamma)}{\sigma_A L_A(\gamma)} \cdot \frac{\lambda_S(E_{K,S})\cos\theta}{\lambda_A(E_{K,A})\cos\theta} \tag{2.37}$$

where n_A / n_S is the relative concentration of absorbate A and substrate S, $E_{K,A} / E_{K,S}$ is the kinetic energy of absorbate A and substrate S, I_A / I_S is the relative intensity (integrated peak area) observed in the XPS measurements, and σ and $L(\gamma)$ have already been defined. $\sigma_S L_S(\gamma)$ and $\sigma_A L_A(\gamma)$ can be determined by calculations as discussed later. $\lambda_S(E_{K,S})\cos\theta / \lambda_A(E_{K,A})\cos\theta$ is the ratio of mean free paths for electrons coming from absorbate A and substrate S.

In order to determine the surface coverages of adsorbates, Equation (2.37) can be rewritten and lead to the Carley-Roberts equation [43, 44].

$$\phi_A = \frac{E_{K,A}}{E_{K,S}} \cdot \frac{I_A}{I_S} \cdot \frac{\mu_S}{\mu_A} \cdot \frac{N\rho_S \lambda_S \cos\theta}{M_S} \tag{2.38}$$

where

$$\mu_i = \sigma_i L_i(\gamma) \tag{2.39}$$

and

$$n_S = N\rho_S / M_S \tag{2.40}$$

where ϕ_A is the surface coverages of absorbate A, μ is the modified photoelectron cross section given by Equation (2.39), N is the Avogadro's number, λ_S is the escape depth of photoelectrons through a substrate S, M_S is the molar mass of the substrate S, and ρ_S is the substrate density. This equation assumes that the adsorbate is non-attenuating and the surface coverages less than a monolayer.

Since many of these parameters will be constant for a particular absorbate, substrate and spectrometer, Equation 2.38 can be simplified as

$$\phi_A = K \cdot \frac{I_A}{I_S} \tag{2.41}$$

where

$$K = \frac{E_{K,A}}{E_{K,S}} \cdot \frac{\mu_S}{\mu_A} \cdot \frac{N\rho_S\lambda_S \cos\theta}{M_S} \tag{2.42}$$

Some calculations and values for K appropriate for the adsorbate atoms used in these experiments are described in appendix A. This expression is used for the calculation of surface coverages less than a monolayer. In the calculation of surface coverages greater than a monolayer, the scattering effect of the adsorbate must be considered.

(b) Ionisation cross section

The values of photoionisation cross section, σ_i, have been calculated and published by Scofield [41] and are often used in XPS. Figure 2.17 shows the general behaviour of calculated cross sections, σ_i, versus the atomic number.

Since the electron spectrometer is usually operated at a constant pass energy, the detector efficiency will be constant and can be ignored.

For unpolarised X-rays, the angular asymmetry factor, $L_i(\gamma)$, is given by [45]

$$L_i(\gamma) = \left[1 - \frac{\beta_A}{2} \cdot \frac{(3\cos^2\gamma - 1)}{2}\right] \tag{2.43}$$

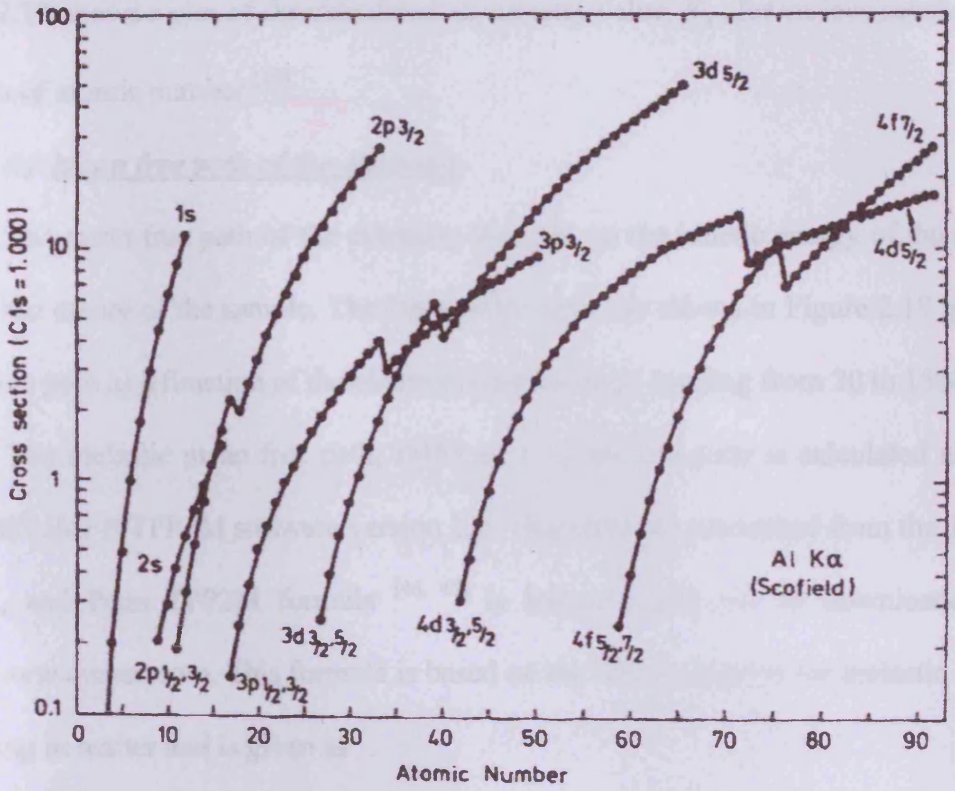

Figure 2.17. Calculated cross sections, σ_i, for Al Kα radiation relative to the C1s cross section. From Scofield [41].

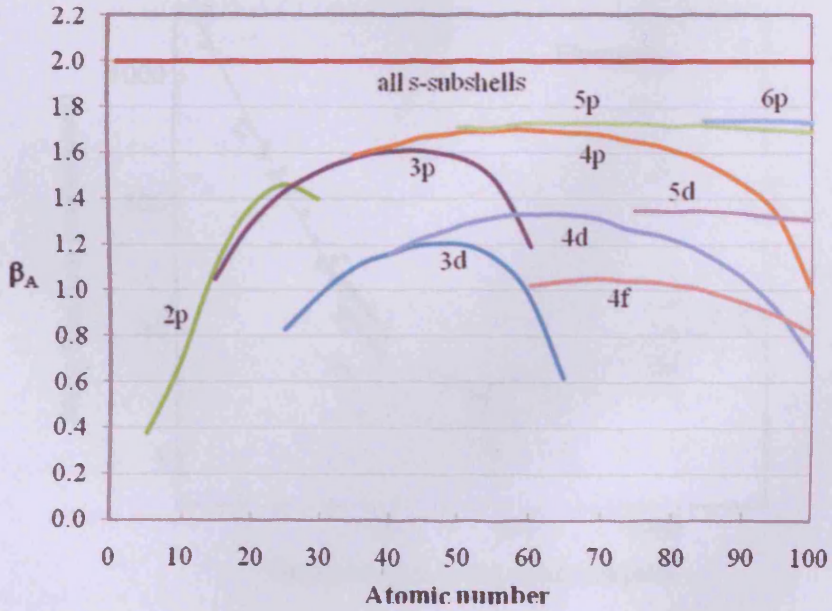

Figure 2.18. Calculated values of asymmetry parameter, β_A, as a function of atomic number for Al Kα (1486.6 eV) X-rays incident on atoms. From Reilman et al. [45].

Figure 2.18 shows a plot of the calculated asymmetry value, β_A, for various subshells as a function of atomic number [45].

(c) Mean free path of the electrons

The mean free path of the electrons depends on the kinetic energy of the electron and on the nature of the sample. The "universal curve" as shown in Figure 2.19 gives the mean free path as a function of the electron kinetic energy ranging from 20 to 1500 eV.

The inelastic mean free path, IMFP or λ, of the substrate is calculated using the QUASES-IMFP-TPP2M software version 2.2. This software calculated from the Tanuma, Powell, and Penn TPP2M formula [46, 47] is freeware and can be downloaded from http://www.quases.com. This formula is based on the Bethe equation for inelastic electron scattering in matter and is given as

$$\lambda = \frac{E}{\{E_P^2[\beta \ln(\gamma E) - (C/E) + (D/E^2)]\}} \tag{2.44}$$

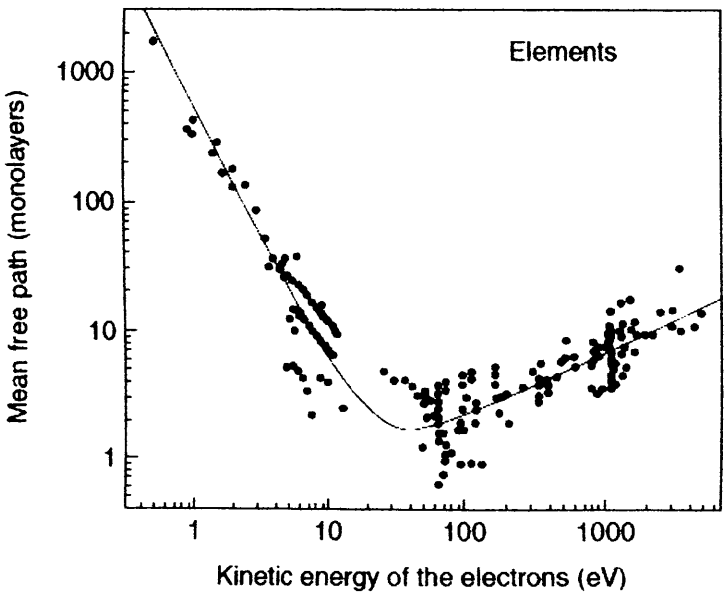

Figure 2.19. Dependence of the mean free path on kinetic energy of the electrons. From Briggs and Seah [48].

where E is the energy of electron (in eV), $E_P = 28.8(N_v \rho / M)^{1/2}$ is the free electron plasmon energy (in eV), ρ is the density of the analysed material (in g.cm^{-3}), N_v is the number of valence electrons per atom (for elements) or molecule (for compounds), and M is the atomic or molecular weight. The terms of β, γ, C, and D were defined in terms of material parameters derive from the fits to calculated IMFP for 27 elements and 14 organic compounds. (see Appendix C for the detailed study of the IMFP calculation).

(d) *The thickness of a thin overlayer*

The intensity of photoemitted electrons (I) as a function of depth (d) is described by the Beer-Lambert equation:

$$I = I_0 \exp\left[-\frac{d}{\lambda \cos\theta}\right] \tag{2.45}$$

where I_0 is the intensity from an infinitely thick, clean substrate and θ is the angle between the surface normal and the direction of electron detection. As illustrated in Figure 2.20, the electron signal decays exponentially as a function of depth.

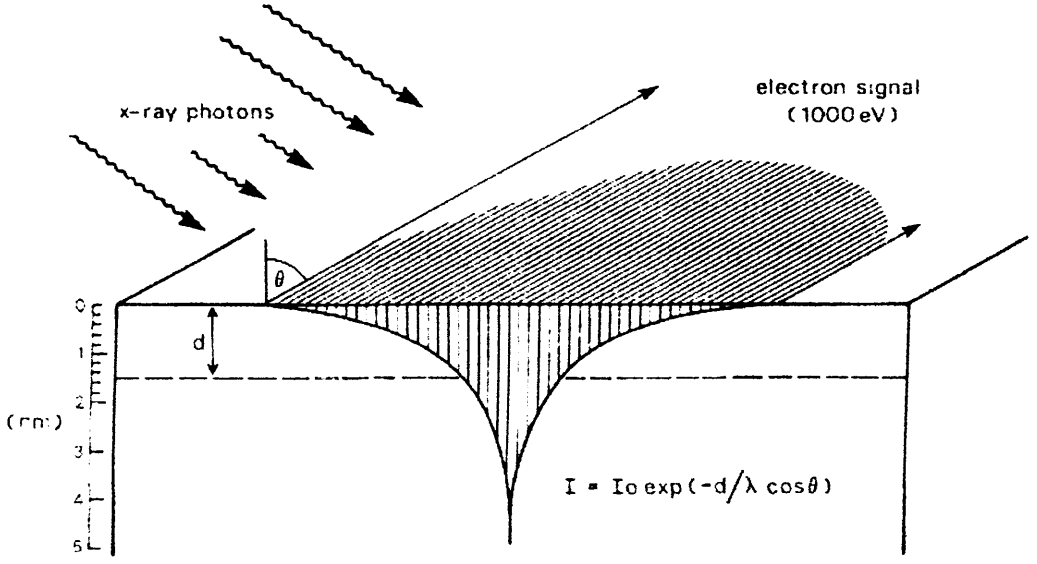

Figure 2.20. Intensity of the photoemission as a function of depth [32].

This simple expression can be applied to estimate the magnitude of a thin overlayer attenuating the XPS signal from a substrate. If A forms a thin overlayer of thickness d on the substrate S, the intensity from substrate S, I_S, is then given by

$$I_S = I_{0,S} \exp\left(-\frac{d}{\lambda_S \cos\theta}\right) \tag{2.46}$$

and that from overlayer A, I_A, by

$$I_A = I_{0,A}\left[1-\exp\left(-\frac{d}{\lambda_A \cos\theta}\right)\right] \tag{2.47}$$

Dividing Equation (2.47) by Equation (2.46)

$$\frac{I_A}{I_S}\cdot\frac{I_{0,S}}{I_{0,A}} = \frac{1-\exp\left(-\frac{d}{\lambda_A \cos\theta}\right)}{\exp\left(-\frac{d}{\lambda_S \cos\theta}\right)} \tag{2.48}$$

If $\lambda_A \approx \lambda_S$, i.e. if two peaks at similar binding energies are considered. The overlayer thickness d can now written as

$$d = \lambda_A \cos\theta \ln\left[1+\frac{I_A}{I_S}\frac{I_{0,S}}{I_{0,A}}\right] \tag{2.49}$$

where $I_{0,A}$ and $I_{0,S}$ are the intensity recorded for the pure element A and substrate S, respectively.

2.3.3. Scanning tunnelling microscopy (STM)

2.3.3.1. Introduction

Scanning tunnelling microscopy (STM) is one kind of scanning probe microscopy (SPM) and is one of the most recently developed techniques for studying surface structure. It was invented by Binnig and Rohrer in the early 1980s, for which they were awarded the Nobel Prize for Physics in 1986 [49]. The development of the scanning tunnelling microscope has proven to be the most important event in the surface science

field. STM is an effective tool for the investigation of surface structure on the Ångstrom scale.

The principle is very simple. A sharp metal tip is brought extremely close (~0.5-1 nm) to a conducting surface. A potential difference is then applied across the tip and the surface and a tunnelling current will flow between tip and surface. By measuring the potential and/or the current as the tip is scanned across the surface, an image of the surface topography is obtained.

2.3.3.2. Basic principles

According to the classical laws, electrons are particles with a specific location and velocity and they cannot travel outside the material of which they are a part due to the energy barrier at the edge of the material. This barrier can be overcome by applying sufficient energy and the electrons can then be drawn out of the surface. The amount of energy required to move an electron from the highest filled level in the metal, called the Fermi level, to the infinite point, called the vacuum level, is called the work function ϕ of the surface which is given by

$$\phi = E_{vac} - E_F \tag{2.50}$$

where E_{vac} is the potential energy of electrons in the vacuum and E_F is the Fermi energy. The value of the work function depends on the materials.

In quantum mechanics, the electron is treated not as a particle, but rather a wave. The wave function of an electron decays exponentially with the distance inside the barrier. When an electron is incident upon a vacuum barrier and the electron's kinetic energy is less than its potential energy, so the electron can tunnel through a finite potential barrier and appear on the other side of the barrier close to the surface. Figure 2.21 shows the finite probability that the electron may be found outside the barrier.

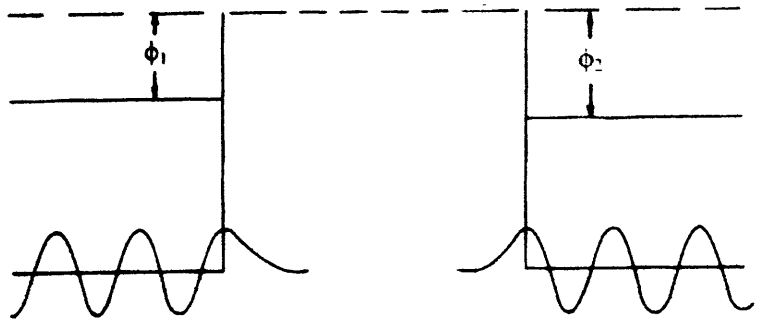

Figure 2.21. Quantum-mechanical treatment of an electron. The electron is found outside the material with some probability. The probability falls exponentially to near zero within a few nanometers at the material surface [50].

As an atomically sharp metallic tip and a conducting sample are brought sufficiently close together (on the order of 1 nanometer), the electron wave functions between the tip and the sample overlap and tunnelling can occur. The electron wave function at the Fermi level has a characteristic exponential inverse length κ given by

$$\kappa = \frac{\sqrt{2m\phi}}{\eta} \tag{2.51}$$

where m is the electron mass, ϕ is the work function or the height of the local tunnelling barrier, and η is Planck's constant divided by 2π. When a small potential V is placed across the tip-sample junction, the overlap of the electron wave function permits quantum mechanical tunnelling and a tunnelling current I will flow across the vacuum gap as shown in Figure 2.22. This current decays exponentially with the gap between the tip and the sample, called tunnelling gap, as

$$I = I_0(V)\exp(-2\kappa d) \tag{2.52}$$

where d is the distance between the tip and the surface. The tunnelling current is very sensitive to the distance between the tip and the surface. If the distance changed by an amount equal to the diameter of a single atom, the tunnelling current would change by a factor of as much as 1000.

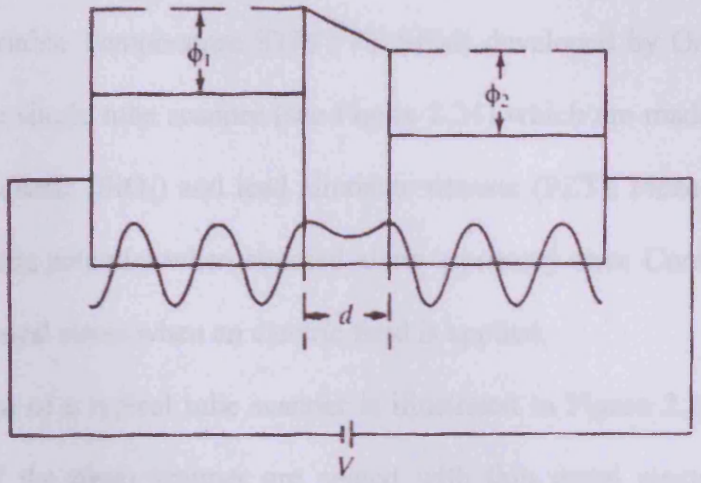

Figure 2.22. Energy diagram representing tunnelling of electron [50].

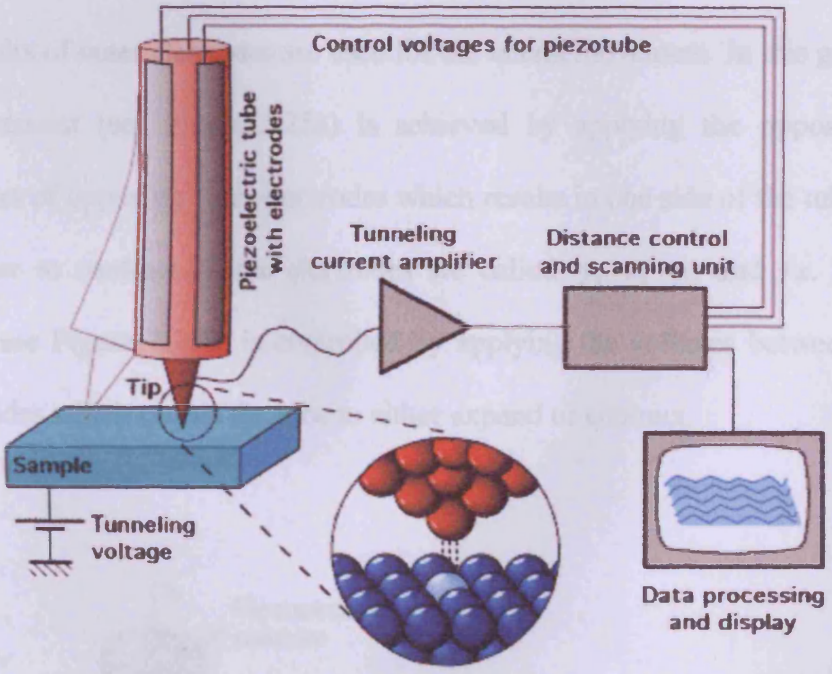

Figure 2.23. Schematic diagram of the STM [51].

2.3.3.3. Instrument for STM

The STM comprises of the scanner, the vibration isolation system, the control circuitry and the computer. A schematic of the STM is shown in Figure 2.23. The operation of these components is discussed below.

(a) Scanner assembly

In the Variable Temperature STM (VT SPM) developed by Omicron, the STM scanner is a piezo single tube scanner (see Figure 2.24) which are made of piezoelectric material such as quartz (SiO_2) and lead zirconate titanate (PZT). Piezoelectric materials generate the electric potential when stressed along a primary axis. Conversely, they will produce a mechanical stress when an electric field is applied.

The design of a typical tube scanner is illustrated in Figure 2.24. The inner and outer surfaces of the piezo scanner are coated with thin metal electrodes. The outer surfaces are separated into four equal sectors of 90 degrees which are electrically isolated from each other. The inner electrode is then used for the vertical displacement, and the opposing pairs of outer electrodes are used for the lateral movement. In this geometry, the lateral movement (see Figure 2.25a) is achieved by applying the opposite voltages between pairs of opposing outer electrodes which results in one side of the tube to expand and the other to contract. These electrodes are called *-y*, *-x*, *+y*, and *+x*. The vertical movement (see Figure 2.25b) is controlled by applying the voltages between inner and outer electrodes which causes the tube to either expand or contract.

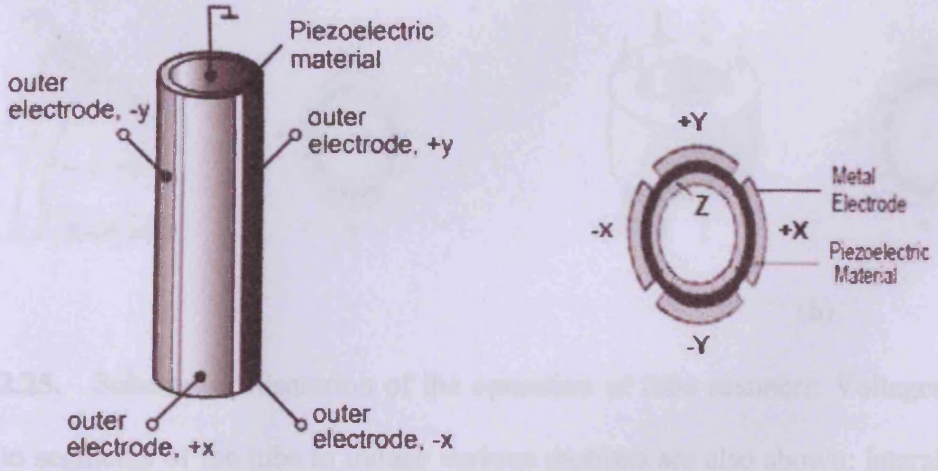

Figure 2.24. Schematic illustration of the piezoelectric single tube scanners.

While the tip is rastered back and forth across the surface, the tunnelling current is monitored and fed into a feedback circuit that controls the voltage applied to the *z*-piezoelectric element. Images are usually obtained in either of two modes, described in the detail below. In the constant current mode, a fixed voltage is applied between the tip and the sample while the feedback circuit adjusts the *z*-piezoelectric element to maintain constant tunnelling current as the tip is scanned across the surface. A topographic image of the surface is produced by monitoring the displacement of *z*-piezoelectric element during scanning. In constant height mode, the *z*-position of the tip is fixed in space as the tip is scanned across the sample with a constant tunnelling bias. An image of the surface is formed by recording the tunnelling current varying with the tip-sample distance. The sensitivity of a piezo scanner of the VT SPM is 9 nm per volt in the *z* direction with a maximum lateral scan range of up to 12 micrometers (μm).

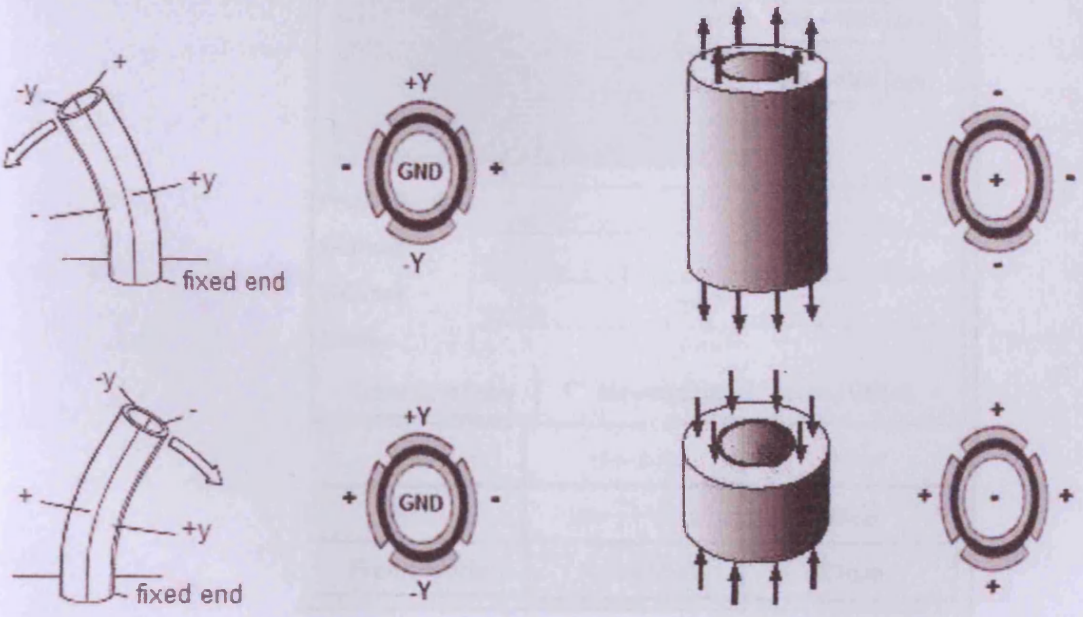

Figure 2.25. Schematic illustration of the operation of tube scanners. Voltages signals applied to segments of the tube to induce various motions are also shown: lateral (a) and vertical (b) motions.

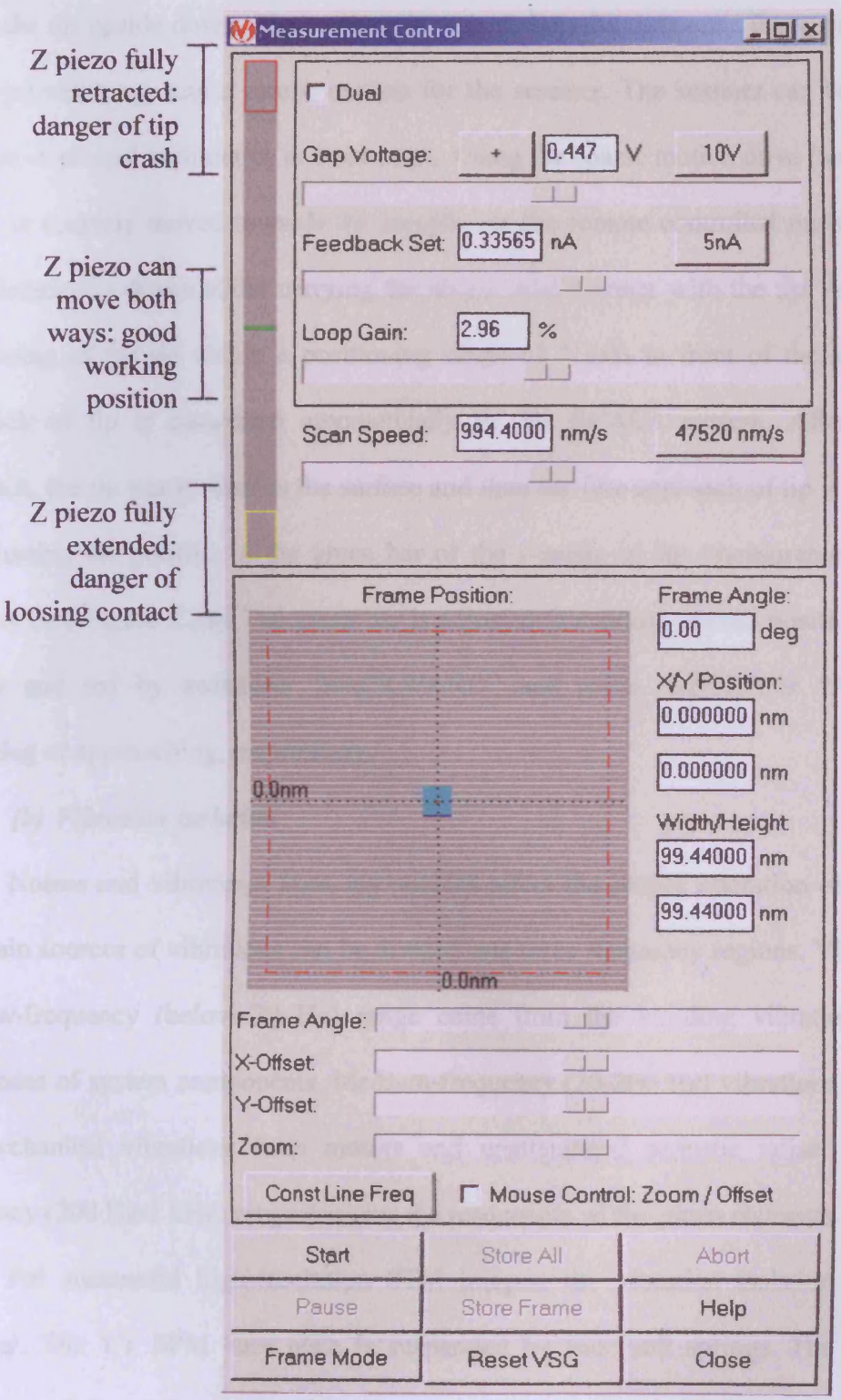

Figure 2.26. The measurement control window [52].

The tip is placed on a tip holder attached magnetically to the top of the piezo scanner, while the sample is pushed in horizontally from the front with the sample surface

facing the tip upside down. The scanner is mounted on the three-axis linear piezo motor which provides *x*, *y* and *z* coarse motion for the scanner. The scanner can be moved a distance of several millimetres in 1 nm steps. Using the coarse motion drive (remote box), the tip is coarsely moved towards the sample via the remote controlled movement of a piezoelectrically driven slider carrying the single tube scanner with the tip. After coarse positioning of the tip within a positioning range of 5 mm in front of the sample, the approach of tip is completed automatically by the SCALA system. After a coarse approach, the tip nearly reaches the surface and then the fine approach of tip is performed by adjusting the position of the green bar of the z-meter in the 'measurement control' window (see Figure 2.26). The green bar is adjusted to a nearly central position between yellow and red by switching "BACKWARD" and press "RETR" or "APPR" for retracting or approaching, respectively.

(b) Vibration isolation

Noises and vibrations from any sources affect the proper operation of the STM. The main sources of vibrations can be divided into three frequency regions. Vibrations in the low-frequency (below 20 Hz) range come from the building vibration and the resonances of system components. Medium-frequency (20-200 Hz) vibrations arise from the mechanical vibrations from motors and unattenuated acoustic noise. The high-frequency (200 Hz-1 kHz) range contains the resonances of the piezo elements.

For successful high-resolution STM images, the vibration isolation system is essential. The VT SPM base plate is suspended by four soft springs. The resonance frequency of the spring suspension system is about 2 Hz. Damping vibrations of the suspension system can be achieved in UHV by using a nearly non-periodic eddy current damping mechanism. For this, a ring of copper plates which come down between permanent magnets is mounted on the STM stage.

In order to enable tip or sample exchange or adjustment, the push-pull motion drive (PPM) is used to lock the STM stage as shown in Figure 2.27.

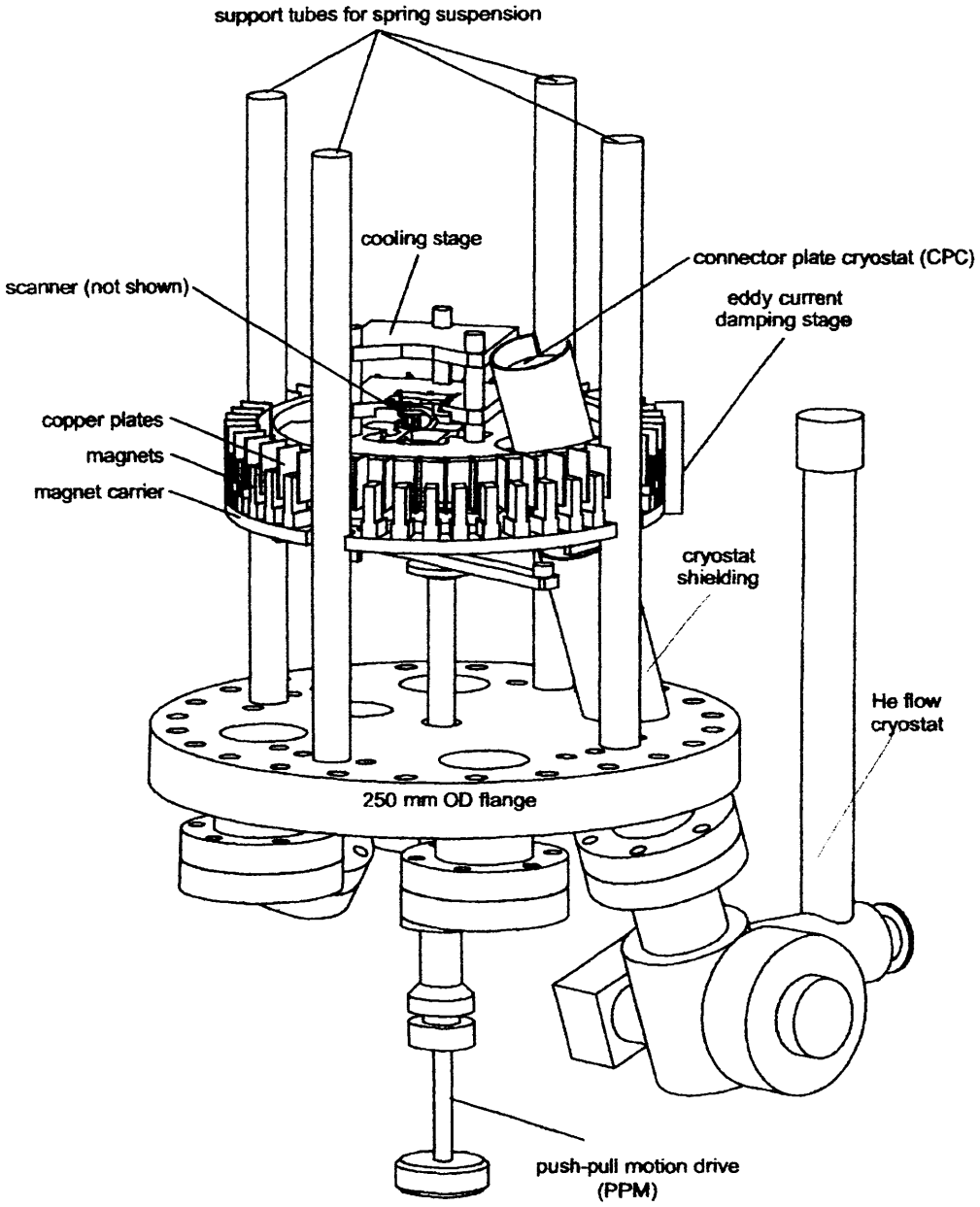

Figure 2.27. Side view of the VT-SPM [52].

2.3.3.4. Modes of STM operation

There are two basic operation modes of the STM such as constant-current mode and constant-height mode as illustrated in Figure 2.28.

(i) Constant current mode

In the constant current mode, the tip is scanned over the surface at a constant potential. A feedback mechanism maintains a constant tunnelling current whilst a constant potential difference is applied between the tip and the surface. Due to the exponential dependence of the tunnelling current on the tunnelling gap, these conditions require a constant tunnelling gap. When the tip is scanned across the surface of the sample, the variation in the vertical tip position is adjusted to maintain the constant tunnelling current. By applying the linear voltage ramp to the x and y piezoelectric elements, the tip can be scanned laterally over the surface and the voltage signal from a feedback circuit is directed to the z piezoelectric element. The image is then formed by plotting the voltage applied to z piezoelectric element (tip height) versus the x, y coordinates of the tip which is a set of constant charge density contours of the surface below the tip. The disadvantage of this mode is that the measurement takes more time, but it can measure the rough surface.

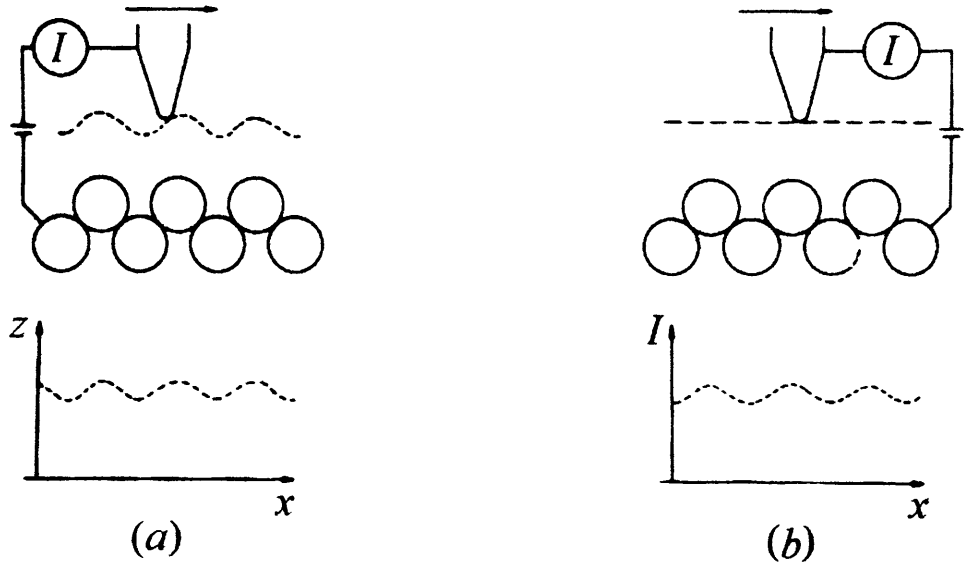

Figure 2.28. Schematic presentation of (a) the constant-current mode and (b) the constant-height mode [50].

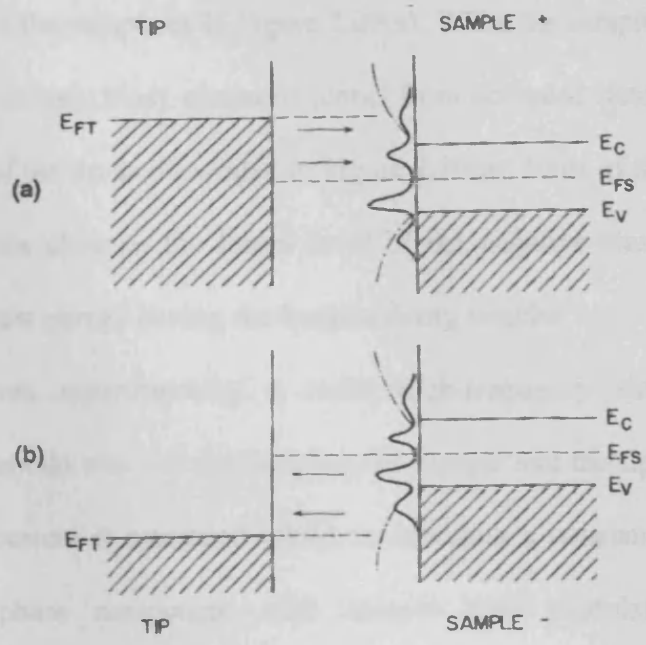

Figure 2.29. Schematic diagram of tunnelling spectroscopy [53].

(ii) Constant height mode

The constant height mode is sometimes called current imaging. In this operation, a tip can be scanned over the surface at the constant height and the constant applied voltage while the variations in tunnelling current *I* occur due to the variation in topographic structure with the tip-sample separation. This technique provides faster imaging of atomically flat surfaces. If the surface is not smooth, the tip may collide with the surface and be damaged. In this instance, the tip current *I* (tunnelling current) is plotted versus the lateral tip position and the result provides contours of different charge density.

(iii) Spectroscopy (STS)

Scanning tunnelling spectroscopy (STS) provides the information about the surface electronic structure by probing the local density of states (LDOS) as a function of energy. As shown in Equation (2.51) and (2.52), the dependence of the STM image upon the voltage forms the basis for the spectroscopic information. Consider the schematic in Figure 2.29, when the sample is positive with respect to the tip (positive sample bias), the tunnelling current arises from electrons that tunnel from the occupied states of the tip into

unoccupied states of the sample as in Figure 2.29(a). When the sample is negative relative to the tip (negative sample bias), electrons tunnel from occupied states of the sample into unoccupied states of the tip as illustrated in Figure 2.29(b). Most of the tunnelling current arises from electrons close to the Fermi level of the negative-biased electrode due to states with the highest energy having the longest decay lengths.

STS involves superimposing a small high-frequency sinusoidal modulation voltage on a constant dc bias voltage between the sample and the tip and the component of the tunnelling current is measured whilst maintaining a constant average tunnelling current. The in-phase component with sample bias modulation gives dI/dV simultaneously with the topography of the sample.

Another method introduced by Hamers, Tromp, and Demuth [54] involves the local measurement of *I–V* curves with the tip stationary at each position in the scan. This technique is called current imaging tunnelling spectroscopy (CITS). Figure 2.30 schematically shows the *I–V* curves expected for conducting and semiconducting materials. The I–V curves of the conducting materials are continuous at low biases, no energy gap at the Fermi level as opposed to the situation in the semiconducting materials.

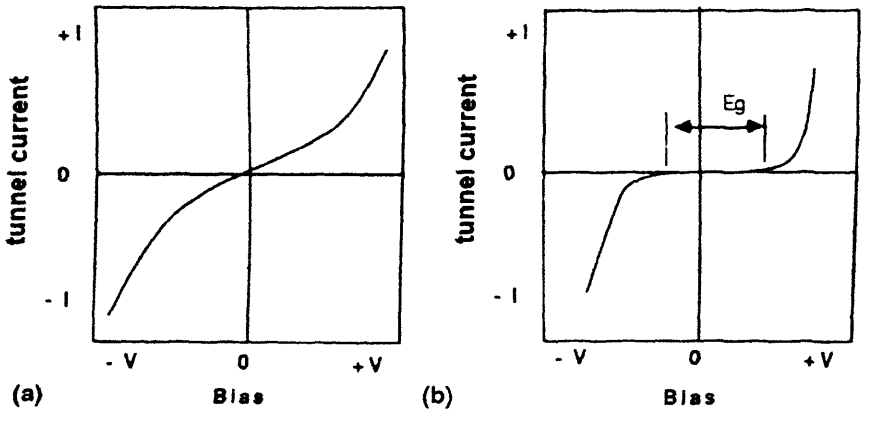

Figure 2.30. The sample-tip junction *I–V* curve of conducting (a) and semiconducting (b) in character [53].

2.3.4. Ion scattering spectroscopy (ISS)

2.3.4.1. Introduction

Ion scattering techniques, in which the scattered primary ions are studied, may be divided into two classes depending on the energy of the ion beam. Low energy ion scattering (LEIS or ISS) includes the projectile energies of 0.5-10 keV and medium or high energy ion scattering (MEIS or HEIS) ranges in energies from 100 keV up to several MeV. The HEIS technique is best known in practice as Rutherford backscattering spectroscopy (RBS).

ISS is one of the most useful surface analysis techniques, since it is an extremely surface sensitive method which provides the atomic composition of the outer atomic layer present on a sample surface.

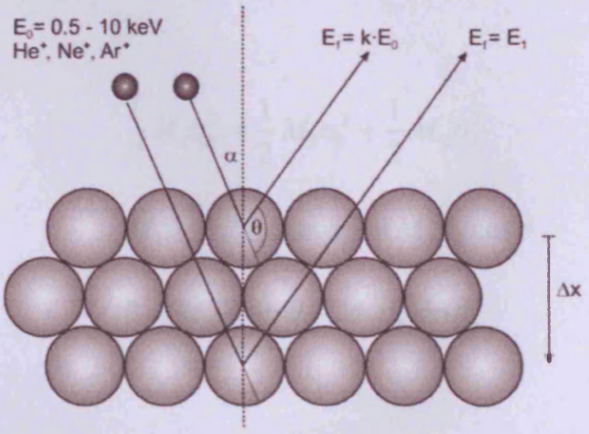

Figure 2.31. Schematic illustration of ISS [55].

2.3.4.2. Classical scattering theory

In ISS, the sample is bombarded with a beam of positively charged ions (helium, neon or argon ions) with energies from 100 eV to about 2 keV. The incident ion beam is directed onto the solid surface at an angle α relative to the surface normal, some of the primary projectiles are backscattered into a solid angle $d\Omega$ at a scattering angle θ (i.e. the

angle between the incident ion beam and the detected ion beam), and the energy distribution of these ions is measured as shown in Figure 2.31.

i) Single collision model

Consider the classical hard-sphere collision between two masses M_1 and M_2. The trajectories for the elastic binary collision in the laboratory and in the centre-of-mass (CM) system are illustrated in Figure 2.32. The projectile of mass M_1 has the energy $E_0 = \frac{1}{2}M_1\upsilon_0^2$ and the target atom of mass M_2 is initially at rest. After the collision into the scattering angle θ, the final energy E_1 of the primary particle is $E_1 = \frac{1}{2}M_1\upsilon_1^2$ and the final energy E_2 of the target is $E_2 = \frac{1}{2}M_2\upsilon_2^2$. From the conservation laws of energy and momentum (parallel and perpendicular to the direction of incidence), the particle energies can be written as

$$\frac{1}{2}M_1\upsilon_0^2 = \frac{1}{2}M_1\upsilon_1^2 + \frac{1}{2}M_2\upsilon_2^2 \tag{2.53}$$

$$M_1\upsilon_0 = M_1\upsilon_1\cos\theta + M_2\upsilon_2\cos\phi \tag{2.54}$$

$$0 = M_1\upsilon_1\sin\theta - M_2\upsilon_2\sin\phi \tag{2.55}$$

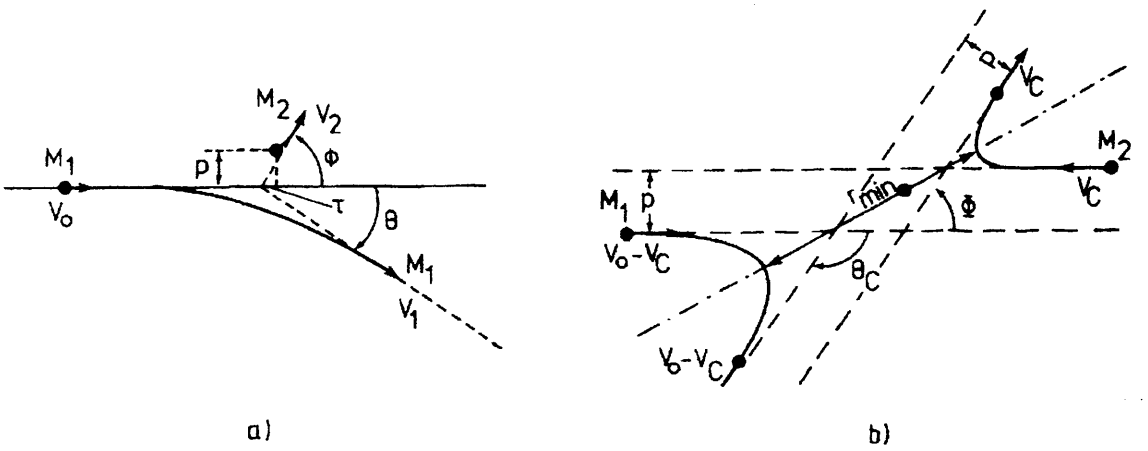

Figure 2.32. Single-scattering geometry for laboratory (a) and centre-of-mass system (b) [56].

Eliminating the velocity components of the recoiling target atom, i.e. recoil angle ϕ and recoil velocity υ_2, then the ratio of the primary particle velocities is given by

$$\frac{\upsilon_1}{\upsilon_0} = \frac{1}{(M_1 + M_2)} \cdot \left\{ M_1 \cos\theta \pm \sqrt{M_2^{\,2} - M_1^{\,2} \sin^2\theta} \right\} \tag{2.56}$$

In order to be convenient for comparison with the experimental data, consider the ratio of the energy which can be written as

$$\frac{E_1}{E_0} = \left(\frac{M_1 \cos\theta \pm \sqrt{M_2^2 - M_1^2 \sin^2\theta}}{M_1 + M_2} \right)^2 \tag{2.57}$$

The energy transfer only depends on the masses of the primary particle and the target and the scattering angle θ. Only the positive sign applies to $M_2 > M_1$ and both positive and negative are solutions if $1 > M_2/M_1 > \sin\theta$.

For θ = 90° and 180°, Equation (2.57) for single scattering becomes particularly simple:

$$\frac{E_1}{E_0} = \left(\frac{M_2 - M_1}{M_2 + M_1} \right), \qquad \text{for } \theta = 90° \tag{2.57a}$$

$$\frac{E_1}{E_0} = \left(\frac{M_2 - M_1}{M_2 + M_1} \right)^2, \qquad \text{for } \theta = 180° \tag{2.57b}$$

In the centre-of-mass (CM) coordinate system as shown in Figure 2.32(b), a similar general expression as in Equation (2.57) can be deduced. With the CM scattering angle θ_c, the energy ratio becomes

$$\frac{E_1}{E_0} = \frac{4M_1M_2 \sin^2\theta_c/2}{(M_1 + M_2)^2} \tag{2.58}$$

The transformation from the CM system (scattering angle θ_c) to the laboratory system with the scattering angle θ for primary particles and ϕ for recoiled surface atoms is given by

$$\tan\theta = \frac{M_2 \sin\theta_c}{(M_1 + M_2 \cos\theta_c)} \tag{2.59}$$

$$\tan\phi = \frac{\sin\theta_c}{(1 - \cos\theta_c)} \tag{2.59a}$$

Similarly, the corresponding expression for the recoiling target atom is

$$\frac{E_2}{E_0} = \frac{4M_1M_2\cos^2\phi}{(M_1 + M_2)^2}, \qquad \text{for } \phi \leq 90° \tag{2.60}$$

where E_2 is the energy of the recoiling target atom and ϕ is the scattering angle of the recoiling target atom relative to the incident ion trajectory. The recoiling target atoms may be scattered either into the bulk or into the vacuum depending on the impact point of the primary ions. A typical ISS spectrum obtained by measuring the energy distribution of the scattered ions leaving the sample is shown in Figure 2.33, the different surface species corresponding to the scattered peak values of E_1 being labelled.

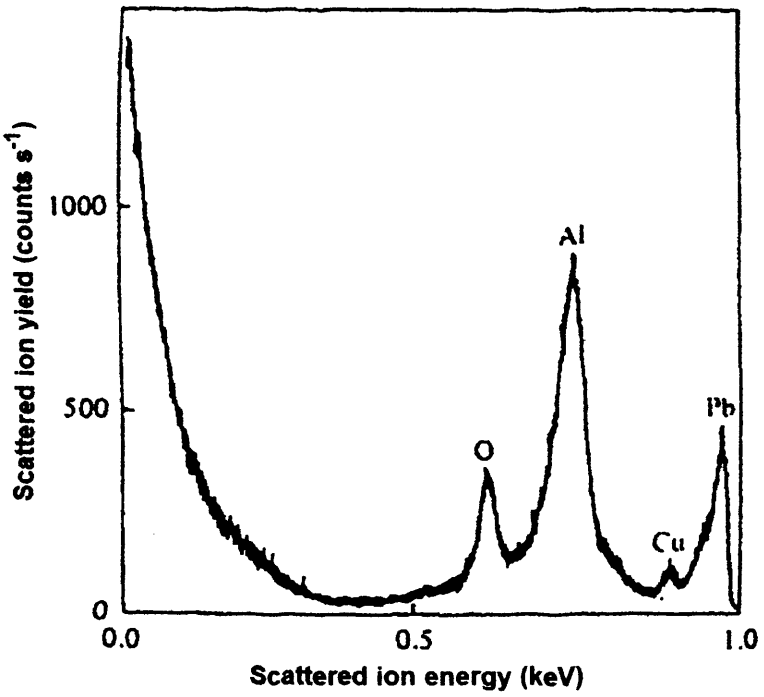

Figure 2.33. 'Typical' 1 keV He^+ ion scattering spectrum of a contaminated alloy surface at a scattering angle of 90° [50].

Consequently, from Equation (2.57), an expression for the mass resolution [57] for ISS in the single-scattering frame can be deduced. For $M_2 > M_1$, it is given by

$$\frac{M_2}{\Delta M_2} = \frac{E}{\Delta E} \cdot \frac{2M_1 M_2}{(M_1 + M_2)} \left(\frac{M_2 + M_1 \sin^2\theta - \cos\theta \sqrt{M_2^2 - M_1^2 \sin^2\theta}}{M_2^2 - M_1^2 \sin^2\theta + M_1 \cos\theta \sqrt{M_2^2 - M_1^2 \sin^2\theta}} \right) \quad (2.61)$$

For the special case of $\theta = 90°$, the mass resolution reduced to

$$\frac{M_2}{\Delta M_2} = \frac{E}{\Delta E} \cdot \frac{2M_1 M_2}{(M_2^2 - M_1^2)} \quad (2.62)$$

With a constant relative energy resolution of the detector of $E/\Delta E = 100$, the best resolution is obtained for large scattering angles and about equal masses of primary ion and target atoms $(M_2 \approx M_1)$.

ii) Interaction potentials and scattering cross section

In principle, surface elemental composition can be determined by measuring the scattered particle intensity as a function of the energy at a given scattering angle. The intensities of the scattered projectile, i.e. the probability for scattering into a certain angular and energy interval, are normally given by a scattering cross-section $\sigma(\theta)$ which depends on the interaction potential $V(r)$.

At first for any potential there is a unique relation between the scattering angle θ_c (in the CM system) and the impact parameter p for any particular incident ion trajectory (see Figure 2.32(b)). For the CM coordinate, the scattering angle θ_c can be obtained by considering the conservation of angular momentum, which is given by

$$\theta_c = \pi - 2\int_{r_{min}}^{\infty} \frac{p\,dr}{r^2 \sqrt{1 - \frac{p^2}{r^2} + \frac{V(r)}{E_{CM}}}} \quad (2.63)$$

where $E_{CM} = E_0 M_2/(M_1 + M_2)$ is the relative energy in the CM system, r_{min} is the distance of closest approach during the collision. Equation (2.63) shows the connection

between the impact parameter p and the scattering angle θ_c which is related to the differential scattering cross-section $d\sigma = 2\pi p dp$. For the energy regime used in ISS, the scattering potentials $V(r)$ is usually taken to be the purely repulsive interaction between the two positive point charges, Coulombic term $(1/r)$, with some account of the screening of the nuclear charges by the electron cloud, screening function. Such a screened Coulomb potential can be written as

$$V(r) = \frac{Z_1 Z_2 e^2}{4\pi\varepsilon_0 r}\Phi(r/a) \tag{2.64}$$

where Z_1 and Z_2 are the nuclear charges of primary particle and target atom, respectively, e is the unit of electrical charge (in SI units), r is the interatomic distance and a is the 'screening length' in the screening function $\Phi(r/a)$ and gives several analytical expressions in the literature. The Molière approximation applied to the Thomas-Fermi model (TFM) [58] has become most widely used in ISS. It is given by a sum of three exponentials:

$$\Phi(r/a) \equiv \Phi(x) = 0.35e^{-0.3x} + 0.55e^{-1.2x} + 0.10e^{-6x} \tag{2.65}$$

The screening length according to either Firsov or Lindhard [59] is used which is given by

$$a_{Firsov} = \frac{0.8854a_0}{\left(\sqrt{Z_1} + \sqrt{Z_2}\right)^{2/3}} \tag{2.66}$$

$$a_{Lindhard} = \frac{0.8854a_0}{\sqrt{Z_1^{2/3} + Z_2^{2/3}}} \tag{2.67}$$

where a_0 is the Bohr radius of 0.529 Å and the numerical factor is $(9\pi^2/128)^{1/3}$.

In the RBS regime, the Coulomb potential can be used to determine the scattering cross-section which is given by

$$(d\sigma/d\Omega)_c = \left(\frac{Z_1 Z_2 e^2}{4E_r \sin^2\theta_c/2}\right)^2 \tag{2.68}$$

This is well known as the Rutherford scattering cross-section [60] in the CM system.

2.3.4.3. Instrumentation

The experimental requirement for ISS is a UHV system. Figure 2.34 is schematic of the typical instrument of ion scattering using an electrostatic energy analyser. The essential components are the ion source and an energy analyser. A fairly monoenergetic beam of positive ions is produced by an ion gun which comprises ion generation, acceleration, extraction, and focussing stages. The ISE 100 fine focus ion source produced by Omicron is used which has a hot filament to produce electrons which are accelerated into a gas ionisation region. The acceleration, extraction, and focussing of the ion beam is then performed electrostatically.

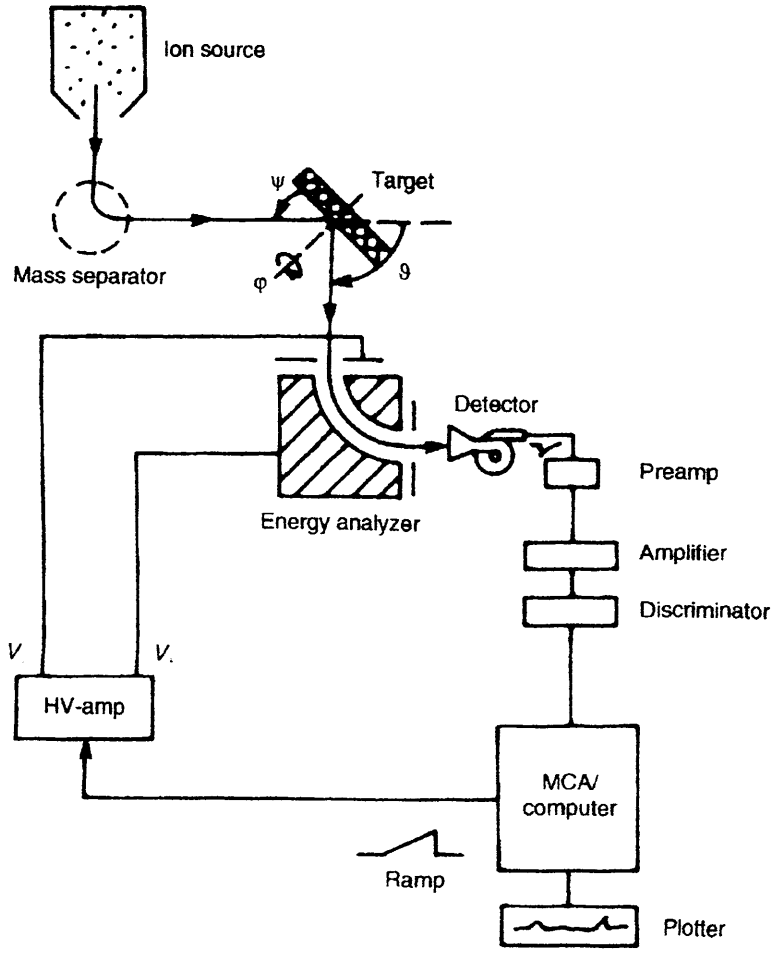

Figure 2.34. Schematic experiment arrangement for ISS [42, 61].

For the energy analysis of the scattered ions, the concentric hemispherical analyser (CHA) is used which is identical to that used for electron spectroscopy. So the energy analyser used for ISS in these experiments is the EA 125 analyser as described in the previous section.

2.3.4.4. Element analysis

In the ISS experiment, the scattering ion signal intensity I_i of the ions scattered from element i can be written as

$$I_i = I_0 N_i S P_i^+ (d\sigma_i / d\Omega) T \Delta\Omega \qquad (2.69)$$

where I_0 is the primary ion beam current, N_i the surface density of element i, S the shadowing component, P_i^+ the ion survival probability, $d\sigma_i / d\Omega$ the differential cross section, T the transmission factor characterising the spectrometer, and $\Delta\Omega$ the acceptance solid angle of the detector. The equation above is seldom used for the quantitative of surface analysis due to the uncertainty in the ion survival probability P_i^+ and the shadowing component.

2.4. Conclusion

The studies of the model based catalyst surfaces are performed in the ultra-high vacuum system using the surface techniques described above to investigate the properties of surfaces such as the compositions and chemical state obtained through XPS, the atomic surface structures and surface defect structures by LEED and STM, and the composition of the outermost surfaces by means of ISS.

2.5. References

[1] M. F. Al-Kuhaili, E. E. Khawaja, D. C. Ingram and S. M. A. Durrani, *Thin Solid Films* **2004**, *460*, 30-35.

[2] M. A. Quevedo-Lopez, O. Mendoza-Gonzalez, R. F. Reidy, R. Ramirez-Bon and R. A. Orozco-Teran, *Journal of Physics and Chemistry of Solids* **2000**, *61*, 727-734.

[3] E. Cazzanelli, L. Papalino, A. Pennisi and F. Simone, *Electrochimica Acta* **2001**, *46*, 1937-1944.

[4] M. Kharrazi, A. Azens, L. Kullman and C. G. Granqvist, *Thin Solid Films* **1997**, *295*, 117-121.

[5] L. Ottaviano, A. Pennisi, F. Simone and A. M. Salvi, *Optical Materials* **2004**, *27*, 307-313.

[6] A. C. Rubin, L. Ying-Li, K. M. Lee and D. H. Steven, *Journal of Applied Physics* **1986**, *60*, 749-753.

[7] J. Scarminio, A. Lourenço and A. Gorenstein, *Thin Solid Films* **1997**, *302*, 66-70.

[8] F. C. Stuart, M. N. Nguyet, J. P. Stephen and R. D. Rauh, *Journal of Applied Physics* **1989**, *66*, 1333-1337.

[9] T. A. Taylor and H. H. Patterson, *Applied Spectroscopy* **1994**, *48*, 674-677.

[10] H. S. Witham, P. Chindaudom, I. An, R. W. Collins, R. Messier and K. Vedam, *39th National Symposium of the American Vacuum Society* (Chicago, Illinois (USA)) **1993**, pp. 1881-1887.

[11] T.-S. Yang, Z.-R. Lin and M.-S. Wong, *Applied Surface Science* **2005**, *252*, 2029-2037.

[12] R. M. Abdel-Latif, *Physica B: Condensed Matter* **1998**, *254*, 273-276.

[13] O. Bohnke, G. Frand, M. Fromm, J. Weber and O. Greim, *Applied Surface Science* **1996**, *93*, 45-52.

[14] Y. Fujita, K. Miyazaki and C. Tatsuyama, *Japanese Journal of Applied Physics* **1985**, *24*, 1082-1086.

[15] W. B. Henley and G. J. Sacks, *Journal of the Electrochemical Society* **1997**, *144*, 1045-1050.

[16] M. Losurdo, D. Barreca, G. Bruno and E. Tondello, *Thin Solid Films* **2001**, *384*, 58-64.

[17] K. Gesheva, A. Szekeres and T. Ivanova, *Solar Energy Materials and Solar Cells* **2003**, *76*, 563-576.

[18] T. Ivanova, K. A. Gesheva, G. Popkirov, M. Ganchev and E. Tzvetkova, *Materials Science and Engineering B* **2005**, *119*, 232-239.

[19] N. Özer, *Thin Solid Films* **1997**, *305*, 80-87.

[20] C. Santato, M. Odziemkowski, M. Ulmann and J. Augustynski, *Journal of the American Chemical Society* **2001**, *123*, 10639-10649.

[21] N. Sharma, M. Deepa, P. Varshney and S. A. Agnihotry, *Thin Solid Films* **2001**, *401*, 45-51.

[22] R. Solarska, B. D. Alexander and J. Augustynski, *Comptes Rendus Chimie* **2006**, *9*, 301-306.

[23] M. A. Bica De Moraes, B. C. Trasferetti, F. P. Rouxinol, R. Landers, S. F. Durrant, J. Scarminio and A. Urbano, *Chemistry of Materials* **2004**, *16*, 513-520.

[24] S. F. Durrant, B. C. Trasferetti, J. Scarmínio, C. U. Davanzo, F. P. M. Rouxinol, R. V. Gelamo and M. A. Bica de Moraes, *Thin Solid Films* **2008**, *516*, 789-793.

[25] F. P. Rouxinol, B. C. Trasferetti, R. Landers and M. A. Bica De Moraes, *Journal of the Brazilian Chemical Society* **2004**, *15*, 324-326.

[26] C. Davisson and L. H. Germer, *Physical Review* **1927**, *30*, 705-740.

[27] K. W. Kolasinski, *Surface science foundations of catalysis and nanoscience*, Wiley, Chichester, **2002**.

[28] L. J. Clarke, *Surface crystallography an introduction to low energy electron diffraction*, Wiley, Chichester, **1985**.

[29] A. W. Adamson and A. P. Gast, *Physical chemistry of surfaces*, Wiley, New York, **1997**.

[30] G. Ertl and J. Küppers, *Low energy electrons and surface chemistry*, VCH, Weinheim, **1985**.

[31] E. A. Wood, *Journal of Applied Physics* **1964**, *35*, 1306-1312.

[32] J. M. Walls and R. Smith, *Surface science techniques*, Pergamon, Oxford, **1994**.

[33] D. W. Davis and D. A. Shirley, *Chemical Physics Letters* **1972**, *15*, 185-190.

[34] L. Ley, S. P. Kowalczyk, F. R. McFeely, R. A. Pollak and D. A. Shirley, *Physical Review B* **1973**, *8*, 2392-2402.

[35] D. A. Shirley, *Chemical Physics Letters* **1972**, *16*, 220-225.

[36] K. Siegbahn, *Reviews of Modern Physics* **1982**, *54*, 709-728.

[37] P. J. Cumpson, S. J. Spencer and M. P. Seah, *Spectroscopy Europe* **1998**, *10*, 8-14.

[38] *DAR 400 x-ray source and power supply, version 2.0*, Omicron NanoTechnology GmbH, Taunusstein, Germany, **2000**.

[39] *EA 125 energy analyzer user's guide, version 2.1*, Omicron NanoTechnology GmbH, Taunusstein, Germany, **2002**.

[40] J. F. Moulder, W. F. Stickle, P. E. Sobol and K. D. Bomben, *Handbook of x-ray photoelectron spectroscopy*, Perkin-Elmer Corp., Eden Prairie, MN, **1992**.

[41] J. H. Scofield, *Journal of Electron Spectroscopy and Related Phenomena* **1976**, *8*, 129-137.

[42] J. C. Vickerman, *Surface analysis : the principal techniques*, Wiley, Chichester, **1997**.

[43] A. F. Carley and M. W. Roberts, *Proc R Soc London Ser A* **1978**, *363*, 403-424.

[44] A. F. Carley, P. R. Davies, K. R. Harikumar, R. V. Jones and M. W. Roberts, *Topics in Catalysis* **2003**, *24*, 51-59.

[45] R. F. Reilman, A. Msezane and S. T. Manson, *Journal of Electron Spectroscopy and Related Phenomena* **1976**, *8*, 389-394.

[46] S. Tanuma, C. J. Powell and D. R. Penn, *Surface and Interface Analysis* **1994**, *21*, 165-176.

[47] S. Tougaard in *QUASES-IMFP-TPP2M™ Software Package, version 2.1, Vol.* University of Southern Denmark, Odense, Denmark, **2000**.

[48] D. Briggs and M. P. Seah, *Practical surface analysis by Auger and x-ray photoelectron spectroscopy*, Wiley, Chichester, **1983**.

[49] G. Binnig, H. Rohrer, C. Gerber and E. Weibel, *Physical Review Letters* **1982**, *49*, 57-61.

[50] D. P. Woodruff and T. A. Delchar, *Modern techniques of surface science*, Cambridge University Press, Cambridge, **1994**.

[51] M. Schmid. 2009. *The scanning tunnelling microscopy* [online]. Institut für Allgemeine Physik, Technische Universität Wien. Available at: http://www.iap.tuwien.ac.at/www/surface/stm_gallery/stm_schmatic. [Accessed: 2 June 2009].

[52] *VT SPM user's guide, version 1.7*, Omicron NanoTechnology GmbH, Taunusstein, Germany, **2002**.

[53] D. A. Bonnell, *Scanning tunneling microscopy and spectroscopy theory, techniques, and applications*, VCH, New York, N.Y, **1993**.

[54] R. J. Hamers, R. M. Tromp and J. E. Demuth, *Physical Review Letters* **1986**, *56*, 1972-1975.

[55] H. H. Brongersma, M. Draxler, M. de Ridder and P. Bauer, *Surface Science Reports* **2007**, *62*, 63-109.

[56] H. Niehus, W. Heiland and E. Taglauer, *Surface Science Reports* **1993**, *17*, 213-303.

[57] E. Taglauer and W. Heiland, *Applied Physics A: Materials Science & Processing* **1976**, *9*, 261-275.

[58] S. A. Cruz, E. V. Alonso, R. P. Walker, D. J. Martin and D. G. Armour, *Nuclear Instruments and Methods in Physics Research* **1982**, *194*, 659-661.

[59] J. Lindhard, M. Scharff and H. E. Schioett, *Kgl. Danske Videnskab. Selskab, Mat.-Fys. Medd.* **1963**, *33*, 42 pp.

[60] E. Rutherford, *Philosophical Magazine (1798-1977)* **1911**, *21*, 669-689.

[61] E. Taglauer, *Applied Physics A Solids and Surfaces* **1985**, *38*, 161-170.

3 Surface Structure and Reactivity of Iron Oxide

Chapter III

Surface Structure and Reactivity of Iron Oxide

In this chapter we describe the iron oxide single crystal surface used in these studies. Using X-ray photoelectron spectroscopy, He^+-ion scattering spectroscopy, low energy electron diffraction, and scanning tunnelling microscopy, we investigated the surface morphology and its reactivity with methanol. Low temperature annealing does not completely restore the damage created by sputtering, whereas high temperature annealing results in the formation of an epitaxial $Fe_3O_4(111)$ layer terminating the iron oxide single crystal surface.

3.1. Introduction

Metal oxides constitute a considerable class of materials that are relevant to technological applications like environmental science, electrochemistry, chemical sensors, and electronics. One of their most significant applications is heterogeneous catalysis. Metal oxides are widely used as catalytic materials for a number of important chemical processes [1], for instance iron oxide is used as a catalyst for dehydrogenation of ethylbenzene to styrene [2, 3]. However, not much is known about the surface chemical and catalytic properties of metal oxides, and an understanding of the basic metal oxide surface chemistry is far from complete, compared with studies on semiconductors and metals. This fundamental understanding, particularly of the surface chemical and catalytic properties, is essential for the catalytic material development.

Consequently, studies of the surface science of metal oxides have gained increasing attention in recent years. One of the most studied metal oxide surfaces is iron

oxide surfaces. Iron oxides and iron-based materials are of importance in a variety of technical areas including corrosion, photoelectrolysis [4, 5], and magnetic films [6]. Furthermore, iron oxides are widely used as heterogeneous catalysts for various synthetic reactions involving selective oxidations, dehydrogenations, oxidative dehydrogenations (oxodehydrogenations), and the water-gas shift reaction [7]. α-Fe_2O_3, known under the mineralogical name of hematite, is the bulk phase thermodynamically stable at room temperature.

In this work, we focus on the iron oxide single crystal surface by studying the adsorption of methanol with X-ray photoelectron spectroscopy (XPS), low energy electron diffraction (LEED), and scanning tunnelling microscopy (STM).

3.1.1. Aims

- To identify the bulk phase of the iron oxide single crystal.
- To elucidate the surface phase of iron oxide formed in oxygen partial pressure below 10^{-6} mbar.
- To explore the iron oxide surface structure and its chemical composition.

3.2. Crystallographic structure of iron oxides

Iron and oxygen form a variety of oxides with different crystal structures and stoichiometries. These phases are: wüstite (FeO), magnetite (Fe_3O_4), hematite (α-Fe_2O_3), maghemite (γ-Fe_2O_3), and ε-Fe_2O_3 [8, 9]. The latter two phases have only been synthesised artificially, but all other phases occur also naturally [8-10]. Under thermodynamic equilibrium, the bulk structure and stoichiometry of iron oxides depend on the pressure of ambient oxygen gas, P_{O2} and on the temperature, T as described by a P_{O2}–T phase diagram. Figure 3.1 is the phase diagram for the Fe–O system [11].

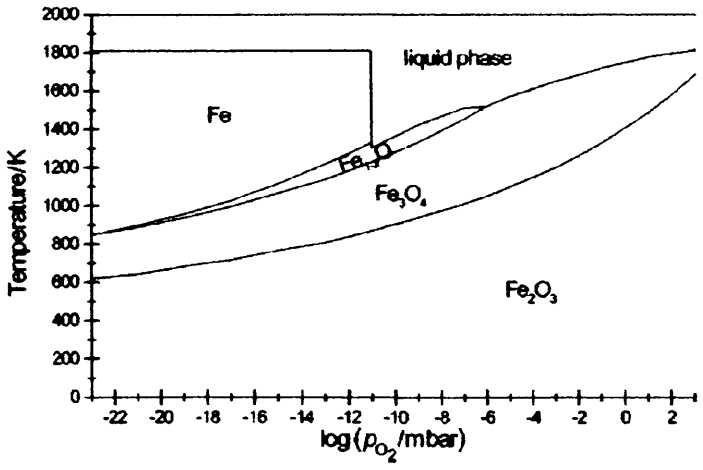

Figure 3.1. Calculated temperature–pressure phase diagram of the Fe-O system [10].

Figure 3.2 presents the perspective side and top views of the four iron oxide crystal structures discussed below. The geometries of their surfaces result from the ideal truncations of the bulk structure. The side views show the bulk structures that consist of O(111) and (0001) layers separated by Fe layers in different coordination sites, while the top views show the unreconstructed (111) and (0001) terminations that expose Fe atoms over a close-packed O layer. The surface unit cell constants are indicated.

FeO wüstite crystallises in the rock salt (NaCl) crystal structure which is composed of a closed-packed face-centred cubic oxygen sublattice with the smaller Fe^{2+} cations located in the octahedral interstices, surrounded by oxygen anions [12]. All the Fe^{2+} cations are situated in octahedral sites of the O^{2-} anion lattice. The phase diagram in Figure 3.1 shows that this phase is stable only for temperatures above 843 K, thus it must be prepared at temperature above 843 K and subsequently cooled down to room temperature. The interatomic distance within these O and Fe(111) planes is 3.04 Å, which corresponds to the lattice constant of the two-dimensional hexagonal unit cell of an unreconstructed FeO(111) surface, as indicated in the top view of Figure 3.2. The Fe and O(111) planes form the cubic ABC stacking sequence with an interlayer distance of 1.25 Å along the [111] axis of FeO. The Fe–O bond length is 2.16 Å.

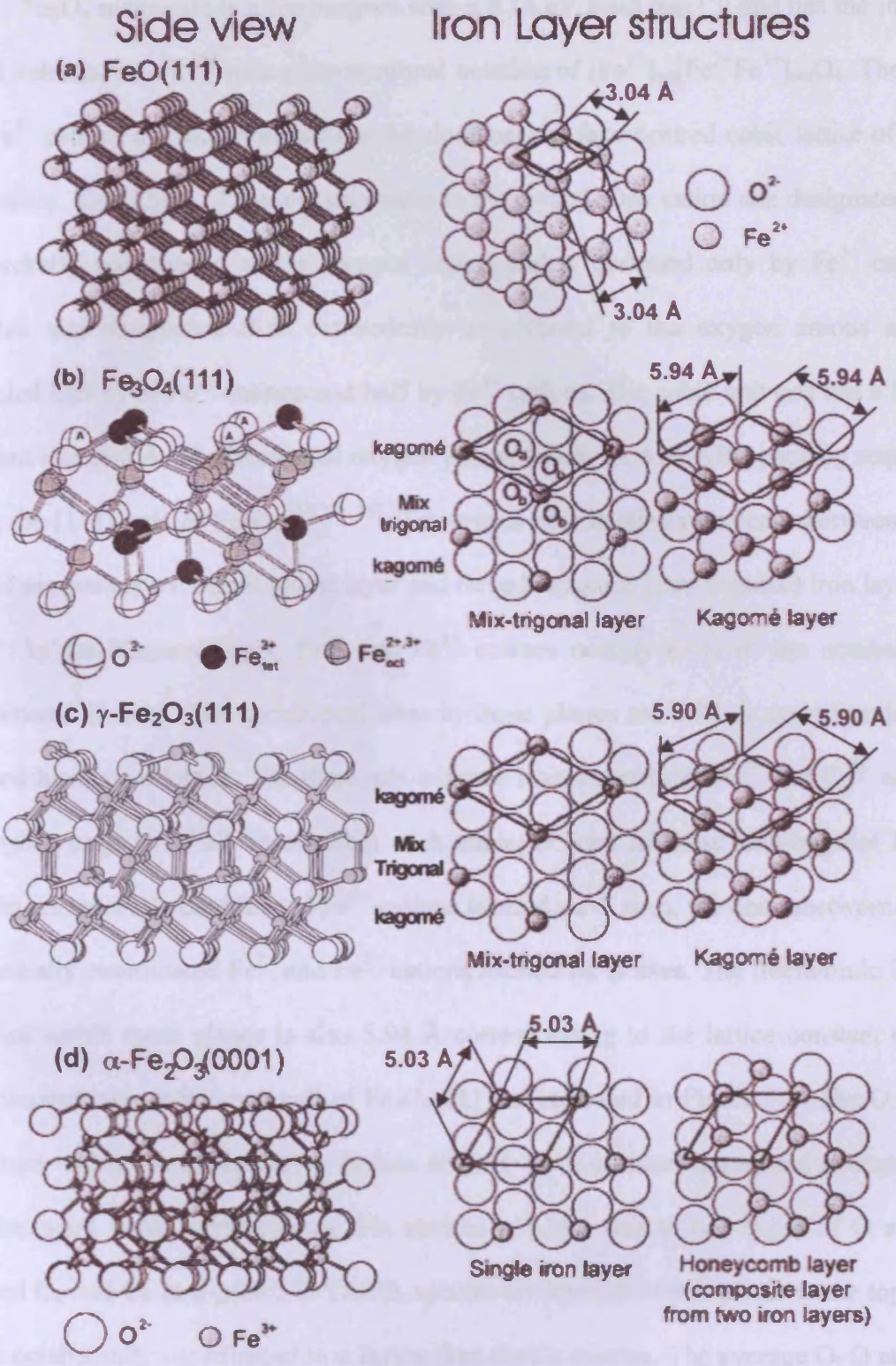

Figure 3.2. Perspective side views of Fe–O crystal structures and top views cut parallel to close-packed O layers. Bulk truncated (111) and (0001) surface structures terminated by outermost Fe planes are shown. Surface unit cells are indicated. Top views are drawn with full cation and anion sizes [10, 11, 13].

Fe_3O_4 magnetite is a ferrimagnet with a 0.14 eV band gap [14] and has the inverse spinel cubic structure [8] with a conventional notation of $[Fe^{3+}]_{tet}[Fe^{2+}Fe^{3+}]_{oct}O_4$. The Fe^{2+} and Fe^{3+} cations are incorporated into the close-packed face-centred cubic lattice of large O^{2-} anions. Two kinds of cations sites exist in the crystal: One cation site designated *A* is tetrahedrally coordinated to the oxygen anions and is occupied only by Fe^{3+} cations. Another site designated *B* is octahedrally coordinated to the oxygen anions and is occupied half by of Fe^{2+} cations and half by Fe^{3+} cations. The cubic unit cell has a lattice constant of 8.396 Å. The hexagonal oxygen planes follow an ABCABC packing sequence along the [111] axis of Fe_3O_4 [10, 15, 16]. Two types of iron sublayers occur between each pair of oxygen layers: one Kagomé layer and three hexagonal (mix-trigonal) iron layers.

In the Kagomé layer, Fe^{2+} and Fe^{3+} cations occupy in ¾ of the octahedrally coordinated B sites. The unoccupied sites in these planes are 5.94 Å apart forming an ordered hexagonal lattice. The three mix-trigonal layers constitute Fe^{2+} and Fe^{3+} cations occupying only ¼ of all sites within each sublayer: two of these mix-trigonal layers contain tetrahedrally coordinated Fe^{3+} cations located on A sites, the one inbetween them octahedrally coordinated Fe^{2+} and Fe^{3+} cations located on B sites. The interatomic Fe–Fe distance within these planes is also 5.94 Å corresponding to the lattice constant of the two-dimensional surface unit cell of $Fe_3O_4(111)$ as indicated in Figure 3.2. The O anion positions within the (111) planes deviate slightly from an ideal hexagonal arrangement and the point group symmetry of this surface is p3m1 due to two types of O anions denoted O_a and O_b in Figure 3.2. The O_a species are located 0.04 Å closer to the topmost single octahedrally coordinated iron layers than the O_b species. The average O–O nearest neighbour distance within the (111) planes is 2.97 Å. Consider the O_a and O_b sublayers, the separation of neighbouring O(111) planes by the Kagomé layer and the mix-trigonal layers are 2.37 and 2.48 Å, respectively. Thus two oxygen layers are separated by 4.85 Å

corresponding to the distance between equivalent (111) surface terminations of Fe_3O_4. The distance among the iron sublayers of the three mix-trigonal layers is 0.6 Å. The Fe–O bond lengths for tetrahedrally and octahedrally coordinated Fe are 1.88 and 2.07 Å, respectively. The (111) surface plane is stable and is natural growth faces of Fe_3O_4.

γ-Fe_2O_3 maghemite crystallises in the deficient spinel structure in which the Fe^{3+} cations occupy both octahedral and tetrahedral sites and has its band gap of 2.03 eV [14]. It is a metastable phase with respect to hematite and has a cubic spinel crystal structure closely related to that of Fe_3O_4 magnetite structure [10]. The main structural difference between maghemite and magnetite is that maghemite has vacancies in an ordered array in the octahedrally-coordinated iron sublattice, leading to a spinel superstructure.

α-Fe_2O_3 haematite is the stable phase at room temperature in thermodynamic equilibrium with ambient oxygen atmospheres as shown in the phase diagram for the Fe-O system in Figure 3.1. It crystallizes in the rhombohedral corundum crystal structure [12] with the hexagonal unit cell containing six formula units and has its band gap of 2.2 eV [17-19]. The lattice parameters are a = 5.035 Å and c = 13.72 Å [12]. The oxygen anions form a hexagonal close-packed sublattice with ABAB-type stacking. The octahedrally coordinated Fe^{3+} species in the interstitials are arranged in distorted octahedral [12] and form two sublayers. The interatomic Fe–Fe distance within these planes is 5.03 Å corresponding to the lattice constant of the two-dimensional unit cell on the unreconstructed (0001) surface, indicated in Figure 3.2. There is a slight deviation of oxygen anion positions within the fully occupied (0001) planes from an ideal hexagonal arrangement. The O–O distances along the shared face of an octahedron are shorter (2.669 Å) than the distance along the unshared edge (3.035 Å) [8]. The average O–O interatomic distance is 2.91 Å. Due to the distortion of octahedra, there are two different Fe–O bond lengths, 1.96 and 2.09 Å, and the Fe^{3+} cations form distorted octahedrons with

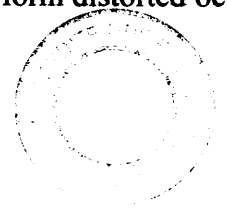

their oxygen neighbours resulting in the formation of two sublayers [10]. The two iron sublayers in-between the oxygen planes are separated by 0.6 Å and the two oxygen layers are separated by 2.29 Å corresponding to the distance between equivalent (0001) surface terminations of α-Fe_2O_3 [10, 20].

The α-Fe_2O_3(0001) surface could produce different surface reconstructions depending on the surface preparation conditions [15, 21]. The different surface structures are dependent on the annealing temperature and the oxygen partial pressure. Under strongly oxidising conditions, an α-Fe_2O_3(0001) surface is formed, whereas under reducing conditions, an FeO(111) surface is created. Fe_3O_4(111) and biphase structures lie in between the two limits. The quasi-hexagonal surfaces of these four iron oxides in Figure 3.2 form four different unit cells, provided no reconstructions occur. They have lattice parameters of 3.04, 5.94, 5.90, and 5.03 Å for wüstite, magnetite, maghemite, and hematite, respectively. Because of the different positions of the iron cations between the oxygen layers, a bulk (111) surface termination would produce different LEED patterns in the four cases. Therefore, provided surface reconstruction can be ruled out, the LEED patterns of these surfaces can be used to discriminate the different Fe–O phases.

3.3. Experimental

The experiments described in this chapter were performed in the Multi-technique UHV system (or Mulitprobe) described in detail in Chapter 2. The base pressure of each chamber in the system was different. The based pressure of preparation chamber, STM chamber, and analysis chamber is approximately 1×10^{-9}, 1×10^{-10}, and 1×10^{-9} mbar, respectively. An Al Kα anode X-ray source (excitation energy of 1486.6 eV) was used for XPS. The energy scale was calibrated to the binding energy E_b of Au $4f_{7/2}$ at 83.8 eV.

The iron oxide single crystal was obtained from Pi-Kem Ltd and was sold as α-Fe_2O_3(0001). However, it will be shown in this chapter that this appears to be incorrect.

The iron oxide single crystal sample was prepared in vacuum by cycles of sputtering, annealing and oxidising. More details on the procedure to clean the iron oxide single crystal surface are provided in Chapter 2. Surface cleanliness was judged based on the absence of carbon and significant amounts of potassium and calcium in the X-ray photoelectron spectroscopy. The structure of iron oxide single crystal surfaces was determined by LEED, XPS, low-energy He^+-ion scattering (LEIS or ISS), and STM. For LEED measurements, a four-grid optics was used with the sample grounded. The low-energy ion scattering experiments were performed with $^4He^+$ ions having 1 keV kinetic energy. STM measurements were carried out with an Omicron STM. For these studies, all measurements were performed with the sample at room temperature in constant current mode. STM tips were made by electrochemically etching a tungsten wire (purity 99.95%, 0.3mm in diameter). The Omicron tip etching kit was employed to provide sharp tungsten tips.

3.4. Results and discussion

3.4.1. Identification of iron oxide sample

The phase of the iron oxide crystal was examined by X-ray diffraction (XRD). Figure 3.9(b) shows the XRD patterns of the iron oxide single crystal. The XRD peaks of iron oxide sample have shifted slightly, which cannot be easily matching. This shift may result from the sample displacement during the run. Most of the diffraction peaks (at $2\theta \approx 18°$, 37°, and 57°) in the XRD spectrum for the iron oxide substrate are in agreement with the Fe_3O_4 phase (JCPDS card 19-0629 is shown in Figure 3.9(a), red line). The XRD patterns of the γ-Fe_2O_3 phase (JCPDS card 39-1346, yellow line) and the α-Fe_2O_3 phase (JCPDS card 33-0664, blue line) are also shown in Figure 3.9(c) and 3.9(d), respectively. The XRD peak intensities of the iron oxide substrate were higher than those of Fe_3O_4 due

to different crystallites of the iron oxide. In Figure 3.9(b), the XRD peak resolved at about 39.3° cannot be correctly indexed to either Fe_3O_4 or Fe_2O_3 phases. The XRD result shows that the iron oxide single crystal appears to be a mixture of predominately Fe_3O_4 with small amount of Fe_2O_3.

Moreover, the magnetic properties of the iron oxide single crystal were tested. This was found that this crystal was attracted to a magnet. This implies that this crystal was not hematite which does not exhibit the magnetic properties. This result further confirmed the XRD analysis, indicating that the iron oxide single crystal obtained from Pi-Kem Ltd was not α-Fe_2O_3.

By combining XRD data with the magnetic properties, the compositions and phases of the iron oxide single crystal can be obtained. From the analysis of above XRD result, it was found that the iron oxide single crystal obtained from Pi-Kem Ltd was a mixture of predominately magnetite (Fe_3O_4) with trace amounts of Fe_2O_3.

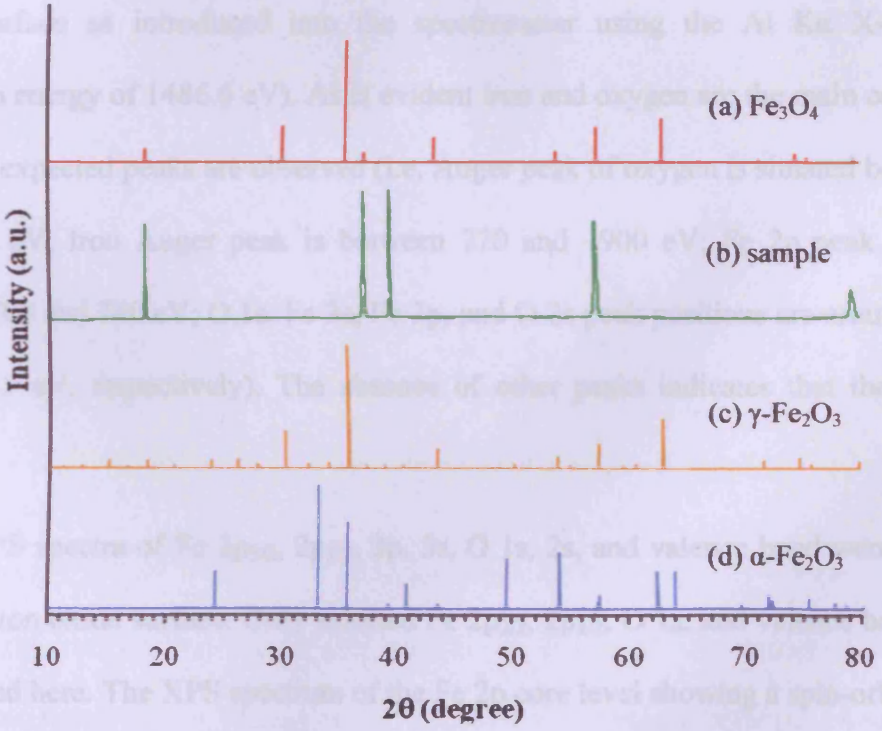

Figure 3.9. X-ray diffraction (XRD pattern) of: (a) bulk Fe_3O_4, (b) iron oxide substrate, (c) bulk γ-Fe_2O_3, and (d) bulk α-Fe_2O_3.

3.4.2. The structure and composition of iron oxide surface in UHV

The observed surface structure of the iron oxide single crystal depends strongly on the preparation condition [15, 21]. Annealing time and temperature, and the oxygen partial pressure play a role, in addition to the previous sample history. When the sample is sputtered, the surface is severely damaged and rough and crystallographic order is destroyed. This treatment makes the sample oxygen deficient and no LEED patterns were observable (i.e. LEED only shows a uniform background) indicating the absence of crystallographic order at the surface of iron oxide single crystal. Re-oxidation for 30 minutes at the temperature of 873 K in 1×10^{-7} mbar of oxygen restores an ordered (2×2) surface structure.

3.4.2.1. Photoemission measurements

Figure 3.3 presents an XPS broad survey scan taken from the iron oxide single crystal surface as introduced into the spectrometer using the Al Kα X-ray source (excitation energy of 1486.6 eV). As is evident iron and oxygen are the main constituents. All of the expected peaks are observed (i.e. Auger peak of oxygen is situated between 950 and 1030 eV; Iron Auger peak is between 770 and ~900 eV; Fe 2p peak position is between 700 and 740 eV; O 1s, Fe 3s, Fe 3p, and O 2s peak positions are around 530, 91, 55. and 25 eV, respectively). The absence of other peaks indicates that the sample is clean.

XPS spectra of Fe $2p_{3/2}$, $2p_{1/2}$, 3p, 3s, O 1s, 2s, and valence band were measured from the iron oxide surface. Only selected Fe $2p_{3/2}$, $2p_{1/2}$, O 1s, and valence band spectra are reported here. The XPS spectrum of the Fe 2p core level showing a spin-orbit splitting into $2p_{1/2}$ and $2p_{3/2}$ components after annealing in 10^{-7} mbar of oxygen is presented in Figure 3.4. The binding energies of the Fe 2p core levels for different oxidation states

have been systematically studies on powder samples, single crystals, and polycrystalline films of several iron oxide phases [2, 22, 23]. The reported values of the binding energies for the Fe^{2+} and Fe^{3+} valence states are indicated by the vertical lines in Figure 3.4. The positions of the satellite peaks that are attributed to the Fe^{2+} and Fe^{3+} oxidation states are also given. The annealed-surface core-level spectrum is broad (the FWHM value for Fe $2p_{3/2}$ is 4.7 eV) and is believed to be due to the presence of Fe^{2+} and Fe^{3+} valence states within the XPS analysis volume.

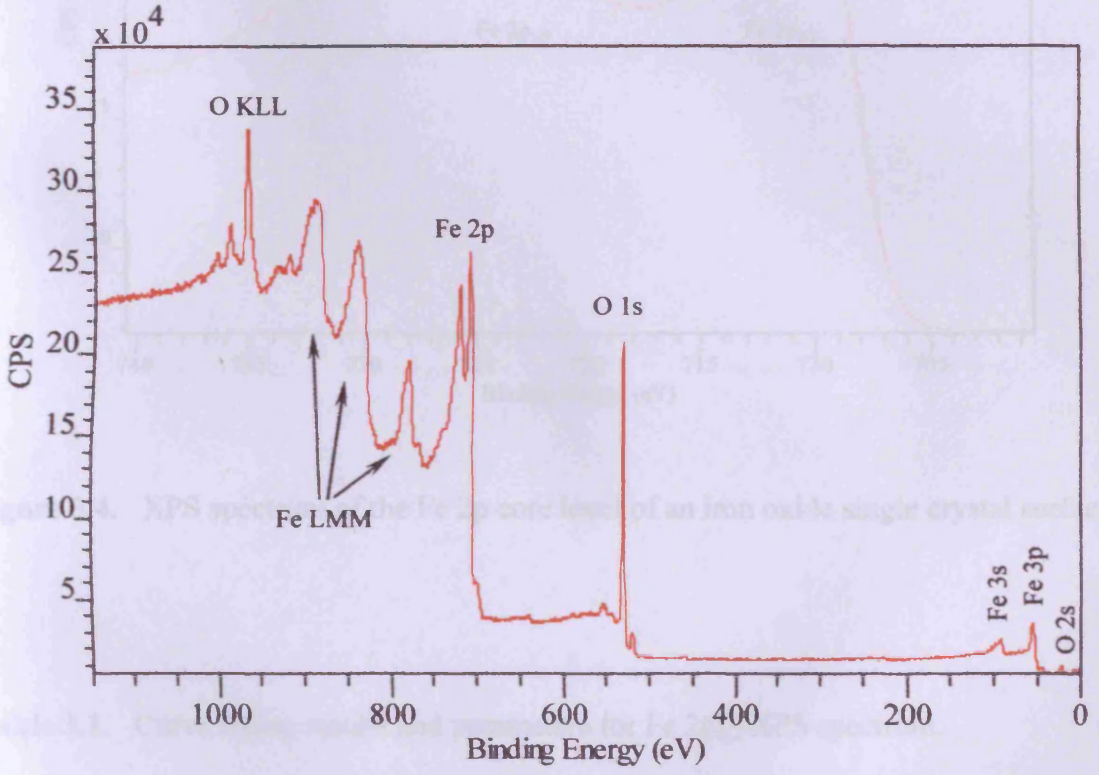

Figure 3.3. XPS survey spectrum of the clean iron oxide single crystal surface.

Curve fitting of Fe 2p spectra are known to be very difficult because of a sharply rising background and broadened line widths. In this work, the fitting of the Fe $2p_{3/2}$ structure has been used to determine the contributions from the different chemical states present by Barbieri et al. [22] and Kurtz and Henrich [24]. Therefore, after the Shirley-type (non-linear) background subtraction [25], the structure in the Fe $2p_{3/2}$ spectrum was fitted

by constructing the parameter-controlled Gaussian/Lorentzian peaks (using 30% Lorentzian character) for different chemical states of the element.

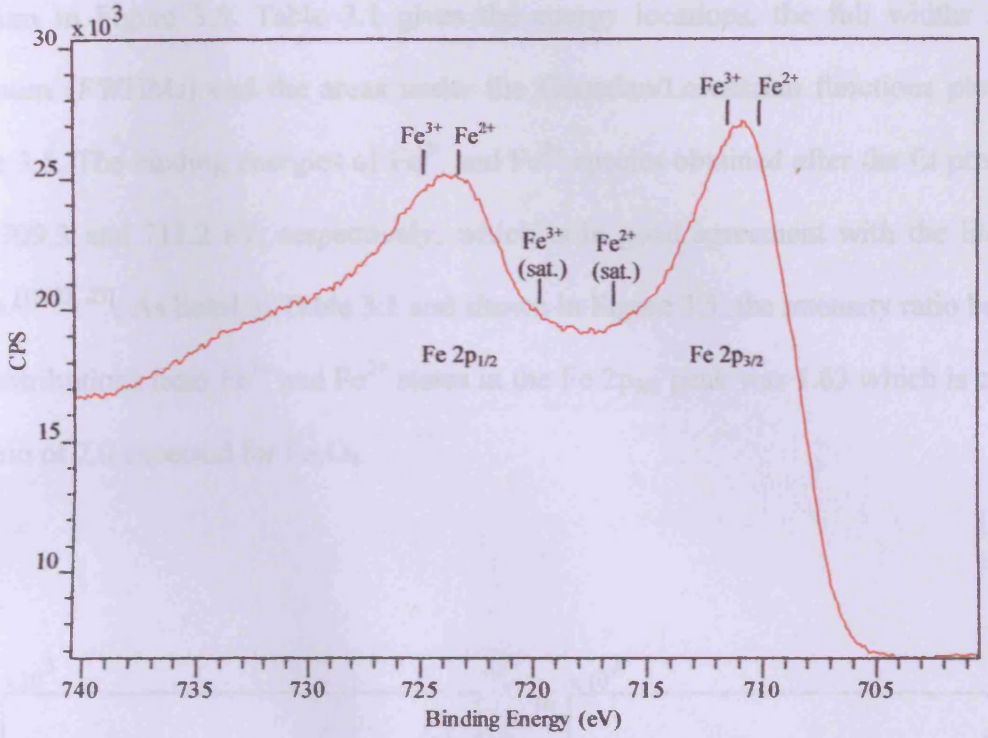

Figure 3.4. XPS spectrum of the Fe 2p core level of an iron oxide single crystal surface.

Table 3.1. Curve fitting results and parameters for Fe $2p_{3/2}$ XPS spectrum.

	Fe $2p_{3/2}$	
	Fe^{2+}	Fe^{3+}
Binding energy (eV)	709.3	711.2
FWHM (eV)	3.3	4.3
Area (% of total area fit)	38	62

Figure 3.5 displays the curve fitting of XPS Fe $2p_{3/2}$ spectra of iron oxide single crystal surface. As previously reported by Kurtz and Henrich [24], the full widths at half maximum (FWHMs) of the peaks were varied to obtain the best fit with the experimental spectrum in Figure 3.5. Table 3.1 gives the energy locations, the full widths at half maximum (FWHMs) and the areas under the Gaussian/Lorentzian functions plotted in Figure 3.5. The binding energies of Fe^{2+} and Fe^{3+} species obtained after the fit procedure were 709.3 and 711.2 eV, respectively, which is in good agreement with the literature values [15, 22, 23]. As listed in Table 3.1 and shown in Figure 3.5, the intensity ratio between the contributions from Fe^{3+} and Fe^{2+} states in the Fe $2p_{3/2}$ peak was 1.63 which is close to the ratio of 2.0 expected for Fe_3O_4.

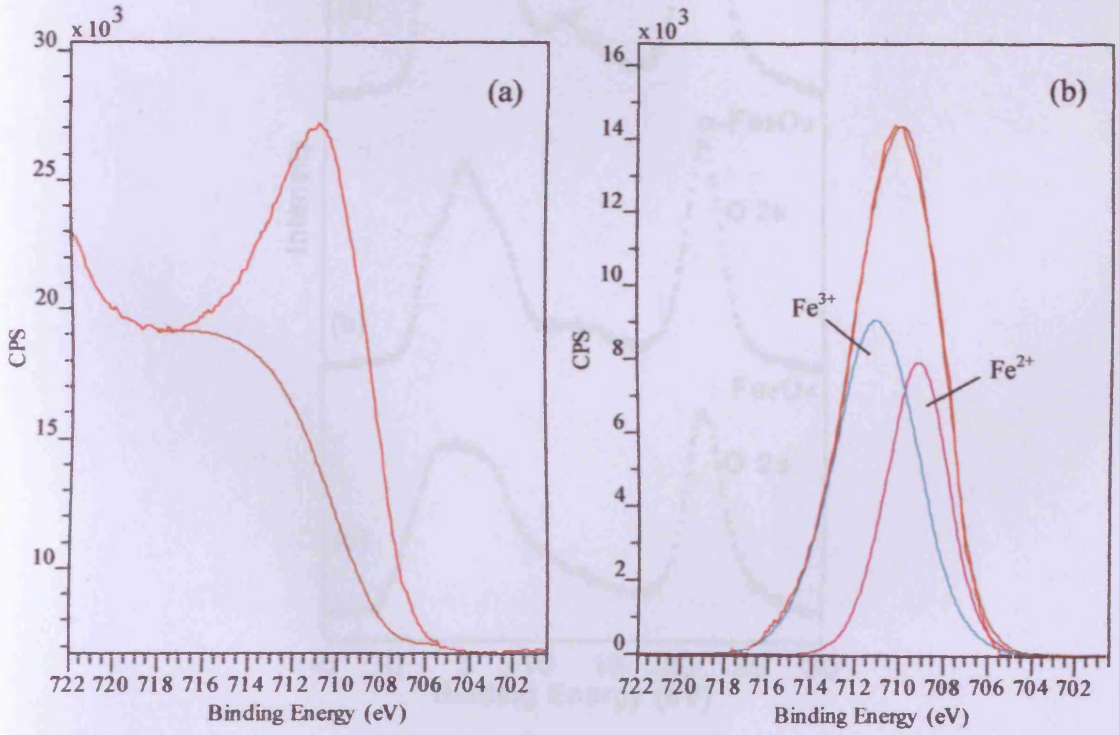

Figure 3.5. Decomposition of the Fe $2p_{3/2}$ core level of the iron oxide single crystal: (a) before and (b) after Shirley-type background subtraction.

Although curve fitting used in this work is a simple method for fitting the Fe $2p_{3/2}$ spectra, it allows easily fitting of the Fe $2p_{3/2}$ spectra of iron oxide single crystal. Recently, the multiplet fit for the Fe 2p XPS spectra of iron oxide is considered. Grosvenor et al. [26] previously reported that the Fe $2p_{3/2}$ spectra of various iron compounds can be well fitted using Gupta and Sen (GS) multiplets [27]. This procedure can be used to fit complex Fe $2p_{3/2}$ spectra for magnetite where both Fe^{2+} and Fe^{3+} species are present. The detail of this fitting procedure is not mentioned in this work. However, the phases of iron oxide single crystal can be identified by valence band XPS observation.

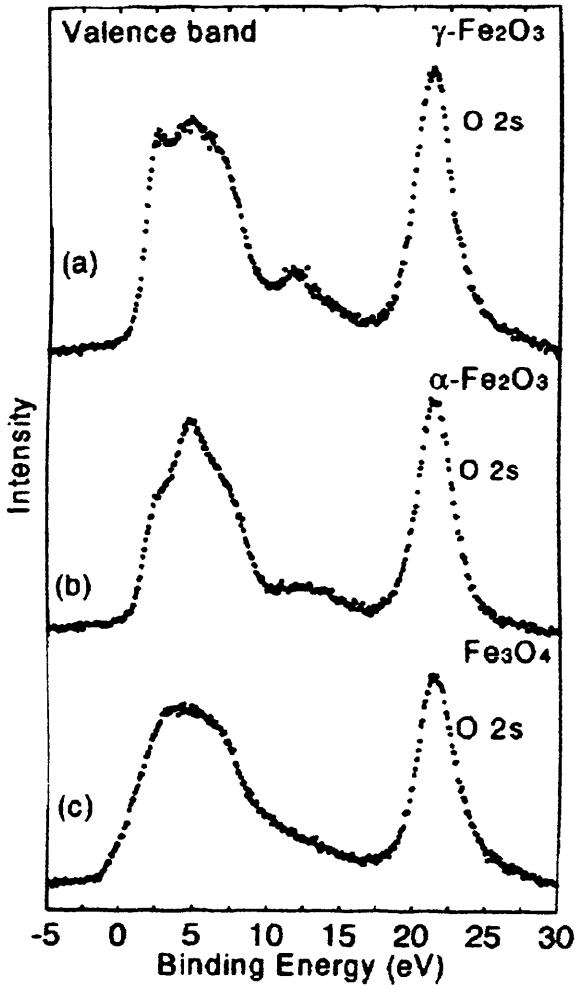

Figure 3.6. XPS spectra of the valence-band region of different iron oxide films. (a) A γ-Fe_2O_3(100) film grown on MgO(100). (b) An α-Fe_2O_3(0001) film grown on α-Al_2O_3(0001). (c) An Fe_3O_4(100) film grown on MgO(100) [28].

The characteristic three-peak structure of the main valence band can be used as a fingerprint to identify iron oxides themselves. Figure 3.6 shows the XPS spectra of the valence-band region of α-Fe_2O_3, γ-Fe_2O_3, and Fe_3O_4 films [28]. The valence-band features for α-Fe_2O_3 [28-32], γ-Fe_2O_3 [28, 31, 32], and Fe_3O_4 [28, 30-32] have been previously studied by various workers and show remarkably different between the different oxidised iron species. All of spectra may divided into the main band (0-10 eV), the satellite band (10-17 eV), and the O 2s level (21.5 eV). In the valence spectra of both γ- and α-Fe_2O_3 (see Figure 3.7(a) and 3.7(b)), a three-peak structure with maxima at approximately 2.7, 4.9, and 7.2 eV in the main band is observed. The intensity of the first peak in the main band at about 2.7 eV is clearly different in the spectra for γ- and α-Fe_2O_3. The XPS spectrum of the valence band region of the Fe_3O_4 (see Figure 3.7(c)) is too complicated to resolve.

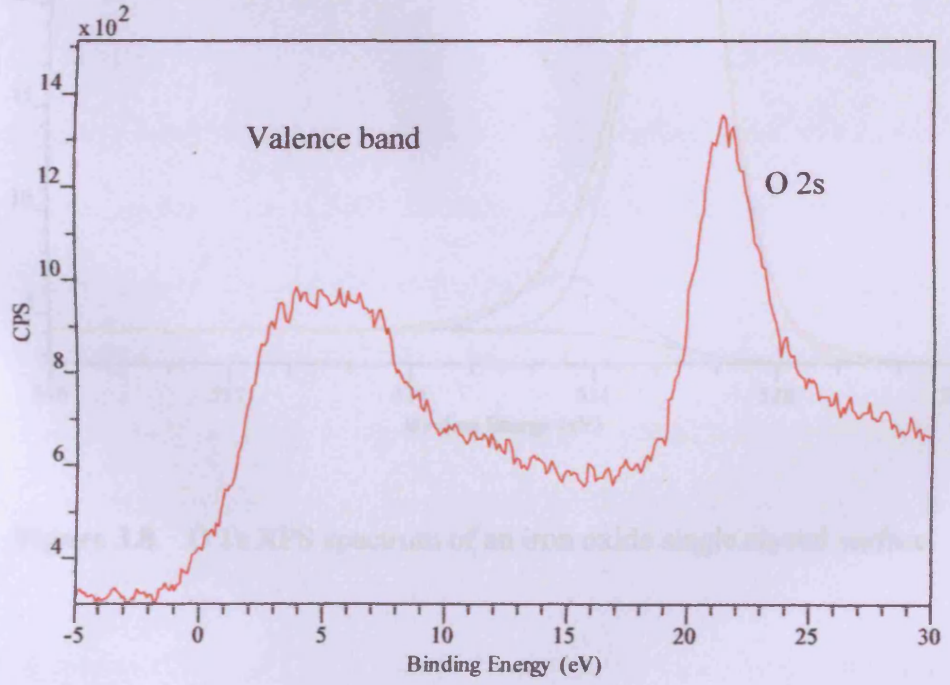

Figure 3.7. Observed valence-band XPS spectra of the iron oxide surface.

Figure 3.7 shows the observed XPS valence-band spectrum of iron oxide single crystal after sputtering with argon ion at room temperature following annealing in oxygen pressure of 10^{-7} mbar at 873 K. The spectral features in the main valence-band spectrum observed in the iron oxide single crystal sample are similar to the valence-band structures of Fe_3O_4 shown in Figure 3.7(c), as previously reported by Fujii et al. [28]. Therefore, both the XPS core-level and valence band emission of the iron oxide single crystal imply that the present termination is $Fe_3O_4(111)$ rather than the other phase.

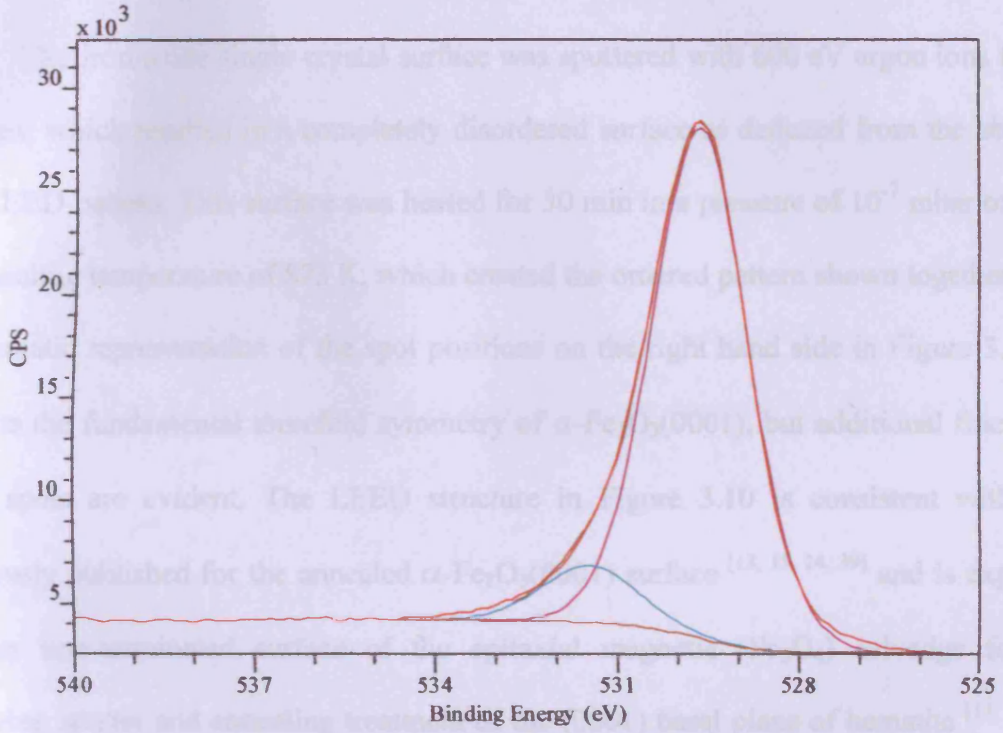

Figure 3.8. O 1s XPS spectrum of an iron oxide single crystal surface.

The O 1s XPS spectra were collected in a direction normal to the iron oxide single crystal face. In such experimental conditions, the O 1s spectrum for iron oxide single crystal was shown in Figure 3.8. The O 1s XPS peak was fitted using Gaussian-Lorentzian fitting function (using 70% Lorentzian character), after a Shirley-type

background subtraction. The O 1s spectrum in Figure 3.8 reveals the presence of two contributions with peaks centred at 529.6 and 531.4 eV which suggests the existence of two chemically equivalent oxygen atoms on the iron oxide surface. The contribution centred at 529.6 eV corresponds to the oxide (O^{2-}) in iron oxide. Another peak located at 531.4 eV is due to the presence of hydroxyl groups (OH^-). The binding energies of O 1s obtained after the fit procedure are in fair agreement with previously reported literature data [33-38].

3.4.2.2. LEED observations

The iron oxide single crystal surface was sputtered with 600 eV argon ions for 30 minutes, which resulted in a completely disordered surface as deduced from the absence of a LEED pattern. This surface was heated for 30 min in a pressure of 10^{-7} mbar oxygen at annealing temperature of 873 K, which created the ordered pattern shown together with a schematic representation of the spot positions on the right hand side in Figure 3.10. It exhibits the fundamental threefold symmetry of α-Fe_2O_3(0001), but additional fractional order spots are evident. The LEED structure in Figure 3.10 is consistent with that previously published for the annealed α-Fe_2O_3(0001) surface [13, 15, 24, 39] and is expected for the iron-terminated surface of the epitaxial magnetic (Fe_3O_4) selvedge formed following sputter and annealing treatment of the (0001) basal plane of hematite [13, 16, 22]. Moreover, the orientation and symmetry of this LEED pattern is similar to previously reported for Fe_3O_4(111) substrate [40].

The interpretation of LEED pattern from the iron oxide single crystal surface is displayed below and is indicated as being due to p(2×2) surface reconstruction, which is characterised by the indicated reciprocal unit cell corresponding to a surface unit cell with a lattice constant of 5.94 Å and an overlayer with reference to the hexagonal close-packed

oxygen sublattice of the (111) plane of bulk Fe_3O_4. This corresponds to the lattice parameter of Fe_3O_4(111). Combining the results of the LEED, XPS, and XRD measurements, it can be drawn a conclusion that the iron oxide substrate used in this experiment was an Fe_3O_4 single crystal.

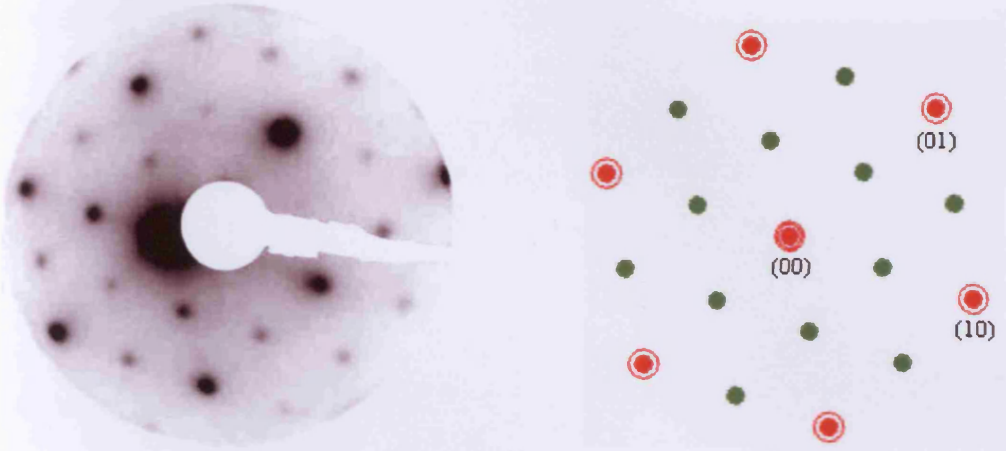

Figure 3.10. *LEED pattern and its schematic representation for the clean iron oxide single crystal surface at 70 eV after annealing in oxygen pressure of 10^{-7} mbar for 30 min at 873 K.*

Interpretation of LEED pattern

From the LEED pattern of the iron oxide single crystal surface shown in Figure 3.10, the unit cell of the iron oxide structure can be obtained. Writing the reciprocal space unit cell vectors of the overlayer, $\bar{b}_1^*$ and $\bar{b}_1^*$, in terms of the substrate, $\bar{a}_1^*$ and $\bar{a}_2^*$

$$\bar{b}_1^* = \frac{1}{2}\bar{a}_1^* + 0\bar{a}_2^* \tag{3.1}$$

$$\bar{b}_2^* = 0\bar{a}_1^* + \frac{1}{2}\bar{a}_2^* \tag{3.2}$$

Therefore,

$$M^* = \begin{bmatrix} 1/2 & 0 \\ 0 & 1/2 \end{bmatrix} \tag{3.3}$$

The matrix of the real space structure is given by:

$$M = \frac{1}{\det M^*} \begin{bmatrix} 1/2 & 0 \\ 0 & 1/2 \end{bmatrix} \tag{3.4}$$

where $\det M^* = \frac{1}{2} \cdot \frac{1}{2} - (0 \cdot 0) = \frac{1}{4}$

Therefore,

$$M = \begin{bmatrix} 2 & 0 \\ 0 & 2 \end{bmatrix} \tag{3.5}$$

where $\vec{b}_1 = 2\vec{a}_1 + 0\vec{a}_2$ and $\vec{b}_2 = 0\vec{a}_1 + 2\vec{b}_2$.

Calculating $\vec{a}_1$ and $\vec{a}_2$

$$|\vec{a}_1| = |\vec{a}_2| = c \tag{3.6}$$

where c is the average O–O interaction distance of iron oxide.

As c = 2.97 Å for $Fe_3O_4(111)$

$$|\vec{a}_1| = |\vec{a}_2| = 2.97 \text{ Å} \tag{3.7}$$

Hence, $|\vec{b}_1| = |\vec{b}_2| = 2 \times 2.97 = 5.94$ Å.

It has been well established that sputtering and annealing the α-$Fe_2O_3(0001)$ surface reduces the near-surface region [41]. FeO (wüstite) crystallises in the rock salt (NaCl) structure, Fe_3O_4 (magnetite) in the inverse-spinel structure and α-Fe_2O_3 (hematite) in the rhombohedral corundum structures. The similarities in structure among α-$Fe_2O_3(0001)$, $Fe_3O_4(111)$, and $FeO(111)$ facilitates the epitaxial growth of the $Fe_3O_4(111)$ selvedge upon α-$Fe_2O_3(0001)$ [11, 42]. The relationships of these planes parallel to the close-packed oxygen sublattices of α-Fe_2O_3, Fe_3O_4, and FeO is illustrated in Figure 3.11.

The average oxygen-oxygen interatomic distances are 3.04 Å for FeO, 2.97 Å for Fe_3O_4, and 2.91 Å for α-Fe_2O_3. The reduced selvedge has been found to give the same STM images as the surface of bulk $Fe_3O_4(111)$ [39]. The structure of the $Fe_3O_4(111)$ surfaces has been extensively studied by LEED crystallography and proposed to be terminated ¼ monolayer of iron cations located over a relaxed hexagonal close-packed oxygen layer underneath [16].

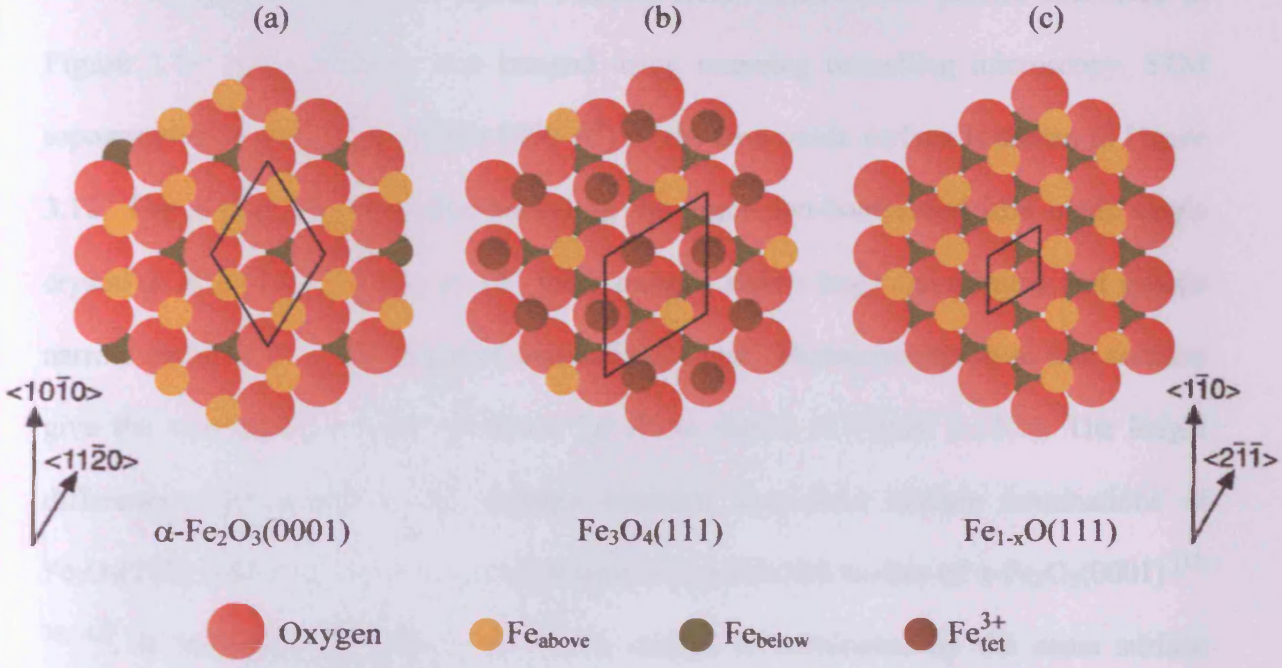

Figure 3.11. Lattice projections of iron oxide structures showing octahedrally coordinated Fe atom positions above (brown circles) and below (yellow circles) on either side of the close-packed oxygen layers (large red circles). In the $Fe_3O_4(111)$ structure, the tetrahedral Fe^{3+} sites are shown as dark brown circles. The surface unit cell constants are: (a) 5.03 Å; (b) 5.92 Å; (c) 3.04 Å. The lattice projection of γ-$Fe_2O_3(111)$ would be essential identical to that shown for $Fe_3O_4(111)$, differing only in that it would contain ordered vacancies in the octahedral sites. The crystallographic directions of α-$Fe_2O_3(0001)$ are indicated on the left, while those of $Fe_3O_4(111)$ and FeO(111) are shown on the right [39].

3.4.2.3. STM measurements

As mentions above, the iron oxide single crystal surface strongly depends on the surface preparation conditions which is associated with annealing conditions following argon-ion bombardment [15]. In these experiments, STM had been used to expose the surface of iron oxide single crystal which was prepared as described in chapter 2.

The iron oxide single crystal surface, from which LEED pattern illustrated in Figure 3.10 were obtained, was imaged using scanning tunnelling microscopy. STM topograph of typical areas (1000×1000 $Å^2$) of the iron oxide surface is shown in Figure 3.12. This image obtained after annealing the argon ion-bombarded iron oxide single crystal at 873 K for 30 min in 10^{-7} mbar oxygen shows large flat terraces and several narrow terraces with step edges of non-defined shape. Measurements from line sections give the average step height of about 5.0 Å, as shown in Figure 3.12(b). The height difference corresponds to the distance between equivalent surface terminations of $Fe_3O_4(111)$, which is also in good agreement with published studies of α-$Fe_2O_3(0001)$ [13, 39, 43]. It indicates that almost the whole surface is terminated by the same surface structure, but contains no information as to which structures correspond to Fe- or O-termination. The surfaces are also covered by a random distribution of small patches which lie about above the surrounding terrace where atomic structures could not be resolved. The size of the patches is not very consistent, the largest being about 20×20 $Å^2$ in area. Since a survey XPS showed no contaminations left on the surface, these patches might be disordered clusters of iron oxide and/or adsorbates.

(a)

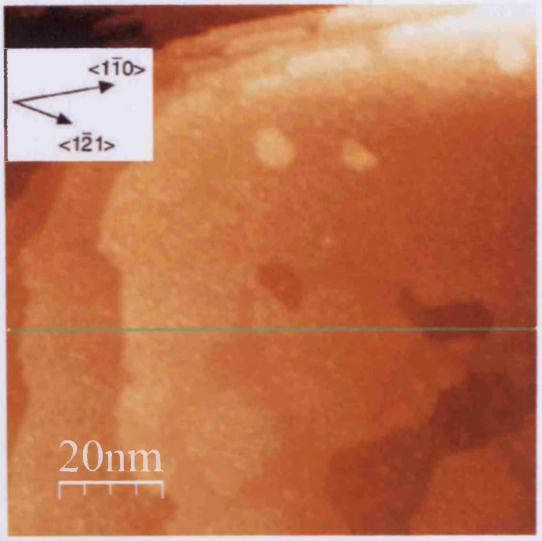

(b)

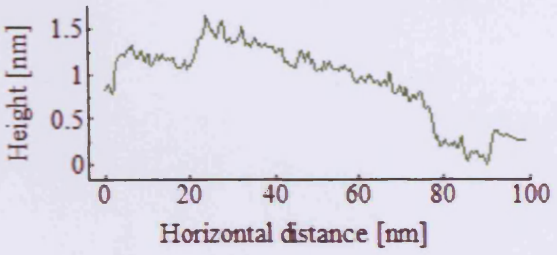

Figure 3.12. (a) A 1000×1000 Å^2 constant current (sample bias +1.2 V, tunnelling current 0.5 nA) STM topograph of iron oxide surface prepared by argon-ion sputtering and annealing in 10^{-7} mbar oxygen at 873 K. The crystallographic direction of the substrate is indicated. The green line defines the line profile shown in (b). (b) Schematic line profile in (a) showing step heights between successive terraces.

The high-resolution STM image (250×250 Å^2) clearly shows resolved features within typical terraces, as illustrated in Figure 3.13(a). These atomic features are arranged in a close-packed array and have a measured separation of 6.2±0.2 Å, similar to those previously observed in STM images of the reduced α-Fe_2O_3(0001) surface [13]. This image, therefore, suggests that the surface of iron oxide single crystal may be described as Fe_3O_4(111). A line section of this image, as shown in Figure 3.13(b), give heights of corrugations varying between ~0.3 and ~ 0.9 Å which represents considerable variation in the heights of individual surface features.

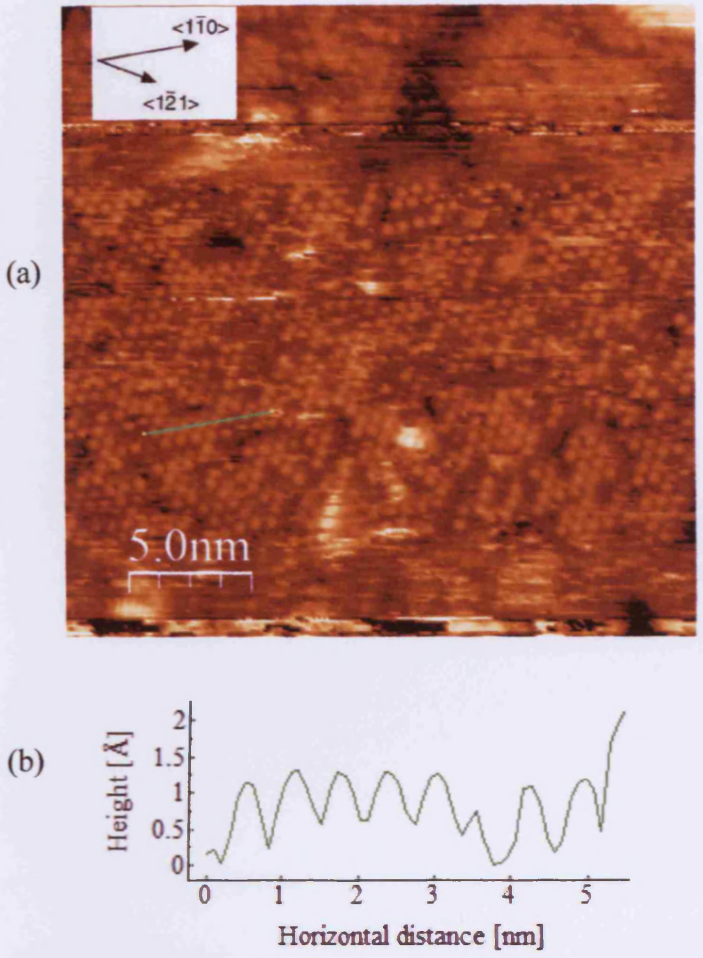

Figure 3.13. (a) A 250×250 Å^2 constant current (sample bias -1.0 V, tunnelling current 0.5 nA) STM image of the same surface as imaged in Figure 3.12, showing a close-packed array of features. Distances between features are 6.2±0.2 Å. Substrate crystallographic directions are indicated. (b) A line profile, defined by the green line in (a), is shown to illustrate the variation in corrugation heights (0.3-0.9 Å).

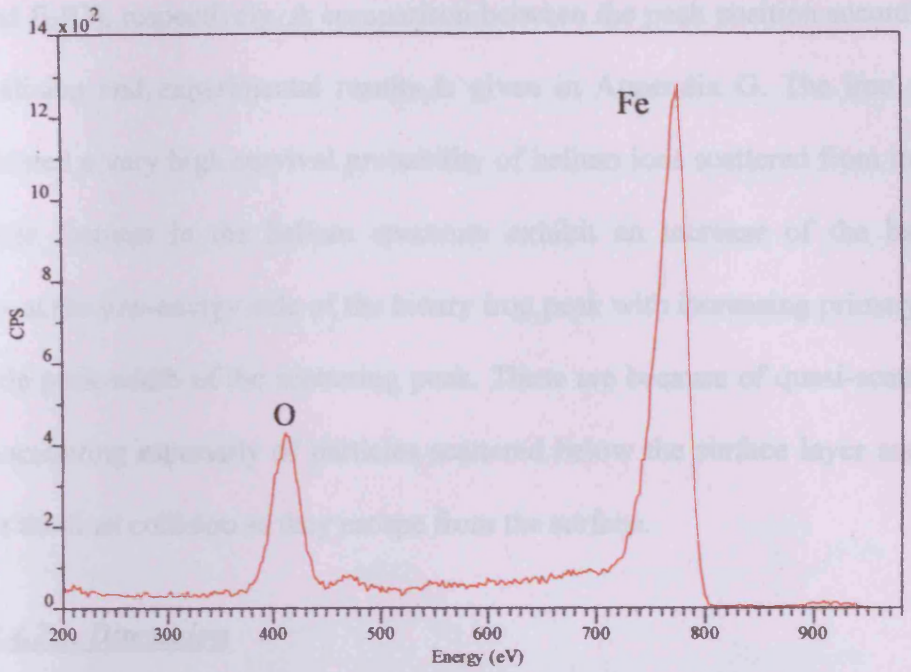

Figure 3.14. Typical energy spectrum of 1 keV $^4He^+$ ions at room temperature for iron oxide single crystal surface following argon-ion sputtering and annealing to 873 K in 10^{-7} mbar oxygen.

3.4.2.4. ISS observations

The iron oxide single crystal prepared in the way described above was investigated by means of ISS technique at room temperature. The ISS spectrum of helium ions bombardment under 1 keV helium ion bombardment from the surface of iron oxide single crystal is displayed in Figure 3.14. The energy spectrum exhibited only two ISS signals from atoms of oxygen and iron which suggests that neither carbon atoms contribute to its intensity and indicated that the iron and oxygen are contained in the outermost surface layer of iron oxide single crystal. The peak at ~773 eV belongs to helium ions scattered after a single binary elastic collision with the iron atoms, while the smaller peak at ~414 eV belongs to helium ions scattered from atoms of oxygen which is in good agreements with the energy positions expected from the binary-collision [44],

E_1(Fe) and E_2(O), respectively. A comparison between the peak position according to the binary-collision and experimental results is given in Appendix G. The iron scattering peak indicated a very high survival probability of helium ions scattered from iron atoms. The visible features in the helium spectrum exhibit an increase of the background especially at the low-energy side of the binary iron peak with increasing primary energies and a wide peak-width of the scattering peak. These are because of quasi-scattering and multiple-scattering especially of particles scattered below the surface layer and then re-ionised at the final collision as they escape from the surface.

3.4.2.5. Discussion

As shown in Figure 3.5, the XPS data analysis reveals the presence of Fe^{2+} and Fe^{3+} contributions in the iron oxide single crystal. The valence band spectrum shown in Figure 3.7 is similar to the spectrum reported for magnetite Fe_3O_4 [28]. The XRD pattern of the iron oxide crystal is in agreement with the reported values for magnetite (JCPDS 19-0629). It was also found that this crystal exhibits the magnetic properties. Combining the results of XPS, XRD, and magnetic properties, it can be concluded that the iron oxide single crystal used in this experiment was magnetite Fe_3O_4. The ISS spectrum shown in Figure 3.14 reveals that the iron and oxygen are contained in the topmost surface layer of the iron oxide crystal.

From our LEED pattern of the iron oxide crystal shown in Figure 3.10, the orientation and the symmetry of this hexagonal LEED pattern is identical to the pattern reported previously for both Fe_3O_4(111) single crystal [40, 43] and Fe_3O_4(111) thin films grown on α-Fe_2O_3(0001) [13, 15] and Pt(111) [16, 22, 45]. It exhibits a set of diffraction spots corresponding to a ~6 Å hexagonal unit cell, a 2×2 surface with reference to the ~3 Å periodicity in the hexagonal close-packed oxygen sub-lattice that is present either in the

(111) crystallographic planes of Fe_3O_4, FeO, or γ-Fe_2O_3 or in the (0001) plane of α-Fe_2O_3. In agreement with the p(2×2) LEED pattern of Figure 3.9, the atomic resolution STM images showed in Figure 3.13 reveals a hexagonal pattern of bright protrusions with a 6.2±0.2 Å periodicity. This symmetry and periodicity corresponds to those previously observed in STM images of $Fe_3O_4(111)$ [10, 43] and those of the reduced α-$Fe_2O_3(0001)$ surface [13, 39].

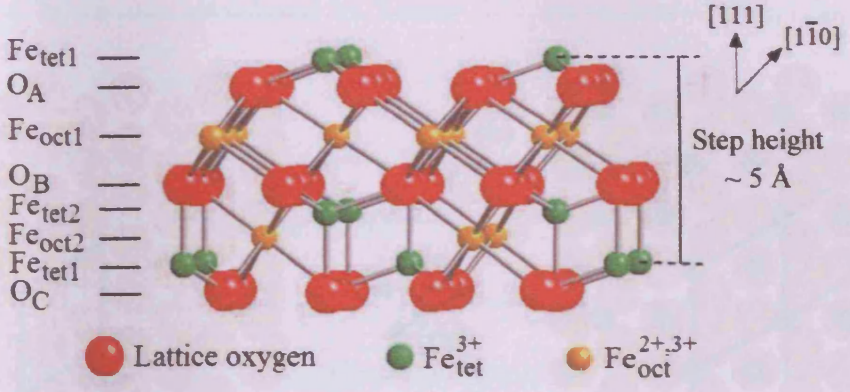

Figure 3.15. Slightly titled side view of the $Fe_3O_4(111)$ surface structure. On the left side the (111) layer sequence with tetrahedrally coordinated Fe_{tet1} or Fe_{tet2} atoms, with octahedrally coordinated Fe_{oct1} or Fe_{oct2} atoms, and with O_A, O_B, and O_C layers is indicated. Fe_3O_4 lattice directions are indicated. The layers along [111] are labelled with their atom types and subscripts indicating stacking sequence (in the case of oxygen) and coordination (in the case of iron).

To interpret our results, the basis of an $Fe_3O_4(111)$ selvedge is considered. As depicted in Figure 3.15, along the [111] direction, the stacking sequence of hexagonal iron and oxygen (111) planes can be schematically represented by Fe_{tet1}–O_A–Fe_{oct1}–O_B–Fe_{tet2}–Fe_{oct2}–Fe_{tet1}–O_C–Fe_{oct1}, where subscripts tet1 and tet2 refer to tetrahedrally coordinated iron atoms, and oct1 and oct2 correspond to iron atoms which are

octahedrally coordinated to oxygen [13, 39, 46]. O_A, O_B, and O_C correspond to the close packed oxygen sub-lattices. There are two types of iron sublayers between the adjacent O(111) layers. The first of these contains all octahedrally coordinated iron atoms (Fe_{oct1}), while the second contains iron atoms in both octahedral (Fe_{oct2}) and tetrahedral (Fe_{tet1} and Fe_{tet2}) sites as illustrated in Figure 3.16. The distance between two locally-equivalent Fe_3O_4(111) termination is 4.85 Å, and the unit cell dimension in the close-packed oxygen sublayer is 2.97 Å.

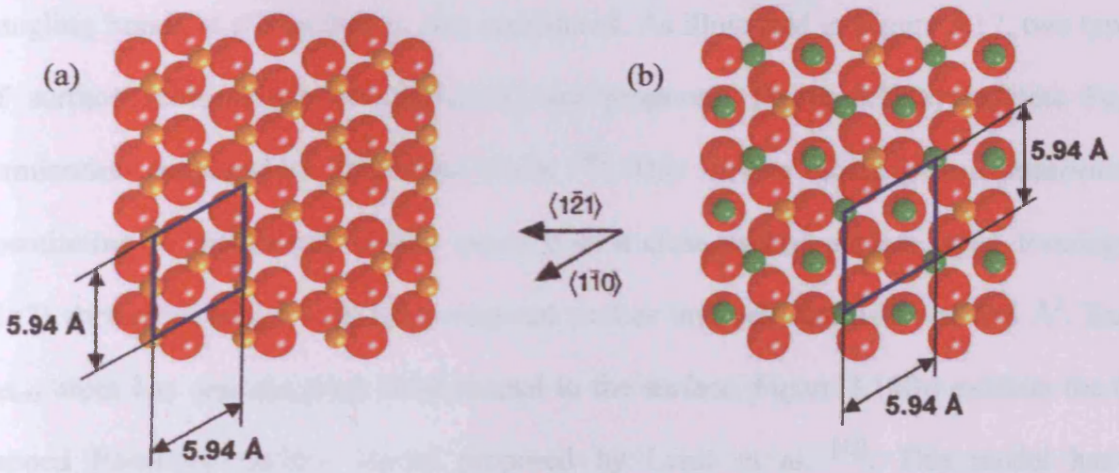

Figure 3.16. The lattice projection of the two types of iron atom arrangement between adjacent (111) oxygen layers in Fe_3O_4. Oxygen anions are shown as red spheres. (a) The Fe_{oct1} sites (yellow spheres) lay 1.21 Å above the oxygen plane. (b) The Fe_{tet1}, Fe_{tet2} (green spheres) and Fe_{oct2} (yellow spheres) sites as shown. Fe_{tet1} atoms in a three-fold hollow site lay 0.61 Å above the oxygen plane. Fe_{oct2} and Fe_{tet2} atoms lie 1.22 Å and 1.82 Å, respectively, above the oxygen plane. These distances are calculated assuming an ideal close-packed oxygen sub-lattice. The surface unit cell constant is indicated (a = 5.94 Å), along with Fe_3O_4 lattice directions [39].

The step heights obtained from the height profile in Figure 3.12 were found to be about 5.0 Å, which are consistent with the separation between locally-equivalent iron

layers in the $Fe_3O_4(111)$ stacking sequence observed in UHV studies of this surface [10, 43]. In principle, there are several possible (111) terminations of the bulk Fe_3O_4. A comparison of the STM shown in Figure 3.12 with the model in Figure 3.16 indicates that this surface is terminated by either an Fe_{tet1}, Fe_{tet2}, or Fe_{oct2} layer. All these terminations have the appropriate periodicity and correspond to a ¼ monolayer of iron atoms overlaying a close-packed oxygen layer. STM cannot be used to discriminate between these difference terminations. Therefore, the electrostatic surface energy of polar surfaces is considered, which was introduced by Tasker [47]. The minimisation of the number of dangling bonds at the surface is also considered. As illustrated in Figure 3.17, two types of surface terminations of $Fe_3O_4(111)$ are proposed. Figure 3.17(a) exhibits Fe_{tet1} termination proposed by Ritter and Weiss [16]. This surface model gave a termination constituting ¼ monolayer of iron atoms over a close-packed oxygen layer, forming a (2×2) surface structure with the hexagonal surface unit cell dimension of 6×6 $Å^2$. Each Fe_{tet1} atom has one dangling bond normal to the surface. Figure 3.18(b) exhibits the O-capped Fe-trimer surface model proposed by Lenie et al. [43]. This model has a termination in which ¼ monolayer of oxygen atoms capping trimers of Fe_{oct1} atoms. Removal of capping oxygen atom with a vertical dangling bond can give access to three iron atoms.

Although the LEED pattern and STM data are entirely consistent with the structures shown in Figure 3.17, they cannot discriminate between an Fe_3O_4 surface terminated by ¼ monolayer of Fe_{tet1} atoms (cf. Figure 3.17(a)) and a surface terminated by ¼ monolayer of oxygen (cf. Figure 3.17(b)). Moreover, they cannot be used to rule out the possible that the selvedge is γ-Fe_2O_3. However, the XPS results evidence the presence of both Fe^{2+} and Fe^{3+} species on the iron oxide surface, and hence point to an Fe_3O_4 selvedge.

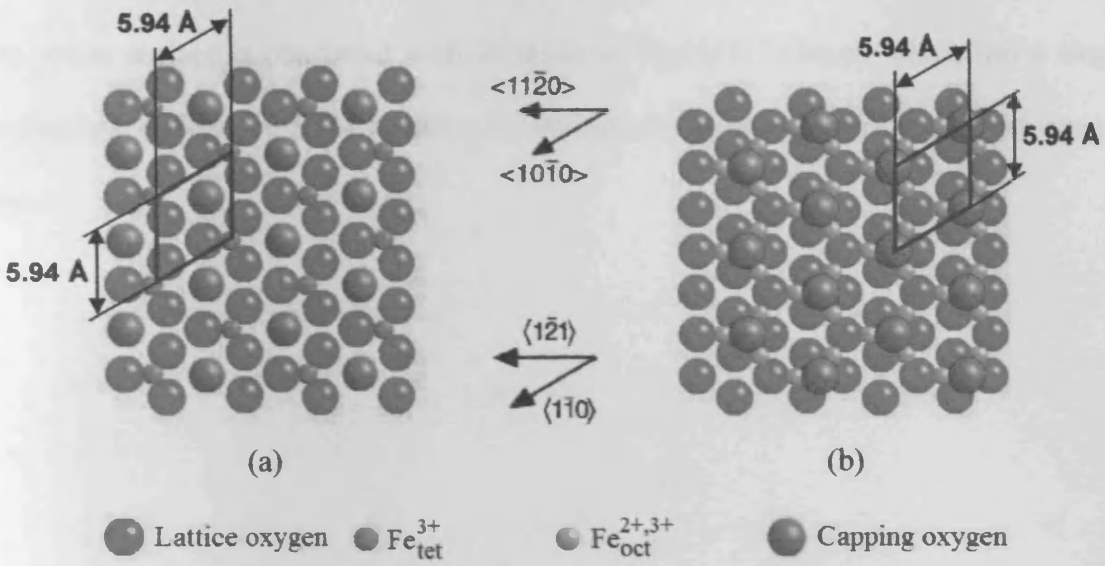

Figure 3.17. Models of $Fe_3O_4(111)$ magnetite surface terminations proposed to explain the features observed in the STM images in Figure 3.12 and 3.13. (a) The iron-terminated $Fe_3O_4(111)$ model surface described by Ritter and Weiss [16]. A ¼ monolayer of iron atoms (Fe_{tet1} in Figure 3.15) forms a (2×2) structure above the oxygen plane (O_A in Figure 3.15). Removal of an uncapped oxygen atoms (blue spheres) give access to three iron atoms (Fe_{oct1} in Figure 3.15) located below the O_A layer. (b) An oxygen-terminated $Fe_3O_4(111)$ model surface described by Lennie et al. ("Termination A") [43]. A ¼ monolayer of oxygen atoms is capping a ¾ monolayer of iron atoms (Fe_{oct1} in Figure 3.15). Crystallographic directions for α-$Fe_2O_3(0001)$ are shown at top, those for $Fe_3O_4(111)$ at bottom. The unit cell dimension for a bulk termination, shown by the dark blue lines, is 5.94 Å.

3.5. Conclusions

The surface structures formed on the iron oxide single crystal are characterised by several techniques of surface science such as XPS, LEED, STM and ISS.

It can be concluded that after sputtering and subsequent annealing in oxygen, the iron oxide surface is consistent with an epitaxial $Fe_3O_4(111)$ layer, which has a single termination defined by STM results and the topmost layer consists of iron and oxygen atoms.

3.6. References

[1] M. V. Twigg and I. Imperial Chemical, *Catalyst handbook*, Manson Publishing, Frome, **1996**, p.

[2] M. Muhler, R. Schlogl and G. Ertl, *Journal of Catalysis* **1992**, *138*, 413-444.

[3] D. Zscherpel, W. Weiss and R. Schlogl, *Surface Science* **1997**, *382*, 326-335.

[4] J. H. Kennedy and J. K. W. Frese, *Journal of the Electrochemical Society* **1978**, *125*, 723-726.

[5] J. H. Kennedy and J. K. W. Frese, *Journal of the Electrochemical Society* **1978**, *125*, 709-714.

[6] S. Yoshii, O. Ishii, S. Hattori, T. Nakagawa and G. Ishida, *Journal of Applied Physics* **1982**, *53*, 2556-2560.

[7] J. W. Geus, *Applied Catalysis* **1986**, *25*, 313-333.

[8] R. M. Cornell and U. Schwertmann, *The iron oxides: structure, properties, reactions, occurrences, and uses*, Wiley-VCH, Weinheim, **2003**, p.

[9] A. V. Palnichenko, A. N. Rossolenko, V. N. Kopylov, I. I. Zver'kova and A. S. Aronin, *Chemical Physics Letters* **2005**, *410*, 436-440.

[10] W. Weiss and W. Ranke, *Progress in Surface Science* **2002**, *70*, 1-151.

[11] G. Ketteler, W. Weiss, W. Ranke and R. Schlogl, *Physical Chemistry Chemical Physics* **2001**, *3*, 1114-1122.

[12] R. W. G. Wyckoff, *Crystal structures Vol.1*, Interscience, New York, **1963**, p.

[13] N. G. Condon, P. W. Murray, F. M. Leibsle, G. Thornton, A. R. Lennie and D. J. Vaughan, *Surface Science* **1994**, *310*, L609-L613.

[14] A. Cabot, V. F. Puntes, E. Shevchenko, Y. Yin, L. Balcells, M. A. Marcus, S. M. Hughes and A. P. Alivisatos, *J. Am. Chem. Soc.* **2007**, *129*, 10358-10360.

[15] R. J. Lad and V. E. Henrich, *Surface Science* **1988**, *193*, 81-93.

[16] M. Ritter and W. Weiss, *Surface Science* **1999**, *432*, 81-94.

[17] S. K. Apte, S. D. Naik, R. S. Sonawane, B. B. Kale and J. O. Baeg, *Journal of the American Ceramic Society* **2007**, *90*, 412-414.

[18] J. H. Bang and K. S. Suslick, *J. Am. Chem. Soc.* **2007**, *129*, 2242-2243.

[19] I. Cesar, A. Kay, J. A. GonzalezMartinez and M. Gratzel, *J. Am. Chem. Soc.* **2006**, *128*, 4582-4583.

[20] S. K. Shaikhutdinov and W. Weiss, *Surface Science* **1999**, *432*, L627-L634.

[21] G. Ketteler, W. Weiss and W. Ranke, *Surface Review and Letters* **2001**, *8*, 661-683.

[22] A. Barbieri, W. Weiss, M. A. Van Hove and G. A. Somorjai, *Surface Science* **1994**, *302*, 259-279.

[23] C. R. Brundle, T. J. Chuang and K. Wandelt, *Surface Science* **1977**, *68*, 459-468.

[24] R. L. Kurtz and V. E. Henrich, *Surface Science* **1983**, *129*, 345-354.

[25] D. A. Shirley, *Physical Review B* **1972**, *5*, 4709-4714.

[26] A. P. Grosvenor, B. A. Kobe, M. C. Biesinger and N. S. McIntyre, *Surface and Interface Analysis* **2004**, *36*, 1564-1574.

[27] R. P. Gupta and S. K. Sen, *Physical Review B* **1975**, *12*, 15-19.

[28] T. Fujii, F. M. F. de Groot, G. A. Sawatzky, F. C. Voogt, T. Hibma and K. Okada, *Physical Review B* **1999**, *59*, 3195-3202.

[29] A. Fujimori, M. Saeki, N. Kimizuka, M. Taniguchi and S. Suga, *Physical Review B* **1986**, *34*, 7318-7328.

[30] R. J. Lad and V. E. Henrich, *Physical Review B* **1989**, *39*, 13478-13485.

[31] N. S. McIntyre and D. G. Zetaruk, *Analytical Chemistry* **1977**, *49*, 1521-1529.

[32] W. Temesghen and P. M. A. Sherwood, *Analytical and Bioanalytical Chemistry* **2002**, *373*, 601-608.

[33] T. Kendelewicz, P. Liu, C. S. Doyle, G. E. Brown, E. J. Nelson and S. A. Chambers, *Surface Science* **2000**, *453*, 32-46.

[34] G. Kurbatov and E. Darque-Ceretti, *Surface and Interface Analysis* **1993**, *20*, 402-406.

[35] G. Kurbatov, E. Darque-Ceretti and M. Aucouturier, *Surface and Interface Analysis* **1992**, *18*, 811-820.

[36] T.-C. Lin, G. Seshadri and J. A. Kelber, *Applied Surface Science* **1997**, *119*, 83-92.

[37] P. Liu, T. Kendelewicz, G. E. Brown, E. J. Nelson and S. A. Chambers, *Surface Science* **1998**, *417*, 53-65.

[38] V. Maurice, W. P. Yang and P. Marcus, *Journal of the Electrochemical Society* **1994**, *141*, 3016-3027.

[39] N. G. Condon, F. M. Leibsle, A. R. Lennie, P. W. Murray, T. M. Parker, D. J. Vaughan and G. Thornton, *Surface Science* **1998**, *397*, 278-287.

[40] N. G. Condon, F. M. Leibsle, T. Parker, A. R. Lennie, D. J. Vaughan and G. Thornton, *Physical Review B* **1997**, *55*, 15885-15894.

[41] M. Hendewerk, M. Salmeron and G. A. Somorjai, *Surface Science* **1986**, *172*, 544-556.

[42] N. G. Condon, F. M. Leibsle, A. R. Lennie, P. W. Murray, D. J. Vaughan and G. Thornton, *Physical Review Letters* **1995**, *75*, 1961-1964.

[43] A. R. Lennie, N. G. Condon, F. M. Leibsle, P. W. Murray, G. Thornton and D. J. Vaughan, *Physical Review B* **1996**, *53*, 10244-10253.

[44] H. Niehus, W. Heiland and E. Taglauer, *Surface Science Reports* **1993**, *17*, 213-303.

[45] W. Weiss, A. Barbieri, M. A. Van Hove and G. A. Somorjai, *Physical Review Letters* **1993**, *71*, 1848-1851.

[46] K. T. Rim, J. P. Fitts, T. Muller, K. Adib, I. I. I. N. Camillone, R. M. Osgood, S. A. Joyce and G. W. Flynn, *Surface Science* **2003**, *541*, 59-75.

[47] P. W. Tasker, *Journal of Physics C: Solid State Physics* **1979**, *12*, 4977-4984.

4 The Fabrication of Iron Molybdate Layers

Chapter IV

The Fabrication of Iron Molybdate Layers

We studied the surface morphology of molybdenum oxide on the iron oxide single crystal surface using XPS, LEED, LEIS and STM. The analysis of Mo 3d core level spectra of molybdenum oxide films grown on $Fe_3O_4(111)$ surface by HFMOD technique indicates that the hexavalent molybdenum is predominant. The results of LEED and STM images of molybdenum oxide on $Fe_3O_4(111)$ annealed at different temperatures showed that the annealing temperature could strongly influence its surface structure: (i) at 873 K, molybdenum oxide clusters dispersed on the surface of $Fe_3O_4(111)$ and formed $p(4\times4)$ structure of molybdenum oxide clusters; (ii) at 973 K, molybdenum oxide appears to react with $Fe_3O_4(111)$ to form iron molybdates which exhibit a crystalline structure with a $(2\sqrt{3}\times2\sqrt{3})R30°$ periodicity relative to $Fe_3O_4(111)$ surface.

4.1. Introduction

Material systems of metal oxides supported on different types of oxide substrate are of considerable interest because of their broad range of physical and chemical properties and their wide applications in technology, environmental protection and, in particular, heterogeneous catalysis. In spite of this considerable interest, the structure and

morphology of the supported metallic oxide, the active sites and role of supporting oxides in catalytic reactions need to be explored further to develop new types of catalytic material.

Supported molybdenum oxide as an active component has been widely employed in the recent past for the selective oxidation of methanol [1, 2]. In addition, molybdenum oxide is extensively used as a catalyst in the petroleum and chemical industry [1, 3-16]. The dispersion of the molybdenum oxide and the structure strongly depend on the nature of the supported oxide. In turn, all these factors can greatly influence the catalytic properties. The most commonly used supports are alumina [17-21], silica [1, 7, 16, 19, 22-24], titania [9, 11, 25, 26], and zirconia [27-30]. In the recent past, iron oxides have been widely used as catalysts within various areas of industrial application. In particular, in heterogeneous catalysis, iron oxide catalysts have been employed, for instance, in the ammonia synthesis, dehydrogenation of butene to butadiene, and dehydrogenation of ethylbenzene to styrene [31, 32]. Since the pioneering work of Adkins and Peterson in 1931 [33], mixed oxides of molybdenum and iron have been widely used as catalysts for the partial oxidation of alcohols and hydrocarbons. Iron-molybdenum oxide catalysts have high activity and selectivity for the oxidation of methanol to formaldehyde. Pernicone [34] reported molybdenum oxide is an active component of this catalyst and iron oxide and a spinel compound $Fe_2(MoO_4)_3$ enhance the activity of molybdenum oxide. Although the iron-molybdenum oxides have been extensively studied [34-39], relatively few studies has been done on the surface state of iron-molybdenum oxide catalysts, such as surface composition, chemical states of component oxides, and surface structure, particularly during the reactions. The knowledge of these surface properties is essential for understanding their physical and chemical properties.

4.1.1. Aims and work strategy

Formaldehyde is an important industrial chemical which is used mainly in the production of phenolic resins and industrially is synthesised over iron-molybdenum oxide catalysts through selective oxidation of methanol. The reaction is exothermic (ΔH = -158 kJ/mol) and is run at atmospheric pressure and at temperature ranges of 250-400°C.

The basic idea as we apply it here is to prepare the model catalyst samples and to characterise their surface structure and composition under UHV conditions using mainly LEED, XPS, LEIS, and STM.

With the help of surface science techniques, the aims are the following:

- To characterise the molybdenum oxide films grown on $Fe_3O_4(111)$ using a variety of techniques.
- To investigate the chemistry of model iron molybdate surfaces towards probe molecules relevant to heterogeneous catalysis.

In this chapter, we report results of molybdenum oxide on iron oxide single crystal obtained through XPS analysis in terms of its chemical composition and electronic structure. The atomic surface structure and surface defects of these films were characterized by STM and low-energy electron diffraction (LEED) crystallography. The atomic composition of this outermost surface is provided by low energy helium ion scattering (LEIS) analysis.

4.2. Structural considerations

Before entering the discussion of our experimental results, it is essential to clarify the structural complexities of the related compounds studied. This is particularly important for an interpretation of the results obtained through our XPS, LEED, LEIS and STM analysis.

4.2.1. Molybdenum oxide

The oxides of molybdenum exhibit a variety of crystalline phases with different stoichiometry and structures [40]. Some of these compounds are MoO_3 (α-MoO_3 orthorhombic and β-MoO_3 monoclinic), MoO_2 (monoclinic), Mo_4O_{11} (monoclinic, orthorhombic), and Mo_9O_{26} (triclinic, monoclinic). The former two phases are the most stable oxides of molybdenum, where the oxidation states of molybdenum are hexavalent and tetravalent, respectively; all other phases between MoO_3 and MoO_2 [41] have been synthesised.

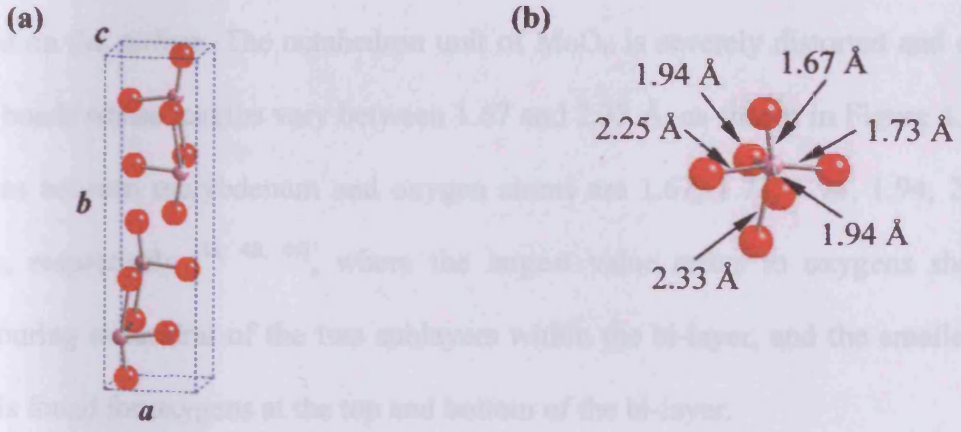

Figure 4.1. Schematic representation of the idealised crystal structure of orthorhombic MoO_3. (a) Elementary unit cell of bulk MoO_3 containing four MoO_3 units. (b) Octahedral MoO_6 building unit with values of interatomic Mo–O distances added.

Molybdenum trioxide, MoO_3, can exist in two crystalline polymorphs, the thermodynamically stable orthorhombic α-MoO_3 and the metastable monoclinic β-MoO_3 phase. The α-MoO_3 exhibits a crystallographic anisotropy and a unit cell containing four formula units of MoO_3 (see Figure 4.1a). Bulk α-MoO_3 has orthorhombic crystal symmetry with lattice parameters of a = 3.963 Å, b = 13.855 Å, c = 3.696 Å, and space group *Pbnm* [42-48]. The geometric models of bulk α-MoO_3 (see Figure 4.2) suggest its

surfaces have a layer type orthorhombic crystal structure with each layer comprising of infinite chains of corner-sharing MoO_6 octahedra [47]. These layers run parallel to the (010) lattice plane and they are connected by sharing the edges of the MoO_6 octahedra, which gives a double chain. Each double layer consists of edge-sharing zigzag rows of (001) and corner-sharing rows of (100). The adjacent crystal lattice layers of MoO_6 octahedra in the (010) direction are held together only by strong van der Waals forces (~50 kcal mol^{-1}), which accounts for the easy cleavage of MoO_3 along (010) plane, but by covalent forces for lattice layers in the (100) and (001) directions [42, 43, 48-50]. Hence the MoO_3(010) surface is thermodynamically most stable, where only oxygen atoms are exposed on the surface. The octahedron unit of MoO_6 is severely distorted and contains Mo–O bonds whose lengths vary between 1.67 and 2.33 Å, as shown in Figure 4.1b. The distances between molybdenum and oxygen atoms are 1.67, 1.73, 1.94, 1.94, 2.25 and 2.33 Å, respectively [42, 48, 49], where the largest value refers to oxygens shared by neighbouring octahedral of the two sublayers within the bi-layer, and the smallest bond length is found for oxygens at the top and bottom of the bi-layer.

The ideal MoO_3 (010) surface is characterised by a simple network of molybdenum and oxygen ions, where there are three structurally different lattice oxygens: asymmetric bridging oxygen (doubly co-ordinated, O_a), symmetric bridging oxygen (triply co-ordinated, O_s), and terminal oxygen (singly co-ordinated, O_t). First, the asymmetric bridging oxygen atoms are coordinated to two Mo centres in the same layer with distances of 1.73 and 2.25 Å. Second, the symmetric bridging oxygen atoms are coordinated to two Mo centres of the surface layer with two bonding distance of 1.95 Å and couple weakly with another Mo centre of the underlying sublayer with a distance of 2.33 Å. Finally, the terminal oxygen atoms are coordinated to only one Mo centre directly below at a distance of 1.67 Å which corresponds to double bond.

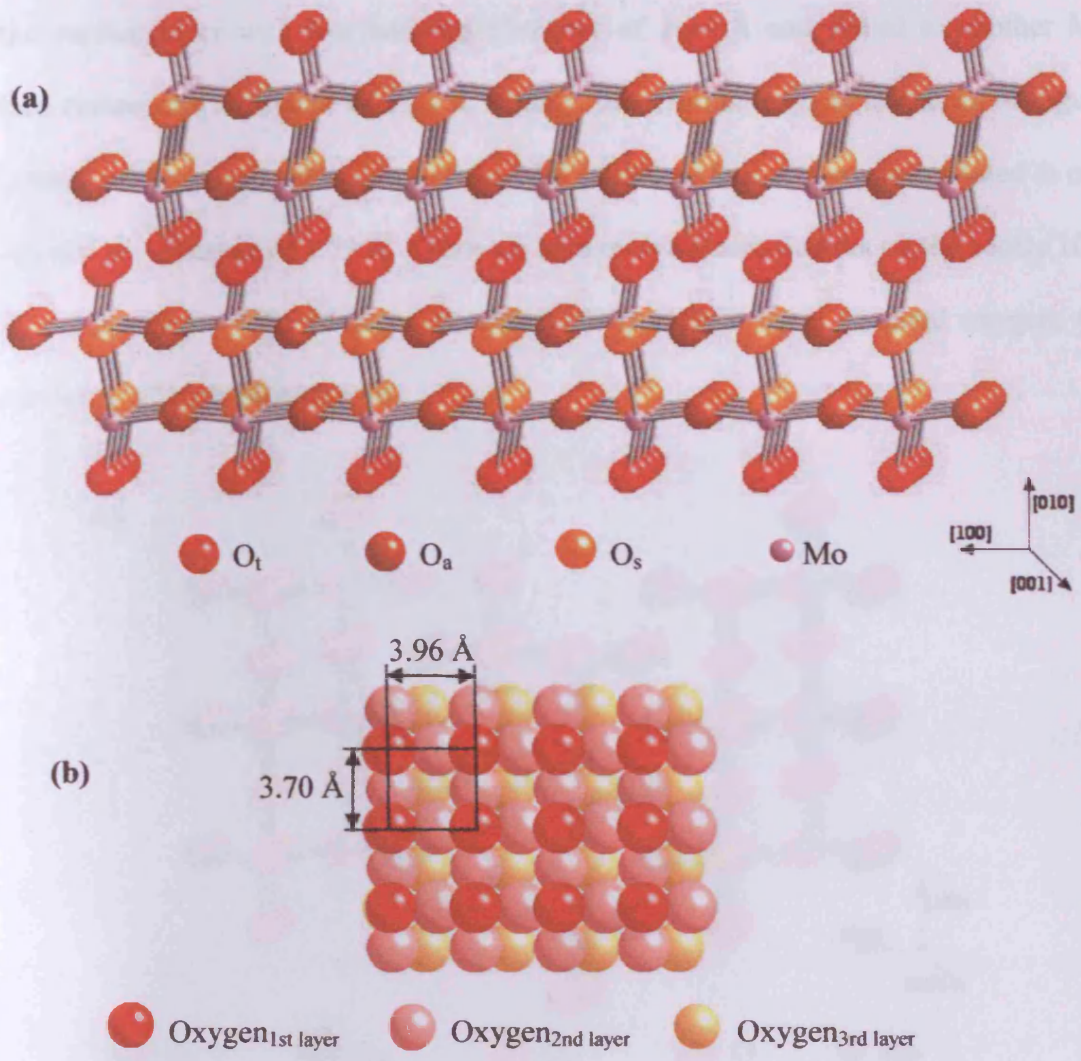

Figure 4.2. Perspective side view (a) and top view (b) of the orthorhombic MoO_3 structure exposing a (010) surface plane [48]. In the top view in (b), the MoO_3(010) surface unit cell with a lattice constant of 3.70 and 3.96 Å is indicated.

The structure of the ideal MoO_3 (100) surface is very different from that of the (010) surface (see Figure 4.2 and 4.3). This surface is much looser and there are several kinds of structurally different surface oxygen centres. The oxygen atoms, O_d of Figure 4.3, which are coordinated to one Mo centre at a distance of 1.67 Å are equivalent to the terminal oxygen atoms of the MoO_3(010) surface. They lie near the plane of the surface molybdenums. The symmetric bridging oxygen atoms, O_s of Figure 4.3, are similar to those of the MoO_3(010) surface. They are placed symmetrically between two Mo centres

of the surface layer with two bonding distances of 1.94 Å and linked to another Mo surface centre with a distance of 2.33 Å. Finally, the terminal oxygen atoms, O_t of Figure 4.3, structurally correspond to those of the $MoO_3(010)$ surface and are coordinated to one Mo centre at a distance of 1.73 Å. There are bare molybdenum centres on the $MoO_3(100)$ surface (see Figure 4.3), while on the $MoO_3(010)$ surface these terminal oxygen, O_t, atoms cover all molybdenum ions.

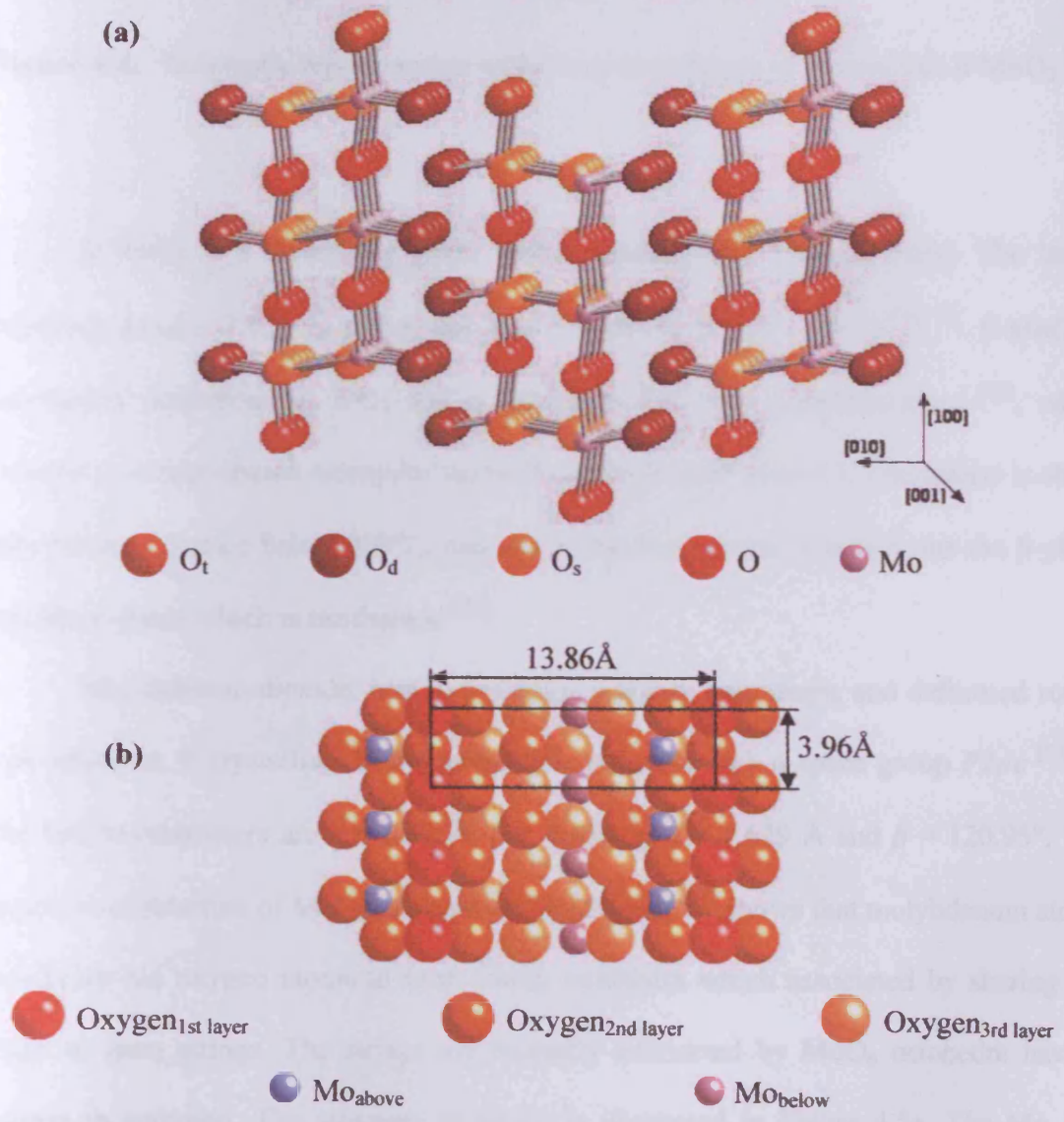

Figure 4.3. Perspective side view (a) and top view (b) of the orthorhombic MoO_3 structure exposing a (100) surface plane. In top view in (b), the $MoO_3(100)$ surface unit cell with unit cell of 3.96 Å × 13.86 Å indicated.

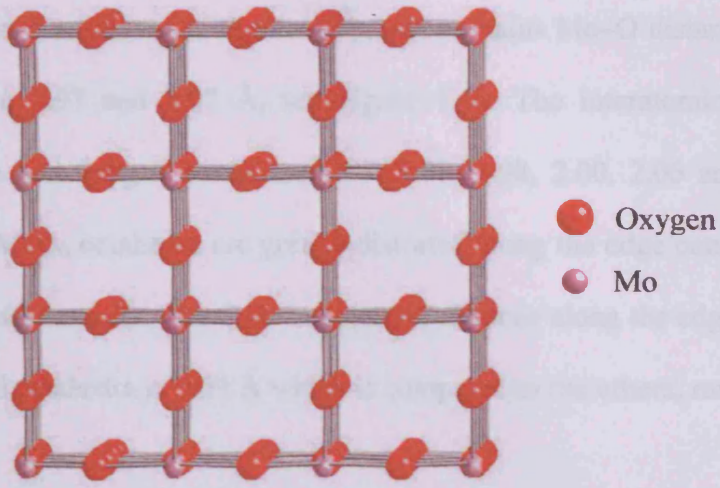

Figure 4.4. Schematic representation of the crystal structure of monoclinic β-MoO_3 [51].

β-MoO_3 is a metastable phase with a monoclinic crystal structure. The lattice constants are a = 7.122 Å, b = 5.366 Å, c = 5.566 Å, and β = 92.01 [46, 51]. β-MoO_3 is structurally analogous to WO_3 and is related to the ReO_3-type structures [52], which consists in corner-shared octahedral network, as shown in Figure 4.4. This phase is stable only for temperature below 450°C, and above this temperature it transforms the β-phase into the α-phase which is exothermic [52].

Molybdenum dioxide, MoO_2, possesses a highly anisotropic and deformed rutile-type structure. It crystallises in the monoclinic structure with a space group $P2_1/c$ [53, 54]. The lattice parameters are a = 5.61 Å, b = 4.856 Å, c = 5.629 Å and β = 120.95°. The geometrical structure of MoO_2 as proposed by Magnéli [55] shows that molybdenum atoms coordinate six oxygen atoms to form MoO_6 octahedra which associated by sharing the edges to form strings. The strings are mutually connected by MoO_6 octahedra having corners in common. The structure of MoO_2 is illustrated in Figure 4.5a. The Mo–Mo distances within strings of MoO_6 octahedra connected by common edges are alternately shorter and longer than in the metal. The octahedral MoO_6 building unit in bulk MoO_2 are

only moderately distorted as shown in Figure 4.5b, and contains Mo–O distances whose lengths range between 1.97 and 2.07 Å, see Figure 4.4b. The interatomic distances between molybdenum and oxygen atoms are 1.97, 1.98, 1.98, 2.00, 2.06 and 2.07 Å, respectively [53]. The MoO_6 octahedra are greatly distorted along the edge containing the very short Mo–Mo bond across it. The O–O interatomic distance along the edge common to two MoO_6-distorted octahedra is 3.09 Å which is compared to the others, ranging from 2.71 to 2.90 Å.

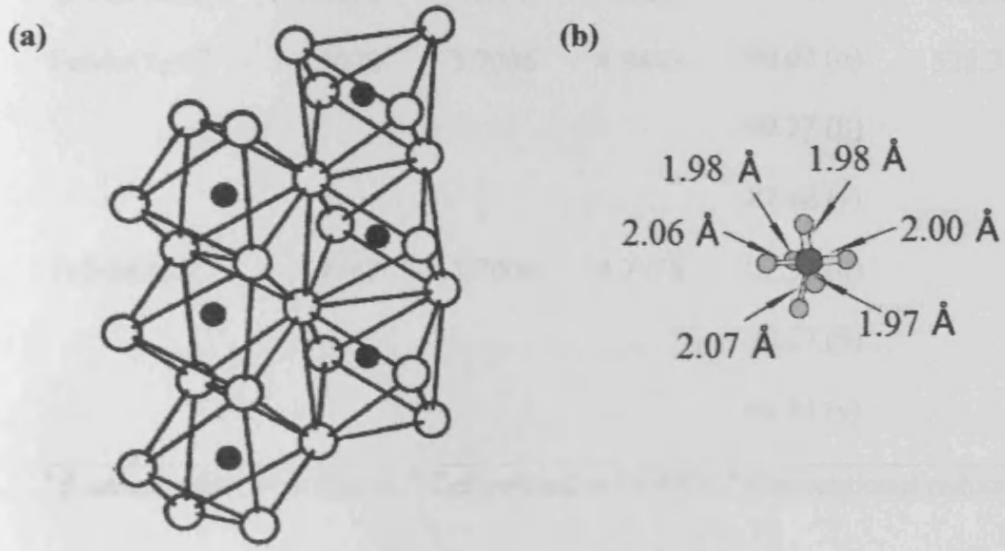

Figure 4.5. Schematic representation of the idealised crystal structure of monoclinic MoO_2. (a) Crystal structure of monoclinic MoO_2 crystal lattice. Molybdenum (oxygen) centres are shown by black (white) balls [55]. (b) Octahedral MoO_6 building unit with values of interatomic Mo–O distance added.

4.2.2. Iron molybdenum oxide

Iron-molybdenum oxides occur with a variety of phases with different stoichiometries and crystal structure. There are four polymorphs of iron molybdates reported, including α-$FeMoO_4$, the low-temperature, low-pressure form [56]; β-$FeMoO_4$,

the high-temperature, low-pressure form [56]; $FeMoO_4$-II, the high-temperature modification [57] and $Fe_2(MoO_4)_3$, the high-temperature, low-pressure form [58]. The latter phase is well known as a selective oxidation catalyst which is employed to convert methanol to formaldehyde.

Table 4.1. Cell dimensions of some $FeMoO_4$ compounds [56, 59].

Compound	Parameters, Å			Angle,[a] Deg	V, Å^3
	a	*B*	*c*		
α-$FeMoO_4$	9.805	8.905	7.660	114.05	613.9
β-$FeMoO_4$	10.290	9.394	7.072	106.31	656.1
$FeMoO_4$-II[b]	4.7078	5.7006	4.9443	90.67 (α)	528.3/4
				90.27 (β)	
				87.68 (γ)	
$FeMoO_4$-II[c]	4.9443	5.7006	4.7078	92.32 (α)	
				90.27 (β)	
				89.33 (γ)	

[a] β unless otherwise stated. [b] Cell related to $NiWO_4$. [c] Conventional reduced cell.

Iron (II) molybdate, $FeMoO_4$, has the nominal valence distribution of $[Fe^{2+}][Mo^{6+}]O_4$. There are three different phases reported [59, 60], α-$FeMoO_4$, β-$FeMoO_4$, and $FeMoO_4$-II. The structure type depends on the conditions of synthesis and temperature. The α and β phase of $FeMoO_4$ crystallise in the monoclinic structure, with the *C2/m* space group. The transformation of α- to β-$FeMoO_4$ takes place at about 400°C [56]. The structure of α-$FeMoO_4$ was reported to be isotypic with that of α-$CoMoO_4$ structure [61], while β-$FeMoO_4$ was reported to be isotypic with α-$MnMoO_4$ [62]. The α and β phase of $FeMoO_4$ can be found at room temperature depending on the cooling rate, but α-$FeMoO_4$ is the stable phase at this temperature. β-$FeMoO_4$ is possibly obtained, nearly free of α-

$FeMoO_4$, by quenching from above the α-β transformation temperature, while α-$FeMoO_4$ is mostly formed by slower cooling. A mixture of α- and β-$FeMoO_4$ obtained at room temperature may be completely converted to α-$FeMoO_4$ by sufficient grinding at room temperature or by cooling to 78 K. The crystal parameters of α- and β-$FeMoO_4$ are given in Table 4.1. The unit cell volume of the β phase is consistently 6 percent larger than that of the α phase [59]. One of the main differences in the crystal structures of α- and β-$FeMoO_4$ is in the change in the coordination of molybdenum atoms located on two crystallographically distinct sites from octahedral (in α-$FeMoO_4$) to tetrahedral (in β-$FeMoO_4$). Meanwhile, both phases have two distinct octahedrally coordinated iron sites [63]. All these sites display some distortion of octahedra or tetrahedra.

Figure 4.6 illustrates the structure of α-$FeMoO_4$ described by Smith and Ibers [61]. Its structure consists of distorted oxygen octahedra of iron and molybdenum atoms. Both the like-filled and unlike-filled octahedra share edges and lead to an infinite chain consisting of edge-sharing octahedra along the *c*-axis direction (see Figure 4.6a). Each chain is surrounded by four other chains and shares corners to other through oxygen atoms, resulting in the chains of unfilled octahedral "holes" along the *c*-axis direction in-between the filled chains.

The structure of β-$FeMoO_4$ contains FeO_6 octahedra and MoO_4 tetrahedra placed three-dimensionally by sharing edges of FeO_6 octahedra to form Fe_4 clusters which are linked by MoO_4 tetrahedra [64]. Rodriguez et. al. described the structure of β-$FeMoO_4$ (see Figure 4.7) that it consists of columns or stacks of four-membered metal-oxygen rings. There are two types of iron and molybdenum atoms. The first type corresponds to metal atoms occupying mixed Fe_1–O–Mo_1–O rings and the second type includes metal atoms occupying pure Mo_2–O–Mo_2–O or Fe_2–O–Fe_2–O rings. Moreover, there are two kinds of oxygen atoms: those that bridge the chains of rings and have only two metal neighbours (O_b) and those that form part

of the rings and have three or four metal neighbours (O_r). Within the rings, one can have metal-oxygen bonds that are either parallel (Fe–O_{rc}, Mo–O_{rc}) or perpendicular (Fe–O_{rnc}, Mo–O_{rnc}) to the c axis [65]. The Fe–O distances for both Fe_1 and Fe_2 lie in the range 2.01-2.17 Å and the Mo–O distances lie between 1.70 and 3.45 Å where largest distance prevent an effective octahedral coordination for each molybdenum atom. β-$FeMoO_4$ is stable in the temperature ranges 25 to 800°C and decompose at temperature above 850°C [65].

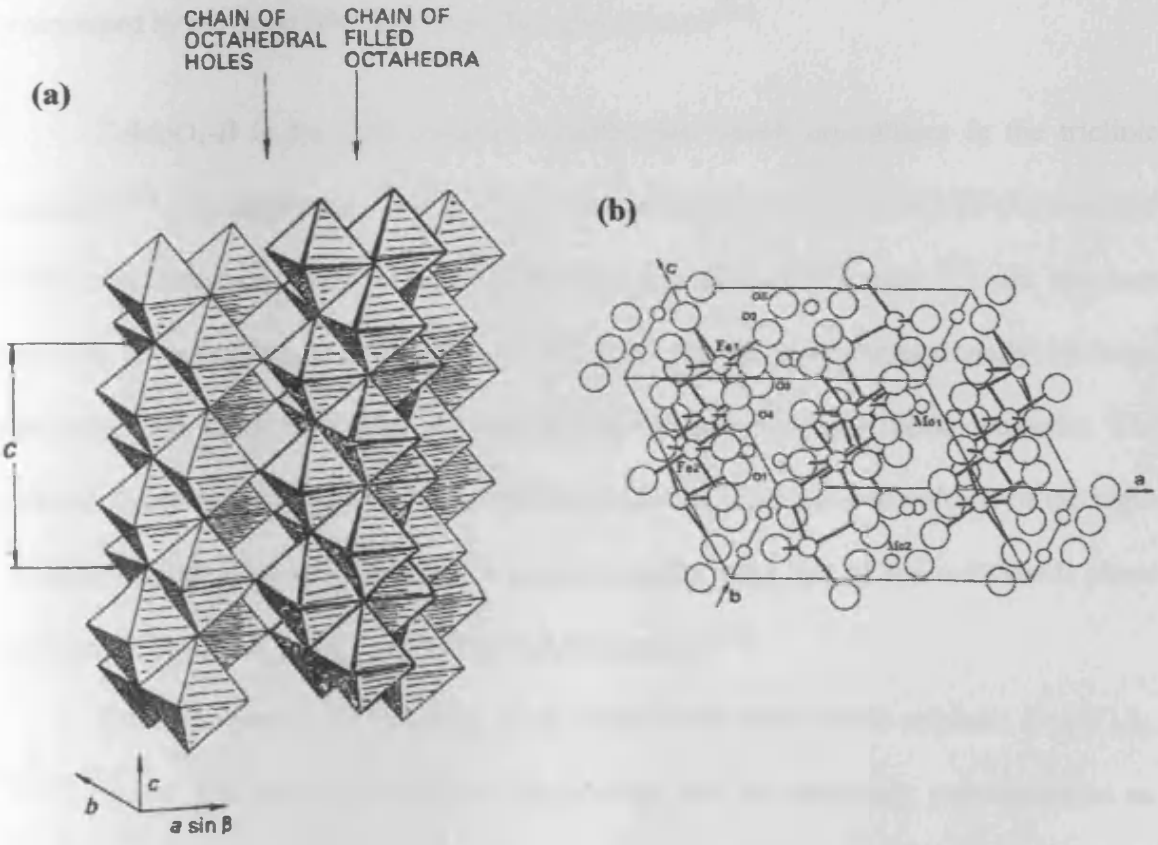

Figure 4.6. (a) Structure of α-$FeMoO_4$ showing the chains of close-packed octahedra parallel to *c* axis. Filled octahedral chains are joined by corner-sharing to other leaving unfilled octahedral holes in-between [61]. (b) The crystal structure of α-$FeMoO_4$. The oxygen atoms are represented by large circles, and the metal atoms by the small circles [66].

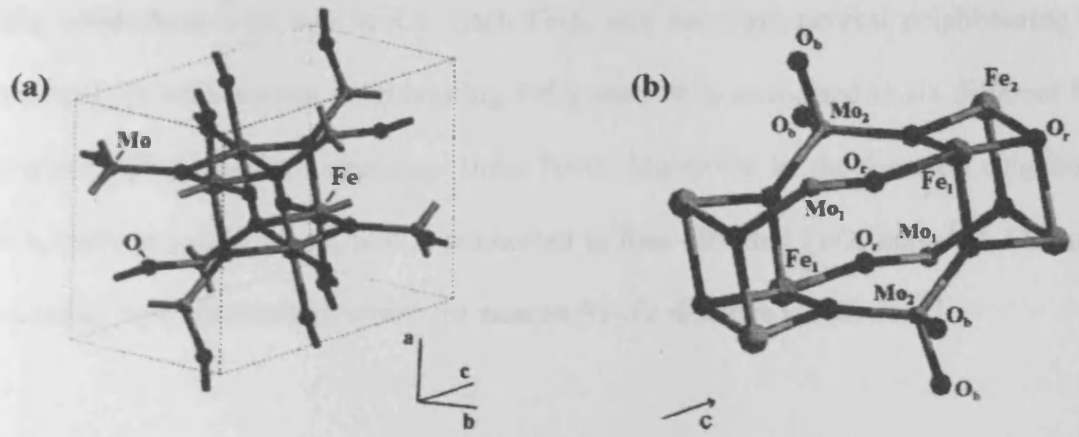

Figure 4.7. a) Primitive cell for the β phase of $FeMoO_4$, and b) Partial view of the crystal structure of β-$FeMoO_4$. The dark spheres represent O atoms. The metal atoms are represented by the small (Mo) and large (Fe) gray spheres [65].

$FeMoO_4$-II is the high-pressure modification which crystallises in the triclinic structure [67]. The structure of $FeMoO_4$-II was to be isotypic with that of $NiWO_4$ (distorted wolframite structure) as has been reported by Young and Schwartz [57]. Its structure consists of octahedra of iron and molybdenum placed three-dimensionally by edge sharing of like metal octahedra and only corner sharing of unlike metal octahedra. The unit cell dimensions for $FeMoO_4$-II are listed in Table 4.1. The unit cell volume of the high-pressure modification is more than 13 percent smaller than that of the α-$FeMoO_4$ phase and about 19 percent smaller than the β-$FeMoO_4$ phase [59].

Ferric molybdate, $Fe_2(MoO_4)_3$, is an isostructure of the ferric sulphate, $Fe_2(SO_4)_3$, [68, 69] phases. The crystal structure of $Fe_2(MoO_4)_3$ can be commonly represented as an open three-dimensional framework of iron-oxygen-molybdenum linkages in which all iron atoms are octahedrally coordinated by oxygen atoms, with average Fe–O bond distance of 1.992 Å and molybdenum atoms are in rather distorted oxygen tetrahedral, with average Mo–O bond distance of 1.756 Å [58]. Both FeO_6 octahedra and MoO_4 tetrahedra share only vertices with oxygen atoms. Each oxygen atom is linked only to one

FeO_6 octahedron with one MoO_4. Each FeO_6 unit has eight nearest neighbouring FeO_6 units and six next-nearest neighbouring FeO_6 units. It is connected to six different MoO_4 units providing eighteen exchange links Fe–O–Mo–O–Fe to the fourteen neighbouring FeO_6 units and each MoO_4 unit is connected to four different FeO_6 units [70]. This results in a rather open network in which the nearest Fe–Fe distance is 5.03 Å [58].

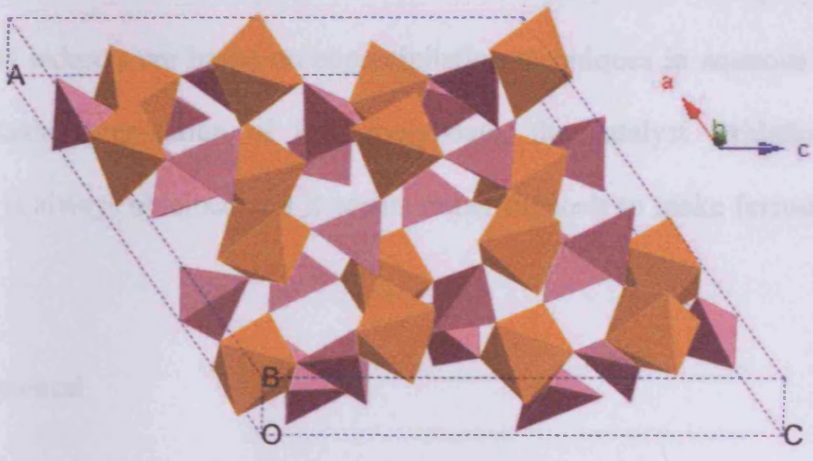

Figure 4.8. Crystal structure of $Fe_2(MoO_4)_3$ with monoclinic structure. The octahedrons around iron ions and the tetrahedrons around molybdenum oxide ions are represented by the brown and purple polyhedrons, respectively. Each vertex of octahedrons and tetrahedrons is occupied by an oxygen ion.

Ferric molybdate exists in two crystalline polymorphs, the monoclinic phase and the orthorhombic β-$Fe_2(MoO_4)_3$ phase [71]. The monoclinic $Fe_2(MoO_4)_3$ crystallises in the space group $P2_1/a$ [68] with a = 15.737(8) Å, b = 9.231(5) Å, c = 18.224(9) Å, and β = 125.46° [71]. The crystal structure of monoclinic $Fe_2(MoO_4)_3$ as determined by Rapposch [58] is represented in Figure 4.8. β-$Fe_2(MoO_4)_3$ crystallises in the orthorhombic structure with cell parameters a = 9.330(3), b = 12.868(5), c = 9.242(3) Å [71] and space group *Pcbn*. Monoclinic $Fe_2(MoO_4)_3$ has also reported to transform reversibly at 499°C [70, 72]

Molybdenum oxide films were grown on the two different single crystal substrates, i.e. silver and iron oxide, by the hot filament metal oxide deposition (HFMOD) technique as described in Chapter 2. A molybdenum filament is supplied with 3.2 A of current. After sufficient outgassing of the filament, the deposition was carried out in oxygen at a pressure of 8×10^{-6} mbar. During the deposition, the sample was at room temperature and its temperature rose by approximately 40 K due to thermal radiation from the filament. Films were also annealed in oxygen pressure of 1×10^{-7} mbar at temperature ranges of 473-973 K.

4.3.2. XPS analysis

The measurements were performed at room temperature by using an EA 125 spectrometer equipped with an aluminium anode. Narrow scans for the Mo 3d, O 1s, Fe 2p, C 1s and Ag 3d regions were recorded. Energy correction was done by using the Au $4f_{7/2}$ peak at 82.8 eV as a reference.

The deconvolution of the XPS spectra into the individual peaks was carried out by a special computer program, CasaXPS version 2.3.10, in which Shirley-type background subtraction was selected, with the following assumptions and constraints:

(i) The shape of lines is Gaussian/Lorentzian;

(ii) The Mo 3d line is deconvoluted using the following constraints:

a. The full width at half maximum (FWHM) of each peak in the doublets was assumed to be the same [78, 79];

b. The splitting energy for the Mo $3d_{5/2}$ – Mo $3d_{3/2}$ doublet was taken at a constant value of 3.2 eV [19, 79, 80];

c. The intensity ratio I($Mo3d_{3/2}$) / I($Mo3d_{5/2}$) for the Mo $3d_{3/2}$ – Mo $3d_{5/2}$ doublet was equal to 0.67 [19, 78, 79, 81].

(iii) O 1s, Ag 3d, and Fe $2p_{3/2}$ (including principal and satellite peaks of Fe $3p_{3/2}$) lines are deconvoluted without any additional constraints.

The deconvolution was reconstructed using an increasing number of individual doublets. Curve fitting resulted in automatic adjustment of the following parameters namely peak position, intensity, and Gaussian/Lorentzian mixing percentage. The spectra were fitted with an 80% Gaussian and 20% Lorentzian peak shape.

Moreover, the surface structure of the films deposited on the substrates was characterised using LEED, LEIS, and STM. All STM measurements were performed in constant current mode at room temperature. Tips were made from electrochemically etched tungsten wire (Goodfellow, 99.95%).

4.4. Results and discussion

4.4.1. The clean surface of iron oxide single crystal

The morphology of the iron oxide surface depends strongly on the surface preparation conditions, e.g. the annealing temperature and the oxygen partial pressure. Although this was already described in Chapter 3, some aspects will be summarised here. The preparation method of iron oxide surface described in this chapter yielded a surface with large terraces shown in Figure 4.9(a). A LEED pattern of the prepared surface exhibits a 2×2 structure with respect to the close-packed oxygen layer which corresponds to the pattern reported previously for a $Fe_3O_4(111)$ surface [82, 83]. It exhibits a set of diffraction spots corresponding to a ~6 Å hexagonal unit cell. In agreement with the LEED pattern, Figure 4.9(b) shows a high-resolution STM image, which reveals the hexagonal pattern of bright protrusions with a 6.2 Å periodicity. The bright protrusions are assigned to the outermost layer iron cations [83, 84]. As shown in Figure 4.9(a), the flat wide terraces separated by steps of about 5 Å in height are observed, which corresponds

into an orthorhombic form by distorting the non-destructive structure of the orthorhombic form into the monoclinic symmetry [58].

Mixed oxide Fe_2O_3-MoO_3 is a well-known catalyst for the commercial oxidation of methanol to formaldehyde [73]. Iron molybdate ($Fe_2(MoO_4)_3$) is likely to be the active phase of Fe_2O_3-MoO_3 mixed oxide catalysts [38, 74-76]. In the industrial preparation, the Mo/Fe atomic ratio is greater than 1.5:1 and a mixture of two phases $Fe_2(MoO_4)_3$ and MoO_3 is present [74, 77]. Most preparations of iron molybdate catalysts in both the laboratory and industry are based on coprecipitation techniques in aqueous phase [75, 77]. In the laboratory preparation of iron molybdate, the catalyst oxidation state (i.e. $Fe_2(MoO_4)_3$) is always obtained and it seems rather difficult to make ferrous molybdate, $FeMoO_4$.

4.3. Experimental

4.3.1. Preparation of molybdenum oxide films as model supports

The experiments described here were performed in the ultrahigh vacuum chamber described in Chapter 2. As was explained there the chamber has a base pressure of 1×10^{-9} mbar. The system is equipped with a system for low energy electron diffraction (LEED) and X-ray photoelectron spectroscopy (XPS), a mass spectrometer, and a scanning tunnelling microscope (STM) which has been described previously. The sample was mounted on a stainless steel sample plate with Ta foil and could be heated from behind by thermal radiation/conduction from a resistive tungsten filament heater.

The iron oxide surface was cleaned by cycles of 600 eV Ar^+-ion sputtering followed by annealing in 1×10^{-7} mbar O_2 at 873 K. Annealing the sample restores the surface structure after sputtering. More details of its preparation are given in Chapter 3. For the Ag(111) substrate, the surface preparation is given in Chapter 2.

to the distance between the equivalent $Fe_3O_4(111)$ surface terminations. The surface defects consisting of the missing protrusions can also be observed in the high-resolution STM image shown in Figure 4.9(b), which are attributed to iron vacancies in the outermost layer according to the density functional theory (DFT) calculations [84]. Hence, the defects in the magnetite structure are iron vacancies and the vacancy in the top layer could expose oxygen anions.

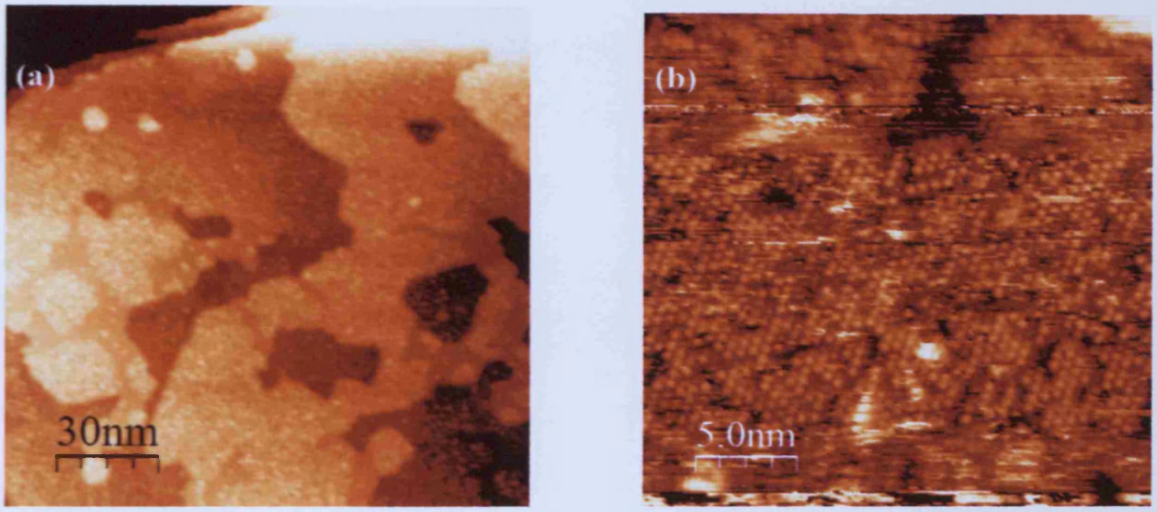

Figure 4.9. STM images of the clean iron oxide surface after sputtering and annealing in 1×10^{-7} mbar of oxygen at 873 K. (a) Large-scale image (1500×1500 Å) in which one can clearly observe individual terraces, separated by single height steps (~5.0 Å). (b) Higher magnification view (250×250 Å) of part of the image in (a). (V_b = -1.0 V, I_t = 0.465 nA)

The (111) surface of magnetite (Fe_3O_4) has a hexagonal (1×1) unit cell with 5.94 Å lattice constant which exposes 0.25 MLE of iron cations above a hexagonal close-packed oxygen layer underneath, as previously determined by LEED analysis [85, 86] and STM images [84]. The hexagonal close-packed oxygen layers in the (111) planes of the bulk Fe_3O_4 has O–O distances of 2.97 Å. Therefore, on the $Fe_3O_4(111)$ surface, the

number of iron cations and oxygen anions are 3.3 and 13.1 per square nanometer, respectively.

4.4.2. Molybdenum oxide films obtained by HFMOD

As described in Chapter 2, the molybdenum oxide films, which were obtained by the hot-filament metal oxide deposition (HFMOD), were deposited on the iron oxide single crystal at the room temperature. The filament heating current, I_F, the oxygen pressure, P_{O2}, and the deposition time, t_d, are the fundamental parameters used to control the molybdenum oxide deposition and their effects were studied.

Figure 4.10 shows the XPS peak intensity as a function of the filament current, I_F, for a constant oxygen pressure, P_{O2}, of 2×10^{-6} mbar and deposition time of 20 min. The molybdenum XPS intensity increased when the filament current increased from 2.8 to 3.0 A and 3.6 to 3.8 A. While molybdenum intensity slightly increase and then decline when the filament current varied from 3.0 to 3.6 A was applied. At the filament current of 3.8 A, the highest molybdenum peak intensity was obtained. This behaviour is explained by using Joule's Law.

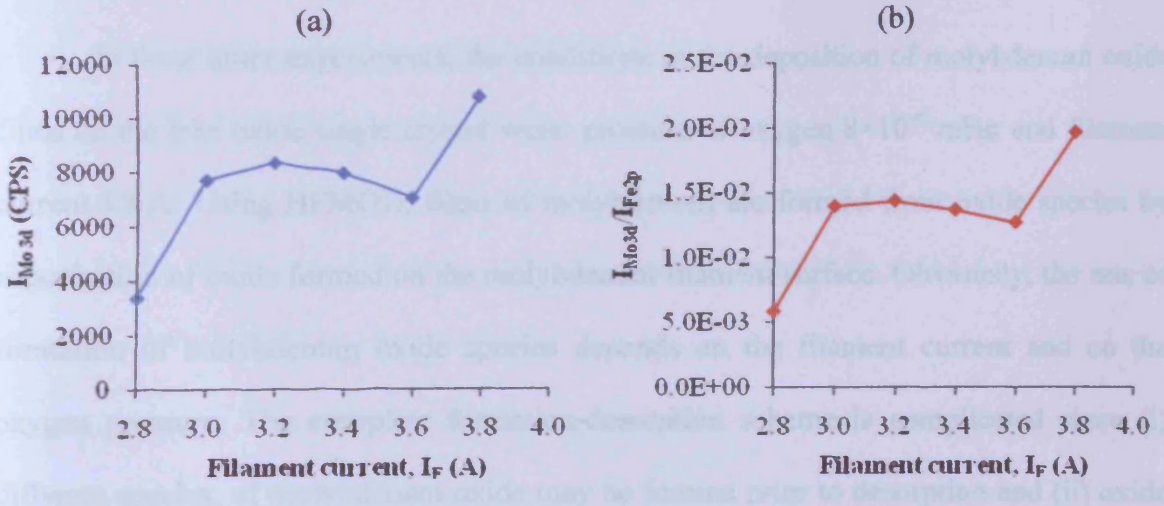

Fig. 4.10. (a) Mo_{3d} intensity and (b) Mo_{3d}/Fe_{2p} intensity ratio as the function of the filament heating current. Total pressure of oxygen: 2×10^{-6} mbar. Time: 20 min.

In a series of depositions in which the filament current and the deposition time was kept constant at 3.8 A and 20 min respectively, the XPS intensity of molybdenum oxide was measured as a function of the total pressure of oxygen. The results are depicted in Figure 4.11, revealing a near-linear increase in the molybdenum intensity with increasing the total pressure of oxygen.

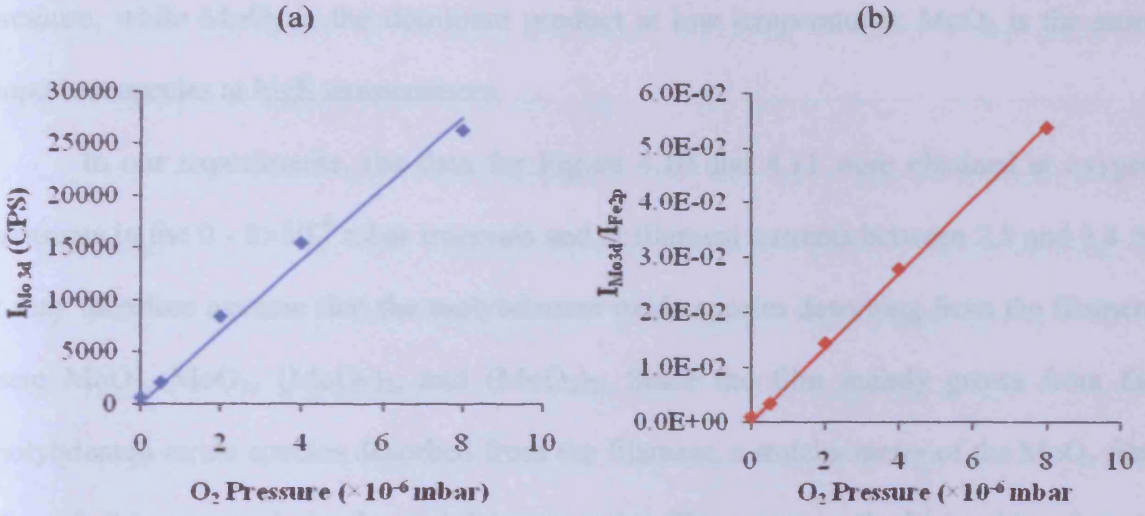

Figure 4.11. (a) Mo_{3d} intensity and (b) Mo_{3d}/Fe_{2p} intensity ratio PS peak intensity as the function of the total pressure of oxygen. Filament current: 3.8 A. Time: 20 min.

In these latter experiments, the conditions of the deposition of molybdenum oxide films on the iron oxide single crystal were: pressure of oxygen 8×10^{-6} mbar and filament current 3.8 A. Using HFMOD, films of molybdenum are formed from oxide species by vaporisation of oxide formed on the molybdenum filament surface. Obviously, the rate of formation of molybdenum oxide species depends on the filament current and on the oxygen pressure. The complete formation-desorption scheme is complicated since (i) different species of molybdenum oxide may be formed prior to desorption and (ii) oxide species with different stoichiometries may be present in the vapour flux, some resulting from dissociation of the species originally formed [87].

In oxidising atmosphere, molybdenum begins to sublime forming a molybdenum trioxide above 800 K [88]. Berkowitz-Mattuck et al. [89] studied the molybdenum oxide species desorbing from a molybdenum surface heated at temperatures between 1500 and 2600 K in an oxygen pressures between 10^{-4} and 10^{-2} mbar using a mass spectrometer. The gas-phase species MoO_2, MoO_3, $(MoO_3)_2$, and $(MoO_3)_3$ were observed. Polymeric oxides, $(MoO_3)_2$ and $(MoO_3)_2$ were formed at the low temperature and high oxygen pressure, while MoO_3 is the dominant product at low temperatures; MoO_2 is the more important species at high temperatures.

In our experiments, the data for Figure 4.10 and 4.11 were obtained at oxygen pressures in the 0 - 8×10^{-6} mbar intervals and at filament currents between 2.8 and 3.8 A. It may therefore assume that the molybdenum oxide species desorbing from the filament were MoO_3, MoO_2, $(MoO_3)_2$, and $(MoO_3)_2$. Since the film mainly grows from the molybdenum oxide species desorbed from the filament, a stoichiometry of the MoO_x film of x = 2–3 is expected. As the molybdenum oxide film grows on the iron oxide substrate in an oxygen atmosphere, however, the chemical incorporation of oxygen atoms from O_2 and iron oxide into the molybdenum oxide film is possible, forming new Mo–O bonds, which may further increase x to values closer to 3.

In order to work out the coverage, a constant flux of molybdenum oxide vapour from a molybdenum filament and a uniform oxide layer growth are assumed. Therefore, the thickness of the molybdenum oxide films can calculated from the Fe 2p intensity decay by applied the following equation:

$$\frac{I}{I_0} = \exp\left[-\frac{d}{\lambda\cos\theta}\right] \qquad (4.1)$$

where I is the intensity of the Fe 2p after molybdenum oxide deposition, I_0 is the intensity of the Fe 2p from the clean iron oxide substrate, λ is the inelastic mean free path (IMFP),

d is the obtained thickness of the film and θ is the angle between the surface normal and the direction of electron detection.

The IMFP has been calculated using a predictive IMFP formula (designated TPP-2M) by Tanuma et al. [90, 91], see more detail in Appendix C. Since the Fe $2p_{3/2}$ binding energy of the samples after the formation of the molybdenum oxide film is around 710.6 eV, its kinetic energy, using Al Kα radiation as an excitation source, is 776.0 eV. At this kinetic energy, the IMFP of Fe $2p_{3/2}$ calculated according to the TPP-2M predictive equation is approximately 1.65 nm. In order to determine the average number of monolayers, the thickness of the molybdenum oxide film was divided by the thickness of one monolayer of molybdenum oxide. From high resolution STM data, as discussed in section 4.4.5.4, they reveal that MoO_3 on $Fe_3O_4(111)$ form a single-layer structure which differs from the bi-layer structure of bulk MoO_3 [92]. The single-layer MoO_3 islands exhibit a height of approximately 0.3 nm. The film thickness and the number of monolayer as a function of the deposition time is shown in Figure 4.12(a) and 4.12(b). They increase continuously with the increase in the deposition time. The growth mode of molybdenum oxide deposition was described latter.

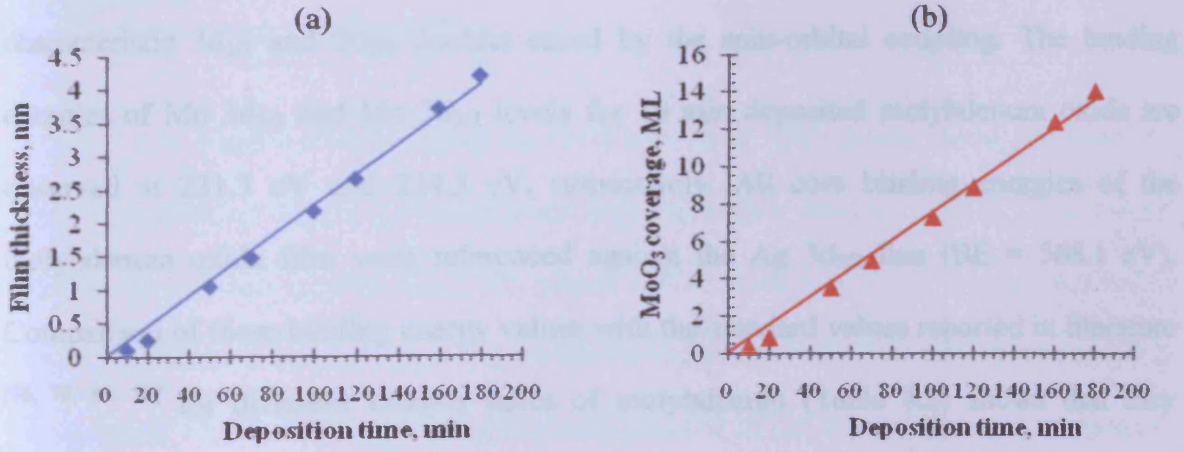

Fig 4.12. (a) The film thickness and (b) MoO_3 coverage as a function of the deposition time. Filament current: 3.8 A. Oxygen pressure: 8.0×10^{-6} mbar.

4.4.3. Growth of molybdenum oxide films

The growth of molybdenum oxide was studied in some detail on $Fe_3O_4(111)$ at room temperature by hot filament metal oxide deposition technique (HFMOD). To help with the interpretation of these data, we also carried out measurements on Ag(111).

4.4.3.1. MoO_x/Ag(111)

In order to investigate the surface structure of the molybdenum oxide films fabricated using HFMOD, Ag(111) is chosen as a substrate since it can be considered as chemically inert. No detectable reactions take place at given preparation conditions. In addition, the Ag(111) substrate is well matched to the iron oxide substrate since the surface lattice constant of bulk Ag(111) (2.89 Å) is not much different from that of iron oxide (3.04 Å, 2.90 Å, and 2.97 Å for FeO, α-Fe_2O_3, and Fe_3O_4 respectively) [97].

The Mo 3d, Ag 3d, and O 1s core-level XPS spectra were recorded before and after molybdenum oxide deposition at room temperature and different intervals. The XPS of the Mo 3d energy region of the silver substrate before and following the depositions of molybdenum oxide in oxygen pressure of 1×10^{-7} mbar at room temperature as a function of deposition time is shown in Figure 4.13. The molybdenum oxide spectra exhibit the characteristic $3d_{5/2}$ and $3d_{3/2}$ doublet cased by the spin-orbital coupling. The binding energies of Mo $3d_{5/2}$ and Mo $3d_{3/2}$ levels for 10 min deposited molybdenum oxide are observed at 231.3 eV and 234.3 eV, respectively. All core binding energies of the molybdenum oxide film were referenced against the Ag $3d_{5/2}$ line (BE = 368.1 eV). Comparison of these binding energy values with the standard values reported in literature [46, 78, 93, 98] for different valence states of molybdenum (Table 4.2) shows that they correspond to the values of Mo^{5+} ions in the lattice. The results of XPS studies suggest that molybdenum is present mainly in +5 oxidation state or probably a 50-50 mixture of MoO_3 and MoO_2. The binding energies of Mo 3d, O 1s, and Ag 3d as obtained by XPS

core level spectra for the sample deposited for different deposition time periods are shown in Table 4.3. As the deposition time increases, the peak positions of Mo $3d_{5/2}$ and Mo $3d_{3/2}$ do not shift appreciably, as shown in Figure 4.13.

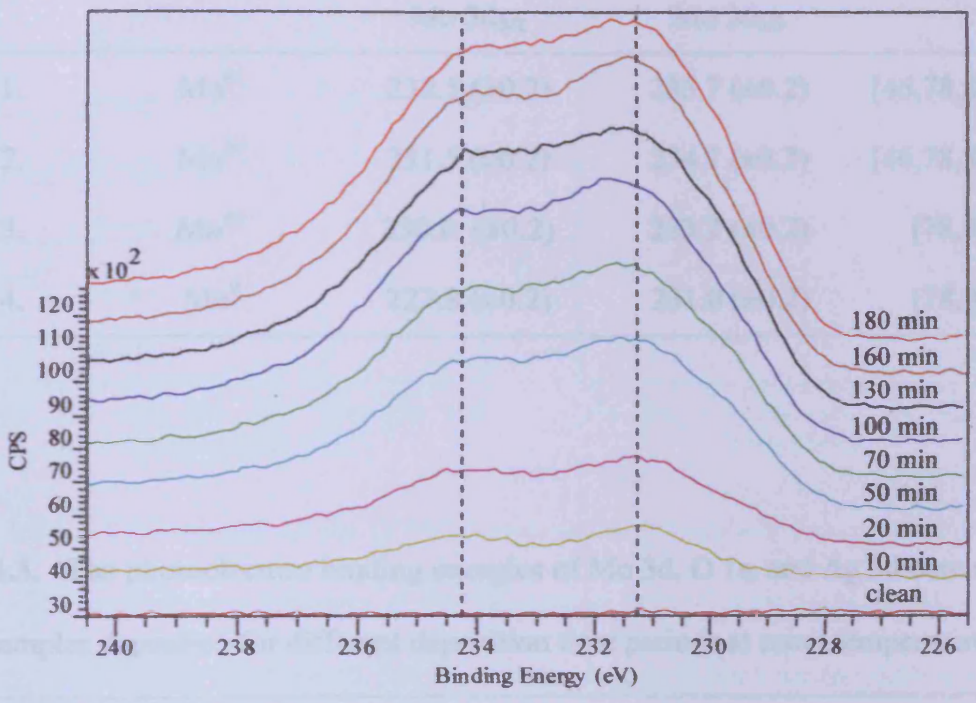

Figure 4.13. Mo 3d XPS spectra of MoO_x/Ag(111) as a function of the deposition time with the clean Ag(111) surface spectrum at the bottom. Vertical dashed lines are to guide the eyes for the peak position shifts.

Figure 4.14(a) shows the O 1s core-level XPS spectra of the molybdenum oxide deposited on Ag(111) for different deposition time periods. The O 1s core-level binding energy was around 530.5 eV which is the characteristic of oxygen bonded to metal. This value is in good agreement with the values reported for molybdenum oxide in the literature [46, 98]. With increasing the molybdenum oxide deposition time, an increase in intensity of the O 1s signal is observed but the O 1s peak position remains nearly unchanged.

Table 4.2. Photoelectron binding energies of Mo 3d core level electrons of various oxidation states present in the deposited films compared to the values of corresponding states reported in literature.

Serial No.	Oxidation state	Standard (reported) values (in eV) for		References
		Mo $3d_{5/2}$	Mo $3d_{3/2}$	
1.	Mo^{6+}	232.5 (±0.2)	235.7 (±0.2)	[46,78,88,93]
2.	Mo^{5+}	231.5 (±0.2)	234.7 (±0.2)	[46,78,88,93]
3.	Mo^{4+}	230.0 (±0.2)	233.2 (±0.2)	[78,88]
4.	Mo^{0}	227.8 (±0.2)	231.0 (±0.2)	[78,93]

Table 4.3. The photoelectron binding energies of Mo 3d, O 1s, and Ag 3d core electrons of the samples deposited for different deposition time periods at room temperature.

MoO_x deposition time (min)	Mo $3d_{5/2}$ (eV)	Mo $3d_{3/2}$ (eV)	O 1s (eV)	Ag $3d_{5/2}$ (eV)	Ag $3d_{3/2}$ (eV)
0 (clean surface)	-	-	-	368.1	374.1
10	231.2	234.4	530.4	368.1	374.1
20	231.1	234.3	530.3	368.1	374.1
50	231.1	234.3	530.5	368.1	374.1
70	231.1	234.3	530.4	368.1	374.1
100	231.2	234.4	530.4	368.1	374.1
130	231.1	234.3	530.4	368.1	374.1
160	231.2	234.4	530.3	368.1	374.1
180	231.1	234.3	530.4	368.1	374.1

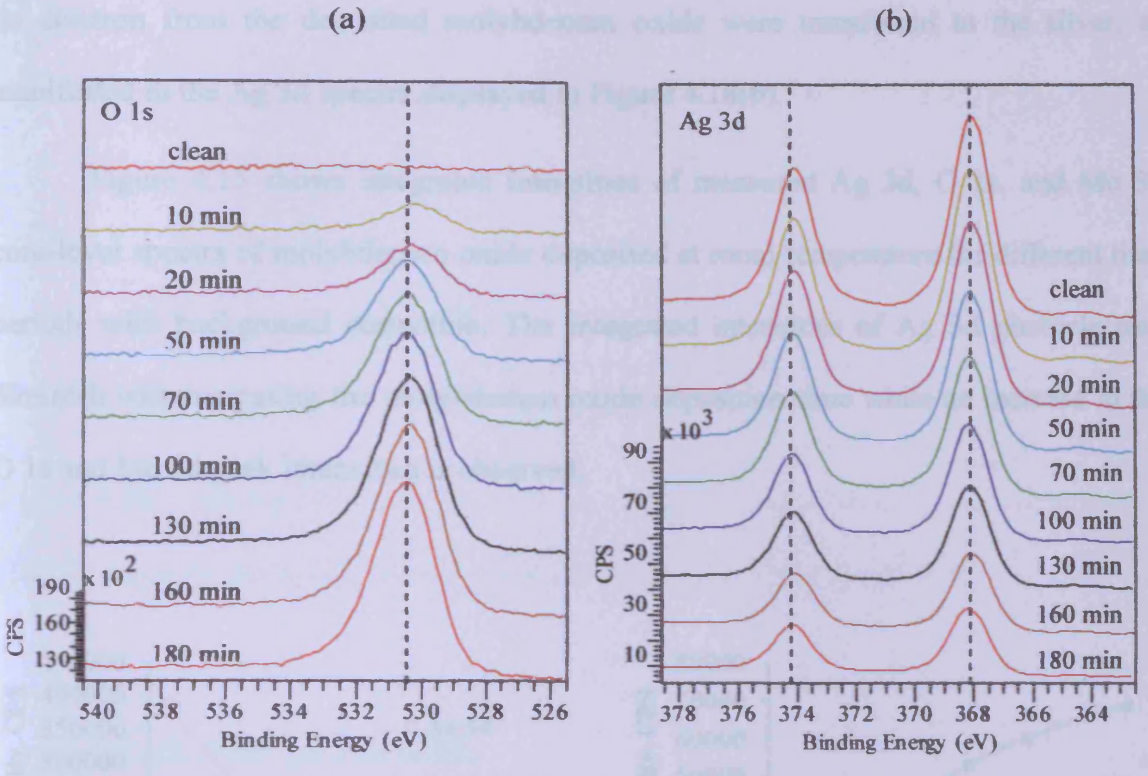

Figure 4.14. XPS spectra of the O 1s (a) and Ag 3d (b) regions for molybdenum oxide on a Ag(111) surface as a function of the deposition time of molybdenum oxide with the clean Ag(111) surface spectrum at the top. Vertical dashed lines are to guide the eyes for the peak position shifts.

Figure 4.14(b) presents a series of the Ag 3d core-level spectra obtained at different molybdenum oxide deposition time periods as indicated in the figure. In Figure 4.14(b), pure silver and molybdenum oxide supported on silver substrate show similar Ag $3d_{5/2}$ binding energy values around 368.1 eV. The binding energies of Ag $3d_{5/2}$ and Ag $3d_{3/2}$ for the samples at different deposition time periods, reported in Table 4.3, remains nearly unshifted with increasing the molybdenum oxide deposition times. since the literatures report the binding energy values of 368.0-368.3 eV, 367.3-367.4 eV, and 367.6-367.8 eV for pure silver, AgO, and Ag_2O, respectively [99-101], it is concluded that

no electron from the deposited molybdenum oxide were transferred to the silver, as manifested in the Ag 3d spectra displayed in Figure 4.18(b).

Figure 4.15 shows integrated intensities of measured Ag 3d, O 1s, and Mo 3d core-level spectra of molybdenum oxide deposited at room temperature for different time periods with background correction. The integrated intensities of Ag 3d photoelectron diminish with increasing the molybdenum oxide deposition time while an increase in the O 1s and Mo 3d peak intensities is observed.

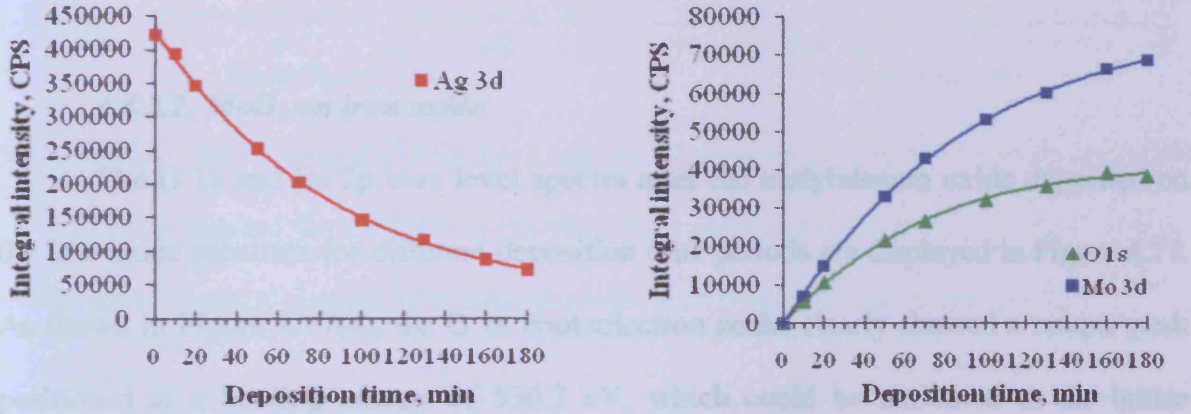

Figure 4.15. Integrated intensities of Mo 3d, Ag 3d, and O 1s spectra as function of the deposition time. Solid lines represent fitting result for changes of Mo 3d, Ag 3d, and O 1s intensities caused by the molybdenum oxide film growth.

Figure 4.16 shows the curve of the Mo 3d to Ag 3d peak intensity ratio as a function of the deposition time on the Ag(111) surface at room temperature. As shown in Figure 4.16, an increase in the peak intensity ratio of Mo 3d to Ag 3d with increasing deposition time is observed.

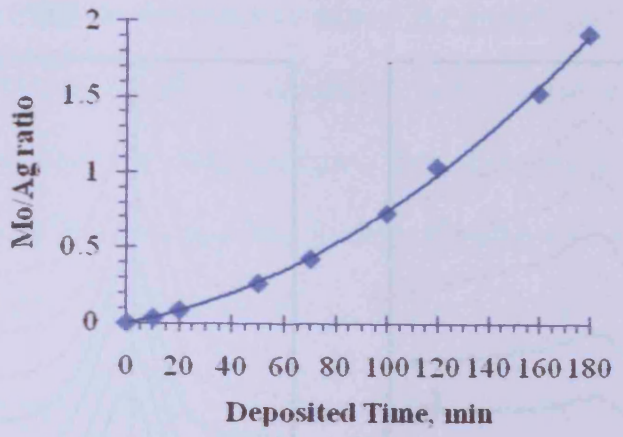

Figure 4.16. Mo/Ag XPS intensity ratio as a function of molybdenum oxide deposition time for stepwise deposition of molybdenum oxide onto Ag(111) substrate.

4.4.3.2. MoO_x on iron oxide

The O 1s and Fe 2p core level spectra after the molybdenum oxide deposited on the iron oxide substrate for different deposition time periods are displayed in Figure 4.17. As shown in Figure 4.17(a), the O 1s photoelectron peaks clearly showed a unique peak positioned at a binding energy of 530.2 eV, which could be attributed to the lattice oxygen of both iron oxide and molybdenum oxide. During a long deposition period, the binding energy of O 1s remained practically constant. Figure 4.17(b) shows the binding energies of Fe 2p photoelectron peaks at 710.1 and 724.0 eV for Fe $2p_{3/2}$ and Fe $2p_{1/2}$ lines, respectively. As manifest in the Fe 2p spectra shown in Figure 4.17(b), the longer deposition time (180 min) causes the Fe 2p overall peak maxima to shift downward in binding energy, to broaden and its spectral intensities to reduce. This may indicate that donated electron from the deposited molybdenum oxide were transferred to the iron. This subsequently decreases the average oxidation state of the iron. As the molybdenum oxide coverage increases, the contribution from the Fe^{2+} ions increases.

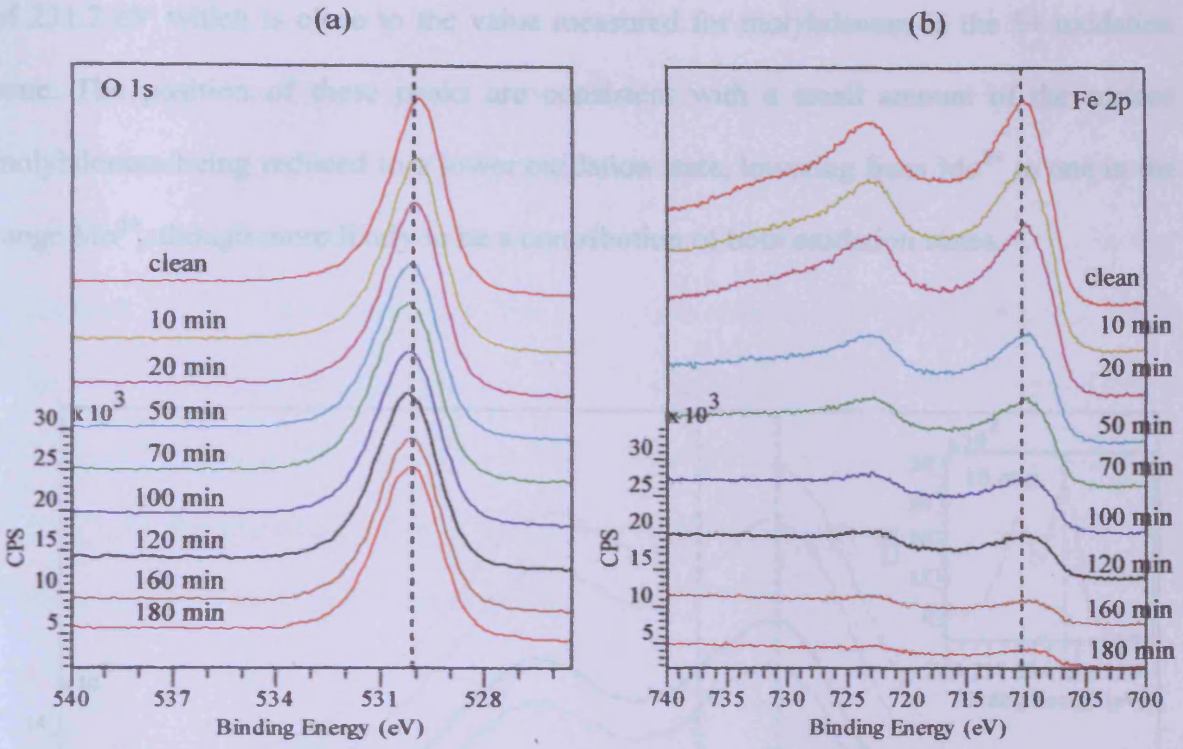

Figure 4.17. (a) O 1s and (b) Fe 2p X-ray photoelectron spectra of molybdenum oxide on iron oxide surface for different deposition time periods of molybdenum oxide at room temperature. Vertical dashed line is to guide the eyes for small peak position shifts.

In Figure 4.18, XPS spectra of the Mo 3d levels are presented as a function of the deposition time. The experimental data clearly shows the characteristic Mo 3d doublet, composed of the $3d_{5/2}$ and $3d_{3/2}$ levels produced by spin-orbit coupling. Obviously, the peak shape and the binding energy of Mo 3d spectra varied with the deposition time. The binding energy of Mo $3d_{5/2}$ was 232.2 eV for a short deposition time, which is close to the molybdenum in the 6+ oxidation state (Mo^{4+} at 229.2-230.1 eV [93], Mo^{5+} at 231.2-231.5 eV [44, 93-95] and Mo^{6+} at 232.1-232.6 eV [93, 96]). As the deposition time increases, there is a shift to lower binding energy (~1.0 eV). These results imply that molybdenum is in the 6+ state for a coverage of a few monolayers, but shifts to lower oxidation state at high coverages. At 180 min deposition time, the Mo $3d_{5/2}$ peak appears with a binding energy

of 231.2 eV which is close to the value measured for molybdenum in the 5+ oxidation state. The position of these peaks are consistent with a small amount of the surface molybdenum being reduced to a lower oxidation state, lowering from Mo^{6+} to one in the range Mo^{5+}, though more likely to be a contribution of both oxidation states.

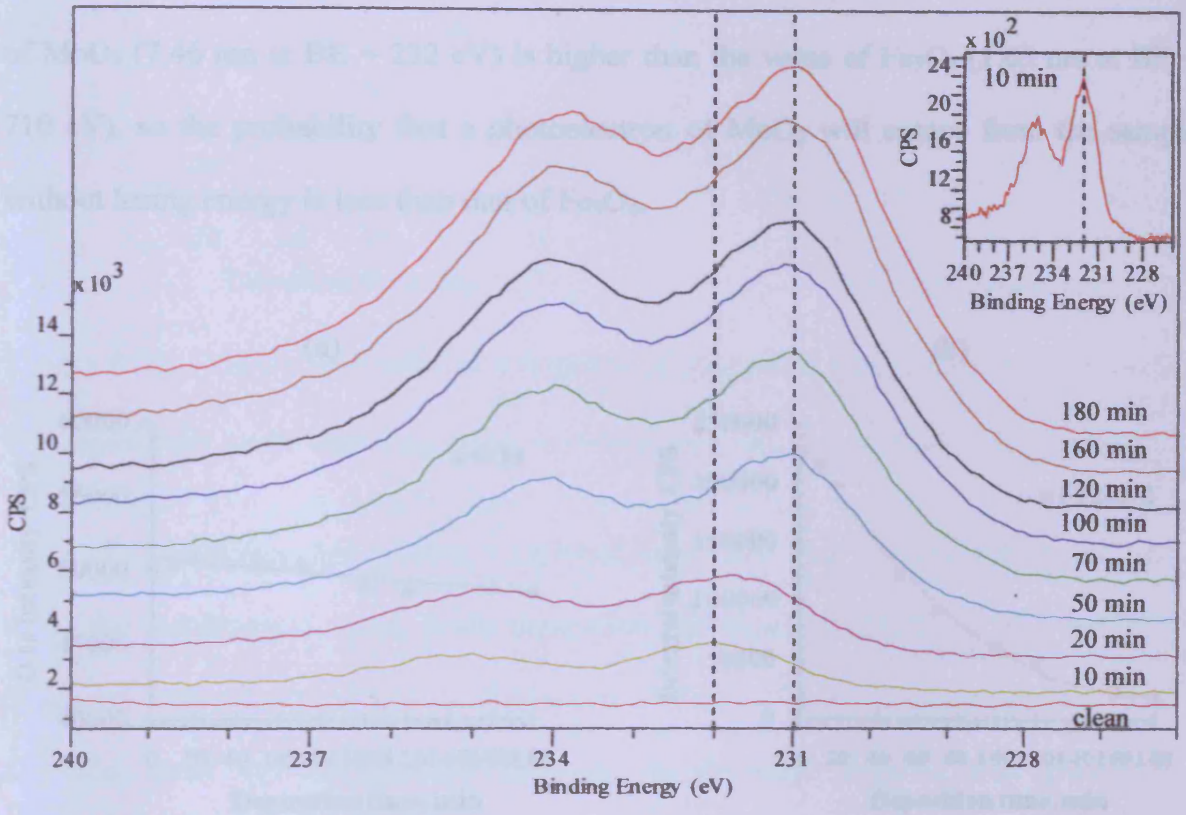

Figure 4.18. Change of Mo 3d XP spectra for molybdenum oxide on iron oxide surface as a function of molybdenum oxide deposition time with the clean iron oxide surface spectrum at the bottom. Vertical dashed line is to guide the eyes for peak position shifts. The inset shows Mo 3d spectrum obtained after 10 min molybdenum oxide deposition.

The integral intensities of measured O 1s and Fe $2p_{3/2}$ spectra (by peak area after subtraction of a Shirley-type background) as a function of the total deposition time are plotted in Figure 4.19. The increase of MoO_3 coverage, as shown in Figure 4.12(b), at the

cost of the Fe $2p_{3/2}$ intensity can clearly be seen while the intensity of O 1s slightly decrease. In fact, the detected photoelectron intensity depends on the number of atoms in the volume element and the IMFP. Therefore, the result for the decrease in intensity of O 1s may be due to the oxygen atom density of the molybdenum oxide film is less than that of the bulk Fe_3O_4 (~54 O atom nm^{-3}) and the oxygen atom density of bulk MoO_3 is ~57 O atom nm^{-3}. Moreover, according to the TPP-2M predictive equation, the calculated IMFP of MoO_3 (7.46 nm at BE = 232 eV) is higher than the value of Fe_3O_4 (1.65 nm at BE = 710 eV), so the probability that a photoelectron of MoO_3 will escape from the sample without losing energy is less than that of Fe_3O_4.

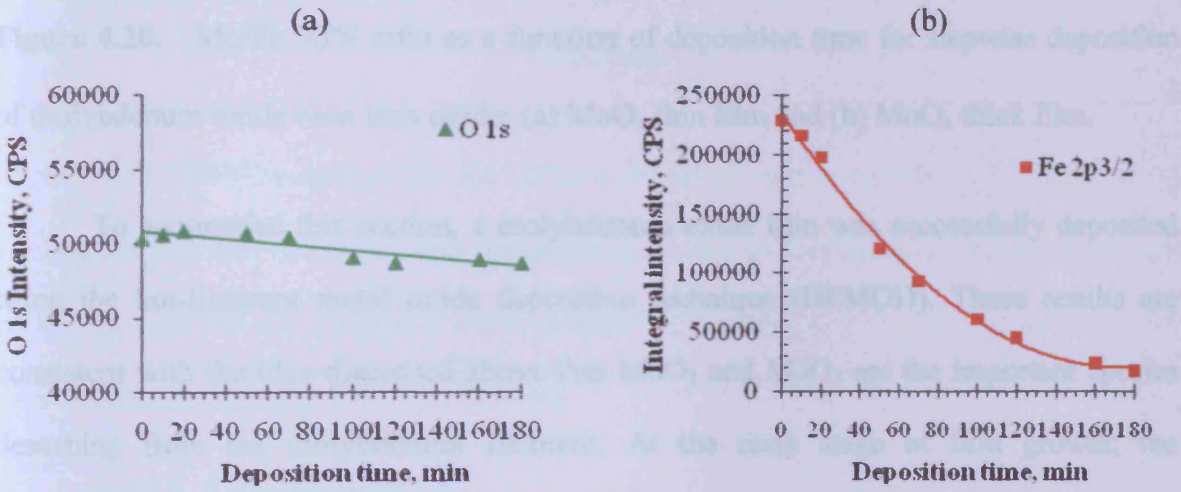

Figure 4.19. Integral intensities of XPS O 1s (a) and Fe $2p_{3/2}$ (b) peaks as a function of deposition time. Solid lines represent fitting result for changes of O1s and Fe $2p_{3/2}$ intensities caused by the molybdenum oxide film growth.

Figure 4.20 shows the XPS intensity ratio of Mo 3d to Fe 2p versus the deposition time. The Mo/Fe XPS intensity ratio increases regularly with the deposition time. The Mo/Fe intensity ratio shows a linear increase during the first stages of the deposition. It can be seen the break points in the Mo/Fe XPS data at approximately 27 and 105 min in

Figure 4.18(a) and 4.18(b), respectively. As shown in Figure 4.20(b), the linear increase of Mo/Fe XPS intensity ratio sharply increases at 105 min.

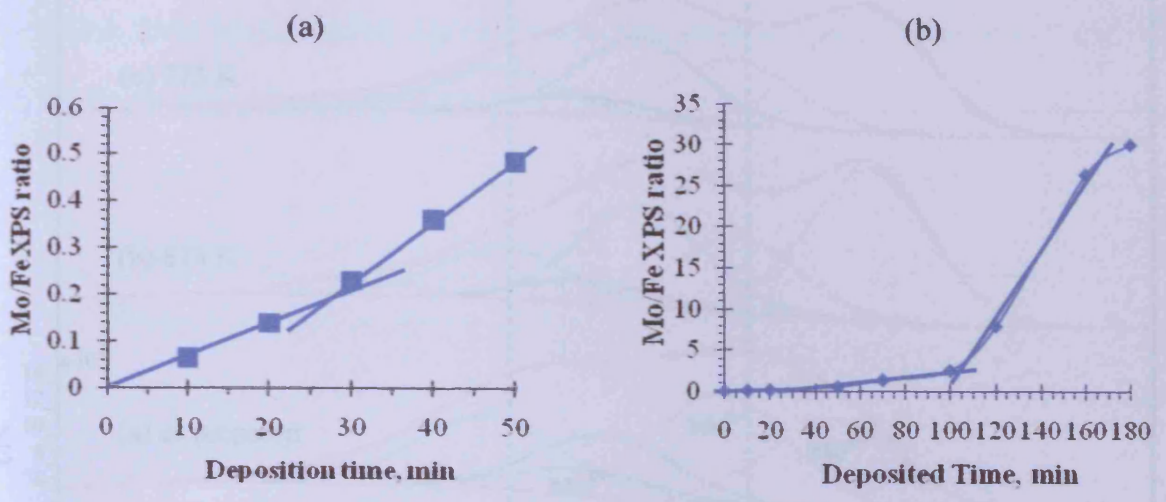

Figure 4.20. Mo/Fe XPS ratio as a function of deposition time for stepwise deposition of molybdenum oxide onto iron oxide: (a) MoO_x thin film and (b) MoO_x thick film.

To summarise this section, a molybdenum oxide film was successfully deposited using the hot-filament metal oxide deposition technique (HFMOD). These results are consistent with the idea discussed above that MoO_2 and MoO_3 are the important species desorbing from the molybdenum filament. At the early stage of film growth, the deposited molybdenum oxide is oxidised to Mo^{6+} after donating electrons to the substrate. The electron transfer also causes some reduction of the substrate iron ion from a 3+ to 2+ oxidation state.

4.4.4. Effect of annealing treatments

Annealing temperature is an important variable which affects the speciation of molybdenum oxide on silver and iron oxide surfaces.

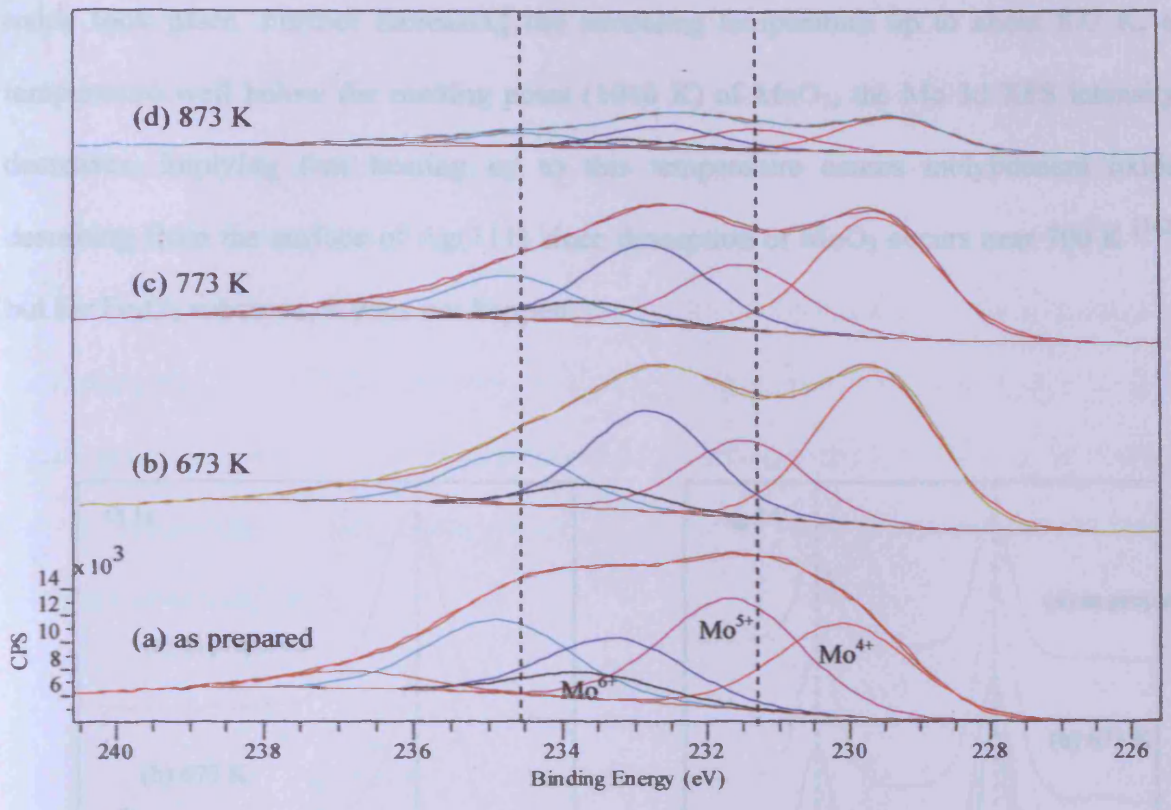

Figure 4.21. XPS spectra of the Mo 3d photoemission lines recorded for $\theta = 90°$ for: (a) the Ag(111) surface after 180 min molybdenum oxide deposition; (b) after a subsequent annealing at 673 K for 15 min; (c) after a second annealing at 773 K for 15 min; and (d) after a third annealing at 873 K for 15 min.

4.4.4.1. MoO_x/Ag(111)

Figure 4.21 shows a series of the Mo 3d XPS spectra taken from the surface heated to the indicated temperatures after molybdenum oxide deposition at room temperature under the oxygen pressure of 8.0×10^{-6} mbar. The binding energy of 231.0 eV of the Mo $3d_{5/2}$ peak at room temperature is close to the molybdenum in the 5+ oxidation state. The binding energy of the Mo 3d doublet changes at higher annealing temperature. At a higher annealing temperature, the binding energy of the Mo 3d doublet is strongly shifted (~2 eV) towards lower binding energy and becomes closer to that of Mo^{4+} species. The continuous shift of the binding energy indicates that partial reduction of molybdenum

oxide took place. Further increasing the annealing temperature up to about 873 K, a temperature well below the melting point (1068 K) of MoO_3, the Mo 3d XPS intensity decreases, implying that heating up to this temperature causes molybdenum oxide desorbing from the surface of Ag(111) since desorption of MoO_3 occurs near 700 K [102] but for Fe_3O_4 substrate, it does not happen.

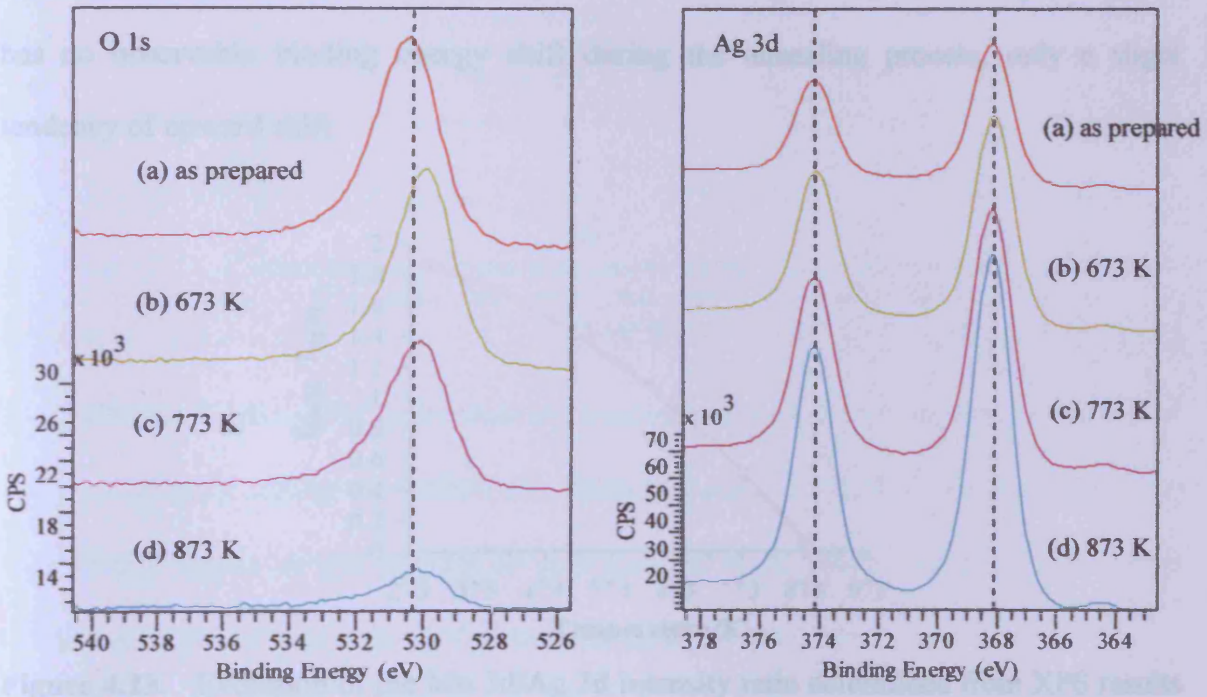

Figure 4.22. XPS spectra of O 1s and Ag 3d obtained after 180 min of the molybdenum oxide dosing. The spectrum (a) is taken after the formation of molybdenum oxide without further annealing. The bottom three spectra are obtained after annealing for 30 min at: (b) 673 K, (c) 773 K, and (d) 873 K. Vertical dashed lines are to guide the eyes for the small peak position shifts.

Figure 4.22 shows the O 1s and Ag 3d XPS spectra of the molybdenum oxide on Ag(111) substrate as a function of annealing temperature. The O 1s binding energy as defined by the peak maximum is 530.4 eV characteristic of oxygen bonded to metal.

Upon heating the sample to 673 K, the binding energy of the O 1s shifted to 530.0 eV. Further treatment at higher temperature causes small position changes (~0.2 eV) for the O 1s. Above 873 K, the peak intensity of the O 1s became very small, but it was not completely eliminated. When the Ag(111) substrate was exposed to the molybdenum oxide, the adsorption layer hinders the photoemission of the underlying silver, drastically decreasing the Ag 3d XPS intensity. With increasing sample temperature, Ag 3d XPS signal grows in intensity, due to desorption of the adsorption layer. The Ag 3d doublet has no observable binding energy shift during the annealing process, only a slight tendency of upward shift.

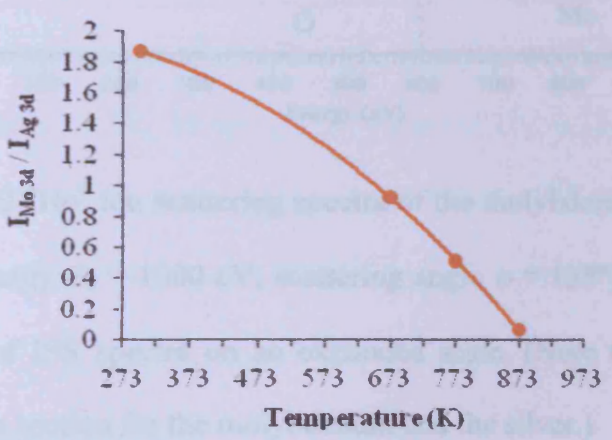

Figure 4.23. Evolution of the Mo 3d/Ag 3d intensity ratio determined from XPS results as a function of the annealing temperature for iron oxide surface covered with thick molybdenum oxide deposit.

Figure 4.23 shows the variation of XPS I_{Mo3d}/I_{Ag3d} intensity ratio as a function of annealing temperature. A decrease in XPS I_{Mo3d}/I_{Ag3d} intensity ratio with increasing annealing temperature is observed. At higher annealing temperatures (873 K), the XPS integral intensity ratio of Mo 3d to Ag 3d is near zero.

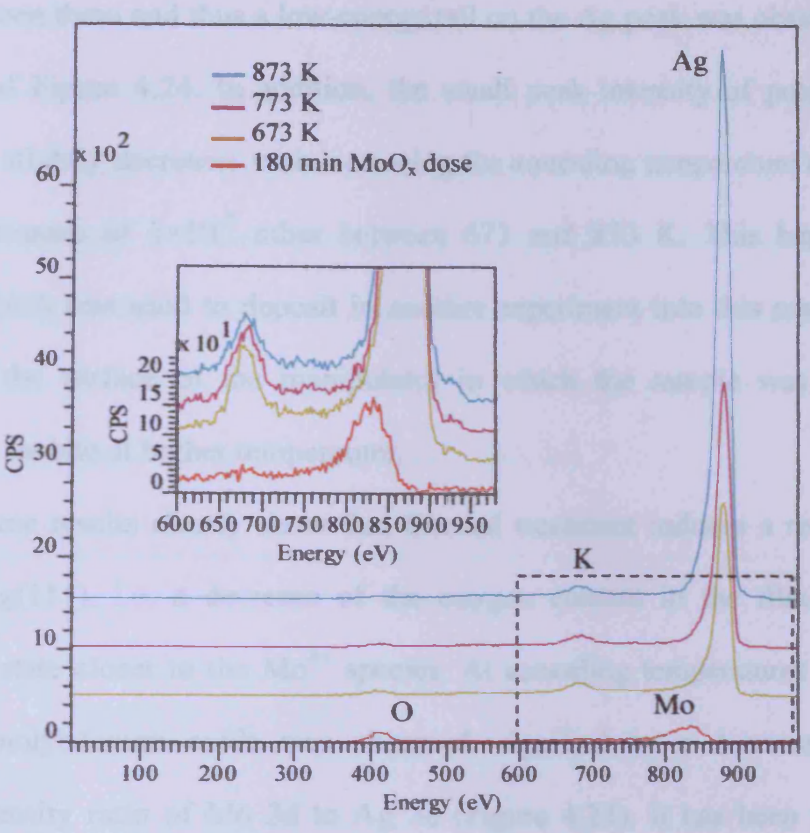

Figure 4.24. Typical $^4He^+$ ion scattering spectra of the molybdenum oxide on the clean Ag(111) (primary energy E_0 = 1000 eV; scattering angle υ = 135°). The inset shows the high energy region of ISS spectra on an expanded scale. (Note that there is the huge difference in the cross section for the molybdenum and the silver.)

The energy spectra of ions scattered from the molybdenum oxide films on the clean Ag(111) surface under 1 keV He^+ bombardments at room temperature is illustrated in Figure 4.24. This spectra exhibited the peaks of silver, molybdenum, potassium, and oxygen at energy in good agreements with the energy positions expected from the binary-collision [103], E_1(Ag), E_2(Mo), E_3(K), and E_4(O), respectively. In agreement with the XPS spectra of Figure 4.21 and 4.22, the LEIS spectra of Figure 4.24 show the distinct increase of the peak intensity of silver peak with increasing the annealing temperature meanwhile the peak intensity of scattering oxygen decreases; the peak of scattering from molybdenum is merged together with the scattering Ag peak due to a very close energy

position between them and thus a low-energy tail on the Ag peak was observed as shown in the inset of Figure 4.24. In addition, the small peak intensity of potassium can be observed and slightly decreases with increasing the annealing temperature after annealing in oxygen pressure of 1×10^{-7} mbar between 673 and 873 K. This happens because potassium, which was used to deposit in another experiment into this machine, may be absorbed on the surface of the manipulator in which the sample was mounted and becomes very mobile at higher temperature.

All these results clearly show that thermal treatment induces a reduction of the deposit on Ag(111), i.e. a decrease of the oxygen content in the film, leading to a molybdenum state closer to the Mo^{4+} species. At annealing temperatures above 800 K, the loss of molybdenum oxide was observed, signified by a decrease in the XPS integrated intensity ratio of Mo 3d to Ag 3d (Figure 4.23). It has been suggested that molybdenum oxide desorbs at temperatures above 700 K [102]. The loss mechanism is unknown, but is presumed to be the evaporation of a molybdenum oxide species, probably MoO_2.

4.4.4.2. MoO_x on iron oxide

The effect of annealing temperature on thin and thicker films of molybdenum oxide prepared on the iron oxide surface was studied. After 180 minutes of the molybdenum oxide dosage, a ~14 monolayer equivalent (MLE) molybdenum oxide thick film was prepared. The Mo 3d photoelectron spectra for this thick film obtained after annealing in the presence of 1×10^{-7} mbar of oxygen at different temperatures are illustrated in Figure 4.25. This figure clearly shows that there are significant differences in the local electronic environment of the surface molybdenum species at different temperatures. Annealing at 873 K has a dramatic effect on the Mo 3d spectrum compared with the initial situation. The broadening of the Mo 3d feature is clearly noticeable

accompanied with the evolution of a peak at about a binding energy of 232 eV. The deconvolution of the Mo 3d peak (see Figure 4.25) presented three contributions. The new contribution, located at 229.4 eV, was appeared corresponding to the Mo^{4+}. This shift of binding energy indicates the reduction of molybdenum ions. After annealing the film to 973 K (see Figure 4.25), the presence of the Mo 3d XP spectrum with $3d_{5/2}$ centred at 232.1 eV can be distinctly noticed. A shoulder at lower binding energy indicates the presence of a small amount of Mo^{4+} species.

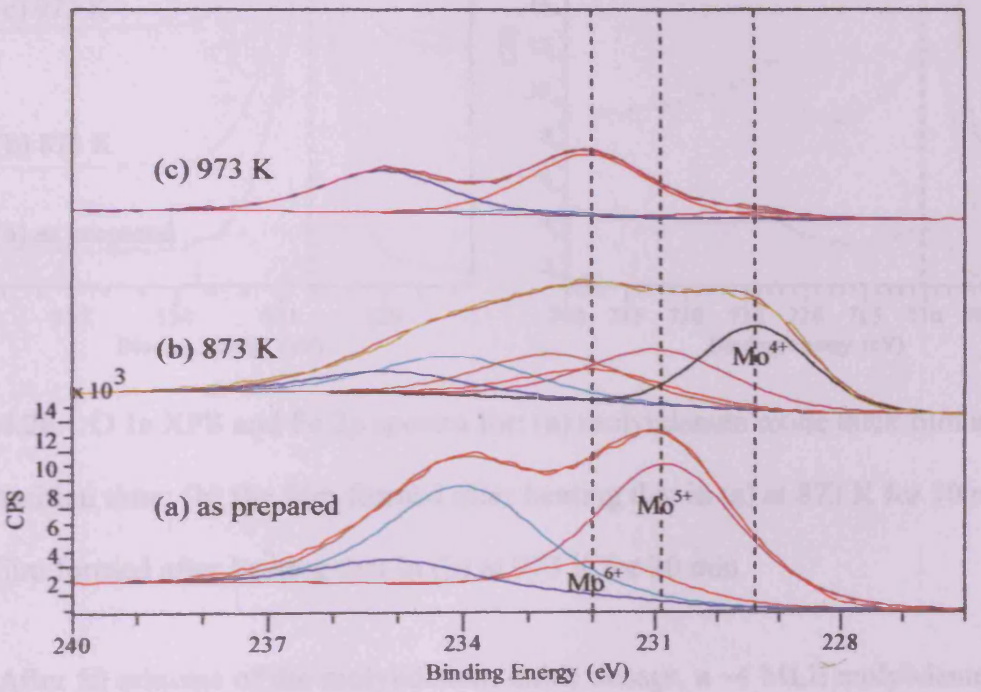

Figure 4.25. Mo 3d XPS spectra for: (a) molybdenum oxide thick film on iron oxide substrate after 180 min deposition time; (b) the film formed after heating that in (a) at 873 K for 30 min; and (c) the film formed after heating that in (b) at 973 K for 30 min.

Figure 4.26 shows the O 1s and Fe 2p core level spectra of the molybdenum oxide on $Fe_3O_4(111)$ as a function of annealing temperature. With increasing the annealing temperature, the shift of the binding energy of O 1s was not observed while the Fe 2p binding energy is shifted to higher value. The increase in the intensity of Fe 2p core level

spectra was also observed with increasing the annealing temperature but for the O 1s, it did not change significantly.

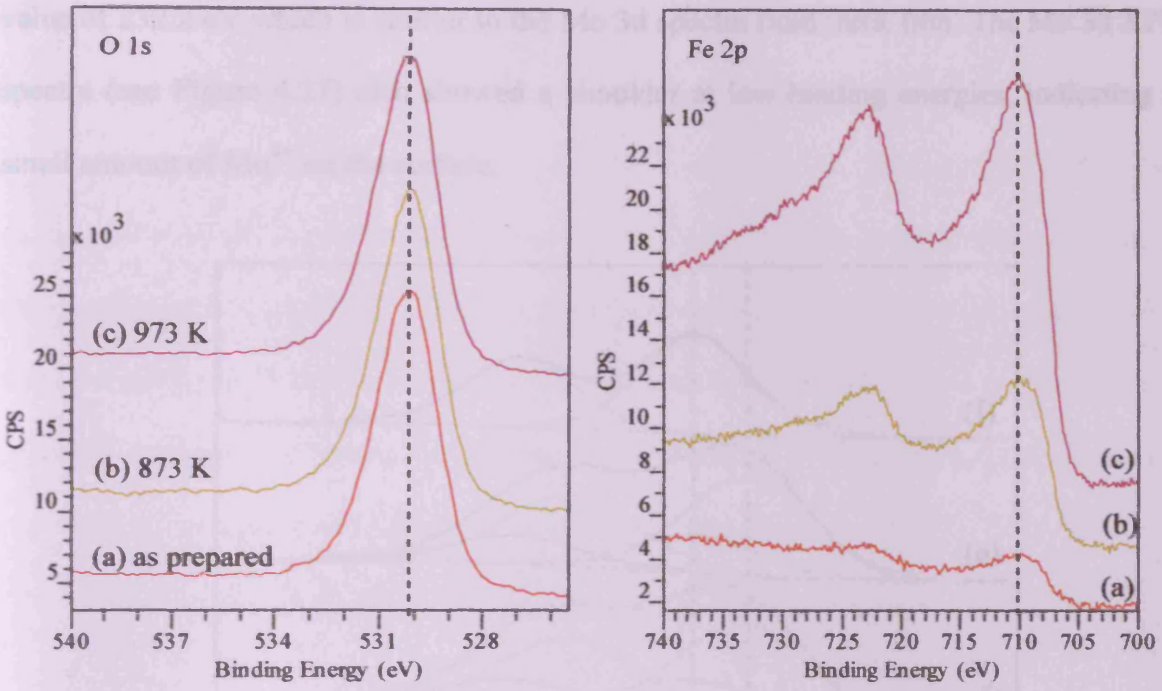

Figure 4.26. O 1s XPS and Fe 2p spectra for: (a) molybdenum oxide thick film after 180 min deposition time; (b) the film formed after heating that in (a) at 873 K for 30 min; and (c) the film formed after heating that in (b) at 973 K for 30 min.

After 50 minutes of the molybdenum oxide dosage, a ~4 MLE molybdenum oxide thin film was prepared. The Mo 3d XP spectra for this thin film taken after heating to 473, 573, 673, 873, and 973 K are shown in Figure 4.27. At an intermediate annealing temperature, the binding energy of the Mo 3d doublet shifted towards lower binding energy and becomes closer to that of Mo^{5+} species. Annealing to 873 K results in a broadening of Mo 3d peaks with the peak shifts to lower binding energy, which does not dramatic change compared with the thicker films as shown in Figure 4.25. The deconvolution of Mo 3d peak (see Figure 4.27) showed an increase in amount of Mo^{5+} when increasing the annealing temperature. The continuous shift of the binding energy

indicates that there is the presence of reduction of the Mo^{6+} oxidation state to lower oxidation states (Mo^{4+} and Mo^{5+}). Further increasing the annealing temperature up to 973 K, the Mo 3d doublet shifted upward in binding energy and narrowed, with a Mo $3d_{5/2}$ value of 232.2 eV which is similar to the Mo 3d spectra from thick film. The Mo 3d XPS spectra (see Figure 4.27) also showed a shoulder at low binding energies, indicating a small amount of Mo^{4+} on the surface.

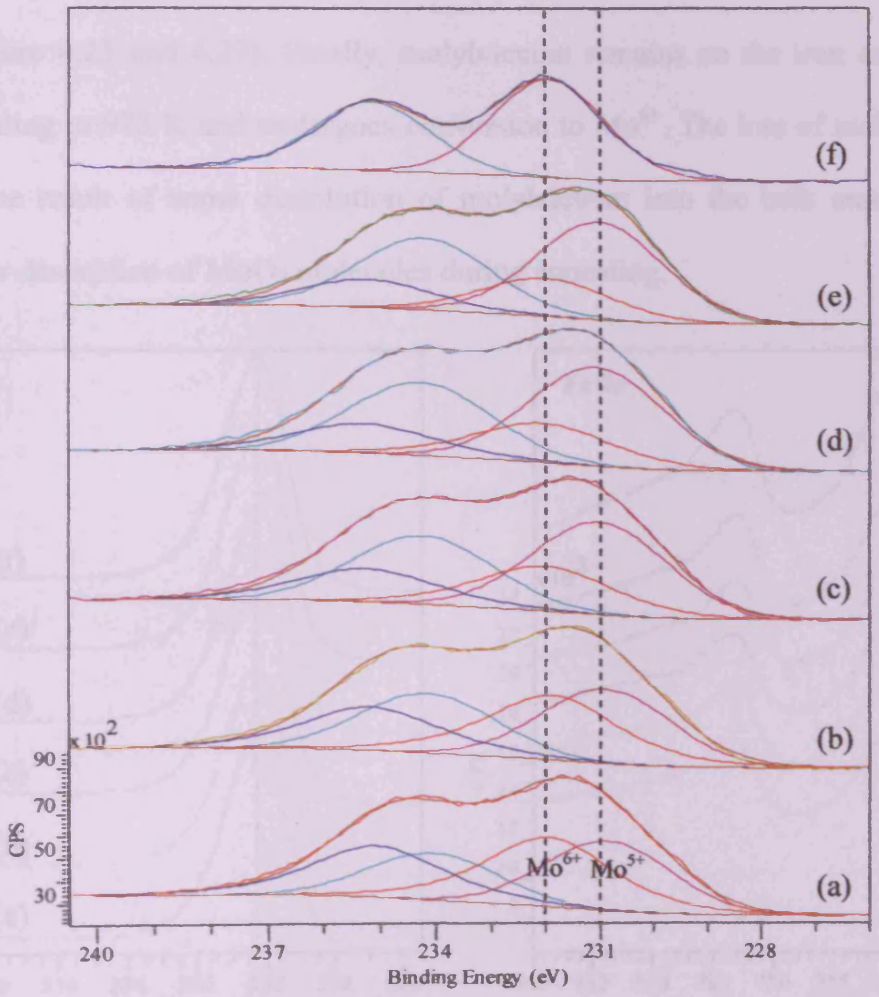

Figure 4.27. XPS spectra of the Mo 3d of molybdenum oxide thin film on iron oxide single crystal after 50 min deposition time. The spectrum (a) is taken after the formation of molybdenum oxide without further annealing. The bottom five spectra are obtained after annealing for 5 min at (b) 473 K, (c) 573 K, (d) 673 K, (e) 873 K, and (f) 973 K. All spectra were collected at room temperature.

Figure 4.28 presents the series of O 1s and Fe 2p core level spectra of this thin film obtained at different annealing temperatures. The shift of binding energies of O 1s and Fe 2p core level spectra did not observed with increasing the annealing temperature as shown in Figure 4.28. With increasing the annealing temperature, the intensity of Fe 2p spectra slightly increases while the O 1s intensity did not change significantly.

The partial reduction of Mo^{6+} to Mo^{5+} presented in thin and thick films is accompanied by the loss of molybdenum signified by a decrease in the intensity of Mo 3d region (Figure 4.25 and 4.27). Finally, molybdenum remains on the iron oxide surface upon annealing to 973 K and undergoes conversion to Mo^{6+}. The loss of molybdenum is probably the result of some dissolution of molybdenum into the bulk associated with reduction or desorption of MoO_3 molecules during annealing.

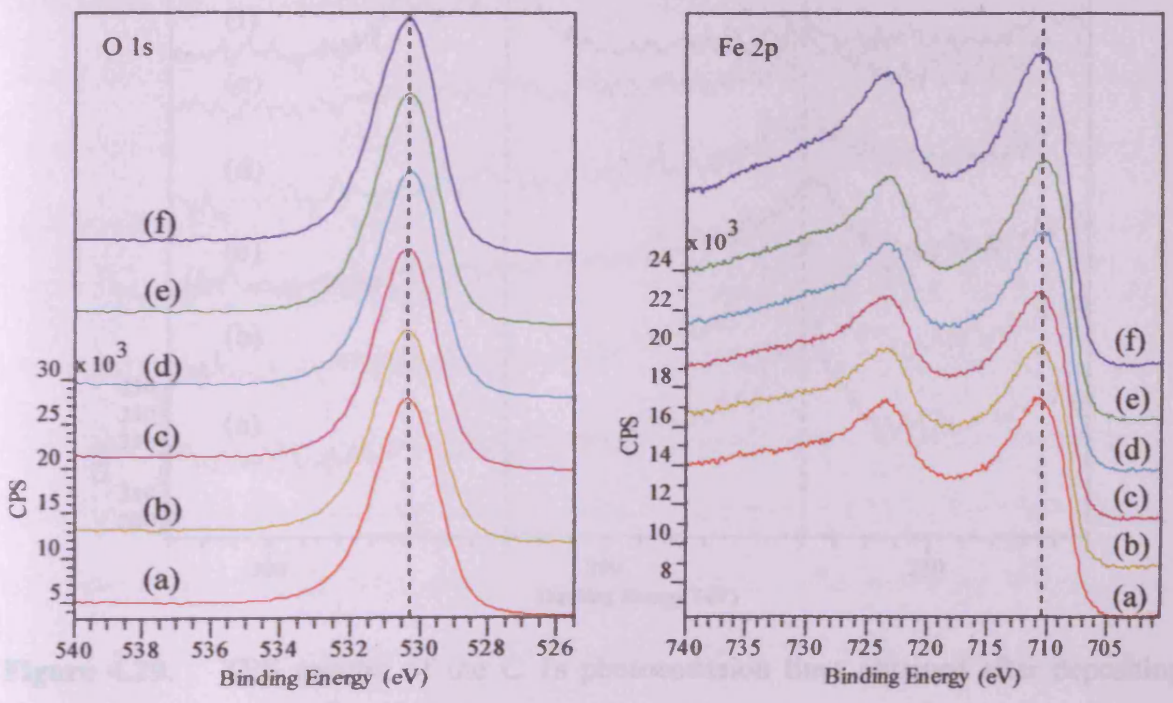

Figure 4.28. O 1s XPS and Fe 2p spectra obtained after 50 min molybdenum oxide deposition time. The spectrum (a) is taken after the formation of molybdenum oxide without further annealing. The top five spectra are obtained after annealing at: (b) 473 K, (c) 573 K, (d) 673 K, (e) 873 K, and (f) 973 K.

Figure 4.29 shows the C 1s XPS spectra of molybdenum oxide thin film taken after heating at different temperatures up to 973 K. After the deposition time of 50 min, the C 1s spectrum (Figure 4.29(a)) reveals the appearance of a small amount of carbon at a binding energy of about 284 eV. With increasing the annealing temperature, an decrease in intensity of the C 1s signal and two new signals at the binding energy of 293.1 and 296.0 eV are observed. These new signals are assigned to the signals of K $2p_{3/2}$ and K $2p_{1/2}$, respectively [104]. A possible explanation for the appearance of K 2p is due to the existence of potassium residue used in another experiment which is difficult to eliminate from the system, as described above.

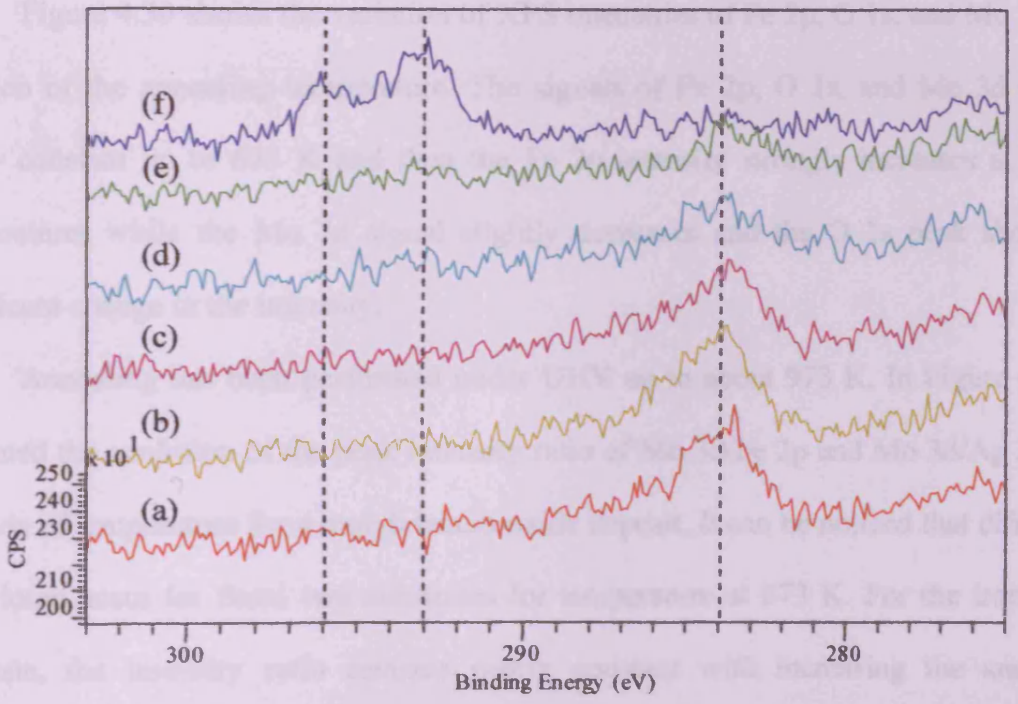

Figure 4.29. XPS spectra of the C 1s photoemission lines obtained after depositing molybdenum oxide on iron oxide for 50 min. The spectrum (a) is taken after the formation of molybdenum oxide without further annealing. The top five spectra are obtained after annealing for 5 min at (b) 473 K, (c) 573 K, (d) 673 K, (e) 873 K, and (f) 973 K. All spectra were collected at room temperature.

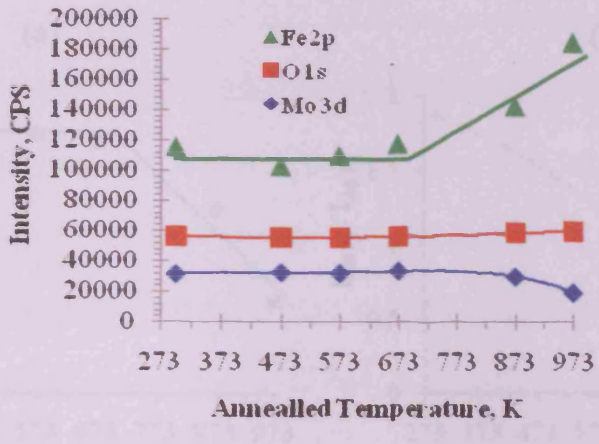

Figure 4.30. Integrated intensity of XPS Fe 2p, O 1s, and Mo 3d peaks as a function of the annealing temperature. Solid lines represent fitting result for changes of Fe 2p, O 1s, and Mo 3d intensities caused by the annealing temperature.

Figure 4.30 shows the variation of XPS intensities of Fe 2p, O 1s, and Mo 3d as a function of the annealing temperature. The signals of Fe 2p, O 1s, and Mo 3d remain nearly constant up to 673 K and then the Fe 2p intensity strongly increases at higher temperatures while the Mo 3d signal slightly decreases and the O 1s peak shows no significant change in the intensity.

Annealing has been performed under UHV up to about 973 K. In Figure 4.31 is presented the evolution of the peak intensity ratio of Mo 3d/Fe 2p and Mo 3d/Ag 3d as a function of temperature for a molybdenum oxide deposit. It can be noticed that difference behaviours occur for these two substrates for temperature at 673 K. For the iron oxide substrate, the intensity ratio remains nearly constant with increasing the annealing temperature to 673 K while for silver substrate, the XPS intensity ratio decreases. At higher temperatures, the XPS peak intensity ratio of Mo 3d/Fe 2p decreases much more slowly than that of Mo 3d/Ag 3d; for the latter annealing to 973 K, reducing the Mo/Ag intensity ratio in the Ag(111) system by ~97%, whereas it is only ~60% for the iron oxide system.

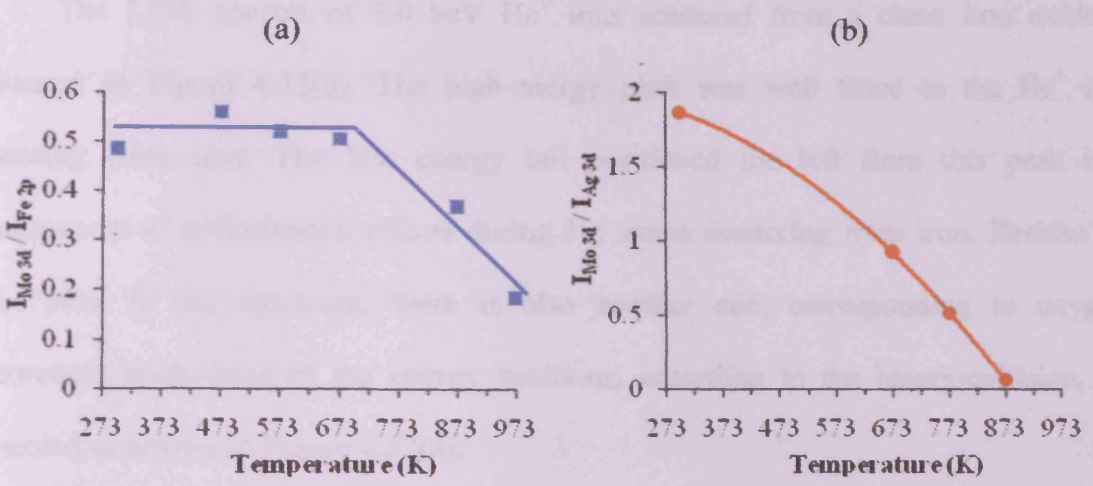

Figure 4.31. Evolution of the peak intensity ratio of (a) Mo3d/Fe2p and (b) Mo3d/Ag3d determined from XPS results as a function of the annealing temperature for different substrate surfaces covered with thin molybdenum oxide deposit.

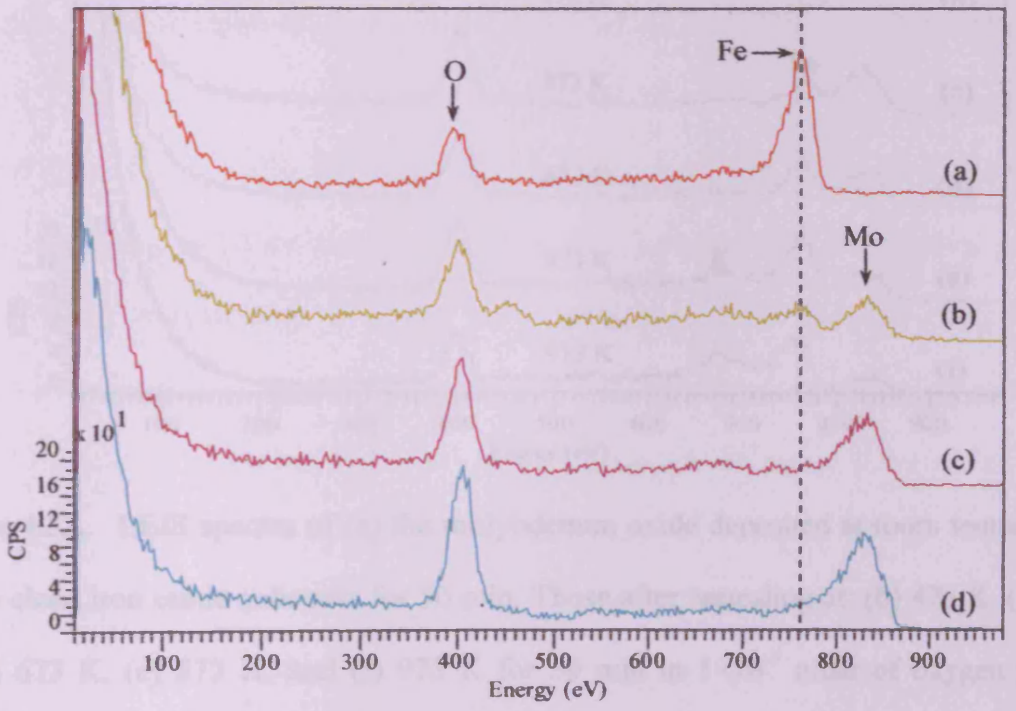

Figure 4.32. LEIS spectra of (a) the clean iron oxide surface. Only iron and oxygen is visible. (b) 10 min deposition of molybdenum oxide on iron oxide surface. (c) 30 min deposition time. Molybdenum can be seen with no iron. (d) 50 min deposition time of molybdenum oxide on iron oxide surface.

The LEIS spectra of 1.0 keV He^+ ions scattered from a clean iron oxide is presented in Figure 4.32(a). The high-energy peak was well fitted to the He^+ ions scattering from iron. The low energy tail positioned the left from this peak is a consequence of re-ionisation effects during He atoms scattering from iron. Besides the main peak in the spectrum, there is also another one, corresponding to oxygen. Theoretical predictions of the energy positions, according to the binary-collision, are presented as arrows in Figure 4.32(a).

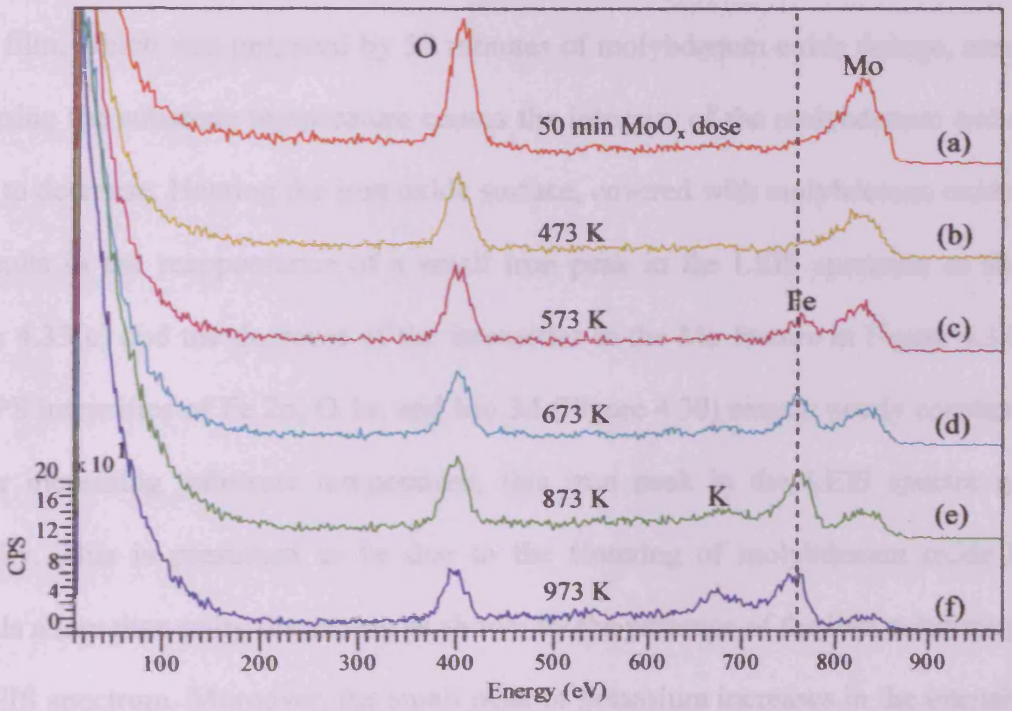

Figure 4.33. LEIS spectra of (a) the molybdenum oxide deposited at room temperature on the clean iron oxide substrate for 50 min. Those after annealing at: (b) 473 K, (c) 573 K, (d) 673 K, (e) 873 K, and (f) 973 K for 30 min in 1×10^{-7} mbar of oxygen partial pressure.

After 10, 30, and 50 minutes of the molybdenum oxide dosage, a ~0.5, ~2.5, and ~4 MLE molybdenum oxide film were prepared. These molybdenum oxide films produced the LEIS spectra shown in Figure 4.32(b)-(d). Just after the 10 min deposition

time of molybdenum oxide (~0.5 MLE molybdenum oxide film), a dramatic decrease in the intensity of the iron peak was found while the intensity of the oxygen peak increased. At the high-energy side of the Fe peak, the additional peak was observed corresponding to molybdenum at the energy in good agreement with the energy position expected from the binary-collision. The intensity of molybdenum and oxygen peaks increased when the deposition time increased.

In Figure 4.33, a series of the ISS spectra under 1.0 keV He^+ ion bombardments taken from the surfaces heated to the indicated temperatures for a ~4 MLE molybdenum oxide film, which was prepared by 50 minutes of molybdenum oxide dosage, are shown. Increasing the substrate temperature causes the intensity of the molybdenum and oxygen peaks to decrease. Heating the iron oxide surface, covered with molybdenum oxide to 573 K, results in the reappearance of a small iron peak in the LEIS spectrum as shown in Figure 4.33(c) and the decrease of the intensities in the Mo feature in Figure 4.33, while the XPS intensities of Fe 2p, O 1s, and Mo 3d (Figure 4.30) remain nearly constant. With further increasing substrate temperature, this iron peak in the LEIS spectra gains in intensity. This is presumed to be due to the sintering of molybdenum oxide leading towards a less than unity dispersion as shown by the presence of the iron substrate peak in the LEIS spectrum. Moreover, the small peak of potassium increases in the intensity after annealing in 1×10^{-7} mbar in oxygen pressure between 473 and 973 K which is in agreement with the XPS spectra of Figure 4.29. It is revealed that, for supported Mo-based catalysts, an interaction between the potassium promoter and the supported molybdenum component occurs [105]. It is therefore possible to consider that an increase in the annealing temperature causes a deposit of potassium residue from another experiment on the molybdenum oxide film and could have some influence on the interaction between them.

4.4.5. Identification of the surface structure

Under different coverages of molybdenum oxide, the growth mechanism of molybdenum oxide thin films after deposition of molybdenum oxide on iron oxide substrate followed by annealing in an oxygen pressure of 1×10^{-7} mbar at different temperatures was investigated by XPS, LEED, and STM.

4.4.5.1. XPS results

The molybdenum oxide coverages of ~0.3, ~0.5, ~1.5, ~2.5, and ~3.5 MLE were prepared on the iron oxide substrate after 5, 10, 20, 30, and 40 min deposition, respectively, at room temperature. The electronic structures of these molybdenum oxide coverages have been examined using XPS before and after an exposure to oxygen at different annealing temperatures. Figure 4.34 and 4.35 show Mo 3d and Fe 2p photoemission spectra acquired from molybdenum oxide thin films with different surface coverages on iron oxide surface prior to and after annealing in oxygen pressure of 1×10^{-7} mbar for 30 minutes at 873 K and 973 K. Before the oxygen treatment, at the molybdenum oxide coverage of ~0.3 and ~0.5 MLE, the binding energies of the Mo $3d_{5/2}$ were observed at around 232.2 eV and shift to lower binding energies as the molybdenum oxide coverage increases while the binding energies of Fe $2p_{3/2}$ for all the molybdenum oxide coverages were observed at around 710.0 eV. At the ~0.3 and ~0.5 MLE molybdenum oxide coverages, the spectra of the as-deposited molybdenum oxide in the Mo 3d region showed the presence of two well resolved spectral lines at 232.2 and 235.3 eV, which were assigned to the Mo $3d_{5/2}$ and Mo $3d_{3/2}$ spin-order components for hexavalent molybdenum (Mo^{6+}), respectively (Figure 4.34(a)). For the molybdenum oxide coverages of ~1.5 to ~3.5 MLE, the Mo 3d spectra show the shift of the Mo 3d binding energies to lower value, indicating that a reduced surface (Mo oxidation state lower than +6) is present. In case of Fe 2p region (Figure 4.35(a)), the binding energies of

Fe $2p_{3/2}$ and Fe $2p_{1/2}$ levels were observed at 710.0 and 723.1 eV respectively. These spectra show the presence of Fe^{2+} and Fe^{3+}.

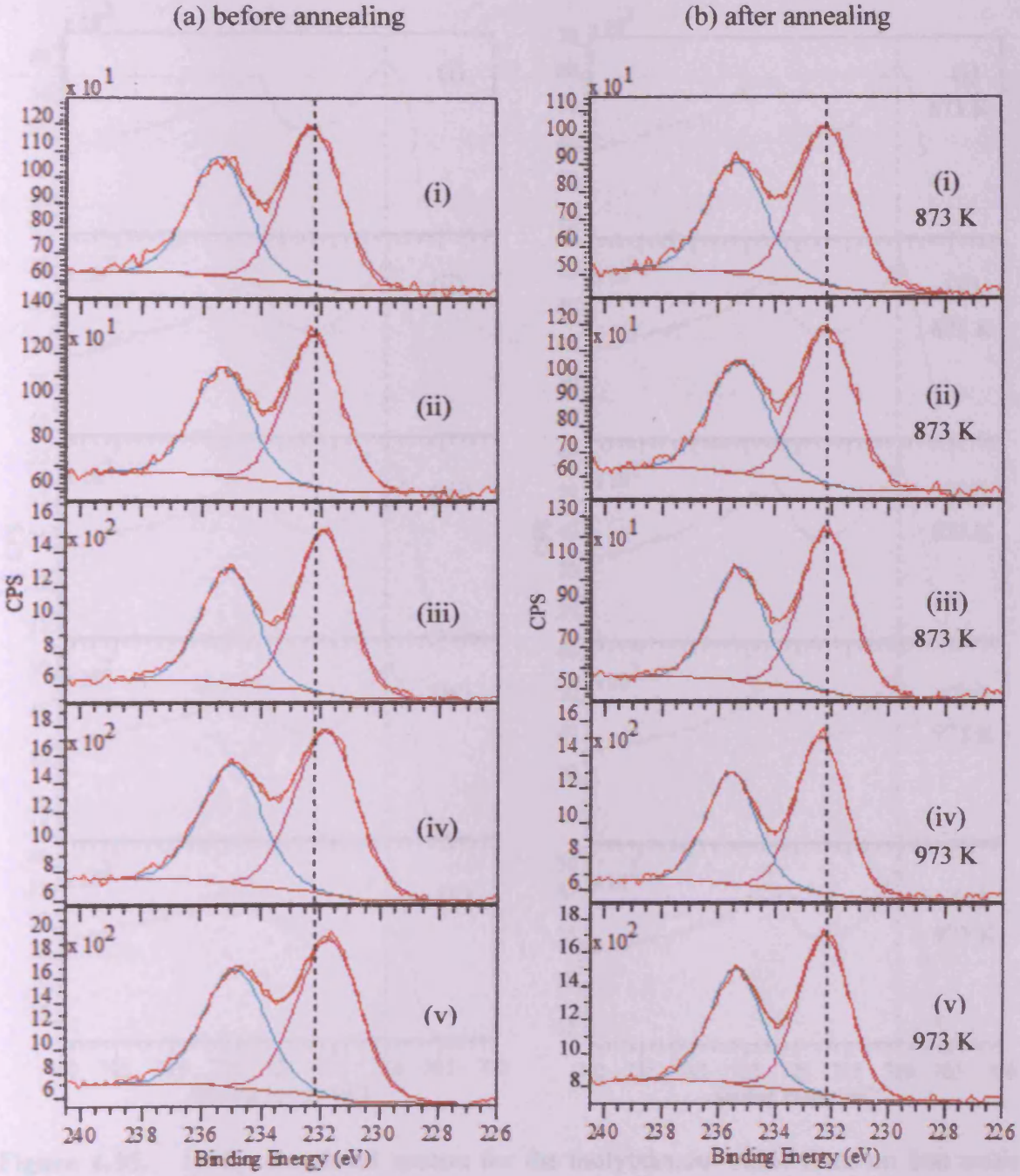

Figure 4.34. Comparison of Mo 3d XPS spectra for the molybdenum oxide thin films on iron oxide recorded prior to (a) and after (b) annealing in oxygen pressure for 30 min at different temperatures and various molybdenum oxide coverages (i-v). (i) ~0.3 MLE; (ii) ~0.5 MLE; (iii) 1.5 MLE; (iv) 2.5 MLE; and (v) 3.5 MLE.

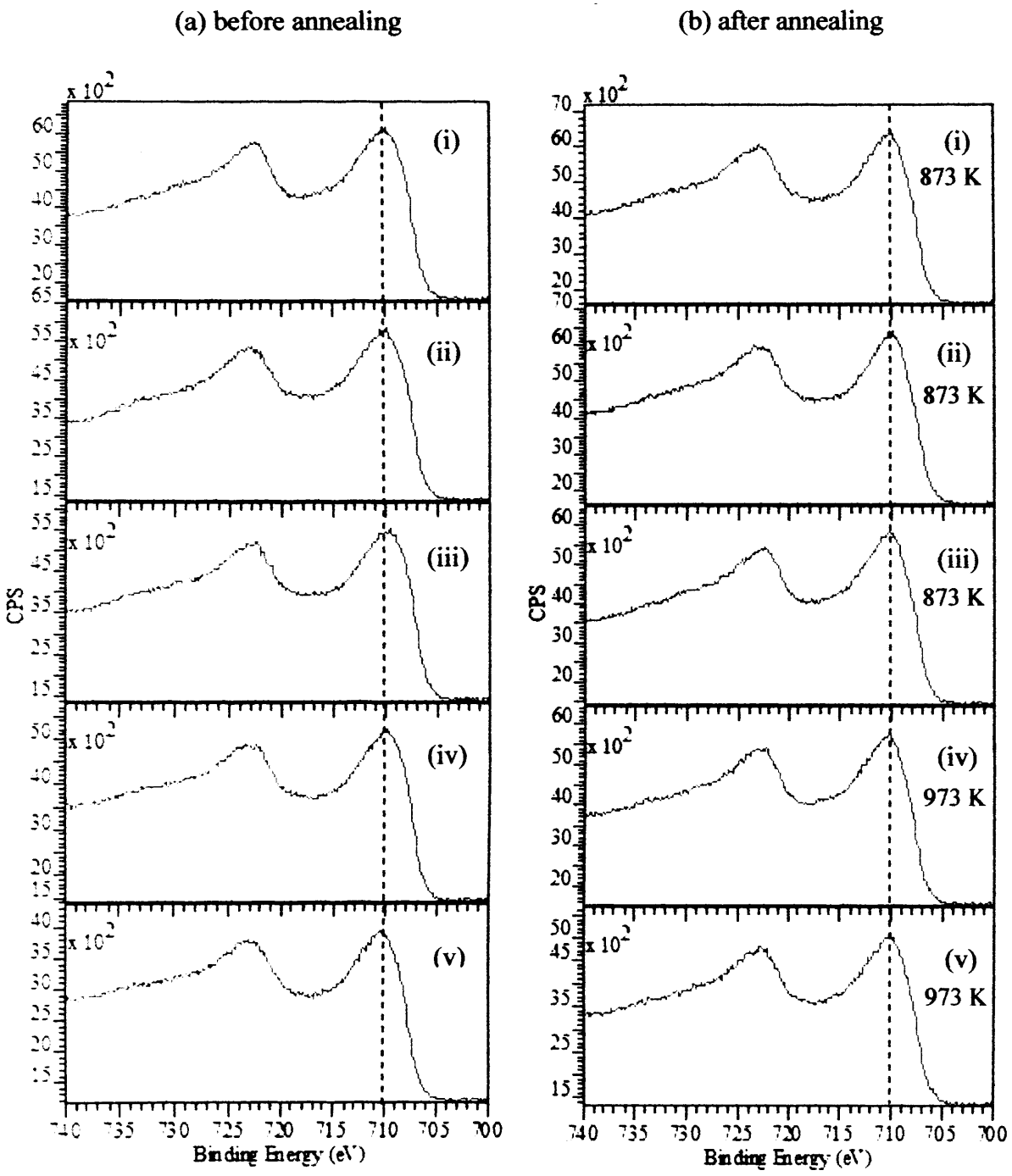

Figure 4.35. Fe 2p core-level spectra for the molybdenum oxide films on iron oxide obtained before (a) and after (b) heating in 1×10^{-7} mbar oxygen for 30 min at different temperatures (molybdenum oxide coverages correspond to ~0.3 (i), ~0.5 (ii), ~1.5 (iii), ~2.5 (iv), and ~3.5 (v) MLE).

After the oxygen treatment, one can hardly see any change for the Fe 2p spectra except that they are slightly narrowed (Figure 4.35(b)), while the Mo 3d binding energies of the ~1.5 to ~3.5 MLE molybdenum oxide coverages show a small shift to higher binding energies (Figure 4.34(b) and reveal the presence of Mo^{6+} oxidation state only. The binding energies of Mo 3d, Fe 2p, and O 1s measured for the molybdenum oxide film after annealing show in Table 4.4. In a previous study on α-Fe_2O_3-supported molybdena catalysts, it was found that MoO_3 reacted with the bulk α-Fe_2O_3 and formed ferric molybdate ($Fe_2(MoO_4)_3$) compound at temperature of above 500°C [106]. It presumably implies that iron molybdate compounds were formed. In addition, for all the molybdenum oxide coverages, photoemission spectra of the O 1s core level (not shown) did not show any significant changes in the intensity and the line position.

Table 4.4. The binding energies measured for molybdenum oxide thin film on iron oxide after annealing in O_2 for different coverages and different temperatures (873 or 973 K). The peak positions are measured from the spectra shown in Figure 4.34 and 4.35. (Referenced against Au $4f_{7/2}$ at 83 eV).

Molybdenum oxide coverage (MLE)	Mo $3d_{5/2}$ (eV)	Mo $3d_{3/2}$ (eV)	O 1s (eV)	Fe $2p_{3/2}$ (eV)
~0.3 (873 K)[a]	232.2	235.4	530.5	710.0
~0.5 (873 K)	232.2	235.4	530.2	710.1
~1.5 (873 K)	232.2	232.4	530.3	710.0
~2.5 (973 K)	232.3	232.5	530.3	710.0
~3.5 (973 K)	232.2	232.3	530.2	710.1

[a] Values in parentheses correspond to annealing temperature.

4.4.5.2. LEED measurements

The structure of iron oxide surface depends on the different heating temperature and surface pre-treatment in vacuum and is well documented as described in Chapter 3. After argon sputtering and heating iron oxide surface in 1×10^{-7} mbar of oxygen at 873 K for 30 minutes, the LEED pattern of the clean iron oxide surface (see Figure 4.36) exhibits diffraction spots similar to the pattern reported previously for an $Fe_3O_4(111)$ surface with the spots of a p(2×2) structure due to the formation of an $Fe_3O_4(111)$ epitaxial layer on the iron oxide single crystal. The spots of this LEED pattern correspond to the distances of 5.82 Å hexagonal unit cell as described in Chapter 3. Utilizing these known distances and their corresponding directions allows us to calculate distances within the molybdenum oxide film and its orientation with respect to the iron oxide surface.

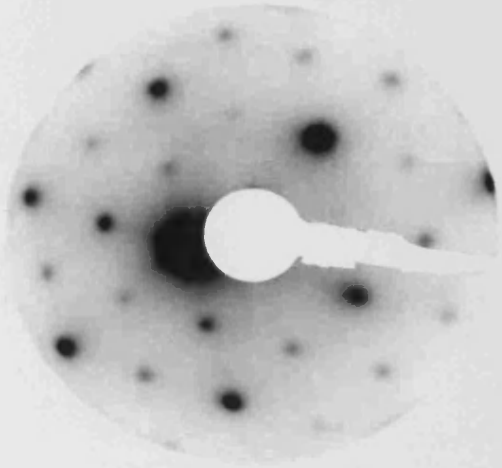

Figure 4.36. LEED pattern from clean iron oxide surface. The energy of the electron beam is 70 eV.

After 5, 10, 20, 30, and 40 minutes of molybdenum oxide dosages, a ~0.3, ~0.5, ~1.5, ~2.5, and ~3.5 MLE molybdenum oxide coverages were prepared. The resulting

films were analysed using XPS as described in section 4.4.5.1. The surface structure of these films were then characterised by means of LEED. Before annealing, for all the molybdenum oxide coverages, the LEED spots become weaker and no extra spots appear. The only change in the LEED pattern following depositing molybdenum oxide at different time periods is an increase in the background intensity (not shown). This indicates that the molybdenum oxide does not form an ordered structure on the iron oxide substrate as deposited. For the molybdenum oxide coverages of ~0.3 to ~1.5 MLE, the observed LEED pattern after annealing in 1×10^{-7} mbar of oxygen partial pressure for 30 minutes at 873 K is shown in Figure 4.37. The LEED spots become much sharper and the background intensity decreases indicating better crystalline quality. No additional LEED beams are observed, and the observed LEED patterns are indistinguishable from the substrate LEED pattern.

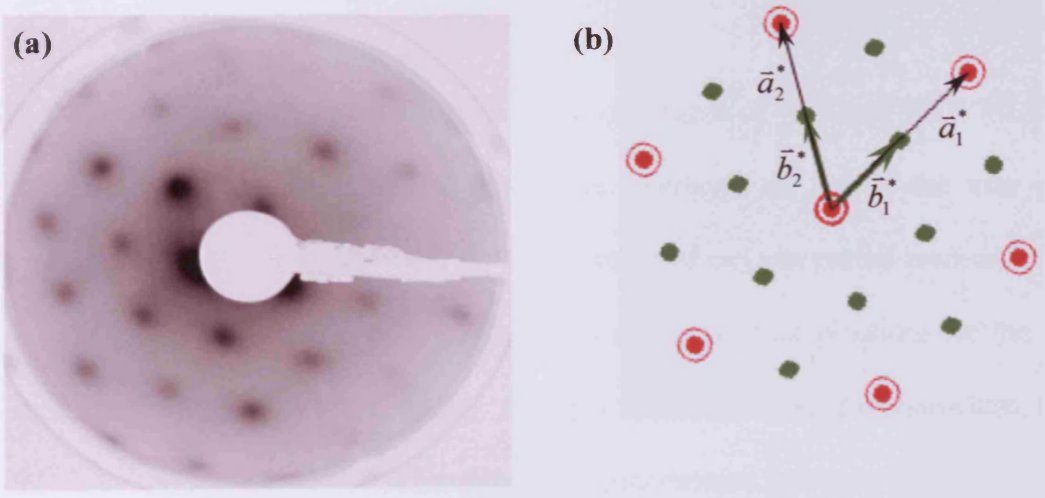

Figure 4.37. (a) LEED pattern for the molybdenum oxide overlayer on the iron oxide surface after heating 30 min to 873 K in 1×10^{-7} mbar of oxygen partial pressure. The pattern is the same as the one obtained from the clean iron oxide substrate. Annealing the films at 873 K results in better order and shaper LEED pattern; (b) Schematic of the LEED pattern in (a). The electron beam energy was 83 eV.

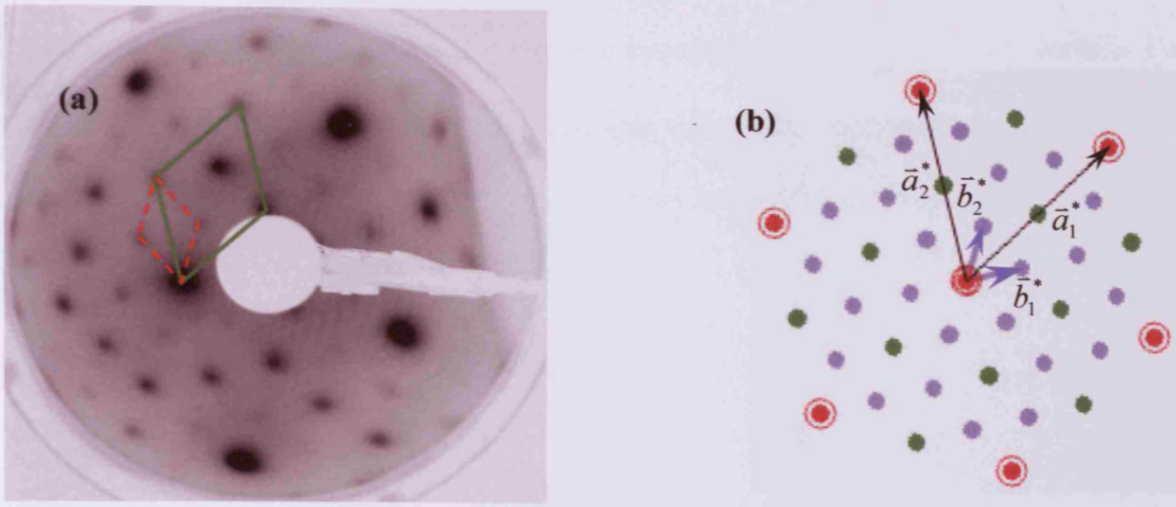

Figure 4.38. (a) LEED pattern for the molybdenum oxide on the $Fe_3O_4(111)$-(2×2) formed by annealing 30 min to 973 K in 1×10^{-7} mbar oxygen partial pressure. The primary beam energy is 50 eV. The unit cells of the $Fe_3O_4(111)$ (2×2) structure (green line) and the new overlayer structure (red dashed line) are shown. (b) Schematic of the LEED pattern in (a).

In Figure 4.38, for the molybdenum oxide coverages of ~2.5 and ~ 3.5 MLE, the LEED pattern formed by the molybdenum oxide overlayer on top of the iron oxide substrate after annealing for 30 minutes in 1×10^{-7} mbar of oxygen partial pressure at 973 K is shown together with a schematic representation of the spot positions on the right hand side. The observed LEED image exhibits the additional superstructure spots originating from the molybdenum oxide film at quarter-integer locations when referred to O(111) beams. Throughout this work, the p(2×2) unit cell of the $Fe_3O_4(111)$ plane is employed as the reference, using its bulk value for the Fe–Fe interatomic distance of a_{sub} = 5.92 Å for calibration purposes.

The LEED patterns in Figure 4.38(a) are resolved into two hexagonal mesh units, as illustrated by the red and light blue circles in Figure 4.38(b), considering two domains

rotated by ~30° with respect to one another, as reported for the $Fe_3O_4(111)$ surface. From the LEED pattern (see Figure 4.38), the unit cell of the molybdenum oxide adsorbate structure can be obtained. Writing the reciprocal space unit cell vectors of the overlayer, $\vec{b}_1^*$ and $\vec{b}_1^*$, in terms of the substrate, $\vec{a}_1^*$ and $\vec{a}_2^*$

$$\vec{b}_1^* = \frac{1}{3}\vec{a}_1^* - \frac{1}{6}\vec{a}_2^* \tag{4.1}$$

$$\vec{b}_2^* = \frac{1}{6}\vec{a}_1^* + \frac{1}{6}\vec{a}_2^* \tag{4.2}$$

Therefore,

$$M^* = \begin{bmatrix} 1/3 & -1/6 \\ 1/6 & 1/6 \end{bmatrix}$$

The matrix of the real space structure is given by:

$$M = \frac{1}{\det M^*}\begin{bmatrix} 1/6 & -1/6 \\ 1/6 & 1/3 \end{bmatrix} \tag{4.3}$$

where $\det M^* = \frac{1}{3}\cdot\frac{1}{6} - \left(-\frac{1}{6}\cdot\frac{1}{6}\right) = \frac{1}{12}$

Therefore,

$$M = \begin{bmatrix} 2 & -2 \\ 2 & 4 \end{bmatrix}$$

The real space matrix of the surface molybdenum oxide is:

$$\begin{bmatrix} \vec{b}_1 \\ \vec{b}_2 \end{bmatrix} = \begin{bmatrix} 2 & -2 \\ 2 & 4 \end{bmatrix}\begin{bmatrix} \vec{a}_1 \\ \vec{a}_2 \end{bmatrix} \tag{4.4}$$

The angle, γ, between two real space unit cell vectors of either the substrate, $\vec{a}_1$ and $\vec{a}_2$, or the overlayer, $\vec{b}_1$ and $\vec{b}_2$, is given by

$$\gamma^* = \gamma + 2\left(\frac{\pi}{2} - \gamma\right) = \pi - \gamma \qquad (4.5)$$

where γ^* is the angle between two reciprocal space unit cell vectors of either the substrate, $\bar{a}_1^*$ and $\bar{a}_2^*$, or the overlayer, $\bar{b}_1^*$ and $\bar{b}_2^*$ which is 60° for both substrate and overlayer. Therefore,

$$\gamma = \pi - \gamma^*$$

$$= 180 - 60 = 120$$

From the matrix in Equation (4.4), the corresponding unit vector size and rotation in the Wood notation can be calculated. The unit cell of the overlayer in terms of a primitive cell (vectors $\bar{b}_1^*$ and $\bar{b}_2^*$) which are rotated with respect to the substrate by 30° can be defined

$$|\bar{b}_1|\cos 30 = 3|\bar{a}_1| \qquad \text{and} \qquad |\bar{b}_2|\cos 30 = 3|\bar{a}_2|$$

$$\therefore \quad \frac{|\bar{b}_1|}{|\bar{a}_1|} = \frac{3}{\cos 30} = 2\sqrt{3} \quad \text{and} \quad \frac{|\bar{b}_2|}{|\bar{a}_2|} = \frac{3}{\cos 30} = 2\sqrt{3}$$

Therefore, the LEED patterns illustrated in Figure 4.38 are equally well referred to as either a $(2\sqrt{3} \times 2\sqrt{3})$R30° or $\begin{bmatrix} 2 & -2 \\ 2 & 4 \end{bmatrix}$ with reference to hexagonal close-packed oxygen sublattice of the (111) plane of bulk Fe_3O_4.

The length $|\bar{b}_1| = 2|\bar{a}_1|\sin\gamma$

$$|\bar{b}_1| = 2|\bar{a}_1|\sin\gamma = 2 \times 5.92 \sin 120 = 2 \times 5.92 \times \frac{\sqrt{3}}{2} = 10.25$$

$$|\bar{b}_2| = 2|\bar{a}_2|\sin\gamma = 2 \times 5.92 \sin 120 = 2 \times 5.92 \times \frac{\sqrt{3}}{2} = 10.25$$

The size of the unit cell of the molybdenum oxide film structure can be obtained when compared to the known size of the substrate lattice. Using the iron–iron distance on the $Fe_3O_4(111)$ surface, the calculated value for unit cell size of the molybdenum oxide film structure, b_{MoOx}(LEED), corresponds to a distance of 10.25 Å.

In summary, the LEED results show that the molybdenum oxide overlayer on the iron oxide surface after heating to 873 K produced no discernable changes in the LEED pattern, thus leading to the same p(2×2) LEED pattern as the clean substrate. Heating to 973 K caused the p(2×2) structure to be replaced by a $(2\sqrt{3} \times 2\sqrt{3})$R30° structure.

4.4.5.3. STM analysis

According to the XPS shown in Figure 4.34, samples prepared on the $Fe_3O_4(111)$ have much less molybdenum oxide after annealing at 873 and 973 K than after the deposition of molybdenum oxide at room temperature. This shows that the coverage of molybdenum oxide is reduced and is still present after heating to 973 K. The molybdenum oxide coverage after heating has been recalculated using equation (4.1). Therefore, the coverages of molybdenum oxide films on the iron oxide surface, from which the XPS spectra illustrated in Figure 4.34 and 4.35, were ~0.2, ~0.3, and ~0.5 MLE after annealing at 873 K and ~1.0, and ~1.5 MLE after annealing at 973 K. These molybdenum oxide films have been studied at room temperature with high resolution using STM. The results of these studies will be presented and discussed in the following.

i. The sub-monolayer of molybdenum oxide on iron oxide

STM images of fairly large scanning ranges will be firstly presented in order to discuss the overall growth morphology and the influence of coverage on morphology and then smaller-range molecularly resolved images will be considered.

(a) ~0.2 MLE MoO_3 after heating at 873 K

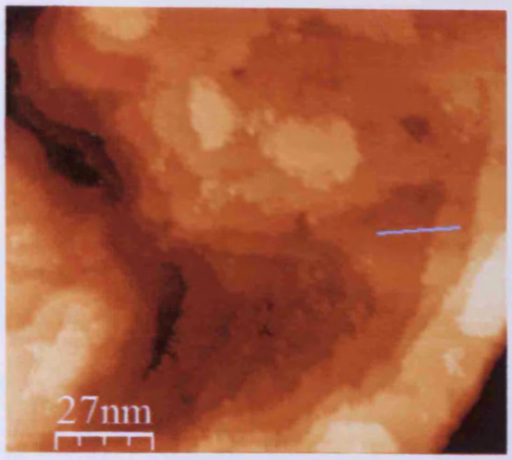

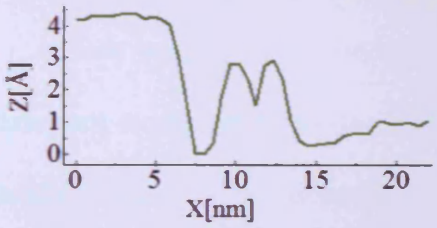

(b) ~0.3 MLE MoO_3 after heating at 873 K

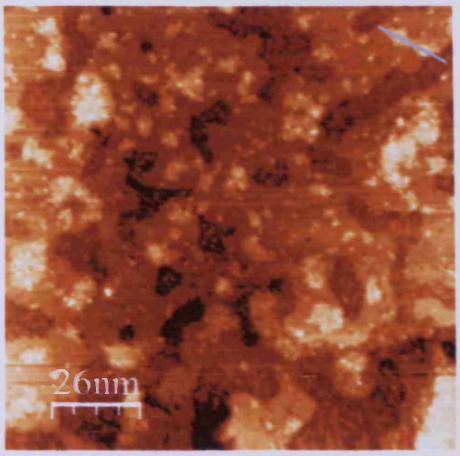

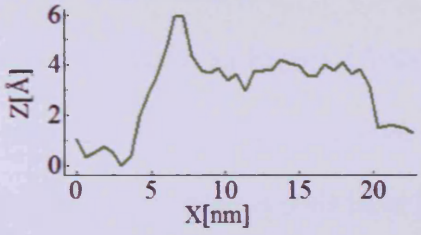

(c) ~0.5 MLE MoO_3 after heating at 873 K

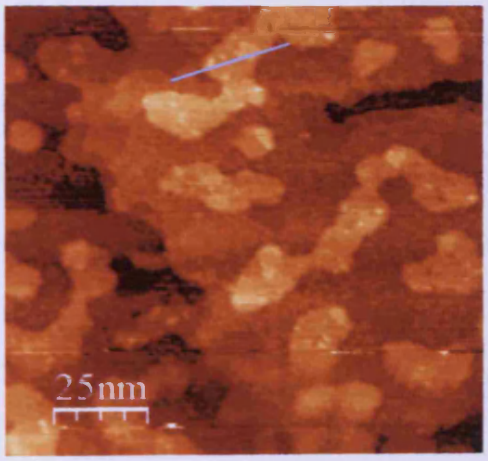

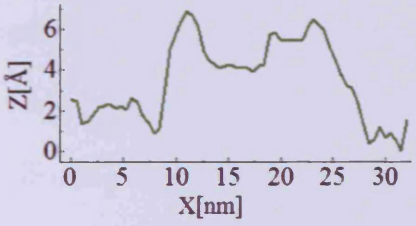

Figure 4.39. Large-scale STM images taken in constant current mode of Mo-oxide growth on $Fe_3O_4(111)$ after annealing at 873 K: (a) 134×134 nm^2 (1.1 V, 1.23 nA) image taken for ~0.2 MLE of MoO_3. (b) 132×132 (1.4 V, 0.34 nA) nm^2 image taken for ~0.3 MLE MoO_3. (c) 125×125 nm^2 (2.6 V, 0.54 nA) image taken for ~0.5 MLE MoO_3.

Large-scan STM images of initial molybdenum oxide growth stages on the iron oxide surface are shown in Figure 4.39. These are constant-current images with sample biases and tunnelling current given in the figure captions. Sub-monolayer amount of molybdenum oxide was obtained after 5, 10, and 20 minutes of molybdenum oxide dosages and subsequently oxidised for 30 minutes in oxygen pressure of 1×10^{-7} mbar at temperature of 873 K. Following this procedure, the molybdenum oxide coverages of ~0.2, ~0.3, and ~0.5 MLE were prepared. In Figure 4.39(a)-(c), the molybdenum oxide overlayer coverage increases from ~0.2 to ~0.5 MLE. For all growth stages, the p(2×2) LEED patterns similar to the one displayed in Figure 4.37 were observed.

At low coverage of molybdenum oxide (~0.2 MLE MoO_3 in Figure 4.39(a)), the molybdenum oxide overlayer shows small islands growing on a generally flat area of the iron oxide terraces during deposition; these small molybdenum oxide islands have grown preferentially near the step edges. With further deposition, the larger islands were formed on the iron oxide surface.

At higher coverages of molybdenum oxide (~0.3 and ~0.5 MLE MoO_3 shown in Figure 4.39(b) and (c)), some larger islands developed on the flat area of the iron oxide terraces appear and these begin to coalesce for ~0.5 MLE MoO_3. The image also shows multilayer growth, with islands of at least two levels being visible during further deposition; by contrast, mostly one level of islands is observed for ~0.2 MLE MoO_3. The molybdenum oxide has grown with what are imaged in the STM as two different heights of the islands; a topmost set about 2.5 Å in height as measured from the islands just below, and a lower set about 3.0 Å in height as measured from the flat base layer. Further deposition resulted in an increase in the number of the larger islands without an increase in their apparent height.

~0.2 MLE MoO_3 after heating at 873 K

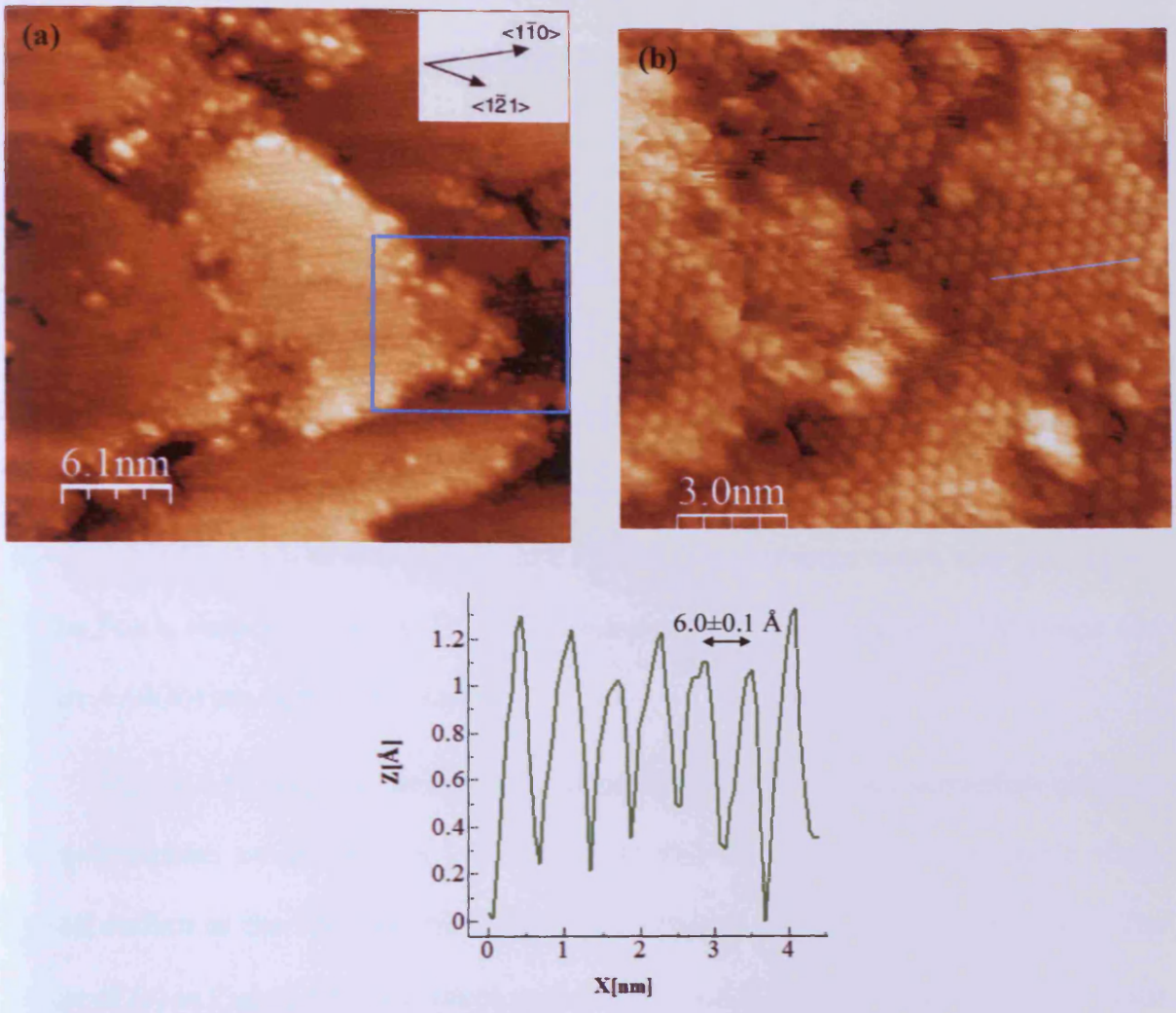

Figure 4.40. (a) 303×303 Å^2 STM image showing Mo-oxide clusters on the iron oxide at coverage of ~0.2 MLE. A few bright features near the step edges and on the flat area of the terrace were observed. (b) High-resolution 150×150 Å^2 STM image showing a hexagonal unit cell with a lattice constant of 6.03 Å. A line profile from the image in (b) was taken along the indicated section. Both images were recorded under the following conditions: $V = +1.1$ V and $I = 1.23$ nA.

An insight into the growth mechanism of molybdenum oxide at the iron oxide surface is provided by the atomically resolved STM image like the one shown in Figure 4.40. The high-resolution STM images for low coverage of molybdenum oxide (~0.2 MLE MoO_3 in Figure 4.40) exhibits the bright features related to deposited molybdenum

oxide. These bright features were observed near the step edges and on the flat area of the iron oxide terrace after dosing and annealing to 873 K, as the XPS spectra of Mo 3d and Fe 2p shown in Figure 4.34(i) and 4.35(i). The apparent heights of the bright features in STM (Figure 4.39(a)) varied between 2.5 and 3.5 Å. All the bright features are believed to be deposits of molybdenum oxide. Unfortunately, a high-resolution STM image of bright features near the step edges cannot be observed. However, a high-resolution image present in Figure 4.40(b) shows that the atomic surface structure has a hexagonal surface lattice with a lattice constant of 6.03 Å, consistent with the observation of a well-defined p(2×2) LEED pattern, as shown in Figure 4.37(a). The distances match well the unit cell of the Fe_3O_4 surface (5.94 Å). Thus, the honeycomb-like lattice in the STM image (see Figure 4.40(b)) are $Fe_3O_4(111)$ surface.

Figure 4.41 displays the high-resolution STM image for the intermediate coverage of molybdenum oxide clusters (~0.3 MLE MoO_3) formed onto an iron oxide single crystal surface as the XPS spectra of this film shown in Figure 4.34(ii) and 4.35(ii). The image of (b) in Figure 4.41 was taken at the bias of 1.4 V and is a zoom of the area in the middle of Figure 4.41(a). It shows that the molecular surface structure of the molybdenum oxide clusters has a quasi-hexagonal surface mesh with a lattice constant of ~12 Å and an angle of ~120° while the p(2×2) LEED pattern was observed as shown in Figure 4.37. The result for this may be due to low coverage of the molybdenum oxide. A lattice constant of molybdenum oxide clusters are approximately twice the lattice spacing of $Fe_3O_4(111)$ surface. Figure 4.41(d) and 4.41(e) contain line scans from Figure 4.41(b) taken along a line (A-A) and (B-B), and indicated in Figure 4.41(b). The STM data further reveal that the molybdenum oxide clusters were aligned with the $[1\,\bar{1}\,0]$ direction of the $Fe_3O_4(111)$ surface. The apparent heights of the molybdenum oxide clusters are in the range of 2.0-2.5 Å.

~0.3 MLE MoO_3 after heating at 873 K

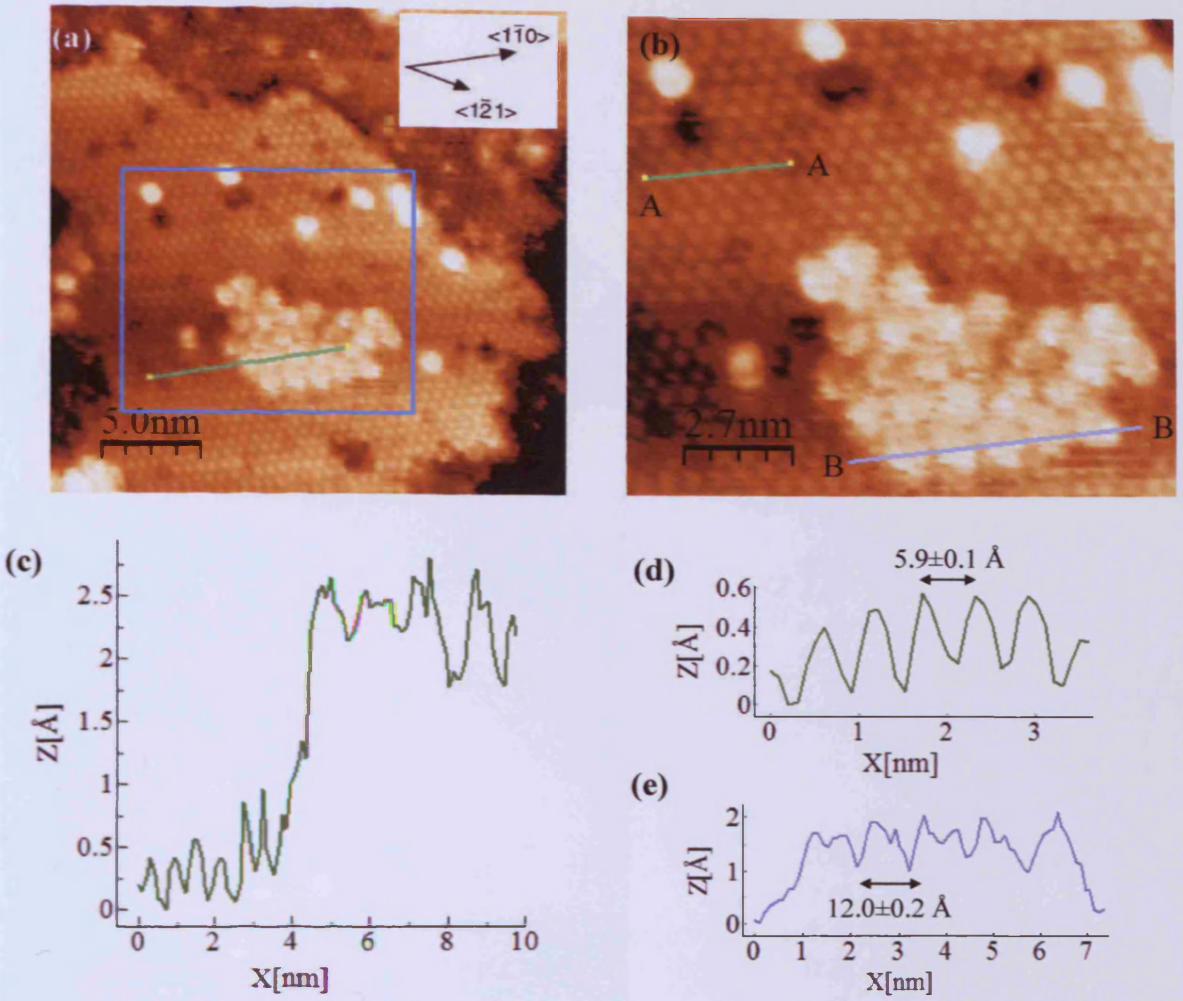

Figure 4.41. STM images of the molybdenum oxide clusters on the iron oxide surface. (a) A high-resolution STM image (250×250 $Å^2$) recorded at the sample bias voltage of 1.4 V and the current of 0.36 nA. (b) A magnified high-resolution STM image (134×119 $Å^2$) is presented of the area marked by the rectangle in panel (a), revealing the periodic protrusions. (c) A line profile along the [1 $\bar{1}$ 0] direction from the image in (a). (d) and (e) Line scans from the image in (b) taken along a line (A-A) and (B-B). The molybdenum oxide clusters form a quasi-hexagonal lattice on the top of the iron oxide with ~12 Å periodicity.

~0.5 MLE MoO_3 after heating at 873 K

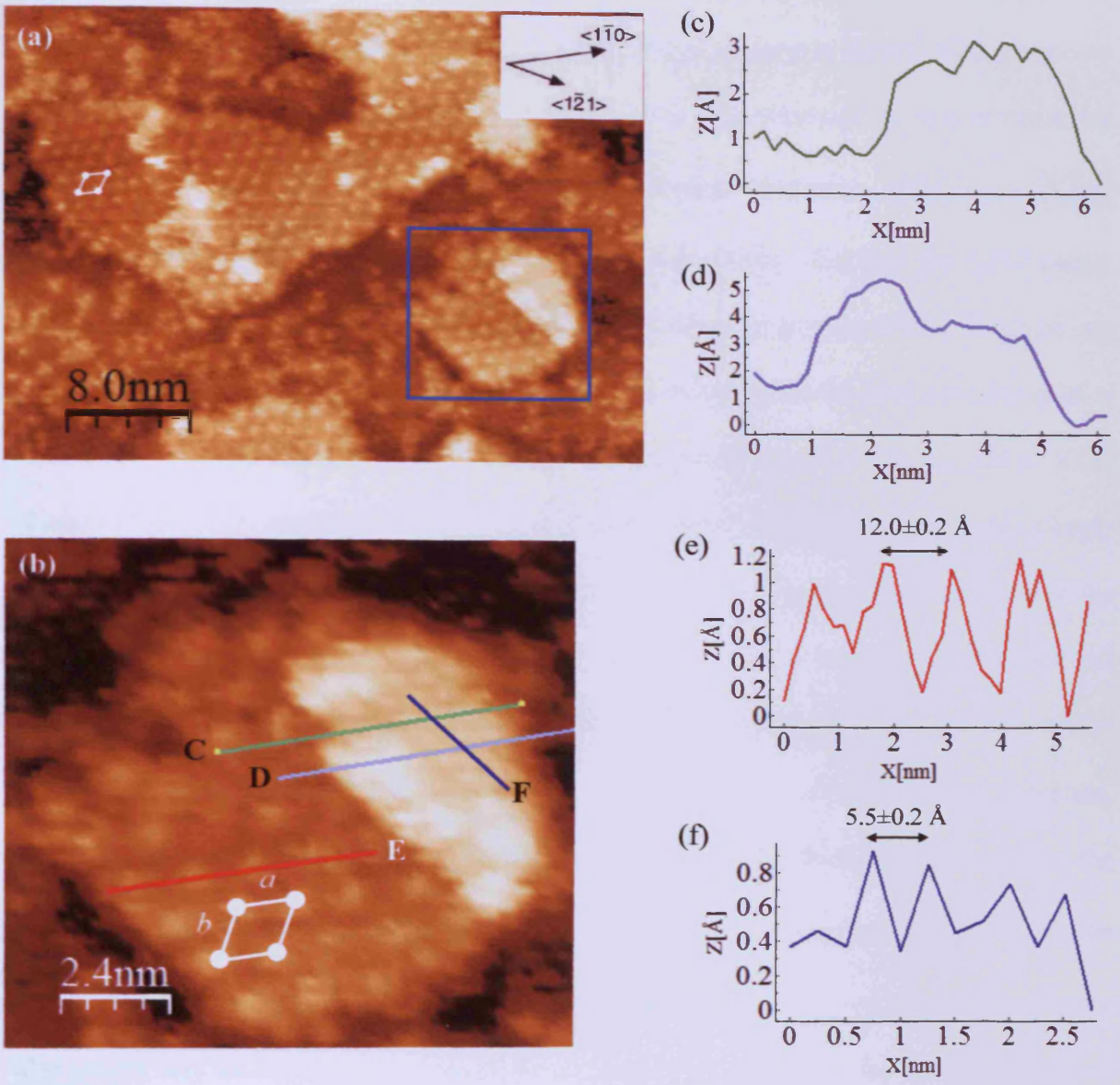

Figure 4.42. STM images of molybdenum oxide on the iron oxide surface at coverage of ~0.5 MLE. (a) High-resolution STM image (400×300 Å^2) recorded at V = 2.6 V, I = 0.54 nA. The multilayer growth of molybdenum oxide is observed. (b) An enlarged view is presented of the area marked by the rectangle in panel (a). Periodic protrusions are evident in both layers. The first layer exhibits a ~12 Å periodicity. (c) and (d) Line profiles along the [1 $\bar{1}$ 0] direction in panel (b). (e) and (f) Line profiles along the lines in panel (b) revealing the ~5.6 Å periodicity of the second layer, smaller than the first layer lattice constant of ~12 Å.

The high-resolution STM image of molybdenum oxide on iron oxide surface at a coverage of ~0.5 MLE is shown in Figure 4.42. The XPS spectra for this film are shown in Figure 4.34(iii) and 4.35(iii). The image shows the presence of two-dimensional islands. Formation of molybdenum oxide clusters running along the $[1\,\bar{1}\,0]$ crystallographic direction of the $Fe_3O_4(111)$ surface is clearly visible in the STM image. As illustrated in Figure 4.42, the islands exhibiting a honeycomb-like structure are formed. The STM image also clearly shows the multilayer growth, with the islands of at least two levels of islands being visible. Figure 4.42(b) displays the magnified STM image of the island acquired at bias of 2.6 V and current of 0.54 nA. The image clearly shows the presence of two coexisting surface phases of the islands. The first layer of the islands in molecular resolution presenting protrusions forms a large hexagonal unit cell while a small quasi-hexagonal lattice is formed over the large hexagonal lattice of the islands. A white diamond with white dots highlights the molecular surface structure, denoting the large hexagonal pattern. These dots have a periodicity of ~12 Å along the side marked *a*, forming molecular rows in the $[1\,\bar{1}\,0]$ crystallographic direction of the $Fe_3O_4(111)$ surface, while the $p(2\times2)$ LEED pattern was still observed as shown in Figure 4.37 which may be due to low coverage of the molybdenum oxide. The line profiles taken along the lines E and F indicated in Figure 4.42(b) show a modulation in the intensity, or height, of the bright features as shown in Figure 4.42(e) and 4.42(f). As the line scan shown in Figure 4.42(f), a new lattice constant of 5.5 Å of the second molybdenum oxide layer, smaller than the first layer lattice constant of ~12 Å is displayed.

Detailed analysis of the data of Figure 4.41 and 4.42 shows that, for line scans along the $[1\,\bar{1}\,0]$ crystallographic direction of $Fe_3O_4(111)$ as shown in Figure 4.41(c), 4.42(c) and 4.42(d), the apparent heights of the bright adsorbates in STM images varied

between 2.0 and 2.5 Å. Along the [1 $\bar{1}$ 0] and [1$\bar{2}$1] crystallographic directions, the spacing between bright features is ~12 Å, as determined from the line profile curve in Figure 4.42(e). This is most likely the result of steric repulsions due to the cluster size. In the high-resolution STM images of a typical terrace (Figure 4.41 and 4.42), the Fe^{3+} positions along [1 $\bar{1}$ 0] direction are resolved. Using these resolved cation positions as references, the bright regions attributed to clusters are centred over alternate of Fe^{3+} cations.

The lattice spacing of the Fe_3O_4(111) surface is 5.94 Å. The unit cell of the molybdenum oxide ordered phase has a separation of ~12 Å along the [1 $\bar{1}$ 0] and [1$\bar{2}$1] directions on the Fe_3O_4(111) surface, which corresponds to twice the lattice spacing of the substrate, i.e., 2×5.94 Å in perfect Fe_3O_4(111). Based on the above results, the proposed models for the ordered molybdenum oxide overlayer are showed later.

ii. The first monolayer of molybdenum oxide on iron oxide

As discussed above, for sub-monolayer of molybdenum oxide, annealing at 873 K results in the formation of molybdenum oxide clusters on the iron oxide single crystal with p(4×4) periodicity which does not correspond to the observed LEED pattern shown in Figure 4.37.

In order to achieve the formation of mixed Fe-Mo oxide, the annealing temperature was increased from 873 to 973 K. Figure 4.43 displays typical large-scale STM images obtained after the deposition of molybdenum oxide on an iron oxide surface followed by post-annealing at temperature of 973 K in the oxygen pressure of 1×10^{-7} mbar for each of the coverages studied. The molybdenum oxide films, from which the XPS spectra as shown in Figure 4.34(iv)-(v), and 4.35(iv)-(v) were obtained, were characterised by STM. The large-scan STM image of ~1.0 MLE MoO_3 coverage in

Figure 4.43(a) generally shows flat terraces, and there is no further evidence of island growth. Step heights of ~5.0 Å are visible in this image, as shown in the line scan in Figure 4.43(c), which is in a good agreement with the ideal $Fe_3O_4(111)$ step height value of 4.8 Å. Very sharp $(2\sqrt{3}\times 2\sqrt{3})R30°$ LEED pattern, as shown in Figure 4.38, of this film was observed and is distinctly different from that found for the molybdenum oxide sub-monolayer after annealing to 873 K. The lattice parameters of the (111) plane calculated from the LEED images have been determined to be approximately 10 Å.

A further increase in the molybdenum oxide coverage, (Figure 4.43(b), ~1.5 MLE MoO_3) leads to growth of molybdenum oxide multilayer. The XPS spectrum in Figure 4.34(iv) reveals the presence of only Mo^{6+} oxidation state and the $(2\sqrt{3}\times 2\sqrt{3})R30°$ LEED pattern was observed as shown in Figure 4.38. Figure 4.43(b) shows a typical STM image (100×100 nm^2) of the film at the molybdenum oxide multilayer coverage on iron oxide. It shows that the flat terraces were fully covered with molybdenum oxide. The terraces are mostly separated by about 5.0 Å as shown in Figure 4.43(d). A step height of ~5.0 Å well corresponds to the height of a step of the $Fe_3O_4(111)$ surface. The STM results imply that the initial growth of molybdenum oxide thin films proceeds via layer-by-layer mode.

The molybdenum oxide structures formed on the iron oxide were studied by high-resolution STM measurement. Figure 4.44(a) displays a high-resolution constant-current STM image (220×220 $Å^2$) of molybdenum oxide layer on the iron oxide surface at a bias of +1.2 V. The iron oxide surface is mostly covered by molybdenum oxide and is composed of the molecularly flat terrace structures, and these are free of pits, islands, and any other surface defects. An interesting feature in the image is a well-ordered structure, which forms a near-hexagonal pattern and extends all over the iron oxide surface. The

unit cell, as the marked diamond in Figure 4.44(a), has the parameters of ~10 Å, almost $2\sqrt{3}$ times of the underlying close-packed oxygen layer that is present in the (111) crystallographic planes of Fe_3O_4. Moreover, the rows of molybdenum oxide cross each other at an angle of ~30 degrees. The line profiles shown in Figure 4.44(b) and 4.44(c), taken along the (A-A) and (B-B) lines in Figure 4.44(a), reveal the 10.4 Å and 11.2 Å periodicities, respectively.

(a) ~1.0 MLE MoO_3 after heating at 973 K **(b) ~1.5 MLE MoO_3 after heating at 973 K**

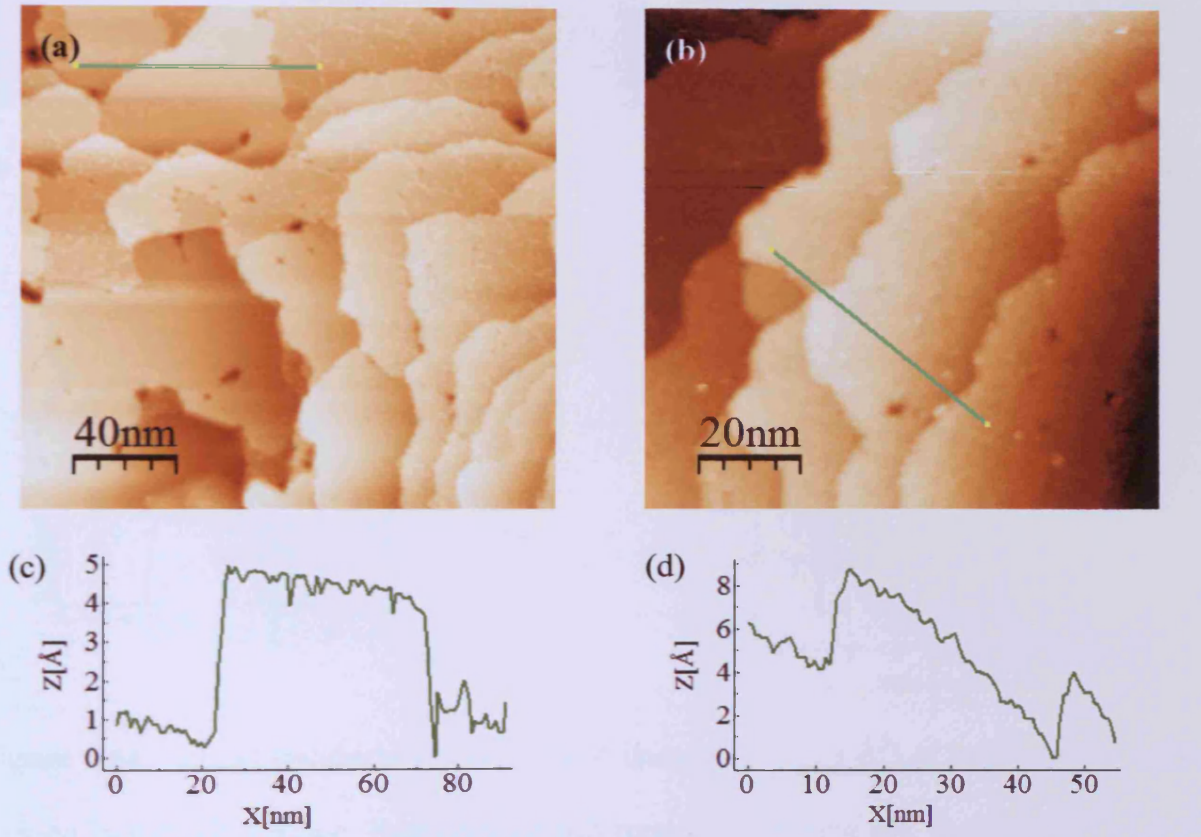

Figure 4.43. Large-scale STM images taken in constant current mode of a well-ordered molybdenum oxide layer on the iron oxide surface at room temperature followed by post-annealing at 973 K: (a) 200×200 nm^2 image taken for ~1.0 MLE of molybdenum oxide. The current is 0.37 nA, and the sample bias voltage is 1.2 V. (b) 100×100 nm^2 image taken for ~1.5 MLE of molybdenum oxide. The current is 0.47 nA, and the sample bias voltage is 1.5 V. (c) and (d) Line profiles from the image in (a) and (b), respectively.

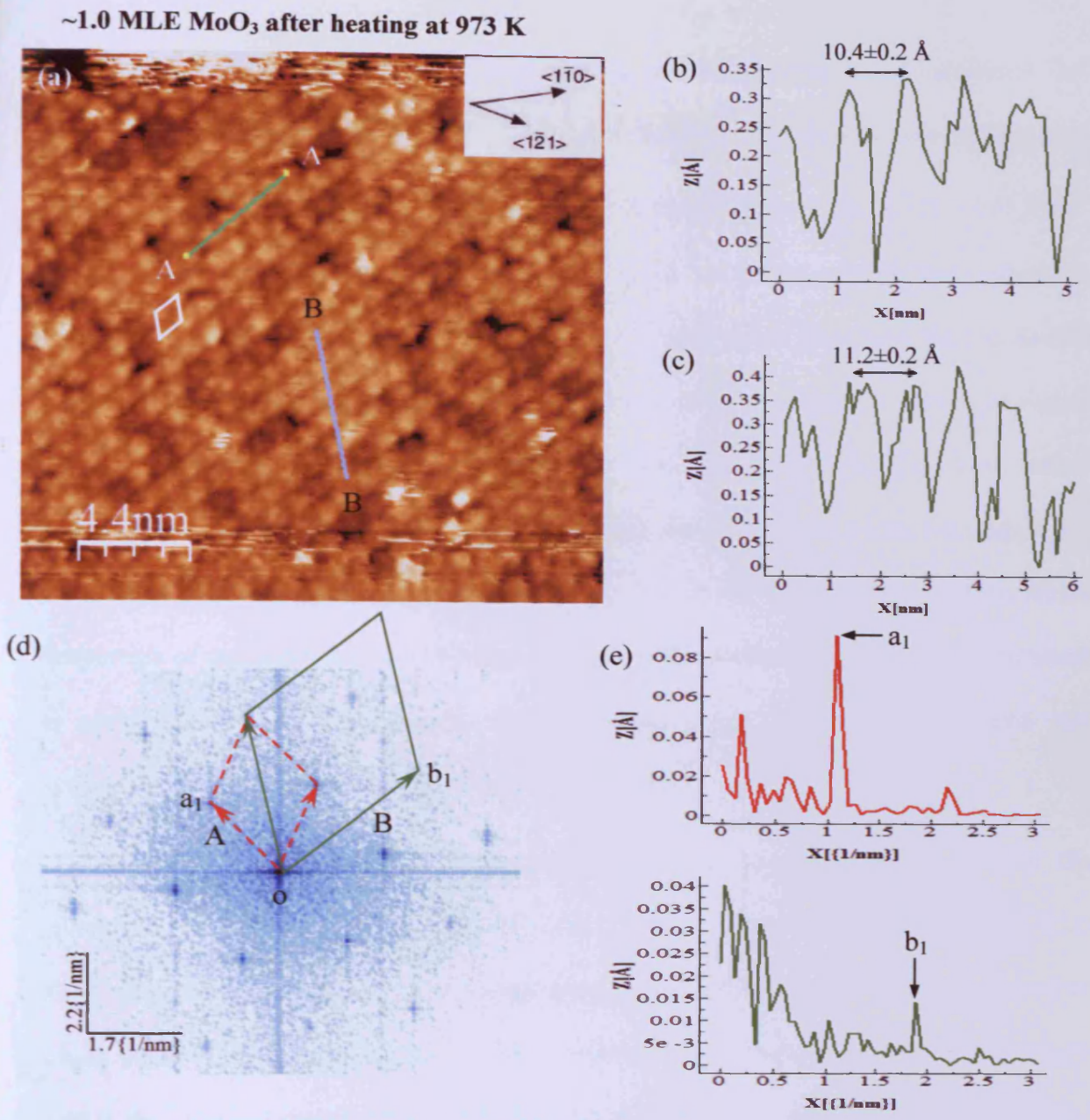

Figure 4.44. (a) Molecularly resolved STM image (220×220 Å^2) of molybdenum oxide film on iron oxide surface. Sample bias and tunnelling current are, respectively, +1.2 V and 0.38 nA. The white diamond frame shows one unit cell. (b) and (c) Line profiles shown in (b) and (c) taken along a line (A-A) and (B-B), respectively. (d) 2D fast Fourier transform (FFT) maps of the STM image (a). Fourier transform of the lattice model gives a simulation of the LEED pattern for one domain of this oxide on the iron oxide. The green line indicates the substrate (2×2) structure, and the red dashed line corresponds to the new overlayer structure. (e) 2D-FFT profiles along each line in the 2D-FFT map.

To investigate the atomic and molecular periodicity, the two-dimensional fast Fourier transform (FFT) (Figure 4.44(d)) and its profile curves (Figure 4.44(e) and 4.44(f)) were obtained from the STM image corresponding to the $(2\sqrt{3}\times 2\sqrt{3})R30°$ LEED pattern as shown in Figure 4.38. This Fourier transform exhibits both substrates and overlayer spots. Substrate spots are connected with green lines, and the red dashed 'diamond' outline corresponds to the molybdenum oxide overlayer as shown in Figure 4.44(d). The blue spots in Figure 4.44(d) indicate the Bragg peaks from the basic lattice structures of the STM image. From Figure 4.44(d), the main peaks of the red dashed (A) and green (B) profiles show ~6 Å and ~10 Å, respectively, which corresponds to lattice parameters of the substrate and overlayer, respectively, observed by LEED measurement as mentioned in previous section. The azimuthal angle between the substrate and overlayer structure is around 30 degrees.

Figure 4.45(a) shows a high resolution STM image (120×120 $Å^2$) of the molybdenum oxide layer on iron oxide surface at a coverage of ~1.5 MLE MoO_3 after 973 K annealing temperature. This image shows the molybdenum oxide covered surface which consists of atomically flat terraces separated by a step. The image (b) in Figure 4.45 is the enlarged image of area indicated by the box in the top of Figure 4.45(a), taken at bias of +1.5 V and current of 0.47 nA. It shows that the quasi-hexagonal-shaped atomic distribution highlighted by the white diamond is visible. The profile curves shown in Figure 4.45(c) and 4.45(d), taken along the green (C) and blue (D) lines in Figure 4.45(b), reveal the 5.0 Å and 4.5 Å periodicities, respectively. This distance is smaller than the lattice parameter period observed on the second molybdenum oxide layer as shown in Figure 4.42.

~1.5 MLE MoO_3 after heating at 973 K

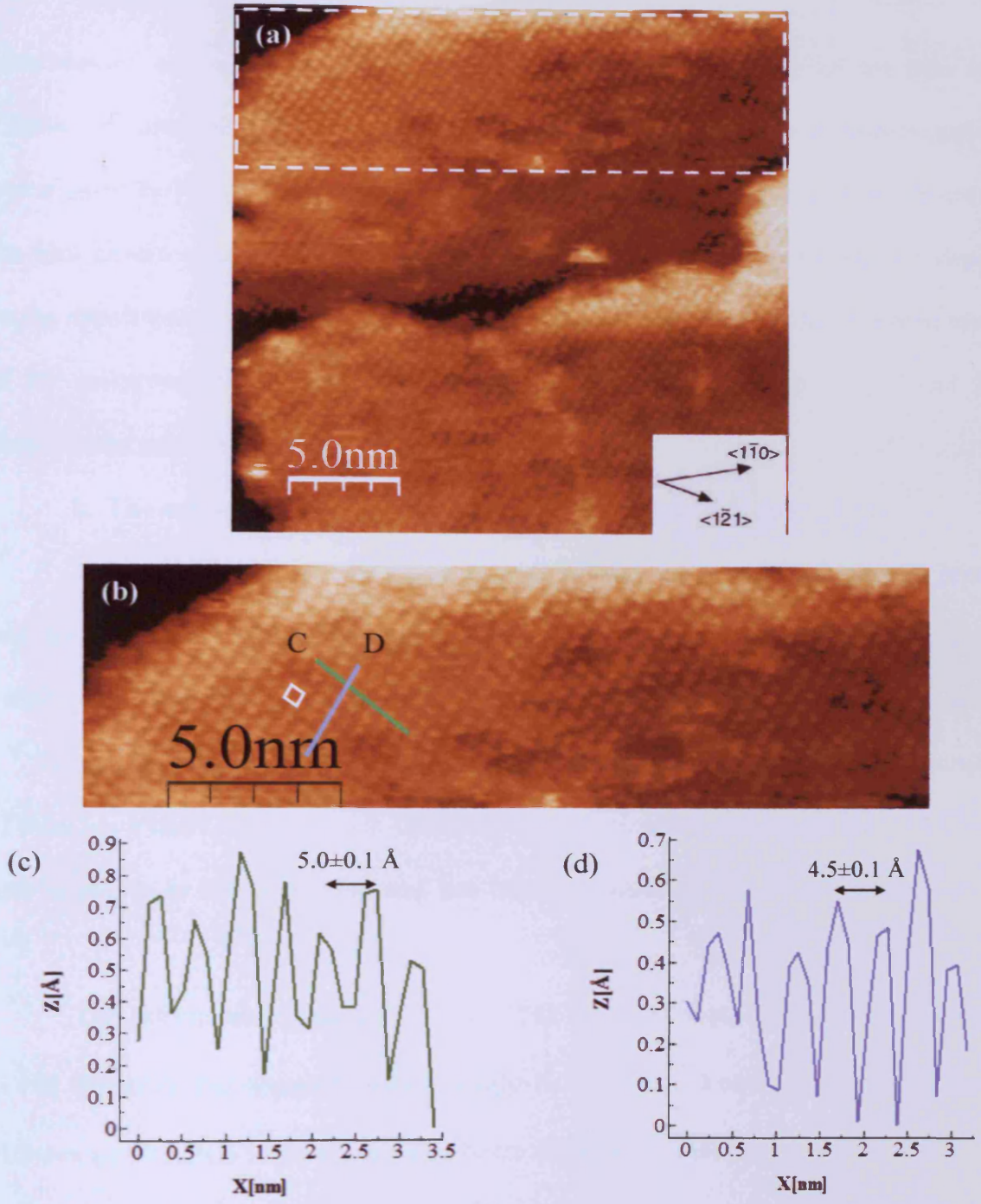

Figure 4.45. (a) STM image (250×250 Å^2) of the molybdenum oxide film on the iron oxide surface at coverage of ~1.5 MLE. The average current was 0.47 nA, and the sample bias voltage was 1.5 V. (b) An enlarged image of area marked by the rectangle in panel (a). The white diamond shape shows one unit cell. (c) and (d) line profiles along the green (C) and blue (D) lines, respectively, in panel (b).

4.4.6. Proposed models of the structures

Under different coverages of molybdenum oxide, the growth mechanism of molybdenum oxide islands after deposition of molybdenum oxide on the iron oxide followed by annealing in oxygen pressure of 1×10^{-7} mbar at different temperatures was investigated by XPS, LEED, and STM. From the experimental results, it was found that the film growth of molybdenum oxide upon the iron oxide annealed in oxygen depends on the molybdenum oxide coverage and the annealing temperature. The structural models of the molybdenum oxide film are proposed that are based on the LEED and STM observations presented above.

i. The sub-monolayer of molybdenum oxide on iron oxide

The oxidation of the molybdenum at low temperature and high oxygen pressure can generate the gaseous dioxide and trioxide, $MoO_2(g)$ and $MoO_3(g)$, and their polymeric oxides, $(MoO_3)_2(g)$ and $(MoO_3)_3(g)$, with the preference given to the trimers [89]. The gas-phase $(MoO_3)_3$ trimer is cyclic with D_{3h} symmetry [107, 108]. The ring structure of $(MoO_3)_3$ trimers is a planar six-membered ring formed by replicating the (–MoO_2–O–) unit as shown in Figure 4.46(a) and has been suggested as the lowest-energy structure [109].

The information provided by the STM suggests that, for line scans along the $[1\,\bar{1}\,0]$ direction, the apparent cluster height is between 2.0 and 2.5 Å and the spacing between nanoclusters is never less than twice the spacing between neighbouring Fe^{3+}, i.e. 2×5.94 Å in perfect $Fe_3O_4(111)$. The XPS results as shown in Figure 4.34(i)-(iii) reveal the presence of Mo^{6+} oxidation state only. Therefore, for sub-monolayer coverage of molybdenum oxide, the cyclic $(MoO_3)_3$ trimers presumably are formed at the iron oxide surfaces, i.e., the bright spots are monodispersed $(MoO_3)_3$ trimer clusters. Before annealing, these appear to be disordered, but order upon annealing.

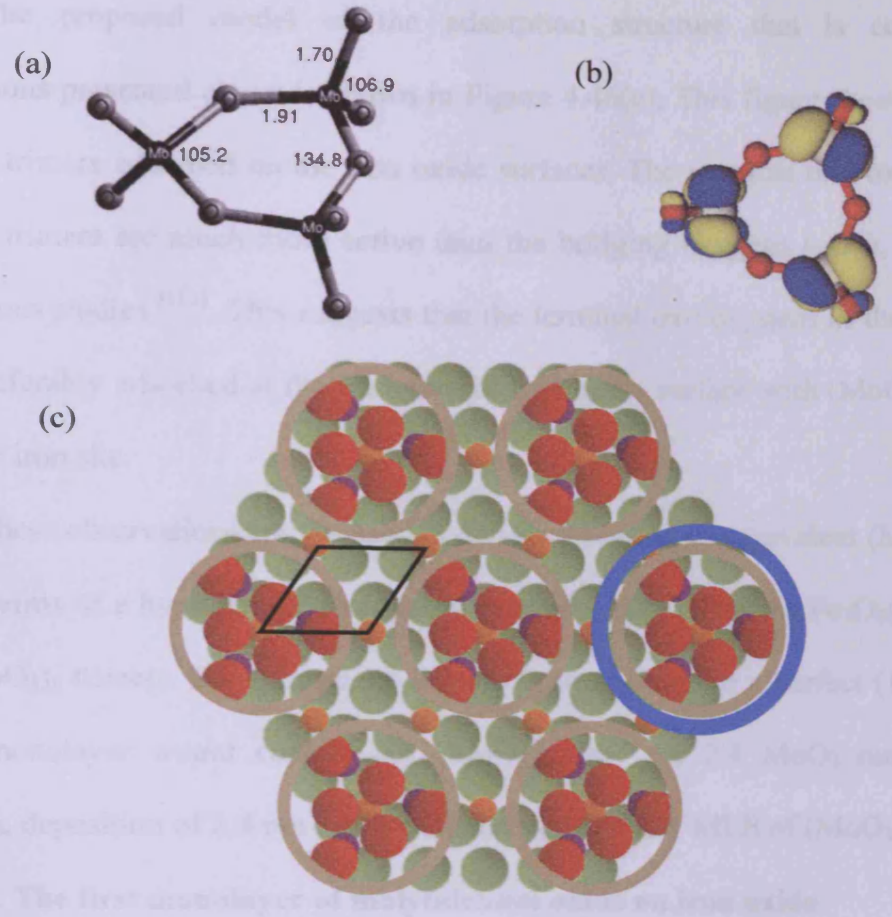

Figure 4.46. (a) Cyclic structure of gas-phase $(MoO_3)_3$ trimers. Selected geometrical parameters (bond lengths and angles) are shown together in Å and in degrees, respectively [110]. (b) One of the empty low-lying out-of-plane molecular orbitals of $(MoO_3)_3$ [107] expected to be the accepting states in the high-resolution STM images of $(MoO_3)_3$. (c) Schematically shown the proposed model of the cyclic $(MoO_3)_3$ trimers adsorbed on the $Fe_3O_4(111)$ surfaces (small brown circles: Fe^{3+}; green circles: first-layer oxygen; red circles: second-layer oxygen; small purple circles: Mo^{6+}). The orientation of the top cluster is identical with that shown in part (b). $(MoO_3)_3$ clusters are shown having the plane of the rings located on top of the Fe^{3+} cations. The hexagonal surface unit cell of $Fe_3O_4(111)$ is indicated. The gray thick shaded lines represent the van der Waals contour of cyclic $(MoO_3)_3$ clusters. An expanded view of one cell is also shown by the bright blue thick shaded line.

The proposed model of the adsorption structure that is consistent with observations presented above is shown in Figure 4.46(c). This figure shows seven cyclic $(MoO_3)_3$ trimers adsorbed on the iron oxide surfaces. The terminal oxo oxygens (=O) in $(MoO_3)_3$ trimers are much more active than the bridging oxygens (–O–), as reported in the previous studies [110]. This suggests that the terminal oxo oxygens of the molybdenum site is preferably adsorbed at the iron sites of iron oxide surface with $(MoO_3)_3$ trimers on top of the iron site.

These observations can be used to define a monolayer equivalent (MLE) coverage scale in terms of a hypothetical structure that would fully cover the $Fe_3O_4(111)$ substrate with $(MoO_3)_3$ trimers. Since there are 3.3 Fe^{3+} cations nm^{-2} in a perfect (111) surface, a perfect monolayer would contain 0.8 $(MoO_3)_3$ nm^{-2} (or 2.4 MoO_3 nm^{-2}). With this definition, deposition of 2.4 nm^{-2} of MoO_3 corresponds to 1 MLE of $(MoO_3)_3$ trimers.

ii. The first monolayer of molybdenum oxide on iron oxide

Considering that the (111) plane of Fe_3O_4, is preferentially exposed [86], in each unit mesh of Fe_3O_4, besides one of the tetrahedral vacancies that have been occupied by Fe^{3+}_{tet1} ions, there are two tetrahedral and three octahedral vacant sites left for the Mo^{6+} ions to incorporate in and the surface Mo species can be formed. In the proposed models, two kinds of Mo species with different coordination environments could be formed: Mo^{6+} ions in the tetrahedral vacant sites, and Mo^{6+} ions in the octahedral vacant sites. Figure 4.47 shows the proposed models of the molybdenum oxide adsorption on the $Fe_3O_4(111)$ surface. Considering the ratio between the surface vacancies (tetrahedral vacancies/octahedral vacancies) being 2:3, there is a higher possibility of Mo^{6+} ions entering the octahedral vacancies with low MoO_3 loading. A possibility of Mo ions enters the tetrahedral vacant sites or enters the octahedral vacancies, which 5 vacant sites exist in a surface unit mesh of this plane. Unfortunately, we could not get the high-resolution

STM images for molybdenum oxide film which show more detail on the surface. We therefore cannot identify the coordination environments of Mo^{6+} ions.

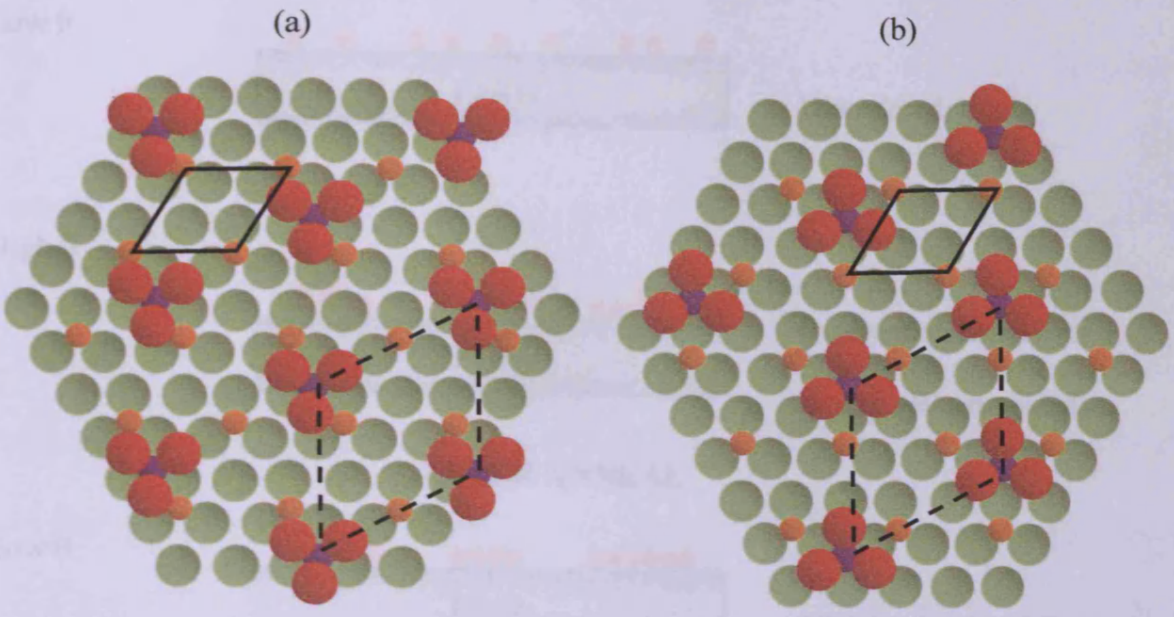

Figure 4.47. Schematically shown the proposed model of the MoO_3 adsorbed on the $Fe_3O_4(111)$ surfaces (small brown spheres: Fe^{3+}; green spheres: first-layer oxygen; red spheres: second-layer oxygen; small purple spheres: Mo^{6+}). (a) Molybdenum oxides enter the tetrahedral vacant sites. (b) Molybdenum oxides enter the octahedral vacant sites.

From the XPS, LEED and STM results, the growth of the molybdenum oxide film can be summarised in Figure 4.48. This shows the possible model of the molybdenum oxide grown on the $Fe_3O_4(111)$ surface. As shown in Figure 4.48, after the molybdenum oxide deposition, the molybdenum oxides are adsorbed and continue to grow to form large disordered islands on the $Fe_3O_4(111)$ surface. The large molybdenum oxide islands coalesce together to form continuous films. After annealing, the iron molybdates may be form and grow in two-dimensional islands at low coverage while, at higher coverage, the three-dimensional islands of molybdates are formed as shown in Figure 4.48.

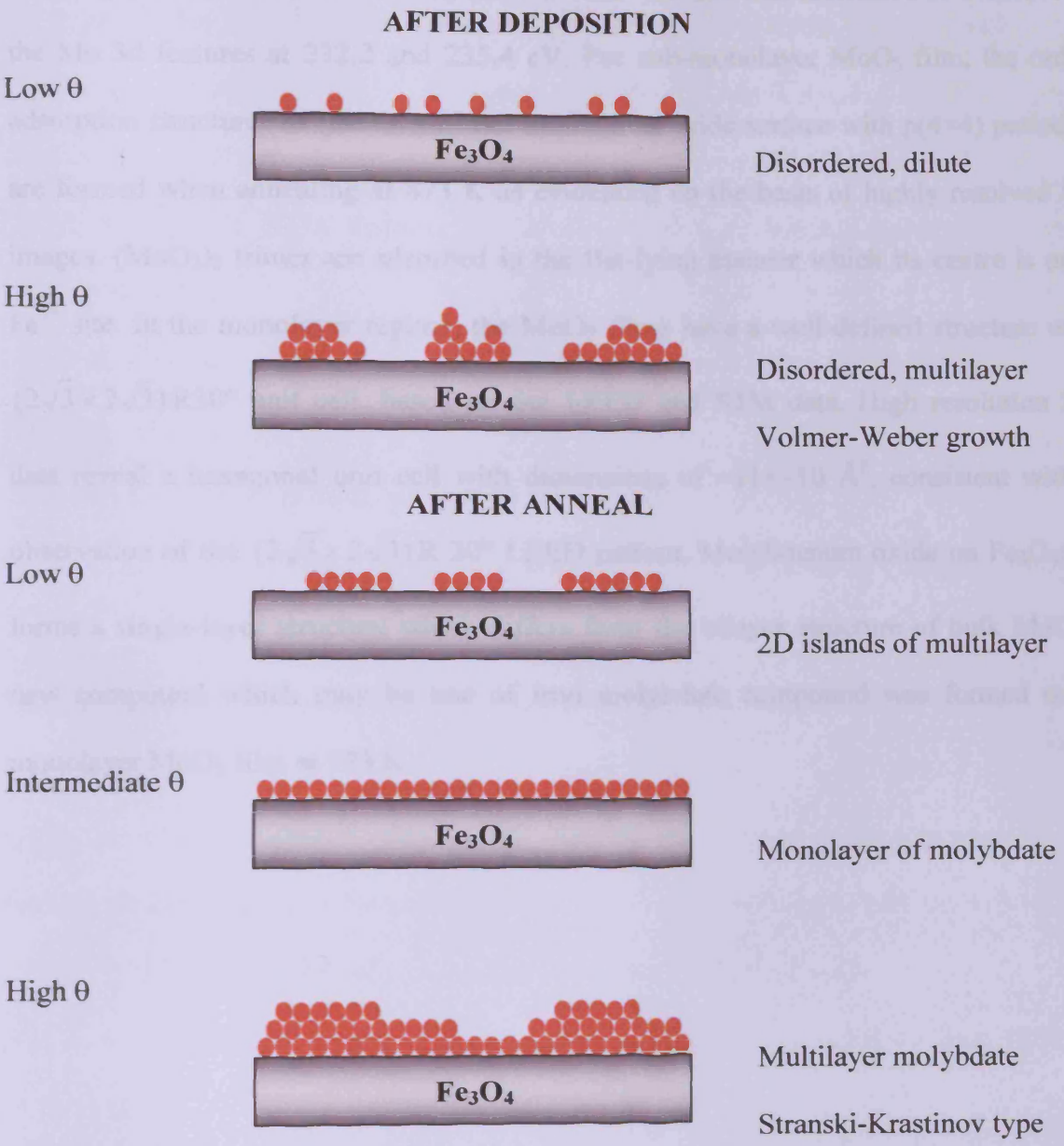

Figure 4.48. The possible model for the growth of molybdenum oxide films on the $Fe_3O_4(111)$ surface. The red circles represent molybdenum oxides adsorbed on the $Fe_3O_4(111)$ surface.

4.5. Conclusions

Molybdenum oxide film deposition on iron oxide single crystal was achieved using the hot-filament metal oxide deposition technique, and subsequent annealing in an

oxygen pressure of 1×10^{-7} mbar at 973 K gave a model surface of iron oxide modified by the molybdenum oxide. The MoO_3 on iron oxide surface was fabricated as evidenced by the Mo 3d features at 232.2 and 235.4 eV. For sub-monolayer MoO_3 film, the ordered adsorption structures of $(MoO_3)_3$ trimer on the iron oxide surface with p(4×4) periodicity are formed when annealing at 873 K as evidenced on the basis of highly resolved STM images. $(MoO_3)_3$ trimer are adsorbed in the flat-lying manner which its centre is on the Fe^{3+} site. In the monolayer regime, the MoO_3 films have a well-defined structure with a $(2\sqrt{3}\times2\sqrt{3})R30°$ unit cell, based on our LEED and STM data. High resolution STM data reveal a hexagonal unit cell with dimensions of ~11×~10 $Å^2$, consistent with the observation of the $(2\sqrt{3}\times2\sqrt{3})R\ 30°$ LEED pattern. Molybdenum oxide on $Fe_3O_4(111)$ forms a single-layer structure which differs from the bilayer structure of bulk MoO_3. A new compound which may be one of iron molybdate compound was formed on the monolayer MoO_3 film at 973 K.

4.6. References

[1] Y. Matsuoka, M. Niwa and Y. Murakami, *J. Phys. Chem.* **1990**, *94*, 1477-1482.

[2] T. Ono, H. Miyata and Y. Kubokawa, *Journal of the Chemical Society, Faraday Transactions 1: Physical Chemistry in Condensed Phases* **1987**, *83*, 1761-1770.

[3] M. A. Banares, N. D. Spencer, M. D. Jones and I. E. Wachs, *Journal of Catalysis* **1994**, *146*, 204-210.

[4] A. N. Desikan, W. M. Zhang and S. T. Oyama, *Journal of Catalysis* **1995**, *157*, 740-748.

[5] P. Grange, *Catalysis Reviews* **1980**, *21*, 135 - 181.

[6] Y. C. Liu, G. L. Griffin, S. S. Chan and I. E. Wachs, *Journal of Catalysis* **1985**, *94*, 108-119.

[7] C. Louis, J.-M. Tatibouet and M. Che, *Journal of Catalysis* **1988**, *109*, 354-366.

[8] I. Matsuura, H. Oda and K. Oshida, *Catalysis Today* **1993**, *16*, 547-554.

[9] H. Miyata, T. Mukai, T. Ono and Y. Kubokawa, *Journal of the Chemical Society, Faraday Transactions 1: Physical Chemistry in Condensed Phases* **1988**, *84*, 4137-4143.

[10] K. Y. S. Ng and E. Gulari, *Journal of Catalysis* **1985**, *95*, 33-40.

[11] R. B. Quincy, M. Houalla, A. Proctor and D. M. Hercules, *J. Phys. Chem.* **1990**, *94*, 1520-1526.

[12] B. M. Reddy, K. V. R. Chary, V. S. Subrahmanyam and N. K. Nag, *Journal of the Chemical Society, Faraday Transactions 1: Physical Chemistry in Condensed Phases* **1985**, *81*, 1655-1667.

[13] N. D. Spencer in *Process and catalyst for the production of formaldehyde from methane, Vol. 4607127* GRACE W R & CO (US), United States, **1986**.

[14] N. D. Spencer and C. J. Pereira, *AIChE Journal* **1987**, *33*, 1808-1812.

[15] N. D. Spencer, *Journal of Catalysis* **1988**, *109*, 187-197.

[16] W. Zhang, A. Desikan and S. T. Oyama, *J. Phys. Chem.* **1995**, *99*, 14468-14476.

[17] F. Barath, M. Turki, V. Keller and G. Maire, *Journal of Catalysis* **1999**, *185*, 1-11.

[18] N. K. Nag, *Journal of Catalysis* **1985**, *92*, 432-437.

[19] Y. V. Plyuto, I. V. Babich, I. V. Plyuto, A. D. Van Langeveld and J. A. Moulijn, *Applied Surface Science* **1997**, *119*, 11-18.

[20] Z. Vit and M. Zdrazil, *Journal of Catalysis* **1997**, *171*, 305-312.

[21] X. Wang, B. Zhao, D.-e. Jiang and Y. Xie, *Applied Catalysis A: General* **1999**, *188*, 201-209.

[22] F. Arena and A. Parmaliana, *J. Phys. Chem.* **1996**, *100*, 19994-20005.

[23] Y. Kikutani, *Journal of Molecular Catalysis A: Chemical* **1999**, *142*, 265-274.

[24] S. T. Oyama and W. Zhang, *J. Am. Chem. Soc.* **1996**, *118*, 7173-7177.

[25] D. S. Kim, K. Segawa, T. Soeya and I. E. Wachs, *Journal of Catalysis* **1992**, *136*, 539-553.

[26] T. Machej, B. Doumain, B. Yasse and B. Delmon, *Journal of the Chemical Society, Faraday Transactions 1: Physical Chemistry in Condensed Phases* **1988**, *84*, 3905-3916.

[27] A. Calafat, L. Avilan and J. Aldana, *Applied Catalysis A: General* **2000**, *201*, 215-223.

[28] K. V. R. Chary, K. R. Reddy, G. Kishan, J. W. Niemantsverdriet and G. Mestl, *Journal of Catalysis* **2004**, *226*, 283-291.

[29] K. Chen, S. Xie, E. Iglesia and A. T. Bell, *Journal of Catalysis* **2000**, *189*, 421-430.

[30] V. Indovina, *Catalysis Today* **1998**, *41*, 95-109.

[31] E. H. Lee, *Catalysis Reviews* **1974**, *8*, 285 - 305.

[32] M. Muhler, R. Schlogl and G. Ertl, *Journal of Catalysis* **1992**, *138*, 413-444.

[33] H. Adkins and W. R. Peterson, *J. Am. Chem. Soc.* **1931**, *53*, 1512-1520.

[34] N. Pernicone, *Journal of the Less Common Metals* **1974**, *36*, 289-297.

[35] M. Carbucicchio and F. Trifiro, *Journal of Catalysis* **1976**, *45*, 77-85.

[36] D. G. Klissurski and M. M. Kancheva, *Journal of the Chemical Society, Faraday Transactions 1: Physical Chemistry in Condensed Phases* **1981**, *77*, 1795-1801.

[37] Y. Okamoto, F. Morikawa, K. Oh-Hiraki, T. Imanaka and S. Teranishi, *Journal of the Chemical Society, Chemical Communications* **1981**, 1018-1019.

[38] F. Trifiro, V. De Vecchi and I. Pasquon, *Journal of Catalysis* **1969**, *15*, 8-16.

[39] F. Trifiro, S. Notarbartolo and I. Pasquon, *Journal of Catalysis* **1971**, *22*, 324-332.

[40] N. N. Greenwood and A. Earnshaw, *Chemistry of the elements*, Butterworth-Heinemann, Oxford, **1997**.

[41] V. E. Henrich and P. A. Cox, *The surface science of metal oxides*, Cambridge University Press, Cambridge, **1994**.

[42] D. Y. Geng, Z. D. Zhang, M. Zhang, D. Li, X. P. Song and K. Y. Hu, *Scripta Materialia* **2004**, *50*, 983-986.

[43] C. Julien, A. Khelfa, O. M. Hussain and G. A. Nazri, *Journal of Crystal Growth* **1995**, *156*, 235-244.

[44] O. Y. Khyzhun, T. Strunskus and Y. M. Solonin, *Journal of Alloys and Compounds* **2004**, *366*, 54-60.

[45] L. Kihlborg, *Arkiv foer Kemi* **1963**, *21*, 357-364.

[46] C. V. Ramana, V. V. Atuchin, V. G. Kesler, V. A. Kochubey, L. D. Pokrovsky, V. Shutthanandan, U. Becker and R. C. Ewing, *Applied Surface Science* **2007**, *253*, 5368-5374.

[47] M. Sing, R. Neudert, H. von Lips, M. S. Golden, M. Knupfer, J. Fink, R. Claessen, J. Mücke, H. Schmitt, S. Hüfner, B. Lommel, W. Aßmus, C. Jung and C. Hellwig, *Physical Review B* **1999**, *60*, 8559.

[48] R. Tokarz-Sobieraj, K. Hermann, M. Witko, A. Blume, G. Mestl and R. Schlogl, *Surface Science* **2001**, *489*, 107-125.

[49] A. Michalak, K. Hermann and M. Witko, *Surface Science* **1996**, *366*, 323-336.

[50] A. Papakondylis and P. Sautet, *The Journal of Physical Chemistry* **1996**, *100*, 10681-10688.

[51] A. D. Sayede, T. Amriou, M. Pernisek, B. Khelifa and C. Mathieu, *Chemical Physics* **2005**, *316*, 72-82.

[52] E. M. McCarron, *Journal of the Chemical Society, Chemical Communications* **1986**, 336-338.

[53] B. G. Brandt and A. C. Skapski, *Acta Chemica Scandinavica* **1967**, *21*, 661-672.

[54] A. K. Santra, B. K. Min and D. W. Goodman, *Surface Science* **2002**, *513*, L441-L444.

[55] A. Magneli and G. Andersson, *Acta Chemica Scandinavica* **1955**, *9*, 1378-1381.

[56] A. W. Sleight, B. L. Chamberland and J. F. Weiher, *Inorg. Chem.* **1968**, *7*, 1093-1098.

[57] A. P. Young and C. M. Schwartz, *Science* **1963**, *141*, 348-349.

[58] M. H. Rapposch, J. B. Anderson and E. Kostiner, *Inorganic Chemistry* **1980**, *19*, 3531-3539.

[59] A. W. Sleight and B. L. Chamberland, *Inorg. Chem.* **1968**, *7*, 1672-1675.

[60] C. Gleitzer and J. B. Goodenough, *J. Mater. Sci. Lett. FIELD Full Journal Title:Journal of Materials Science Letters* **1987**, *6*, 939-941.

[61] G. W. Smith and J. A. Ibers, *Acta Crystallographica* **1965**, *19*, 269-275.

[62] S. C. Abrahams and J. M. Reddy, *The Journal of Chemical Physics* **1965**, *43*, 2533-2543.

[63] J. A. Rodriguez, J. C. Hanson, S. Chaturvedi, A. Maiti and J. L. Brito, *J. Phys. Chem. B* **2000**, *104*, 8145-8152.

[64] S. T. Ochsenbein, G. Chaboussant, A. Sieber, H. U. Güdel, S. Janssen, A. Furrer and J. P. Attfield, *Physical Review B* **2003**, *68*, 092410.

[65] J. A. Rodriguez, J. C. Hanson, S. Chaturvedi, A. Maiti and J. L. Brito, *The Journal of Physical Chemistry B* **2000**, *104*, 8145-8152.

[66] H. Ehrenberg, G. Wltschek, F. Trouw, T. Kroener, H. Weitzel and H. Fuess, *Journal of Magnetism and Magnetic Materials* **1994**, *135*, 355-360.

[67] A. W. Sleight and M. S. Licis, *Materials Research Bulletin* **1971**, *6*, 365-369.

[68] H.-y. Chen, *Materials Research Bulletin* **1979**, *14*, 1583-1590.

[69] G. J. Long, G. Longworth, P. Battle, A. K. Cheetham, R. V. Thundathil and D. Beveridge, *Inorg. Chem.* **1979**, *18*, 624-632.

[70] Z. Jirak, R. Salmon, L. Fournes, F. Menil and P. Hagenmuller, *Inorg. Chem.* **1982**, *21*, 4218-4223.

[71] V. Massarotti, G. Flor and A. Marini, *Journal of Applied Crystallography* **1981**, *14*, 64-65.

[72] A. W. Sleight and L. H. Brixner, *Journal of Solid State Chemistry* **1973**, *7*, 172-174.

[73] Y. Huang, L. Cong, J. Yu, P. Eloy and P. Ruiz, *Journal of Molecular Catalysis A: Chemical* **2009**, *302*, 48-53.

[74] S. D. M. Jacques, O. Leynaud, D. Strusevich, A. M. Beale, G. Sankar, C. M. Martin and P. Barnes, *Angewandte Chemie International Edition* **2006**, *45*, 445-448.

[75] A. P. V. Soares, M. F. Portela and A. Kiennemann, *Catalysis Reviews: Science and Engineering* **2005**, *47*, 125 - 174.

[76] A. P. V. Soares, M. Farinha Portela, A. Kiennemann, L. Hilaire and J. M. M. Millet, *Applied Catalysis A: General* **2001**, *206*, 221-229.

[77] M. P. House, A. F. Carley, R. Echeverria-Valda and M. Bowker, *The Journal of Physical Chemistry C* **2008**, *112*, 4333-4341.

[78] J. G. Choi and L. T. Thompson, *Applied Surface Science* **1996**, *93*, 143-149.

[79] P. Gajardo, D. Pirotte, C. Defosse, P. Grange and B. Delmon, *Journal of Electron Spectroscopy and Related Phenomena* **1979**, *17*, 121-135.

[80] T.-J. Yang and J. H. Lunsford, *Journal of Catalysis* **1987**, *103*, 55-64.

[81] Y. Sakashita, *Surface Science* **2001**, *489*, 45-58.

[82] A. R. Lennie, N. G. Condon, F. M. Leibsle, P. W. Murray, G. Thornton and D. J. Vaughan, *Physical Review B* **1996**, *53*, 10244-10253.

[83] M. Ritter and W. Weiss, *Surface Science* **1999**, *432*, 81-94.

[84] S. K. Shaikhutdinov, M. Ritter, X. G. Wang, H. Over and W. Weiss, *Physical Review B* **1999**, *60*, 11062-11069.

[85] W. Weiss, A. Barbieri, M. A. Van Hove and G. A. Somorjai, *Physical Review Letters* **1993**, *71*, 1848-1851.

[86] W. Weiss and W. Ranke, *Progress in Surface Science* **2002**, *70*, 1-151.

[87] M. A. Bica De Moraes, B. C. Trasferetti, F. P. Rouxinol, R. Landers, S. F. Durrant, J. Scarmi?nio and A. Urbano, *Chemistry of Materials* **2004**, *16*, 513-520.

[88] T. Saburi, H. Murata, T. Suzuki, Y. Fujii and K. Kiuchi, *Journal of Plasma and Fusion Research* **2002**, *78*, 3-4.

[89] J. B. Berkowitz-Mattuck, A. Buchler, J. L. Engelke and S. N. Goldstein, *The Journal of Chemical Physics* **1963**, *39*, 2722-2730.

[90] C. J. Powell, A. Jablonski, I. S. Tilinin, S. Tanuma and D. R. Penn, *Journal of Electron Spectroscopy and Related Phenomena* **1999**, *98-99*, 1-15.

[91] S. Tanuma, C. J. Powell and D. R. Penn, *Surface and Interface Analysis* **1994**, *21*, 165-176.

[92] M. Itoh, K. Hayakawa and S. Oishi, *Journal of Physics: Condensed Matter* **2001**, *13*, 6853-6864.

[93] P. A. Spevack and N. S. McIntyre, *J. Phys. Chem.* **1992**, *96*, 9029-9035.

[94] Z. Song, T. Cai, Z. Chang, G. Liu, J. A. Rodriguez and J. Hrbek, *Journal of the American Chemical Society* **2003**, *125*, 8059-8066.

[95] C. D. Wagner, W. M. Riggs, L. E. Davis, J. F. Moulder and G. E. Muilenberg, *Handbook of x-ray photoelectron spectroscopy*, Perkin-Elmer, Eden Prairie, Minnesota, **1979**.

[96] A. P. V. Soares, M. F. Portela, A. Kiennemann and L. Hilaire, *Chemical Engineering Science* **2003**, *58*, 1315-1322.

[97] G. D. Waddill and O. Ozturk, *Surface Science* **2005**, *575*, 35-50.

[98] T. H. Fleisch and G. J. Mains, *The Journal of Chemical Physics* **1982**, *76*, 780-786.

[99] S. W. Gaarenstroom and N. Winograd, *The Journal of Chemical Physics* **1977**, *67*, 3500-3506.

[100] J. F. Moulder, W. F. Stickle, P. E. Sobol and K. D. Bomben, *Handbook of x-ray photoelectron spectroscopy*, Perkin-Elmer Corp., Eden Prairie, MN, **1992**.

[101] J. F. Weaver and G. B. Hoflund, *The Journal of Physical Chemistry* **1994**, *98*, 8519-8524.

[102] X. Deng, S. Y. Quek, M. M. Biener, J. Biener, D. H. Kang, R. Schalek, E. Kaxiras and C. M. Friend, *Surface Science* **2008**, *602*, 1166-1174.

[103] H. Niehus, W. Heiland and E. Taglauer, *Surface Science Reports* **1993**, *17*, 213-303.

[104] A. Miyakoshi, A. Ueno and M. Ichikawa, *Applied Catalysis A: General* **2001**, *219*, 249-258.

[105] M. Jiang, G.-Z. Bian and Y.-L. Fu, *Journal of Catalysis* **1994**, *146*, 144-154.

[106] F. Xu, Y. Hu, L. Dong and Y. Chen, *Chinese Science Bulletin* **2000**, *45*, 214-219.

[107] X. Huang, H.-J. Zhai, B. Kiran and L.-S. Wang, *Angewandte Chemie International Edition* **2005**, *44*, 7251-7254.

[108] S. Li and D. A. Dixon, *The Journal of Physical Chemistry A* **2006**, *110*, 6231-6244.

[109] E. F. Fialko, A. V. Kikhtenko, V. B. Goncharov and K. I. Zamaraev, *The Journal of Physical Chemistry A* **1997**, *101*, 8607-8613.

[110] Y. H. Jang and W. A. Goddard III, *The Journal of Physical Chemistry B* **2002**, *106*, 5997-6013.

5 Summary and conclusions

Chapter V

Summary and conclusions

In this chapter, a summary of the thesis is given, the main results of this research are explained and the overall conclusions of the thesis are provided. Finally, some indications for future research directions in this subject are given.

5.1. Introduction

The work presented in this thesis was oriented towards a study of well-defined single-crystalline mixed-metal oxide model systems, utilising surface science investigations in ultrahigh vacuum (UHV) conditions. The goal was to learn about the surface chemistry of mixed metal oxide catalyst for oxidation of methanol to formaldehyde.

Samples for this work were produced by the growth of well-ordered molybdenum oxide films onto iron oxide substrates. The molybdenum oxide films, fabricated using the hot filament metal oxide deposition (HFMOD) technique, were used to study their oxide composition and surface structure using several surface characterisation techniques including x-ray photoelectron spectroscopy (XPS), low energy electron diffraction (LEED), low-energy He^+-ion scattering (LEIS), and scanning tunnelling microscopy (STM).

5.2. Iron oxide surfaces

In these experiments, the iron oxide single crystal was prepared by argon ion bombardment and subsequent annealing in oxygen. The p(2×2) reconstruction on clean, well-ordered iron oxide surface was observed after a final oxidation treatment in an oxygen background pressure at 10^{-7} mbar and temperatures of 873 K. The LEED pattern and atomic resolution STM images reveal a lateral repeat distance of 6.2 Å. STM images also show a average step height of about 5 Å corresponding to two oxygen layers which appeared to confirm a structural model of an Fe_3O_4(111) terminated iron oxide substrate. Moreover, XPS measurements on this surface also revealed the relative Fe^{2+} and Fe^{3+} stoichiometry close to that of Fe_3O_4. The binding energy value of the oxide peaks is nearly invariant at ~530.0 eV. The spectral features in the main valence-level spectrum of this oxide surface correspond to the valence-band structures of Fe_3O_4. LEIS measurements showed that both iron and oxygen are contained on the topmost layer of this surface. The best fit structure for this preparation corresponds to an unreconstructed (111) termination of Fe_3O_4 that expose ¼ monolayer (ML) of iron ions over a hexagonal close packed oxygen plane.

5.3. Molybdenum oxide films

The hot-filament metal oxide deposition (HFMOD) technique is a novel method, which is based on the formation of volatile oxide species on the surface of a heated molybdenum filament from reaction between oxygen and molybdenum. The oxygen partial pressure, the filament heating current, and the deposition time are the fundamental parameters to be controlled for the deposition of molybdenum oxide. In these experiments, the molybdenum oxide coverage was measured as a function of the deposition time while the oxygen partial pressure and the filament current were kept constant at 8×10^{-6} mbar and 3.2 A, respectively.

The results from LEED, XPS, LEIS, and STM were used to give a detail analysis of the oxide surface structure. For molybdenum oxide coverage of ~0.2, ~0.3 and ~0.5 MLE MoO_3, the highly resolved STM images show clear hexagonal-shaped atomic distributions with the periods of about 12 Å along the $[1\,\bar{1}\,0]$ and $[1\bar{2}1]$ directions on the $Fe_3O_4(111)$ surface, which corresponds to twice the lattice spacing of the substrate, i.e., 2×5.94 Å in perfect $Fe_3O_4(111)$. A height of the molybdenum oxide island is between 2.0 and 2.5 Å. The STM analysis suggests that the molybdenum oxide clusters supported on iron oxide substrate are adsorbed in the flat-lying manner which their centre might be on the Fe^{3+} site. On small regions of the so-prepared film, a (4×4) structure was observed while the observed LEED pattern does not change. Moreover, XPS measurements revealed the stoichiometry of the deposited material close to that of MoO_3 and the binding energy of Mo 3d XPS is characteristic of Mo^{6+} (fully oxidised). LEIS measurements exhibited the presence of molybdenum, iron, and oxygen at the topmost surface layers. On the basis of results from XPS and STM, we conclude that at coverage of ~0.2, ~0.3, and ~0.5 MLE MoO_3, the molybdenum oxide clusters presumably are the cyclic $(MoO_3)_3$ trimers formed on the iron oxide substrate.

For the growth of thicker layers of molybdenum oxide in coverages of ~1.0 and ~1.5 MLE MoO_3, a blurred p(2×2) LEED mesh was observe. After annealing to 973 K, the p(2×2) LEED pattern was replaced by the $(2\sqrt{3}\times 2\sqrt{3})R30°$ pattern. The molybdenum oxide grew layer by layer forming a very stable first layer on the iron oxide surface. The adsorption configuration can be described by a matrix $\begin{bmatrix} 2 & -2 \\ 2 & 4 \end{bmatrix}$ with reference to hexagonal close-packed oxygen sublattice of the (111) plane of bulk Fe_3O_4. High resolution STM images of the molybdenum oxide film showed a clear hexagonal unit cell with dimensions of $1.1\times1.0\ nm^2 \pm 0.1$ nm which is consistent with the calculation

of the $(2\sqrt{3}\times 2\sqrt{3})$R 30° LEED pattern. The XPS-derived stoichiometry and Fe $2p_{3/2}$ binding energy are found to indicate the presence of Fe^{2+} and Fe^{3+}. LEIS measurements showed the reappearance of iron in the topmost surface layer after molybdenum oxide deposition and annealing it in oxygen afterwards. These results suggest the possibility of formation of iron molybdate. With increasing coverage, different structures with different lattice constants were formed. At a coverage of ~1.5 MLE MoO_3, the high-resolution STM images showed that after 973 K annealing temperature, molybdenum oxide formed well-ordered structure with lattice parameters of 5.02 Å and 4.52 Å, respectively. These results suggest that iron molybdate presumably starts to grow in its bulk structure, forming islands on top of the first layer.

5.4. Future research directions

It would be of interest to conduct further research to better understand the metal-oxide catalysed reaction by an integrated surface science study. As particular reaction, the oxidation of methanol to formaldehyde was chosen, which performed industrially over iron molybdate catalysts. There are some aspects of this research that need further investigation and research. Specifically, the formation of the iron molybdate on the single crystal iron oxide needs to be identified. Raman spectroscopy is utilised to characterise the interactions between molybdenum oxide and single crystal iron oxide, which allows for the observation of vibrational modes associated with the incorporated molybdenum compounds.

Moreover, future research needs to examine the catalytic oxidation mechanism and the surface chemistry of iron molybdate catalysts and the dispersion of active component in Mo-Fe oxide systems to understand the role of the active site on catalytic activity/selectivity during the oxidation reactions. A detailed understanding of the catalytic oxidation mechanism of iron molybdate model catalyst films can be obtained

using temperature-programmed desorption (TPD) technique. The catalytic properties are evaluated for the oxidation of methanol to formaldehyde. Another step is bridging the pressure-gap to obtain information more relevant for real catalysts. To achieve this, the surface science experiments were combined with the catalytic reaction experiments at high pressures which will enable us to understand the structure-reactivity relationships of metal oxide catalysts for a targeted catalyst development.

APPENDICES

APPENDIX A

Calculations of surface concentration of adsorbates

For the surface coverages less than a monolayer, the calculation of surface coverages is given by the Carley-Roberts equations [1]:

$$\sigma_A = \frac{KE_A}{KE_S} \times \frac{I_A}{I_S} \times \frac{\mu_S N \lambda_S \rho_S \cos\phi}{\mu_A M_S} \quad \text{(A-1)}$$

where σ_A is the surface concentration, A is the adsorbate, S is the substrate, KE is the kinetic energy, ϕ is the photoelectron take-off angle with respect to surface normal, μ is the modified photoelectron cross section, I is the integrated peak intensity (or peak area), N is the Avagodro's number, λ_S is the escape depth of photoelectrons through a substrate, M_S is the molar mass of the substrate, and ρ_S is the substrate density.

This expression is used for the calculation of surface coverages less than a monolayer. In the calculation of surface coverages greater than a monolayer, the scattering effect of the adsorbate must be considered.

$KE_{A,\,Mo}$ = 1254.4 eV (for Mo $3d_{5/2}$)

$KE_{S,\,Fe}$ = 776 eV (for $Fe2p_{3/2}$)

$\phi = 0°$ (angle between sample and analyzer)

$\mu_{S,\,Fe\ modified}$ = 18.45 (combined RSF of $2p_{1/2}$ and $2p_{3/2}$)

$\mu_{A,\,Mo\ modified}$ = 10.45 (combined RSF of $3d_{3/2}$ and $3d_{5/2}$)

N (Avagadro's number) = 6.02×10^{23} mol^{-1}

$\lambda_{S,\,Fe}$ for Fe_3O_4 at 776 eV is 16.5 Å = 1.65×10^{-7} cm [2].

M_S = 231.53

ρ_S = 5.18 g cm^{-3}

Therefore, the surface concentration for molybdenum on iron oxide

$$\sigma_A = \frac{1254}{776} \times \frac{I_A}{I_S} \times \frac{18.45 \times 6.02 \times 10^{23} \times 1.65 \times 10^{-7} \times 5.18 \times \cos 0}{10.45 \times 231.53}$$

$$\sigma_A = \frac{1254}{776} \times \frac{I_A}{I_S} \times \frac{9.51 \times 10^{18}}{2419.49}$$

$$\sigma_A = \frac{I_A}{I_S} \times \frac{1.19 \times 10^{22}}{1.88 \times 10^{6}}$$

$$\sigma_A = \frac{I_A}{I_S} \times 6.33 \times 10^{15} \qquad atom/cm^2$$

References

[1] A. F. Carley and M. W. Roberts, *Proc R Soc London Ser A* **1978**, *363*, 403-424.

[2] S. Tanuma, C. J. Powell and D. R. Penn, *Surface and Interface Analysis* **1994**, *21*, 165-176.

APPENDIX B

Calculations of ionization cross-sections

The angular distribution of photoelectrons ionized by unpolarized x-ray impinging on an nl-subshell is given by [1]

$$\sigma'_A = \sigma_A\left[1-\frac{\beta_A}{2}P_2(\cos\gamma)\right] \qquad \text{(B-1)}$$

where β_A is the asymmetry parameter, γ is the angle between photon and photoelectron direction, and $P_2(\cos\gamma) = (3\cos^2\gamma - 1)/2$. The calculated values of the asymmetry parameter, β_A, are illustrated in Figure B-1.

Substitution of $P_2(\cos\gamma) = (3\cos^2\gamma - 1)/2$ into Equation (B-1) and then rearrangement yields

$$\sigma'_A = \sigma_A\left[1+\frac{1}{2}\beta_A\left(\frac{3}{2}\sin^2\gamma - 1\right)\right] \qquad \text{(B-2)}$$

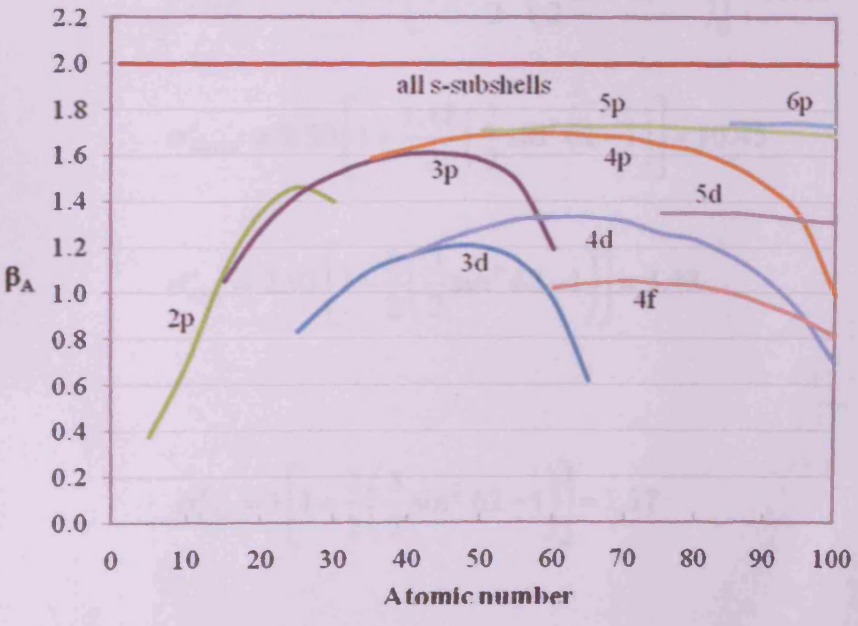

Figure B-1. Calculated asymmetry parameter, β_A, as a function of atomic number for Al Kα (1486.6 eV) x-rays incident on atoms [1].

where β_A for Fe 2p, Mo 3d, and C 1s obtained from Figure B-1 are 1.46, 1.18, and 2 respectively. The angle γ between photon direction (x-ray source) and the electron direction (lens of the analyser) for Omicron's Multiprobe MXSPS system is 62° [2].

The calculated cross-sections should give the overall sum of the multiplets from a given vacancy state and all excitations in the outer orbitals. Thus the cross sections of the interesting samples are equal to

$$\sigma_{Fe2p} = \sigma_{Fe2p_{3/2}} + \sigma_{Fe2p_{1/2}} = 10.82 + 5.60 = 16.42 \quad \text{(B-3)}$$

$$\sigma_{Mo3d} = \sigma_{Mo3d_{5/2}} + \sigma_{Mo3d_{3/2}} = 5.62 + 3.88 = 9.50 \quad \text{(B-4)}$$

$$\sigma_{O1s} = \sigma_{O1s_{1/2}} = 2.93 \quad \text{(B-5)}$$

$$\sigma_{C1s} = \sigma_{C1s_{1/2}} = 1 \quad \text{(B-6)}$$

Substitution of the values of σ_A, β_A, and γ into Equation (B-2). Thus, the modified photoionisation cross sections are

$$\sigma'_{Fe2p} = 16.42\left[1+\frac{1.46}{2}\left(\frac{3}{2}\sin^2 62-1\right)\right] = 18.45 \quad \text{(B-7)}$$

$$\sigma'_{Mo3d} = 9.50\left[1+\frac{1.18}{2}\left(\frac{3}{2}\sin^2 62-1\right)\right] = 10.45 \quad \text{(B-8)}$$

$$\sigma'_{O1s} = 2.93\left[1+\frac{2}{2}\left(\frac{3}{2}\sin^2 62-1\right)\right] = 3.43 \quad \text{(B-9)}$$

and

$$\sigma'_{C1s} = 1\left[1+\frac{2}{2}\left(\frac{3}{2}\sin^2 62-1\right)\right] = 1.17 \quad \text{(B-10)}$$

References

[1] R. F. Reilman, A. Msezane and S. T. Manson, *Journal of Electron Spectroscopy and Related Phenomena* **1976**, *8*, 389-394.

[2] *EA 125 energy analyzer user's guide, version 2.1*, Omicron NanoTechnology GmbH, Taunusstein, Germany, **2002**.

[2] *DAR 400 x-ray source and power supply, version 2.0*, Omicron NanoTechnology GmbH, Taunusstein, Germany, **2000**.

APPENDIX C

Calculations of inelastic mean free paths

The mean free path of the electrons is the average distance an electron can travel between two inelastic interactions (with a loss of kinetic energy). It depends on the nature of the sample and the kinetic energy of the electrons [1].

$$\lambda = E/\left\{E_p^2\left[\beta \ln(\gamma E) - (C/E) + (D/E^2)\right]\right\} \quad \text{(C-1)}$$

In the equation (C-1), λ is the IMFP (in Å), E is the energy of electron (in eV), $E_P = 28.8(N_v \rho / M)^{1/2}$ is the free electron plasmon energy (in eV), ρ is the density (in g.cm^{-3}), N_v is the number of valence electrons per atom (for elements) or molecule (for compounds), and M is the atomic or molecular weight. The terms of β, γ, C, and D are regarded as adjustable parameters which are defined as the following expressions in terms of material parameters [2]:

$$\beta = -0.10 + 0.944/\left(E_p^2 + E_g^2\right)^{1/2} + 0.069\rho^{0.1} \quad \text{(C-2a)}$$

$$\gamma = 0.191\rho^{-0.50} \quad \text{(C-2b)}$$

$$C = 1.97 - 0.91U \quad \text{(C-2c)}$$

$$D = 53.4 - 20.8U \quad \text{(C-2d)}$$

$$U = N_v \rho / M = E_p^2 / 829.4 \quad \text{(C-2e)}$$

where E_g is the bandgap energy (in eV) for nonconductor.

To calculate the IMFP for Fe_3O_4:

$$\lambda = E/\left\{E_p^2\left[\beta \ln(\gamma E) - (C/E) + (D/E^2)\right]\right\} \quad \text{(C-1)}$$

where ρ = 5.18 g.cm^{-3}, N_v = 48, M = 231.53, and E_g = 0.0 eV, we get

$$E_p = 28.8(N_v \rho / M)^{1/2} = 28.8 \times (48 \times 5.18/231.53)^{1/2} = 29.85 \quad eV \quad \text{(C-3)}$$

Therefore, the values of γ, U, C, D, and β are

$$\gamma = 0.191\rho^{-0.50} = 0.191 \times 5.18^{-0.50} = 0.084 \quad \text{(C-4a)}$$

$$U = N_v \rho / M = (48 \times 5.18)/231.53 = 1.07 \quad \text{(C-4b)}$$

$$C = 1.97 - 0.91U = 1.97 - 0.91 \times 1.07 = 0.996 \quad \text{(C-4c)}$$

$$D = 53.4 - 20.8U = 53.4 - 20.8 \times 1.07 = 31.144 \quad \text{(C-4d)}$$

$$\beta = -0.10 + 0.944/\left(E_p^2 + E_g^2\right)^{1/2} + 0.069\rho^{0.1}$$
$$= -0.10 + 0.944/\left(29.85^2 + 0^2\right)^{1/2} + 0.069 \times 5.18^{0.1}$$

$$\therefore \quad \beta = 0.013 \quad \text{(C-4e)}$$

Substitute Equation (C-3) to (C-4e) into the equation (C-1); the IMFP for Fe_3O_4 is

$$\lambda_{776} = 776/\left\{29.85^2\left[0.013\ln(0.084 \times 776) - (0.996/776) + (31.144/776^2)\right]\right\}$$

$$\lambda_{776} = 1.65 \quad nm \quad \text{(C-5)}$$

References

[1] C. J. Powell, A. Jablonski, I. S. Tilinin, S. Tanuma and D. R. Penn, *Journal of Electron Spectroscopy and Related Phenomena* **1999**, *98-99*, 1-15.

[2] S. Tanuma, C. J. Powell and D. R. Penn, *Surface and Interface Analysis* **1994**, *21*, 165-176.

APPENDIX D

Asymmetry parameter, β, for Al K_α (1486.6 eV) x-rays incident on atoms

	Z	β		Z	β		Z	β		Z	β
2p	5	0.38	3d	25	0.83	4d	40	1.16	5p	50	1.71
	10	0.69		30	0.98		45	1.23		55	1.71
	15	1.09		35	1.10		50	1.28		60	1.73
	20	1.35		40	1.16		55	1.32		65	1.73
	25	1.46		45	1.20		60	1.33		70	1.73
	30	1.40		50	1.20		65	1.33		75	1.73
				55	1.14		70	1.31		80	1.72
3p	15	1.05		60	0.97		75	1.26		85	1.72
	20	1.28		65	0.62		80	1.23		90	1.71
	25	1.43					85	1.16		95	1.70
	30	1.52	4p	35	1.59		90	1.06		100	1.69
	35	1.58		40	1.63		95	0.91			
	40	1.61		45	1.67		100	0.69	5d	75	1.35
	45	1.61		50	1.69					80	1.35
	50	1.58		55	1.70	4f	60	1.02		85	1.35
	55	1.48		60	1.70		65	1.04		90	1.34
	60	1.19		65	1.69		70	1.05		95	1.32
				70	1.68		75	1.04		100	1.31
				75	1.65		80	1.03			
				80	1.62		85	1.00	6p	85	1.74
				85	1.56		90	0.95		90	1.74
				90	1.47		95	0.89		95	1.74
				95	1.33		100	0.81		100	1.73
				100	0.99						

References

[1] R. F. Reilman, A. Msezane and S. T. Manson, *Journal of Electron Spectroscopy and Related Phenomena* **1976**, *8*, 389-394.

APPENDIX E

Table E-1. Photoionisation cross sections at 1254 eV in units of the C1s cross section of 22,200 barns [1].

	Z	Total	1s1/2	2s1/2	2p1/2	2p3/2	3s1/2	3p1/2	3p3/2	3d3/2	3d5/2	4s1/2	4p1/2	4p3/2
H	1	0.0032	0.0032											
He	2	0.0087	0.0087											
Li	3	0.0632	0.0593	0.0008										
Be	4	0.207	0.1997	0.0074										
B	5	0.515	0.492	0.0220	0.0001	0.0002								
C	6	1.05	1.00	0.0470	0.0006	0.0012								
N	7	1.87	1.77	0.0841	0.0025	0.0049								
O	8	3.01	2.85	0.1345	0.0073	0.0145								
F	9	4.51	4.26	0.1988	0.0178	0.0352								
Ne	10	6.34	5.95	0.277	0.0381	0.0751								
Na	11	8.60	7.99	0.390	0.0714	0.1406	0.0059							
Mg	12	0.912		0.525	0.1214	0.239	0.0261							
Al	13	1.31		0.68	0.1935	0.380	0.0485	0.0012	0.0023					
Si	14	1.87		0.855	0.292	0.573	0.0726	0.0050	0.0097					
P	15	2.49		1.05	0.422	0.828	0.0998	0.0129	0.0253					
S	16	3.21		1.25	0.590	1.15	0.1302	0.0269	0.0527					
Cl	17	4.15		1.48	0.800	1.55	0.1632	0.0493	0.0964					
Ar	18	5.28		1.71	1.06	2.07	0.1989	0.0823	0.1605					
K	19	6.61		1.95	1.37	2.67	0.249	0.1221	0.238			0.0061		
Ca	20	8.17		2.21	1.74	3.39	0.305	0.1693	0.330			0.0233		
Sc	21	9.90		2.45	2.18	4.24	0.356	0.216	0.420	0.0020	0.0030	0.0273		
Ti	22	11.87		2.72	2.68	5.22	0.408	0.268	0.521	0.0064	0.0095	0.0308		
V	23	14.06		2.98	3.26	6.33	0.462	0.326	0.633	0.0145	0.0213	0.0339		
Cr	24	16.47		3.23	3.92	7.60	0.511	0.382	0.740	0.0303	0.0445	0.0139		
Mn	25	19.18		3.48	4.63	8.99	0.575	0.460	0.892	0.0484	0.0711	0.0398		
Fe	26	22.11		3.70	5.43	10.54	0.634	0.535	1.04	0.0788	0.1156	0.0425		
Co	27	25.25		3.92	6.28	12.23	0.693	0.616	1.19	0.1220	0.1787	0.0451		
Ni	28	28.56		4.16	7.18	13.92	0.753	0.701	1.36	0.1814	0.265	0.0476		
Cu	29	32.18		4.38	8.18	15.87	0.805	0.779	1.50	0.268	0.390	0.0188		
Zn	30	36.25		4.55	9.29	18.01	0.873	0.882	1.70	0.365	0.532	0.0520		
Ga	31	36.17			10.56	20.47	0.945	0.993	1.92	0.485	0.708	0.0742	0.0056	0.0106
Ge	32	27.20				21.22	1.02	1.11	2.15	0.631	0.920	0.0939	0.0179	0.0340
As	33	6.92					1.10	1.24	2.40	0.802	1.17	0.1137	0.0372	0.0710
Se	34	7.99					1.18	1.37	2.65	1.00	1.46	0.1343	0.0642	0.1228
Br	35	9.17					1.26	1.50	2.92	1.24	1.80	0.1557	0.0996	0.1906
Kr	36	10.48					1.35	1.64	3.20	1.50	2.19	0.1779	0.144	0.276
Rb	37	11.91				0.0058	1.43	1.79	3.48	1.81	2.63	0.209	0.1868	0.361
Sr	38	13.47				0.0209	1.52	1.93	3.78	2.15	3.14	0.242	0.230	0.445
Y	39	15.14	0.0128	0.0185	0.0255		1.61	2.08	4.09	2.54	3.70	0.273	0.268	0.521
Zr	40	16.96	0.0353	0.0510	0.0290		1.70	2.24	4.40	2.97	4.33	0.305	0.307	0.596
Nb	41	18.90	0.0816	0.1176	0.0131		1.79	2.39	4.71	3.45	5.01	0.333	0.340	0.661
Mo	42	21.01	0.1296	0.1865	0.0141		1.89	2.58	5.03	3.97	5.77	0.368	0.379	0.739
Tc	43	23.28	0.1915	0.276	0.0149		1.98	2.69	5.36	4.54	6.60	0.397	0.419	0.818
Ru	44	25.71	0.269	0.387	0.0157		2.07	2.88	5.68	5.17	7.51	0.429	0.460	0.899
Rh	45	28.32	0.365	0.524	0.0164		2.15	2.98	6.00	5.84	8.48	0.463	0.501	0.981
Pd	46	31.10	0.495	0.707			2.24	3.12	6.33	6.58	9.54	0.494	0.538	1.06
Ag	47	34.06	0.616	0.884	0.0176		2.33	3.25	6.64	7.36	10.68	0.531	0.586	1.15
Cd	48	37.20	0.747	1.07	0.0464		2.40	3.39	6.96	8.22	11.91	0.571	0.636	1.26

	4d3/2	4d5/2	5s1/2

Table E-1. (continued). Cross sections at 1254 eV in units of 22,200 barns.

	Z	Total	3s1/2	3p1/2	3p3/2	3d3/2	3d5/2	4s1/2	4p1/2	4p3/2	4d3/2	4d5/2	4f5/2	4f7/2
In	49	40.54	2.48	3.51	7.27	9.13	13.23	0.611	0.689	1.37	0.893	1.29		
Sn	50	44.02	2.54	3.62	7.58	10.09	14.63	0.653	0.743	1.48	1.05	1.51		
Sb	51	47.69	2.60	3.71	7.86	11.13	16.13	0.696	0.799	1.60	1.22	1.76		
Te	52	51.51	2.67	3.79	8.14	12.21	17.70	0.741	0.856	1.73	1.40	2.0		
I	53	55.43	2.75	3.87	8.37	13.33	19.33	0.785	0.913	1.86	1.58	2.29		
Xe	54	59.64	2.83	3.95	8.64	14.55	21.08	0.831	0.971	1.99	1.78	2.57		
Cs	55	64.02	2.84	4.04	8.94	15.90	22.93	0.877	1.03	2.12	1.99	2.88		
Ba	56	65.53		4.10	9.26	17.04	24.75	0.924	1.09	2.26	2.21	3.20		
La	57	69.64		4.06	9.52	18.25	26.49	0.971	1.15	2.40	2.44	3.53		
Ce	58	69.82			9.67	19.67	28.57	1.00	1.18	2.49	2.58	3.74	0.0689	0.088
Pr	59	74.30			9.75	21.13	30.72	1.04	1.23	2.60	2.77	4.01	0.1256	0.161
Nd	60	69.16				22.56	32.96	1.07	1.27	2.71	2.96	4.28	0.200	0.257
Pm	61	74.06				24.32	35.33	1.11	1.30	2.81	3.14	4.55	0.296	0.379
Sm	62	79.35				26.12	37.90	1.14	1.34	2.91	3.33	4.82	0.416	0.531
Eu	63	85.36				28.20	40.87	1.17	1.37	3.01	3.51	5.09	0.562	0.718
Gd	64	85.24				24.35	43.43	1.20	1.41	3.13	3.73	5.41	0.693	0.887
Tb	65	89.20					20.80	1.22	1.43	3.21	3.88	5.61	0.949	1.21
Dy	66	19.55						1.25	1.45	3.30	4.05	5.87	1.20	1.52
Ho	67	20.78						1.27	1.47	3.39	4.22	6.13	1.49	1.89
Er	68	22.09						1.29	1.49	3.48	4.39	6.37	1.82	2.31
Tm	69	23.48						1.31	1.50	3.56	4.56	6.62	2.20	2.78
Yb	70	24.97						1.32	1.51	3.64	4.72	6.85	2.63	3.33
Lu	71	26.65						1.34	1.52	3.73	4.91	7.13	3.05	3.87
Hf	72	28.45						1.36	1.53	3.83	5.10	7.42	3.50	4.45
Ta	73	30.35						1.38	1.54	3.93	5.29	7.71	3.99	5.08
W	74	32.36						1.39	1.55	4.03	5.48	8.01	4.52	5.75
Re	75	34.48						1.41	1.55	4.13	5.67	8.31	5.08	6.46
Os	76	36.70						1.42	1.55	4.24	5.86	8.60	5.67	7.22
Ir	77	39.08						1.43	1.55	4.34	6.05	8.90	6.30	8.03
Pt	78	41.50						1.44	1.54	4.45	6.24	9.20	6.97	8.89
Au	79	44.03						1.45	1.53	4.55	6.42	9.50	7.68	9.79
Hg	80	46.63						1.45	1.52	4.65	6.60	9.79	8.43	10.75
Tl	81	49.35						1.46	1.50	4.75	6.78	10.08	9.22	11.77
Pb	82	52.15						1.46	1.47	4.86	6.94	10.37	10.05	12.83
Bi	83	55.03						1.45	1.45	4.96	7.11	10.64	10.93	13.95
Po	84	58.01						1.44	1.42	5.06	7.27	10.92	11.84	15.12
At	85	61.08						1.44	1.38	5.15	7.42	11.20	12.80	16.35
Rn	86	64.22						1.44	1.34	5.24	7.56	11.46	13.80	17.63
Fr	87	67.45						1.44	1.30	5.34	7.69	11.70	14.84	18.97
Ra	88	70.74						1.41	1.26	5.42	7.82	11.95	15.92	20.36
Ac	89	74.34						1.58	1.22	5.50	7.95	12.21	17.05	21.80
Th	90	76.27							1.17	5.59	8.05	12.45	18.21	23.30
Pa	91	79.91							1.12	5.68	8.13	12.66	19.38	24.81
U	92	82.57								5.77	8.21	12.84	20.61	26.38
Np	93	86.45								5.87	8.31	13.02	21.87	28.02
Pu	94	90.56								5.95	8.39	13.22	23.14	29.67
Am	95	94.61								6.03	8.43	13.43	24.44	31.35
Cm	96	98.65								6.08	8.45	13.57	25.80	33.09

Table E-1. (continued). Cross sections at 1254 eV in units of 22,200 barns.

	Z	5s1/2	5p1/2	5p3/2	5d3/2	5d5/2	5f5/2	5f7/2	6s1/2	6p1/2	6p3/2	6d3/2	6d5/2	7s1/2
In	49	0.0626	0.0058	0.0107										
Sn	50	0.0765	0.0169	0.0318										
Sb	51	0.0899	0.0331	0.0629										
Te	52	0.1036	0.0542	0.1040										
I	53	0.1175	0.0805	0.1555										
Xe	54	0.1319	0.1123	0.218										
Cs	55	0.1523	0.1397	0.278					0.0049					
Ba	56	0.1737	0.1661	0.334					0.0171					
La	57	0.1933	0.1887	0.382	0.0187	0.0267			0.0206					
Ce	58	0.1891	0.1805	0.365					0.0178					
Pr	59	0.1958	0.1864	0.378					0.0181					
Nd	60	0.202	0.1917	0.390					0.0183					
Pm	61	0.208	0.1964	0.402					0.0184					
Sm	62	0.213	0.201	0.413					0.0186					
Eu	63	0.219	0.205	0.422					0.0187					
Gd	64	0.235	0.223	0.465	0.0219	0.0306			0.0222					
Tb	65	0.228	0.211	0.440					0.0189					
Dy	66	0.232	0.214	0.449					0.0189					
Ho	67	0.237	0.216	0.457					0.0190					
Er	68	0.240	0.219	0.464					0.0190					
Tm	69	0.244	0.220	0.471					0.0191					
Yb	70	0.247	0.222	0.478					0.0191					
Lu	71	0.261	0.237	0.519	0.0212	0.0290			0.0231					
Hf	72	0.276	0.253	0.562	0.0541	0.0747			0.0261					
Ta	73	0.291	0.268	0.606	0.0976	0.1357			0.0287					
W	74	0.306	0.283	0.651	0.1518	0.212			0.0310					
Re	75	0.322	0.299	0.697	0.217	0.303			0.0330					
Os	76	0.337	0.314	0.743	0.293	0.410			0.0349					
Ir	77	0.350	0.328	0.774	0.431	0.593								
Pt	78	0.366	0.340	0.829	0.508	0.709			0.0167					
Au	79	0.381	0.353	0.877	0.619	0.865			0.0173					
Hg	80	0.397	0.368	0.935	0.707	0.997			0.0410					
Tl	81	0.413	0.383	0.996	0.804	1.13			0.0513	0.0042	0.0079			
Pb	82	0.430	0.398	1.06	0.900	1.29			0.0597	0.0115	0.0233			
Bi	83	0.446	0.412	1.13	0.997	1.44			0.0676	0.0210	0.0456			
Po	84	0.462	0.426	1.19	1.09	1.58			0.0753	0.0329	0.0745			
At	85	0.478	0.439	1.26	1.19	1.73			0.0830	0.0469	0.1099			
Rn	86	0.493	0.451	1.33	1.29	1.88			0.0906	0.0631	0.1520			
Fr	87	0.508	0.462	1.40	1.39	2.04			0.1008	0.0738	0.1928			0.0037
Ra	88	0.523	0.472	1.48	1.49	2.20			0.1109	0.0837	0.230			0.0122
Ac	89	0.537	0.480	1.55	1.60	2.36			0.1207	0.0935	0.262	0.0125	0.0174	0.0152
Th	90	0.551	0.488	1.63	1.70	2.52			0.1301	0.1007	0.293	0.0316	0.0446	0.0176
Pa	91	0.561	0.492	1.69	1.77	2.63	0.1907	0.239	0.1304	0.0986	0.290	0.0138	0.0191	0.0159
U	92	0.572	0.495	1.76	1.85	2.76	0.324	0.407	0.1343	0.1006	0.301	0.0142	0.0196	0.0160
Np	93	0.581	0.497	1.82	1.93	2.88	0.482	0.606	0.1379	0.1022	0.312	0.0145	0.0199	0.0161
Pu	94	0.589	0.496	1.88	1.99	2.98	0.747	0.933	0.1370	0.0988	0.304			0.0138
Am	95	0.596	0.494	1.95	2.07	3.10	0.960	1.20	0.1398	0.0995	0.313			0.0138
Cm	96	0.603	0.492	2.02	2.15	3.25	1.11	1.40	0.1463	0.1042	0.340	0.0149	0.0200	0.0163

References

[1] J. H. Scofield, *Journal of Electron Spectroscopy and Related Phenomena* **1976**, *8*, 129-137.

APPENDIX F

Table F-1. Photoionisation cross sections at 1487 eV in units of the C1s cross section of 13,600 barns [1].

	Z	Total	1s1/2	2s1/2	2p1/2	2p3/2	3s1/2	3p1/2	3p3/2	3d3/2	3d5/2	4s1/2	4p1/2	4p3/2
H	1	0.0002	0.0002											
He	2	0.0083	0.0083											
Li	3	0.0576	0.0568	0.0008										
Be	4	0.202	0.1947	0.0072										
B	5	0.508	0.486	0.0220	0.0001	0.0001								
C	6	1.05	1.000	0.0477	0.0005	0.0010								
N	7	1.89	1.80	0.0867	0.0022	0.0043								
O	8	3.09	2.93	0.1405	0.0065	0.0120								
F	9	4.68	4.43	0.210	0.0161	0.0317								
Ne	10	6.70	6.30	0.296	0.0347	0.0683								
Na	11	9.14	8.52	0.422	0.0654	0.1287	0.0064							
Mg	12	12.11	11.18	0.575	0.1125	0.221	0.0285							
Al	13	1.35		0.753	0.1811	0.356	0.0535	0.0011	0.0022					
Si	14	1.87		0.955	0.276	0.541	0.0808	0.0047	0.0093					
P	15	2.52		1.18	0.403	0.789	0.1116	0.0124	0.0248					
S	16	3.33		1.43	0.567	1.11	0.1465	0.0262	0.0512					
Cl	17	4.31		1.69	0.775	1.51	0.1852	0.0486	0.0947					
Ar	18	5.49		1.97	1.03	2.01	0.227	0.0821	0.1597					
K	19	6.90		2.27	1.35	2.62	0.286	0.1225	0.239			0.0069		
Ca	20	8.55		2.59	1.72	3.35	0.351	0.1720	0.335			0.0268		
Sc	21	10.39		2.91	2.17	4.21	0.411	0.221	0.429	0.0017	0.0025	0.0314		
Ti	22	12.48		3.24	2.69	5.22	0.473	0.276	0.537	0.0055	0.0081	0.0355		
V	23	14.84		3.57	3.29	6.37	0.538	0.339	0.657	0.0125	0.0184	0.0394		
Cr	24	17.43		3.91	3.98	7.69	0.596	0.400	0.773	0.0264	0.0387	0.0161		
Mn	25	20.39		4.23	4.74	9.17	0.674	0.485	0.938	0.0424	0.0622	0.0464		
Fe	26	23.61		4.57	5.60	10.82	0.745	0.569	1.10	0.0694	0.1017	0.0497		
Co	27	27.10		4.88	6.54	12.62	0.818	0.660	1.27	0.1082	0.1582	0.0529		
Ni	28	30.90		5.16	7.57	14.61	0.892	0.757	1.46	0.1619	0.236	0.0560		
Cu	29	34.90		5.46	8.66	16.73	0.957	0.848	1.63	0.240	0.349	0.0221		
Zn	30	39.22		5.76	9.80	18.92	1.04	0.968	1.86	0.330	0.480	0.0618		
Ga	31	44.09		6.07	11.09	21.40	1.13	1.10	2.11	0.442	0.643	0.0882	0.0062	0.0116
Ge	32	49.42		6.31	12.52	24.15	1.23	1.24	2.39	0.578	0.842	0.1119	0.0199	0.0377
As	33	48.73			14.07	27.19	1.32	1.39	2.68	0.741	1.08	0.1357	0.0417	0.0792
Se	34	51.78			13.66	28.90	1.43	1.55	2.98	0.934	1.36	0.1605	0.0724	0.1376
Br	35	9.91					1.53	1.72	3.31	1.16	1.68	0.1863	0.1129	0.215

	4d3/2	4d5/2	5s1/2								
Kr	36	11.34				1.64	1.89	3.65	1.46	2.06	0.213	0.1643	0.312
Rb	37	12.91			0.0070	1.75	2.07	4.00	1.72	2.49	0.251	0.218	0.411
Sr	38	14.62			0.0251	1.85	2.25	4.37	2.06	2.99	0.291	0.265	0.510
Y	39	16.45	0.0125	0.0181	0.0306	1.98	2.48	4.75	2.48	3.54	0.329	0.317	0.599
Zr	40	18.44	0.0348	0.0502	0.0348	2.10	2.64	5.14	2.87	4.17	0.367	0.357	0.689
Nb	41	20.57	0.0812	0.1166	0.0157	2.22	2.84	5.53	3.35	4.86	0.402	0.398	0.767
Mo	42	22.90	0.1298	0.1864	0.0169	2.34	3.04	5.94	3.88	5.62	0.440	0.445	0.860
Tc	43	25.39	0.1934	0.277	0.0179	2.45	3.23	6.36	4.46	6.47	0.479	0.494	0.955
Ru	44	28.08	0.274	0.393	0.0188	2.57	3.44	6.78	5.10	7.39	0.519	0.544	1.05
Rh	45	30.97	0.373	0.535	0.0197	2.70	3.64	7.21	5.80	8.39	0.560	0.595	1.15
Pd	46	34.03	0.510	0.725		2.81	3.83	7.63	6.56	9.48	0.598	0.641	1.24
Ag	47	37.33	0.638	0.911	0.0212	2.93	4.03	8.06	7.38	10.66	0.644	0.700	1.36
Cd	48	40.87	0.778	1.11	0.0558	3.04	4.22	8.50	8.27	11.95	0.692	0.762	1.49

Table F-1. (continued). Cross sections at 1487 eV in units of 13,600 barns.

	Z	Total	3s1/2	3p1/2	3p3/2	3d3/2	3d5/2	4s1/2	4p1/2	4p3/2	4d3/2	4d5/2	4f5/2	4f7/2
In	49	44.59	3.16	4.40	8.93	9.22	13.32	0.742	0.828	1.62	0.935	1.34		
Sn	50	48.54	3.26	4.58	9.35	9.75	14.00	0.794	0.897	1.77	1.11	1.59		
Sb	51	52.73	3.36	4.76	9.77	11.35	16.39	0.848	0.968	1.91	1.29	1.85		
Te	52	57.11	3.46	4.92	10.21	12.52	16.06	0.903	1.04	2.07	1.49	2.14		
I	53	61.70	3.53	5.06	10.62	13.77	19.87	0.959	1.11	2.23	1.69	2.44		
Xe	54	66.52	3.62	5.20	10.99	15.10	21.79	1.02	1.19	2.39	1.92	2.76		
Cs	55	71.46	3.73	5.29	11.38	16.46	23.76	1.08	1.27	2.56	2.15	3.10		
Ba	56	76.65	3.84	5.42	11.71	17.92	25.84	1.13	1.34	2.73	2.40	3.46		
La	57	82.21	3.89	5.55	12.11	19.50	28.12	1.19	1.42	2.91	2.67	3.85		
Ce	58	87.45	3.93	5.66	12.53	21.12	30.50	1.24	1.47	3.03	2.84	4.09	0.0609	0.078
Pr	59	92.91	3.96	5.75	12.94	22.72	32.85	1.28	1.53	3.17	3.07	4.41	0.1115	0.143
Nd	60	94.31		5.75	13.35	24.27	35.29	1.33	1.59	3.31	3.29	4.74	0.1788	0.228
Pm	61	99.79		5.72	13.66	26.08	37.65	1.38	1.64	3.45	3.52	5.07	0.265	0.339
Sm	62	99.90			13.84	27.96	40.37	1.42	1.70	3.59	3.76	5.40	0.374	0.477
Eu	63	106.32			14.30	29.91	43.24	1.46	1.75	3.72	3.99	5.74	0.506	0.647
Gd	64	98.46				31.98	46.23	1.51	1.80	3.88	4.26	6.14	0.630	0.804
Tb	65	104.92				34.20	49.42	1.54	1.84	3.99	4.46	6.41	0.867	1.10
Dy	66	112.10				36.65	52.83	1.58	1.88	4.12	4.69	6.74	1.10	1.39
Ho	67	119.88				39.19	56.66	1.61	1.91	4.24	4.92	7.08	1.37	1.73
Er	68	122.63				36.70	60.42	1.64	1.95	4.37	5.15	7.41	1.69	2.13
Tm	69	68.10					41.01	1.67	1.98	4.48	5.38	7.74	2.05	2.59
Yb	70	28.76						1.70	2.00	4.60	5.61	8.07	2.47	3.11
Lu	71	30.68						1.73	2.03	4.74	5.87	8.45	2.87	3.63
Hf	72	32.74						1.76	2.06	4.88	6.13	8.84	3.32	4.20
Ta	73	34.92						1.79	2.08	5.02	6.40	9.24	3.80	4.82
W	74	37.23						1.81	2.10	5.16	6.68	9.65	4.32	5.48
Re	75	39.67						1.84	2.12	5.30	6.95	10.06	4.88	6.20
Os	76	42.24						1.86	2.13	5.45	7.23	10.48	5.48	6.96
Ir	77	44.99						1.88	2.14	5.59	7.51	10.90	6.12	7.78
Pt	78	47.79						1.90	2.14	5.74	7.78	11.32	6.81	8.65
Au	79	50.75						1.92	2.14	5.89	8.06	11.74	7.54	9.58
Hg	80	53.79						1.94	2.14	6.04	8.33	12.17	8.32	10.57
Tl	81	56.97						1.95	2.13	6.19	8.60	12.60	9.14	11.62
Pb	82	60.25						1.96	2.12	6.33	8.87	13.02	10.01	12.73
Bi	83	63.65						1.96	2.10	6.48	9.14	13.44	10.93	13.90
Po	84	67.17						1.97	2.07	6.62	9.40	13.87	11.90	15.14
At	85	70.79						1.96	2.04	6.77	9.65	14.29	12.92	16.44
Rn	86	74.53						1.95	2.00	6.92	9.90	14.70	14.00	17.81
Fr	87	78.37						1.95	1.97	7.07	10.16	15.11	15.12	19.24
Ra	88	82.33						1.95	1.91	7.20	10.40	15.53	16.30	20.74
Ac	89	86.41						1.95	1.86	7.33	10.61	15.93	17.53	22.30
Th	90	90.58						1.95	1.80	7.46	10.82	16.31	18.81	23.94
Pa	91	94.93						1.92	1.74	7.61	11.04	16.67	20.12	25.60
U	92	99.42						1.90	1.68	7.71	11.25	17.05	21.50	27.36
Np	93	104.17						2.00	1.61	7.83	11.44	17.44	22.91	29.18
Pu	94	106.95							1.54	7.95	11.60	17.81	24.36	31.03
Am	95	111.82							1.47	8.08	11.74	18.14	25.87	32.95
Cm	96	115.41								8.21	11.88	18.43	27.45	34.97

Table F-1. (continued). Cross sections at 1487 eV in units of 13,600 barns.

	Z	5s1/2	5p1/2	5p3/2	5d3/2	5d5/2	5f5/2	5f7/2	6s1/2	6p1/2	6p3/2	6d3/2	6d5/2	7s1/2
In	49	0.0755	0.0069	0.0126										
Sn	50	0.0922	0.0204	0.0377										
Sb	51	0.1085	0.0356	0.0747										
Te	52	0.1251	0.0653	0.1237										
I	53	0.1421	0.0974	0.1894										
Xe	54	0.1596	0.1361	0.260										
Cs	55	0.1843	0.1697	0.332					0.0059					
Ba	56	0.210	0.202	0.400					0.0206					
La	57	0.234	0.230	0.458	0.0205	0.0291			0.0248					
Ce	58	0.230	0.221	0.439					0.0215					
Pr	59	0.238	0.229	0.456					0.0218					
Nd	60	0.247	0.236	0.472					0.0221					
Pm	61	0.254	0.243	0.487					0.0224					
Sm	62	0.261	0.249	0.501					0.0226					
Eu	63	0.268	0.255	0.515					0.0228					
Gd	64	0.286	0.279	0.566	0.0249	0.0347			0.0271					
Tb	65	0.261	0.265	0.539					0.0230					
Dy	66	0.287	0.270	0.551					0.0232					
Ho	67	0.293	0.274	0.562					0.0233					
Er	68	0.298	0.277	0.572					0.0233					
Tm	69	0.303	0.281	0.583					0.0234					
Yb	70	0.308	0.284	0.592					0.0235					
Lu	71	0.326	0.304	0.645	0.0252	0.0341			0.0285					
Hf	72	0.344	0.325	0.699	0.0644	0.0882			0.0322					
Ta	73	0.363	0.346	0.754	0.1168	0.1610			0.0354					
W	74	0.383	0.367	0.811	0.1824	0.252			0.0383					
Re	75	0.402	0.387	0.869	0.261	0.363			0.0408					
Os	76	0.422	0.408	0.928	0.354	0.493			0.0431					
Ir	77	0.438	0.422	0.967	0.524	0.714								
Pt	78	0.459	0.444	1.04	0.620	0.857			0.0207					
Au	79	0.479	0.463	1.10	0.758	1.05			0.0214					
Hg	80	0.500	0.484	1.17	0.869	1.21			0.0508					
Tl	81	0.520	0.505	1.25	0.991	1.39			0.0637	0.0054	0.0098			
Pb	82	0.542	0.526	1.33	1.11	1.58			0.0742	0.0148	0.0291			
Bi	83	0.563	0.546	1.41	1.24	1.76			0.0840	0.0273	0.0568			
Po	84	0.584	0.566	1.50	1.36	1.95			0.0937	0.0428	0.0928			
At	85	0.605	0.584	1.58	1.49	2.14			0.1033	0.0612	0.1370			
Rn	86	0.625	0.602	1.67	1.62	2.33			0.1129	0.0824	0.1895			
Fr	87	0.645	0.618	1.77	1.75	2.53			0.1257	0.0966	0.240			0.0046
Ra	88	0.665	0.633	1.86	1.86	2.73			0.1383	0.1099	0.286			0.0150
Ac	89	0.684	0.647	1.95	2.02	2.94			0.1506	0.1216	0.326	0.0156	0.0215	0.0187
Th	90	0.702	0.660	2.05	2.15	3.15			0.1625	0.1325	0.366	0.0397	0.0552	0.0216
Pa	91	0.718	0.667	2.13	2.25	3.29	0.204	0.255	0.1630	0.1300	0.361	0.0174	0.0237	0.0195
U	92	0.732	0.674	2.22	2.36	3.46	0.349	0.435	0.1682	0.1330	0.375	0.0179	0.0243	0.0197
Np	93	0.746	0.678	2.31	2.46	3.62	0.522	0.652	0.1729	0.1354	0.390	0.0183	0.0248	0.0199
Pu	94	0.758	0.680	2.38	2.56	3.76	0.812	1.01	0.1720	0.1313	0.380			0.0170
Am	95	0.769	0.680	2.47	2.66	3.92	1.05	1.30	0.1758	0.1325	0.391			0.0170
Cm	96	0.780	0.680	2.56	2.78	4.11	1.22	1.52	0.1842	0.1390	0.425	0.0190	0.0251	0.0202

References

[1] J. H. Scofield, *Journal of Electron Spectroscopy and Related Phenomena* **1976**, *8*, 129-137.

APPENDIX G

Calculations of low energy ion scattering energy

According to the classical mechanics, the energy of the scattered ion/particle can be described in a good approximation by this formula [1,2]:

$$\frac{E_1}{E_0} = \frac{M_1^{\,2}}{(M_1 + M_2)^2} \bullet \left\{ \cos\theta \pm \sqrt{\left(\frac{M_2}{M_1}\right)^2 - \sin^2\theta} \right\}^2 \qquad \text{(G-1)}$$

where E_0 is the primary ion energy, θ is the scattering angle, M_1 and M_2 are the primary and scattered ion and target atom mass respectively. Both positive and negative are solutions if $1 > M_2/M_1 > \sin\theta$ and only the positive sign applies to $M_2 > M_1$. This equation directly relates the energy of the scattered particle to the target mass.

In practice, working at a fixed angle ($\theta = 135°$), the primary beam was $^4He^+$ at an incident energy of 1.0 keV. Therefore, the LEIS energy of molybdenum, Mo, (m = 95.94 amu), iron, Fe, (m = 55.845 amu), and oxygen, O, (m = 16 amu) ion

$$\frac{E_{Mo}}{1000} = \frac{4^2}{(4+95.94)^2} \bullet \left\{ \cos 135 + \sqrt{\left(\frac{95.94}{4}\right)^2 - \sin^2 135} \right\}^2$$

$$E_{Mo} = 1.60 \bullet \left\{ \cos 135 + \sqrt{575.28 - \sin^2 135} \right\}^2$$

$$E_{Mo} = 867.24 \ \text{eV}$$

$$\frac{E_{Fe}}{1000} = \frac{4}{(4+55.845)^2} \bullet \left\{ \cos 135 + \sqrt{\left(\frac{55.845}{4}\right)^2 - \sin^2 135} \right\}^2$$

$$E_{Fe} = 4.47 \bullet \left\{ \cos 135 + \sqrt{194.92 - \sin^2 135} \right\}^2$$

$$E_{Fe} = 782.69 \ \text{eV}$$

And finally,

$$\frac{E_O}{1000} = \frac{4}{(4+16)^2} \bullet \left\{ \cos 135 + \sqrt{\left(\frac{16}{4}\right)^2 - \sin^2 135} \right\}^2$$

$$E_O = 40 \bullet \left\{ \cos 135 + \sqrt{16 - \sin^2 135} \right\}^2$$

$$E_O = 417.05 \text{ eV}$$

For an ion energy of 1000 eV, He ions scattered from iron (M_1 = 55.845 amu) were found at an energy of 783 eV, molybdenum (M_1 = 95.94 amu) at 867 eV, and oxygen (M_1 = 16 amu) at 417 eV. The calculated values of the kinematic factor, E_1/E_0, at 135° scattering angle are illustrated in Figure G-1.

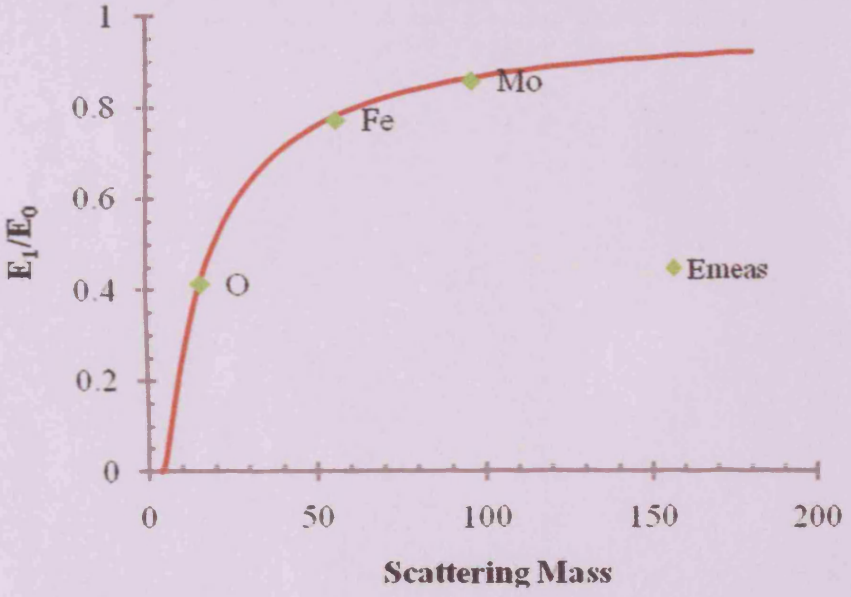

Figure G-1. Positions of the peaks in the energy spectra for scattering from various elements; data are taken at primary energy of 1000 eV. The scattering angle is 135°. The solid line is calculated using equation (G-1).

A comparison between the calculated peak positions according to equation (G-1) and experimental results is given in Figure G-1 and small deviations are detected. The measured energies of He^+ ions backscattered at the surface are in good agreements with the energy positions expected from the binary-collision [2] (see Figure G-1).

References

[1] J. C. Vickerman, *Surface analysis : the principal techniques*, Wiley, Chichester, **1997**.

[2] H. Niehus, W. Heiland and E. Taglauer, *Surface Science Reports* **1993**, *17*, 213-303.